

# CONTROLLING MOTION IN QUANTUM LOGIC CLOCKS

Von der Fakultät für Mathematik und Physik  
der Gottfried Wilhelm Leibniz Universität Hannover  
zur Erlangung des Grades

DOKTOR DER NATURWISSENSCHAFTEN

Dr. rer. nat.

genehmigte Dissertation  
von

Dipl.-Phys. Jannes Bernhard Wübbena

geboren am 17.07.1986, in Hannover

2014



# CONTROLLING MOTION IN QUANTUM LOGIC CLOCKS

JANNES B. WÜBBENA



Referent: Prof. Piet O. Schmidt  
Korreferent: Prof. Christian Ospelkaus  
Korreferent: Prof. Patrick Gill  
Tag der Promotion: 09.07.2014  
Hannover, 2014



## ABSTRACT

---

In first demonstrations, quantum logic clocks based on single trapped aluminum ions have outperformed the best primary caesium standards by more than one order of magnitude in terms of relative frequency accuracy and qualify as a candidate for a future redefinition of the second. Further improvements of the accuracy require a reduction of the ion's motion, which accounts for more than 80% of the remaining inaccuracy of realized clocks.

In this work, a second generation aluminum ion clock is prepared and possible ways to overcome the present limitations are evaluated. The aluminum ion must be sympathetically laser cooled, and so far beryllium and magnesium ions have been chosen for this task. Here, the potential use of calcium ions is investigated theoretically. The resulting cooling limit in the presence of realistic external heating rates is a factor of roughly 2 lower than for magnesium and comparable to beryllium.

Most of the apparatus for the new clock has been set up and first characterizing measurements with single calcium ions are presented. A novel, high bandwidth phase transfer lock is implemented, that effectively transfers the phase stability of an optical reference to otherwise unstabilized commercial diode lasers via a frequency comb. Phase coherence between lasers ranging from 397 nm to 1542 nm is achieved and laser linewidths of less than 3 kHz are measured. A laser stabilized this way is used to perform sideband ground state cooling of calcium with final ground state populations of 97% and to implement more than 97% fidelity coherent electronic state flops, meeting the requirements for the quantum logic gates necessary in aluminum ion clocks.

The phase coherence of the transfer laser lock allowed the first demonstration of double-EIT cooling, where quantum interference between optical transitions separated by more than 400 THz is used to perform ground state cooling without any heating processes up to 3rd order in the Lamb Dicke parameter. Rapid cooling to the ground state with characteristic cooling times of 5  $\mu$ s is achieved. Simulations indicate that EIT cooling can be used to reduce the secular motion contribution in future quantum logic clocks by one order of magnitude.

The demonstrated experimental techniques might also prove useful outside of metrology, for example in quantum information processing, where they enable rapid ground state cooling of multiple modes and fast Raman processes between optically separated states.

**Keywords:** Quantum Optics, Atomic Clocks, Metrology

## ZUSAMMENFASSUNG

---

Quantenlogikuhren basierend auf einzelnen gefangenen Aluminium-Ionen haben die besten primären Caesium-Frequenzstandards um mehr als eine Größenordnung bezüglich der relativen Frequenzgenauigkeit übertroffen. Für weitere Verbesserungen der Genauigkeit ist eine Verringerung der Ionenbewegung notwendig, die momentan mehr als 80 % des Fehlerbudgets dieser Uhren ausmacht.

In dieser Arbeit wird eine Aluminium-Ionenuhr der zweiten Generation vorbereitet, wobei Möglichkeiten evaluiert werden, die Limitierungen der gegenwärtigen Uhren zu überwinden. Das Aluminium-Ion muss mit Hilfe eines zweiten Ions Laser-gekühlt werden, wofür bis jetzt Beryllium und Magnesium-Ionen genutzt wurden. Hier wird die Verwendung von Calcium Ionen für diese Aufgabe theoretisch untersucht. Das erreichbare Kühllimit bei realistischen externen Heizraten ist circa einen Faktor 2 geringer als für Magnesium und vergleichbar mit Beryllium.

Die experimentelle Apparatur für die zukünftige Uhr wurde aufgebaut und erste Messungen mit einzelnen Calcium-Ionen werden präsentiert. Ein Phasentransferlock mit hoher Bandbreite ist verwirklicht, der die Stabilität einer optischen Referenz auf nicht vorstabilisierte kommerzielle Diodenlasersysteme überträgt. Phasenkohärenz zwischen Lasern mit Wellenlängen von 397 nm bis 1542 nm wird hiermit erreicht und optische Linienbreiten unter 3 kHz werden gemessen. Ein so stabilisierter Laser wird verwendet, um einzelne Calcium-Ionen seitenbandzukühlen, wobei Grundzustandsbesetzungen von etwa 97 % erzielt werden. Zudem werden interne elektronische Zustandsmanipulationen von mehr als 97 % Güte demonstriert, die für die Quantenlogik-Gatter der zukünftigen Uhr notwendig sind.

Die Phasenkohärenz des Transferlocks erlaubte zudem die erste experimentelle Realisierung von Doppel-EIT-Kühlen. Dort wird die Quanteninterferenz zwischen optischen Übergängen, die mehr als 400 THz voneinander getrennt sind, verwendet, um Grundzustandskühlen ohne Heizprozesse bis zur dritten Ordnung im Lamb-Dicke-Parameter durchzuführen. Schnelles Grundzustandskühlen mit Kühlzeiten von 5  $\mu$ s wird erreicht. Durchgeführte Simulationen deuten an, dass die Sekularbewegung in Quantenlogikuhren mit Hilfe von EIT-Kühlen um eine Größenordnung verringert werden kann.

Die experimentellen Techniken könnten zudem außerhalb der Metrologie Verwendung finden, beispielsweise in der Quanteninformatonsverarbeitung, wo sie schnelles Grundzustandskühlen von mehreren Moden oder effiziente Raman-Prozesse zwischen optisch getrennten Zuständen erlauben.

**Schlagworte: Quantenoptik, Atomuhren, Metrologie**

# CONTENTS

---

<b>i</b>	<b>INTRODUCTION</b>	<b>1</b>
1	INTRODUCTION	3
2	THE QUANTUM LOGIC CLOCK	7
2.1	Atomic clocks . . . . .	7
2.1.1	Figures of merit of atomic clocks . . . . .	8
2.2	The aluminum ion quantum logic clock . . . . .	9
2.2.1	Error budget of aluminum ion clocks . . . . .	12
<b>ii</b>	<b>THEORY</b>	<b>15</b>
3	MOTION IN ION TRAPS	17
3.1	Equations of motion of ions in Paul traps . . . . .	18
3.2	Linear Paul traps . . . . .	19
3.3	Excess micromotion . . . . .	23
3.4	Two ion crystals . . . . .	23
4	QUANTUM MECHANICAL DESCRIPTION OF MOTION AND ATOM LIGHT INTERACTION	27
4.1	Stability of the QM equations of motion . . . . .	27
4.2	Quantum mechanical basis states . . . . .	28
4.3	Thermal states . . . . .	28
4.4	Atom light interactions . . . . .	29
4.5	Temperature measurements . . . . .	32
4.6	Calcium level scheme . . . . .	33
5	LASER COOLING	35
5.1	General approach to cooling in an ion trap . . . . .	35
5.2	Doppler Cooling . . . . .	38
5.2.1	Realization in calcium . . . . .	38
5.3	Sideband cooling . . . . .	38
5.3.1	Realization in calcium . . . . .	39
5.4	EIT-cooling . . . . .	40
5.4.1	Dressed atom - the Fano profile . . . . .	42
5.4.2	Single EIT cooling . . . . .	44
5.4.3	Double-EIT cooling . . . . .	45
5.4.4	Noise sensitivity of EIT cooling . . . . .	46
5.4.5	Realization in calcium . . . . .	48
5.4.6	Simulations of EIT cooling . . . . .	50
5.4.7	Discussion of the simulations . . . . .	51
6	DOPPLER COOLING OF TWO ION CRYSTALS	53
6.1	Cooling and heating rates . . . . .	53
6.1.1	External heating influence on axial modes . . . . .	55
6.1.2	External heating influence on radial modes . . . . .	56
6.1.3	Micromotion considerations . . . . .	57

6.1.4	Total Doppler shift in aluminum ion quantum logic clocks for different cooling ion species . . .	58
6.2	Cooling times . . . . .	59
iii	<b>EXPERIMENT</b>	65
7	<b>EXPERIMENTAL SETUP</b>	67
7.1	Vacuum setup . . . . .	67
7.2	Evaporation ovens . . . . .	68
7.2.1	Oven design . . . . .	68
7.2.2	Oven temperature and time constant . . . . .	69
7.3	Ion trap . . . . .	71
7.3.1	Design . . . . .	71
7.3.2	Alignment and x-ray tomography . . . . .	72
7.3.3	FEM simulations . . . . .	72
7.3.4	Thermal characterization of the ion trap . . . . .	77
7.4	Trap voltage supply . . . . .	77
7.5	The laser system . . . . .	79
7.5.1	Calcium ionization lasers . . . . .	80
7.5.2	Calcium repump lasers . . . . .	81
7.5.3	Calcium doppler cooling and detection laser . . . . .	82
7.5.4	Calcium sideband cooling and logic laser . . . . .	84
7.5.5	Vacuum chamber breadboard . . . . .	84
7.6	Imaging optics . . . . .	86
7.7	Experiment control system . . . . .	87
8	<b>FREQUENCY COMB AND LASER LOCKS</b>	89
8.1	The frequency comb . . . . .	90
8.2	Phase stability transfer via the frequency comb . . . . .	90
8.2.1	The noise contributions in fiber frequency combs . . . . .	92
8.2.2	Locking of the repetition rate and offset frequency . . . . .	92
8.2.3	Transfer lock scheme . . . . .	94
8.2.4	Rabi flop error for observed phase noise . . . . .	95
9	<b>EXPERIMENTS</b>	99
9.1	Loading of single ions . . . . .	99
9.1.1	Fluorescence detection . . . . .	100
9.2	The calcium transitions . . . . .	101
9.2.1	The 397 nm transition . . . . .	101
9.2.2	The 866 nm transition . . . . .	104
9.2.3	The 729 nm transition . . . . .	106
9.3	Micromotion compensation . . . . .	107
9.3.1	Camera method . . . . .	108
9.3.2	Parametric heating method . . . . .	109
9.3.3	Micromotion sideband spectroscopy . . . . .	109
9.4	Cooling experiments . . . . .	111
9.4.1	Doppler cooling . . . . .	111
9.4.2	Sideband cooling . . . . .	112
9.5	EIT cooling . . . . .	117



<b>iv</b>	<b>OUTLOOK AND SUMMARY</b>	<b>123</b>
<b>10</b>	<b>OUTLOOK AND SUMMARY</b>	<b>125</b>
10.1	Aluminum ion quantum logic clock error budget prediction . . . . .	125
10.2	Summary of the thesis . . . . .	128
<b>v</b>	<b>APPENDIX</b>	<b>131</b>
<b>A</b>	<b>APPENDIX</b>	<b>133</b>
A.1	Derivation of the two ion Doppler cooling and heating rates . . . . .	133
A.2	Doppler Shift Contribution of Intrinsic Micromotion .	134
A.3	Estimation of the double-EIT cooling noise sensitivity .	137
A.4	Double-EIT cooling Hamiltonian . . . . .	139
	<b>BIBLIOGRAPHY</b>	<b>141</b>

## LIST OF FIGURES

---

Figure 1	Working principle of atomic clocks . . . . .	8
Figure 2	The electron shelving technique . . . . .	10
Figure 3	Aluminum level scheme . . . . .	11
Figure 4	Quantum logic spectroscopy . . . . .	11
Figure 5	Stability diagram of Mathieu’s equation . . . . .	19
Figure 6	Linear ion trap . . . . .	20
Figure 7	Single ion trajectory . . . . .	21
Figure 8	Normal mode frequencies and normalized amplitudes for a two-ion two-species crystal . . . . .	26
Figure 9	Relative transition strengths of carrier and sideband transitions . . . . .	32
Figure 10	$^{40}\text{Ca}^+$ level scheme . . . . .	34
Figure 11	Elementary cooling and heating processes . . . . .	37
Figure 12	Doppler cooling in $^{40}\text{Ca}^+$ . . . . .	39
Figure 13	Sideband cooling in $^{40}\text{Ca}^+$ . . . . .	41
Figure 14	Comparison between Doppler and sideband Cooling . . . . .	42
Figure 15	EIT cooling schemes . . . . .	43
Figure 16	EIT cooling resonance . . . . .	44
Figure 17	Double-EIT cooling resonance . . . . .	47
Figure 18	Double-EIT cooling in $^{40}\text{Ca}^+$ . . . . .	49
Figure 19	Simulation of double-EIT . . . . .	50
Figure 20	Detuning dependence of optimal Rabi frequencies and EIT cooling limit . . . . .	52
Figure 21	Normalized axial clock ion energy vs. mass ratio . . . . .	56
Figure 22	Normalized radial clock ion energy plotted against the mass ratio . . . . .	57
Figure 23	Total clock ion energy of a clock ion in a Doppler cooled crystal along one radial direction . . . . .	58
Figure 24	Comparison of secular motion-induced second-order Doppler shifts for $\text{Al}^+/\text{X}^+$ crystals with different cooling ions . . . . .	59
Figure 25	Time needed to cool an $\text{Al}^+/\text{Ca}^+$ ion pair from 19.3 K to 1000 Doppler limits . . . . .	61
Figure 26	Cooling evolution of an $\text{Al}^+/\text{Ca}^+$ ion pair after a collision event with an $\text{H}_2$ -molecule . . . . .	62
Figure 27	Vacuum setup . . . . .	67
Figure 28	Evaporation temperatures of calcium and aluminum . . . . .	69
Figure 29	Evaporation oven design . . . . .	70
Figure 30	Oven temperature and time constant . . . . .	70

Figure 31	Photographs of the ion trap . . . . .	71
Figure 32	Computer tomography of the ion trap . . . . .	73
Figure 33	Comparison of trap wiring schemes . . . . .	73
Figure 34	Simulation of the DC potential . . . . .	74
Figure 35	Simulation of the RF potential . . . . .	75
Figure 36	Temperature characterization of the ion trap .	78
Figure 37	CAD drawing of the helical resonator . . . . .	79
Figure 38	Quality factor of the loaded helical resonator .	80
Figure 39	Symmetry of the helical resonator . . . . .	81
Figure 40	Reduced $^{40}\text{Ca}$ level scheme . . . . .	81
Figure 41	423 nm laser system . . . . .	82
Figure 42	Repump laser system . . . . .	82
Figure 43	Cooling/Detection laser system . . . . .	83
Figure 44	Calcium logic laser system . . . . .	84
Figure 45	Optical access to ion trap . . . . .	85
Figure 46	Simulations and measurements of the beam radius for 397 nm and 866 nm light emerging from the PCF . . . . .	87
Figure 47	Output spectrum of a frequency comb . . . . .	89
Figure 48	Schematics of the frequency comb . . . . .	91
Figure 49	Lock of the repetition rate . . . . .	93
Figure 50	Phase noise of the frequency comb and 729 nm laser . . . . .	94
Figure 51	Transfer lock schematic . . . . .	96
Figure 52	Expected phase noise induced Rabi flop error	97
Figure 53	Camera imaging of two $^{40}\text{Ca}^+$ -ions . . . . .	100
Figure 54	Dark and bright state histograms . . . . .	101
Figure 55	Interleaved spectroscopy scheme . . . . .	103
Figure 56	397 nm frequency scan and spectroscopy stability	104
Figure 57	Comparison of the 397 nm transition absolute frequency measurement with previous experiments . . . . .	105
Figure 58	Dark state spectroscopy . . . . .	106
Figure 59	Spectroscopy of motional sidebands . . . . .	107
Figure 60	Radial trap frequency RF power dependence and narrow line scan . . . . .	108
Figure 61	Micromotion compensation by sideband spectroscopy . . . . .	110
Figure 62	Doppler cooling performance . . . . .	112
Figure 63	Generic sideband cooling sequence . . . . .	113
Figure 64	Sideband cooling results . . . . .	114
Figure 65	Heating rate measurement . . . . .	116
Figure 66	Rabi flopping results . . . . .	117
Figure 67	Double-EIT cooling results . . . . .	120
Figure 68	Relative micromotion energy of the clock ion in the in-phase and out-of-phase radial modes	136

Figure 69	Double-EIT cooling noise estimation . . . . .	138
-----------	---	-----

## LIST OF TABLES

---

Table 1	Error budget of Al <sup>+</sup> clocks . . . . .	12
Table 2	Simulated electric field gradients . . . . .	76
Table 3	Error budget of 397 nm absolute frequency measurement . . . . .	105

## ACRONYMS

---

AC	alternating current
AOM	acusto optical modulator
ASE	amplified spontaneous emission
BSB	blue sideband
CAR	carrier
CIPM	International Committee for Weights and Measures
CMI	Czech Metrology Institute
CW	continuous wave
DC	direct current
DDS	direct digital synthesizer
ECDL	external cavity diode laser
EDFA	erbium doped fiber amplifier
EIT	electromagnetically induced transparency
EMCCD	electron multiplied charge coupled device
EMRP	European Metrology Research Programme
EOM	electro optical modulator
FEM	finite element method
FPGA	field programmable gate array

FWHM full width at half maximum

HNLF highly nonlinear fiber

MIKES Centre for Metrology and Accreditation - Finland

PCF photonic crystal fiber

PD photo detector

PID proportional-integral-derivative

PLL phase locked loop

PMMA polymethyl methacrylate, also Plexiglas

PMT photomultiplier tube

PTB Physikalisch-Technische Bundesanstalt

QM quantum mechanical

RF radio frequency

RSB red sideband

SA spectrum analyzer

SI International System of Units

SM-PM single mode, polarization maintaining (fiber)

TA tapered amplifier

ULE ultra low expansion glass

## SYMBOLS FOR FREQUENCIES

---

In this thesis, several different types of frequencies appear. The mathematical symbols were chosen so that the type of frequency discussed is obvious from the symbol used. These are:

$\Omega_{\text{RF}}$  for the ion trap drive angular frequency

$\nu$  for secular motion trap angular frequencies

$\omega$  for optical laser angular frequencies

$\Delta$  for laser detuning angular frequencies

$\Gamma$  for optical transition linewidths in angular frequencies

$\Omega$  for laser interaction Rabi angular frequencies

$f$  for noise Fourier frequencies (not angular)



Part I

INTRODUCTION





## INTRODUCTION

---

*"When you aim for perfection, you discover it's a moving target."*  
George Fisher

The measurement of time is a basis for human civilization and already the ancient cultures used calendars for timekeeping, the earliest reports of which date back more than 5000 years [68]. These calendars and all absolute timescales until the second half of the twentieth century were based on astronomical observations of the day, month or year which provided a natural, highly precise timescale, available to everyone by looking into the sky. Especially the solar day, defined as the duration between two successive transits of the Sun at local meridian [8] served as a metronome for the organization of human life. The day has therefore also been used to define shorter time intervals as parts of the day, known as hours, minutes and seconds. In ancient times, a half day was divided into twelve hours between sunrise and sunset with the consequence that depending on local latitude the hour could vary strongly during the time of year, for example in Hannover by a factor of circa 2.2 between June and December. The equinoctial hours defined as a twentyfourth of a solar day represented a first improvement to this definition. However, also the length of a solar day varies by roughly 0.06% during the year because of the combined effects of the ellipticity of the earth's orbit around the sun and the tilting of earth's rotation axis relative to the ecliptic[112]. Known to astronomers for many centuries [132], this effect only became relevant for practical timekeeping when mechanical clocks were stable enough to measure it. It was corrected by the definition of the mean solar day as the average length of a solar day during a year [8]. History repeated itself when, by the use of quartz clocks, it was found that the length of a mean solar day also fluctuates, this time on the order of  $10^{-3}$  s a day [153]. After the invention of the Cs atomic clock [51], the International Committee for Weights and Measures (CIPM) therefore decided in 1967 to decouple the definition of the second as the unit of time from astronomical observations and instead define it by the use of a physical constant as *the duration of 9,192,631,770 periods of the radiation corresponding to the transition between the two hyperfine levels of the ground state of the caesium 133 atom* [168, 14].

Time and frequencies have henceforth developed into the physical quantities that can be measured with the highest precision and accuracy. Many other quantities are measured by transferring their value into a frequency together with a precise determination of the latter.

Examples include the measurements of velocities by the Doppler effect or voltages via the Josephson effect [141]. Another unit of the international system of units (SI), the meter, is defined by fixing the speed of light to be exactly 299,792,458 m/s. Any realization of the SI meter therefore requires a frequency measurement traceable to the primary realizations of the SI second. It is planned that with the next generation of SI definitions, *all* units except the mol will be linked to the second, making the primary atomic clocks a reference for almost all measurements performed by mankind [106, 107].

The suitability of atomic transition frequencies for a definition of time was already suggested in the nineteenth century by Maxwell and Kelvin [56], pointing out that atoms of a certain species are all "absolute alike in every physical property" [81] and the light emitted by them would be "independent of any changes in the dimensions of the earth" [101]. These are still the main reasons for the success of atomic frequency standards. But while the emitted or absorbed radiation does not depend on the dimensions of the earth, it does depend on the environment of the atoms. Especially the electromagnetic and gravitational potentials and the motion of the atoms relative to the observer induce significant frequency shifts between the observed and unperturbed transitions. Since the atomic definition of the second, it has hence been the duty of time and frequency metrologists to characterize these dependencies and realize the ideal, unperturbed frequency of the atomic clocks as accurately as possible.

Different ways have been implemented to prepare the atoms in a way that the uncertainties of the frequency shifts can be reduced further and further, including the use of thermal beams [51], laser cooled atoms in atomic fountains [29] and atoms in optical lattices [165, 186]. Yet another approach is the preparation of charged atoms in electrodynamic Paul traps which stands out because of the possibility to confine single atomic particles in vacuum in the center of a steep trapping potential, where the trapping fields vanish. This comes already quite close to the ideal case of resting atoms in free space without any background fields.

Different atomic species are currently used in single ion frequency standards, including  $\text{Sr}^+$  [46],  $\text{Hg}^+$  [121],  $\text{Yb}^+$  [73, 85],  $\text{In}^+$  [134] and  $\text{Al}^+$  [24, 148]. Out of these, a clock based on  $\text{Al}^+$  has achieved the lowest fractional frequency uncertainty in the realization of the unperturbed transition of all ion clocks. Its uncertainty of 8.6 parts in  $10^{-18}$  was only recently outperformed by a neutral Sr lattice clock [16]. The success of the  $\text{Al}^+$  clock can to a large extent be traced to the very low sensitivity to thermal blackbody radiation [146, 151, 108]. This is due to an almost exact cancellation of the polarizability of the two clock states, leading to room temperature relative frequency shifts one to two orders smaller in magnitude than for most other investigated atomic species.

The use of aluminum ions does, however, also have drawbacks. Most of these can be directly linked to their relatively small mass of 27 atomic mass units. This implies that at similar temperatures, aluminum ions have significantly higher velocities than the other, substantially heavier ions used for clocks. Doppler shifts, which scale with the squared velocity are therefore increased. This means that for the best  $\text{Al}^+$  standard, 86% of the remaining uncertainty can be attributed to ion motion and the required cooling. To overcome the dominant motional limits, a next-generation  $\text{Al}^+$  clock must replace the Doppler laser cooling technique used in prior experiments with a scheme realizing sub-Doppler temperatures. Sideband cooling [114] as frequently used in ion trapping experiments achieves this but proves difficult to implement once multiple modes must be cooled simultaneously. A technique called electromagnetically induced transparency (EIT) cooling [110, 144] has successfully been implemented to cool multiple modes of an ion crystal close to the motional ground state [94] and promises to be useful also in  $\text{Al}^+$  ion clock experiments.

The focus of this work is to investigate the motion of one or two laser-cooled ions confined in a Paul trap both theoretically and experimentally with the aim to prepare the realization of a single aluminum ion quantum logic clock with a fractional frequency uncertainty of a few parts in  $10^{-18}$ . The thesis is structured as follows:

In Chapter 2 the working principle of atomic clocks and more specific that of  $\text{Al}^+$  quantum logic clocks is introduced, motivating the use of a cooling/logic ion of a different species in these devices. Chapter 3 revisits the motional dynamics of particles confined in a linear Paul ion trap, and focuses on the special case of two simultaneously trapped particles of unequal mass. In Chapter 4, the quantum mechanical (QM) description of a trapped ion is given and extended to incorporate the interaction with laser fields. These results are applied in Chapter 5, where the traditional Doppler cooling and sideband cooling techniques as well as the novel EIT-cooling with single and double quantum interference are treated theoretically. Simulation results of Doppler cooling of two-ion crystals in the presence of external heating are presented in Chapter 6, ending the theoretical part of this work.

Chapter 7 then commences the experimental part by giving a detailed account of the setup that was used to perform the measurements described later. This includes the vacuum setup, the laser system and the trap apparatus. The frequency comb and the optical phase locks that were implemented to realize double-EIT cooling are described in Chapter 8. The measurements on single ions are afterwards presented in Chapter 9. There, the characterization of the laser system, including absolute frequency measurements of some of the atomic transitions in  $^{40}\text{Ca}^+$ , Doppler and sideband cooling results as

well as the first experimental results on double-EIT-cooling are presented.

The thesis then concludes in Chapter 10 with a prediction of the error budget of the future  $\text{Al}^+$  quantum logic clock being assembled in this setup and an outlook describing the next experimental steps required to realize it. A summary of the scientific achievements and how they might prove useful also outside metrology laboratories is given.

Out of all possible means to measure time, atomic clocks are the most long term stable and accurate solutions. This is due to mainly two reasons. First, atomic transitions provide robust oscillators with frequencies that are only weakly perturbed by external influences. And second, it is possible to prepare the atoms in well controlled states so that the remaining perturbations can be characterized and reproduced to a high degree. These characteristics do, however, also impose restrictions on the choice of suitable species used in atomic clocks. Candidates should provide both an excellent clock transition that is exceptionally insensitive to perturbations and at the same time the necessary transitions required for the state preparation and detection schemes.

In quantum logic clocks, these requirements are separated onto two different species. One, owing a remarkable clock transition and another one being well suited for the preparation tasks. This way, a much broader range of species comes available to choose from, potentially enabling a performance gain compared to traditional atomic clocks.

In this chapter the quantum logic clock is introduced by first reviewing the general operating principle of atomic clocks before presenting a description of the quantum logic clocks that operated till date. The chapter concludes with an outlook on how this thesis work aims to overcome some of the remaining limitations of these clocks.

## 2.1 ATOMIC CLOCKS

Any clock consists of two main constituents being first a stable oscillator producing a periodic signal and second a clockwork measuring the phase or the cycles of the oscillator. If the clockwork is dropped, one is left with what is called a *frequency standard* that can be used as a frequency reference but not to measure time. Frequency standards are divided into active and passive standards [141]. In active standards, the frequency stability and accuracy is derived directly from the oscillator itself as for example in active hydrogen masers, lasers, quartz crystals or sun dials. In passive standards, a steerable oscillator is used to interrogate a medium that shows a well defined frequency dependent response to this interrogation. This response signal is then used in a feedback loop to lock the oscillators frequency to the medium. Examples are macroscopic optical and microwave resonators and atomic clocks. In the latter, the frequency dependent

medium are single or multiple atoms of the same species that have an absorption line at a well defined frequency.

Figure 1 shows this working principle of passive atomic clocks in a simplified sketch. Atomic clocks are divided into two different classes, microwave and optical clocks depending on the frequency range of the deployed oscillator. The working principle is the same for both. A laser (optical clocks) or microwave oscillator produces a signal at a frequency that is close to the atoms absorption line  $\omega_a$  but additionally carries some noise  $n(t)$ . The atoms are prepared in the ground state  $|\downarrow\rangle$  and then interrogated for some time. After this interrogation, the atom can either still be in the ground state when no transition took place or in the excited state  $|\uparrow\rangle$  if the transition took place. The state of the atoms is detected by a state detector and the resulting signal is some function of the noise  $n(t)$  which is fed back to the laser/oscillator to correct its frequency. In microwave clocks the counter used to count this frequency is available electronically but in optical clocks a frequency comb [138, 80, 41] is typically used to first divide the signal into a lower frequency regime, where electronic counting is possible.

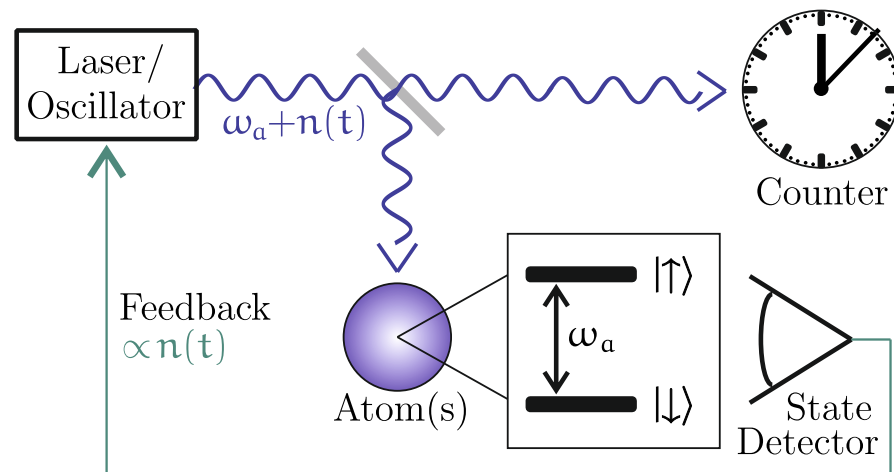


Figure 1: Working principle of atomic clocks. A laser or microwave oscillator generates an electromagnetic signal around the atomic absorption frequency  $\omega_a$  that is used to interrogate the atom(s). Deviations  $n(t)$  from the absorption line are measured by detecting the atoms state and fed back to the oscillator to keep it locked to the atomic resonance. This stabilized frequency is counted to establish a clock.

### 2.1.1 Figures of merit of atomic clocks

There are two important figures of merit needed to assess the performance of a clock, stability and accuracy. Stability of a clock or frequency standards refers to the absence of large discrepancies of frequency measurements performed at different times. It is most of-

ten expressed in terms of the Allan deviation  $\sigma(\tau)$  [1, 2] defined as

$$\sigma^2(\tau) = \frac{1}{2} \langle (\bar{N}(t+\tau) - \bar{N}(t))^2 \rangle. \quad (1)$$

where  $\bar{N}(t) = \frac{1}{\tau} \int_t^{t+\tau} \frac{n(t')}{\omega_a} dt'$  is the average fractional frequency deviation of the oscillator between times  $t$  and  $t + \tau$ . The  $\langle \cdot \rangle$  brackets denote the expectation value for measurements at arbitrary  $t$ . The Allan deviation gives the expectation value for the squared difference of consecutive relative frequency measurements where each measurement is an average over time  $\tau$ . It provides both the information on how long the frequency standard needs to be averaged to achieve certain measurement precisions and at what timescales the standard potentially worsens due to e.g. drifts. Additionally it allows the discrimination between different noise processes of the frequency standard. Even though stability is a very important measure, this work is mainly concerned about the second figure of merit, accuracy.

Accuracy is defined as the degree of conformity of the measured frequency to its definition [141]. In terms of atomic clocks this definition frequency is the frequency corresponding to the unperturbed transition  $\omega_0$  between two different states in a certain isotope of an atomic species. This means it refers to the frequency of the atoms at rest (not perturbed by Doppler and recoil shifts) and in the presence of zero magnetic and electric fields.

In the laboratory, these conditions can not be realized and there is always some remaining atomic motion and electromagnetic field. This shifts the center of the absorption line  $\omega_a$  away from the definition frequency  $\omega_0$ . For atomic frequency standards this shift  $\omega_a - \omega_0$  is measured and estimated as good as possible and the accuracy of atomic clocks is then typically given by the standard deviation ( $1\sigma$ ) of its uncertainty (see for example table 1).

## 2.2 THE ALUMINUM ION QUANTUM LOGIC CLOCK

The uncertainty with which a shift from the unperturbed resonance can be estimated scales in many cases with the magnitude of the shift itself. Therefore high accuracy atomic clocks often not only show small uncertainties in the shifts but also small shifts themselves. Hence, atomic species with transitions that intrinsically have small sensitivities to line-shifts due to electric and magnetic fields are chosen preferably for atomic clocks. One such transition is the  $^1S_0 \rightarrow ^3P_0$  intercombination transition in atoms having an alkaline earth level scheme. It is doubly forbidden because of being an intercombination line and a  $J = 0 \rightarrow J = 0$  transition as well. This makes the  $^3P_0$  state long lived, resulting in a narrow transition which is a prerequisite for stable clocks.

For clocks based on single trapped ions, these transitions are especially useful because both clock states possess zero quadrupole momentum and therefore the transition is not shifted due to electric field gradients of the trapping potential. This has been realized by Dehmelt who first proposed thallium [36] and later aluminum [188] as potential frequency standards, both being group 13 elements, having the alkaline earth level structure in their singly ionized versions.

As mentioned above, having a suitable clock transition is not sufficient for an atomic species to make it a good ion clock candidate. It must also be coolable and provide the means to detect its internal state. For cooling, typically fast Doppler cooling from room temperatures down to mK is desirable. This requires a broad internal cooling transition where rapid scattering is possible. As an estimate, for a single  $^{27}\text{Al}^+$  ion roughly  $10^4$  photon recoils must be transferred onto the ion to achieve this. If the cooling should have completed in maximal 100 ms, this poses a lower bound of 30 kHz on the minimal natural width of the cooling transition. In practice, transitions with a linewidth of several MHz are used.

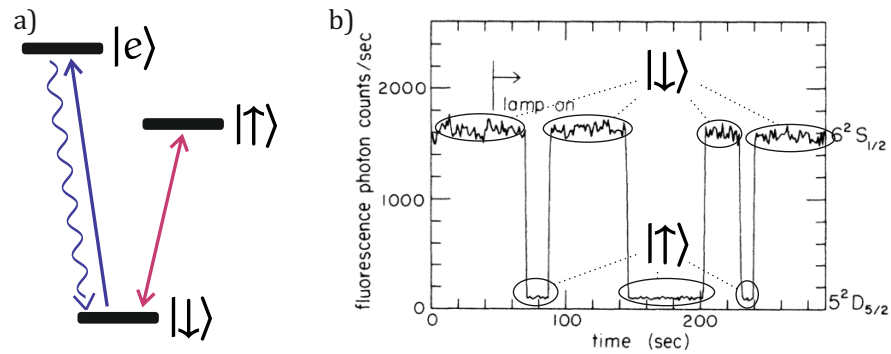


Figure 2: The electron shelving technique. Figure a) shows the participating levels, consisting of the (meta-)stable ground and excited state  $|\downarrow\rangle$ ,  $|\uparrow\rangle$  and the rapidly decaying fluorescence state  $|e\rangle$ . The detection of fluorescence photons or the absence thereof is used to determine the electronic state of the ion. Figure b) shows one of the first implementations of this technique with a single  $\text{Ba}^+$  ion. Adopted from [113], reprinted with permission.

State detection of single trapped ions can be implemented via the electron shelving technique [35]. The presence of the ion in the ground state  $|\downarrow\rangle$  is tested by applying a laser on a broad, rapidly decaying transition. The detection of fluorescence photons from this transition confirms the ion to be in the ground state, since no scattering would occur if the ion was in the metastable excited state  $|\uparrow\rangle$ . This scheme is shown in Figure 2. The minimal required linewidth for this technique to work reliably can be estimated as follows. If the photon imaging system has a noise level of 100 counts/s and a detection efficiency of 0.5%, a linewidth of roughly 60 kHz is required to achieve signal to



noise levels of 10. This is again a lower bound and in practice usually MHz transitions are favored.

Figure 3 shows the five lowest lying electronic levels of  $^{27}\text{Al}^+$ . The lowest energy state having a line broad enough to qualify for Doppler cooling and electron shelving state detection is the  $^1\text{P}_1$  state. However, this state requires a laser at 167 nm to drive it, which is not readily available.

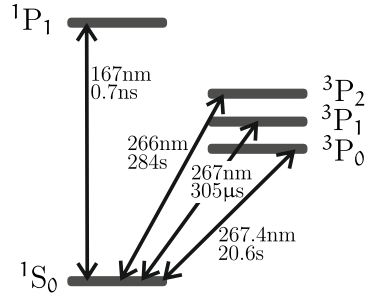


Figure 3:  $^{27}\text{Al}^+$  level scheme. The ground state and the four lowest lying excited states are shown. The  $^1\text{S}_0 \rightarrow ^3\text{P}_0$  transition is the clock transition and the  $^1\text{S}_0 \rightarrow ^3\text{P}_1$  can be used for state preparation. The potential  $^1\text{S}_0 \rightarrow ^1\text{P}_1$  broad cooling/detection transition is at the time of writing not accessible by readily available cw laser sources. The inverse decay rates are taken from [54] ( $^1\text{P}_1$ , calculated), [20] ( $^3\text{P}_2$ , calculated), [169] ( $^3\text{P}_1$ , measured) and [147] ( $^3\text{P}_0$ , measured).

Therefore, the way  $\text{Al}^+$  clocks were implemented so far is by shifting the state detection and cooling tasks to another ion of a different species that interacts with the  $\text{Al}^+$  ion. The cooling is achieved by Doppler cooling of this auxiliary ion (called logic or cooling ion in the following). Via the Coulomb interaction, the  $\text{Al}^+$  ions motion is strongly coupled to the cooling ions motion and thermalisation of the ions occurs rapidly (see also Chapter 6). This cooling technique is dubbed "sympathetic cooling" [91].

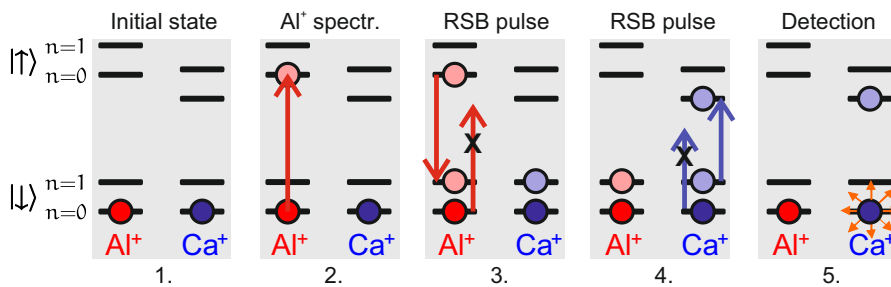


Figure 4: Quantum logic spectroscopy. Via the use of two red sideband pulses (RSB), the state after the clock interrogation of the spectroscopy ion (here  $\text{Al}^+$ ) is transferred first to the motional mode and then to the logic ion (here  $\text{Ca}^+$ ).

The state detection is implemented by facilitating the shared motional modes of the two ions. By cooling one of the 6 modes (see

Shift	$\Delta\nu_{\text{Al1}}$	$\sigma_{\text{Al1}}$	$\Delta\nu_{\text{Al2}}$	$\sigma_{\text{Al2}}$
Excess Micromotion	-20	20	-9	6
Secular Motion	-16	8	-16.3	5
Blackbody Radiation	-12	5	-9	3
Cooling Laser Stark	-7	2	-3.6	1.5
Total		23		8.6

Table 1: Error budget of  $\text{Al}^+$  clocks. All numbers presented as  $10^{-18}$  relative frequency shifts. The error budgets of the two previously realized aluminum clocks are given, considering shifts with an uncertainty larger than  $1 \times 10^{-18}$ . Al1 refers to the first  $\text{Al}^+$  clock with a single  $\text{Be}^+$  logic ion [148] and Al2 refers to the second  $\text{Al}^+$  clock where a  $\text{Mg}^+$  ion is used [24].

Section 3.4) to the motional ground state, the further excitation of so called red sidebands (RSB) on  $\text{Al}^+$  is inhibited. Red sideband transitions are transitions that require motional phonon energy additionally to the photon. This only holds if the  $\text{Al}^+$  is in the  $|\downarrow\rangle$  state because the same laser frequency does create phonons if driven starting from the  $|\uparrow\rangle$  state. This means that by applying the RSB pulse on the  $\text{Al}^+$  ion, the internal state can be mapped to the state of the motional mode  $a|\downarrow\rangle + b|\uparrow\rangle \rightarrow a|n=0\rangle + b|n=1\rangle$ . Another RSB pulse, this time on the logic ion, transfers the motional state information to the electronic state of the logic ion, completing the full state transfer. The logic ions broad transition is then used to detect its state via electron shelving. This scheme is shown in Figure 4, called quantum logic spectroscopy and was first proposed in [180] and demonstrated in [158].

### 2.2.1 Error budget of aluminum ion clocks

The aluminum ion quantum logic clock has been realized twice previously, both times by the same group [148, 24]. Table 1 summarizes the major contributions to the error budget of these two clocks. All shifts that have an uncertainty larger than  $1 \times 10^{-18}$  are listed. Three shifts arise as a consequence of the motion of the ion, being the excess micromotion Doppler shift, the secular motion Doppler shift and indirectly the cooling laser Stark shift. The fourth shift is the blackbody shift, that is the Stark shift due to the thermal background radiation.

Within this thesis, the experimental approach to reduce all four of these shifts for a new  $\text{Al}^+$  clock at PTB are described. The micromotion is reduced by the implementation of a symmetric ion trap drive (Section 7.3.3.4) and the secular motion by implementation of a novel cooling scheme called double-EIT cooling (Sections 5.4 and 9.5). The cooling laser Stark shift is avoided by having a trap with low heating rates and no immediate need to cool during the clock interrogation

(Section 9.4.2.1). Finally the blackbody radiation shift is tackled by using a trap that does not heat up significantly and characterization of this heating (Sections 7.3 and 7.3.4).



Part II

THEORY



## MOTION IN ION TRAPS

As mentioned in the introduction, aluminum quantum logic clocks rely on an aluminum ion being confined in a small and well-localized region where it is brought to almost a standstill via laser cooling. These aspects will be investigated theoretically in this part of the thesis, where this and the next chapter concentrate on the confinement or trapping of the ion and the subsequent chapters on the laser cooling aspects.

Trapping ions is not possible with only an electrostatic potential  $\Phi(x, y, z)$ , as illustrated by Laplace's equation

$$\Delta\Phi(x, y, z) = \frac{d^2}{dx^2}\Phi + \frac{d^2}{dy^2}\Phi + \frac{d^2}{dz^2}\Phi = 0. \quad (2)$$

When studying this equation, Samuel Earnshaw realized that "since one at least of the quantities  $\frac{d^2}{dx^2}\Phi$ ,  $\frac{d^2}{dy^2}\Phi$ ,  $\frac{d^2}{dz^2}\Phi$  is negative, and one at least positive, there will be at least one principal axis parallel to which a disturbed particle can vibrate, and at least one parallel to which a disturbed particle *cannot* vibrate" [48]. Hence, this fact has been named Earnshaw's theorem.

So instead of using purely electrostatic potentials, physicists have come up with different ways to use the electromagnetic force to trap particles. These include adding static magnetic fields (Penning traps [126, 22]), placing electrostatic monopoles at the center of the trap ([93]) and using electrodynamic potentials. This latter trapping mechanism is implemented in the so called Paul traps and will be explained in the following.

Assuming properly chosen initial conditions, a charged particle with charge  $e$  and mass  $m$  in a spatially homogeneous electric field  $E_0$ , oscillating at  $\Omega_{\text{RF}}$  will undergo driven oscillations

$$E = E_0 \cos(\Omega_{\text{RF}}t) \Rightarrow x(t) = -\frac{eE_0}{m\Omega_{\text{RF}}^2} \cos(\Omega_{\text{RF}}t). \quad (3)$$

If the field is slightly inhomogeneous, the particle will experience a slightly larger force on one half cycle, resulting in a net force towards the region with smaller absolute field

$$E = E_0(1 + \alpha x) \cos(\Omega_{\text{RF}}t) \Rightarrow x(t) = -\frac{eE_0}{m\Omega_{\text{RF}}^2} \cos(\Omega_{\text{RF}}t) - \frac{\alpha e^2 E_0^2}{4m^2 \Omega_{\text{RF}}^2} t^2. \quad (4)$$

Here,  $\alpha \ll 1$  describes the small inhomogeneity and higher orders of  $\alpha$  and harmonics of  $\Omega_{\text{RF}}$  have been neglected. In an oscillating elec-

tric quadrupole field where the absolute field increases in all directions, this effect will lead to a confining potential, trapping charged particles in the minimum of the field.

A particle trap of this type is called Paul trap and was originally invented by Wolfgang Paul as a mass spectrometer ([122]) before being developed into a three-dimensional trap ([123]).

In this chapter, the equations of motion of ions in Paul traps will be derived and the trajectories analyzed classically. Additionally, the consequences of having two particles in the same trap will be studied.

### 3.1 EQUATIONS OF MOTION OF IONS IN PAUL TRAPS

The argument in the introduction of this chapter suggests confinement in oscillatory potentials with a well defined absolute field minimum. The simplest potential having this minimum is the quadrupole potential which is therefore most often used in Paul traps. However, not every oscillating quadrupole potential will lead to confinement of all charged particles. This is because resonances between the motion of the particle in the trap and the trap drive frequency can occur. Parametric heating [90] of the ions inside the trap then leads them to leave it eventually.

The conditions for a confining potential can be inferred by solving the equations of motion, as follows. For many applications it is useful to superimpose the oscillating quadrupole potential with a static potential, resulting in a total potential of

$$\Phi(x, y, z, t) = U_0/d^2 (\alpha_x x^2 + \alpha_y y^2 + \alpha_z z^2) + V_0/R^2 \sin(\Omega_{RF}t) (\beta_x x^2 + \beta_y y^2 + \beta_z z^2). \quad (5)$$

$U_0, V_0$  are the applied static and radio frequency (RF) voltages and  $\alpha_{x,y,z}, \beta_{x,y,z}$  are coefficients defining the shape of the respective quadrupoles. The characteristic distances  $d$  and  $R$  are proportional to the distance between the electrodes of the trap (see Figure 6). According to Equation 2 it has to hold that  $\alpha_x + \alpha_y + \alpha_z = \beta_x + \beta_y + \beta_z = 0$ . The equation of motion of a charged particle with mass  $m$  and charge  $e$  can be solved independently for the three principal axes. As an example along the  $x$ -axis it is given by

$$\frac{d^2}{dt^2}x = -\frac{e}{m} \left( \alpha_x \frac{U_0}{d^2} + \beta_x \frac{V_0}{R^2} \cos(\Omega_{RF}t) \right) x. \quad (6)$$

With the substitutions

$$\tau = \Omega_{RF}t/2, \quad (7)$$

$$a_x = 8eU_0\alpha/m\Omega_{RF}^2d^2, \quad (8)$$

$$q_x = -4eV_0\beta/m\Omega_{RF}^2R^2, \quad (9)$$



this is Mathieu's equation in standard form [9, 120]:

$$\frac{d^2}{d\tau^2}x + (\alpha_x - 2q_x \cos(2\tau))x = 0. \quad (10)$$

Because of the resonance heating mentioned earlier, this equation does not have bounded solutions for all  $\alpha$  and  $q$  parameters. In fact, stable solutions only exist for  $\alpha$ ,  $q$  parameters in certain regions, the so called stability regions. Figure 5 shows a portion of the stability region with lowest  $\alpha$  and  $q$  values. The secular frequency  $\nu$ , that is the frequency of oscillation in the trapping potential, is depicted in the color coding as a ratio of the drive frequency  $\Omega_{\text{RF}}$ . Once the frequency of the secular motion reaches the resonance condition  $2\nu = \Omega_{\text{RF}}$ , the solutions of the Mathieu equation are no longer bounded and the particles cannot be trapped. There are stability regions beyond this one but they have not been used for ion trapping [97]. In fact, most ion traps are operated in the very left of the diagram where  $\alpha, q^2 \ll 1$ .

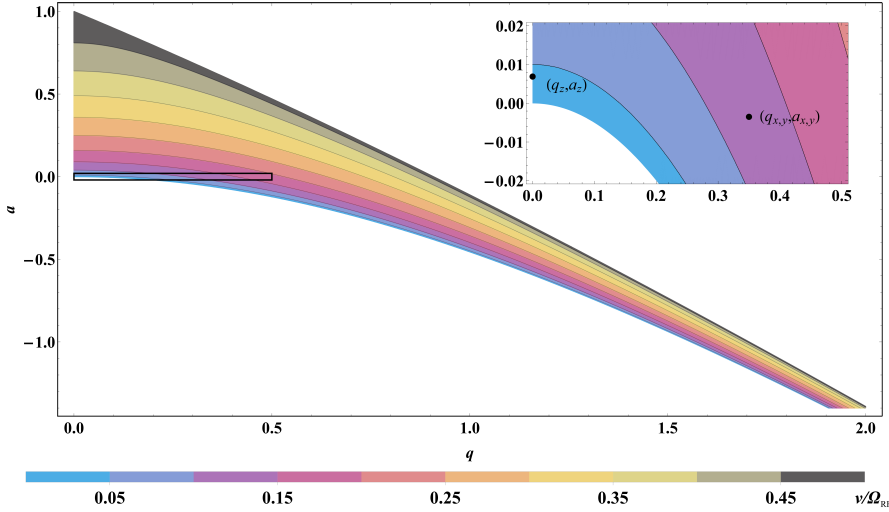


Figure 5: Stability diagram of Mathieu's equation. The color code represents the secular frequency  $\nu$  of trapped particles given in fractions of the drive frequency  $\Omega_{\text{RF}}$ . White regions correspond to an instable trap. The inset shows a zoom to the region where the trap in the experiments described here is operated. These points are indicated for the axial  $(q_z, \alpha_z)$  and radial  $(q_{x,y}, \alpha_{x,y})$  directions.

### 3.2 LINEAR PAUL TRAPS

The Paul trap used in the experiments of this thesis has parameters  $\beta_x = -\beta_y$ ,  $\beta_z = 0$  and  $\alpha_x = \alpha_y = -1/2\alpha_z$ . This is advantageous because it creates a trap without any oscillating field along the  $z$  direction. This configuration is named "Linear Paul trap" and was first realized by Raizen et al. [136]. The  $z$ -axis (from now on "the trap axis") confinement is achieved solely by a static electric potential. The static field at the same results in an anti-confining potential in the radial

( $x, y$ ) directions that has to be overcompensated with the oscillating fields to achieve trapping. Multiple ions arranged along the trap axis will all reside on the "saddle line" of the RF quadrupole and therefore ideally not experience any oscillating field at all. For clocks based on ion traps this is essential since the excess micromotion (see Section 3.3) of a particle that does not reside in the trap center would lead to significant second order Doppler shifts, worsening the clock performance.

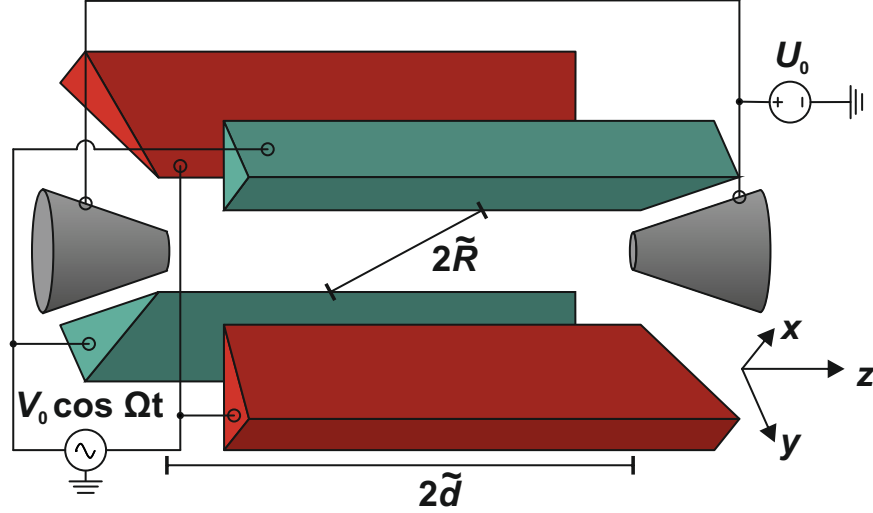


Figure 6: Geometry of a linear Paul trap. The four "blade"-electrodes provide the RF-quadrupole potential, whereas the two "tip"-electrodes realize the axial confinement. The trap used in the experiments described here has electrode distances of  $2\tilde{d} = 5$  mm and  $2\tilde{R} = 1.6$  mm.

Figure 6 shows a typical realization of a linear ion trap with six electrodes. The RF-voltage is applied between the blade pairs consisting of two opposing electrodes each. These produce the radial RF-quadrupole. The axial confinement is realized by a static voltage on the two "tip"-electrodes. With the given  $\alpha$  and  $\beta$  parameters, the total potential at the trap center follows from Equation 5 :

$$\Phi(x, y, z, t) = \frac{V_0}{2} \cos(\Omega_{\text{RF}} t) \frac{x^2 - y^2}{R^2} + U_0 \left( \frac{z^2 - \frac{1}{2}x^2 - \frac{1}{2}y^2}{d^2} \right) . \quad (11)$$

Here  $R$  and  $d$  can differ significantly from the entities  $\tilde{R}$ ,  $\tilde{d}$  depicted in Figure 6. They represent effective distances that depend on the complete shape of the electrodes and should not be confused with the geometric nearest distance of the electrodes (cf. Section 7.3.3.1). As shown in Chapter 7.3.3, these entities differ strongly, especially for the trap axis parameter  $d$ . The  $a$  and  $q$  parameters can be calculated according to Equations 8 & 9. A typical set used in the experiment is

$a_x = a_y = -0.0035$ ,  $a_z = 0.007$ ,  $|q_{x,y}| = 0.35$ ,  $q_z = 0$  which results in trap oscillation frequencies of 1 MHz axially and 3 MHz radially for a trap drive frequency of 24 MHz. They are shown in the inset of Figure 5 and lie well within the stability region. Since  $a, q < 1$ , Equation 10 can be solved in first order in  $a$  and  $q$ , in the so called adiabatic approximation, as [13, 97]

$$x(t) \approx x_0 \left( 1 - \frac{q}{2} \cos(\Omega_{\text{RF}} t) \right) \cos(\nu t) \quad (12)$$

where the secular trap frequency is given by

$$\nu = \frac{\Omega_{\text{RF}}}{2} \sqrt{a + \frac{q^2}{2}}. \quad (13)$$

The first term in Equation 12 shows the secular motion of the ion and the second term is the driven motion, called *micromotion*, at the drive frequency that is responsible for the confining potential. This unavoidable micromotion is also called *intrinsic* micromotion which has to be differentiated from the so called excess micromotion that arises in non ideal trap configurations and cannot be cooled [13] (cf. Section 3.3). Figure 7 shows the validity of the approximation by comparing to the exact solution of Mathieu's equation for the radial  $a$  and  $q$  parameters given above.

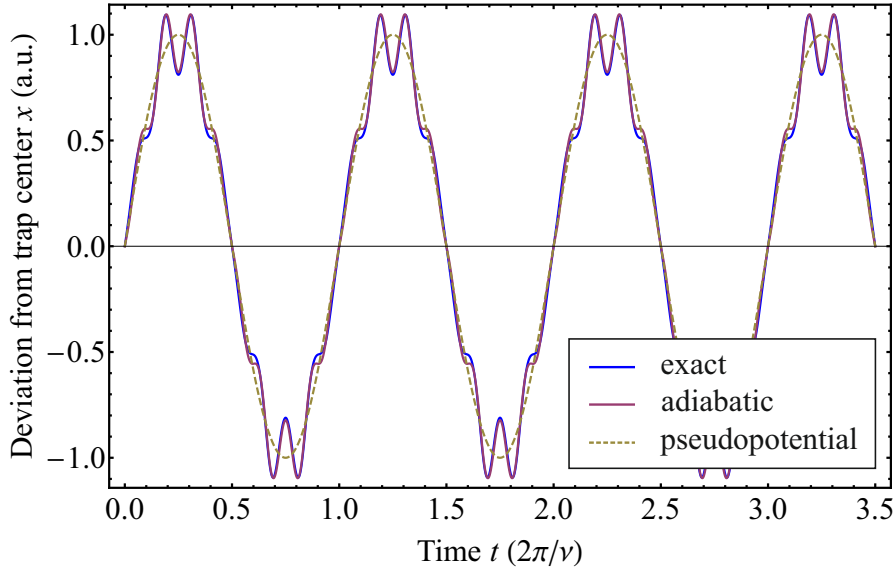


Figure 7: Trajectory of a single ion in a linear Paul trap along a radial direction. The blue line shows the exact solution of Mathieu's equation, the red line the adiabatic approximation and the dashed, yellow line the pseudopotential approximation. The Mathieu parameters are  $a \approx -0.0035$  and  $q \approx 0.35$  which correspond to single ion trap frequencies of 1 MHz axially and 3 MHz radially for a trap drive at 24 MHz.

It is often helpful to neglect the micromotion of the trapped particle and assume it to reside in a so called ponderomotive pseudo-potential [34] of the form

$$U(x, y, z) = \frac{1}{2}m\nu_x^2x^2 + \frac{1}{2}m\nu_y^2y^2 + \frac{1}{2}m\nu_z^2z^2, \quad (14)$$

where the  $\nu_{x,y,z}$  are the secular frequencies as given in Equation (13). This pseudo-potential is a static three-dimensional harmonic oscillator that is mass dependent. This means that heavier particles experience weaker effective restoring forces than lighter ones. This difference results in a high degree of asymmetry in the oscillatory modes, once particles with different masses are trapped in the same potential as described in Section 3.4. For the oscillating potential given in Equation 11 the trap frequencies are given by

$$\nu_z = \sqrt{\frac{2eU_0}{md^2}} \quad (15)$$

$$\nu_{x,y} = \sqrt{\nu_p^2 - \frac{1}{2}\nu_z^2} \quad (16)$$

where

$$\nu_p = \frac{eV_0}{\sqrt{2}\Omega_{\text{RF}}mR^2} \quad (17)$$

describes the contribution of the RF potential to the radial trap frequencies [179]. Introducing  $\epsilon = \nu_p/\nu_z$  as in [84] simplifies the radial trap frequencies to

$$\nu_{x,y} = \nu_z \sqrt{\epsilon^2 - \frac{1}{2}}. \quad (18)$$

Typically,  $\nu_x$  and  $\nu_y$  are not exactly equal due to asymmetries in the trap or the trap wiring (cf. Section 7.3.3). The ion's secular motion can be described by six parameters  $x_0, y_0, z_0$  and  $\phi_x, \phi_y, \phi_z$  representing the modal amplitudes and phases

$$\mathbf{r}(t) = (x_0 \sin(\nu_x t + \phi_x), y_0 \sin(\nu_y t + \phi_y), z_0 \sin(\nu_z t + \phi_z)). \quad (19)$$

The secular kinetic energy of the particle averaged over one cycle of each oscillation is then given by

$$E_{\text{kin,secular}} = \frac{1}{4}m(x_0^2\nu_x^2 + y_0^2\nu_y^2 + z_0^2\nu_z^2). \quad (20)$$

The kinetic energy in the micromotion can be calculated from Equation 12 and is in the same limits ( $a \ll 1, q^2 \ll 1$ ) given by [13]

$$E_{\text{kin,micromotion}} \approx \frac{1}{4}m \left( x_0^2\nu_x^2 \frac{q_x^2}{q_x^2 + 2a_x} + y_0^2\nu_y^2 \frac{q_y^2}{q_y^2 + 2a_y} + z_0^2\nu_z^2 \frac{q_z^2}{q_z^2 + 2a_z} \right). \quad (21)$$

$$\approx \frac{1}{4}m(x_0^2\nu_x^2 + y_0^2\nu_y^2) \quad (22)$$

where  $q_z = 0$  and  $q_{x,y}^2 \gg |2a_{x,y}|$  was used. This means that the kinetic energy in the radial directions is essentially equal for secular motion and micromotion. Laser cooling of the ion will therefore both reduce the secular energy and the associated micromotion energy. This is essential to reduce Doppler shifts of the clock ion as far as possible for highest accuracy.

### 3.3 EXCESS MICROMOTION

The micromotion described in the previous section was the intrinsic micromotion that is unavoidable in a Paul trap since it generates the trapping potential. A different kind of micromotion is the so called "excess micromotion" that occurs whenever the origins of the static and RF quadrupoles do not coincide. A displacement of the static potential origin of  $x_s$  results in a displacement of the minimum of the total potential of

$$x_d = -\frac{v_z^2}{2v_p^2 - v_z^2} x_s \quad (23)$$

and the trajectory is given by [13]

$$x(t) \approx [x_d + x_0 \cos(v_x t)] (1 + q_x/2 \cos(\Omega_{RF} t)) \quad (24)$$

which implies an additional kinetic energy of

$$E_{\text{kin,excess}} = m x_d^2 q^2 \Omega_{RF}^2 / 16 \quad (25)$$

that cannot be cooled since it is driven motion. It has to be compensated by shifting the static quadrupole back onto the RF quadrupole using compensation fields (see Section 7.3). Another source for excess micromotion is a phase shift between opposing electrodes generating the quadrupole [13]. It can not be compensated by compensation fields and must be intrinsically small to reach small kinetic energies and corresponding Doppler shifts.

### 3.4 TWO ION CRYSTALS

As mentioned in the introductory Chapter 2, in quantum logic clocks two ions of in general different mass are trapped. Therefore, the implications of trapping multiple ions in the same potential must be investigated. Generally, trapping multiple ions in a linear trap is the basis not only for quantum logic clocks [148, 24] but also for trapped ion quantum computing [26, 84, 61], quantum logic spectroscopy [30, 158, 173] and many other experiments. Especially for quantum computing applications the multi-ion dynamics have therefore been studied thoroughly [179, 76, 84, 119]. Based on those results, the dynamics of exactly two ions in a linear trap with different masses  $m_1$

and  $m_2$  will be evaluated. This represents quantum logic clocks and from now on the cooling/logic ion is numbered ion 1 and the spectroscopy/clock ion is numbered ion 2.

*Parts of the following were published before by the author and his co-authors in [185].*

Assuming an ion trap in which the trap frequencies for ion 1 are given by Equations 15 & 16, the trap frequencies for a single ion 2 in the same trap would be

$$\nu_{z,2} = \sqrt{\frac{m_1}{m_2}} \nu_{z,1} \quad (26)$$

$$\nu_{x,2} = \sqrt{\frac{m_1}{m_2}} \sqrt{\frac{\frac{m_1}{m_2} \epsilon^2 - \frac{1}{2}}{\epsilon^2 - \frac{1}{2}}} \nu_{x,1} \quad (27)$$

$$\nu_{y,2} = \sqrt{\frac{m_1}{m_2}} \sqrt{\frac{\frac{m_1}{m_2} \epsilon^2 - \frac{1}{2}}{\epsilon^2 - \frac{1}{2}}} \nu_{y,1}. \quad (28)$$

The axial trap frequency depends only on the square root of the mass ratio, whereas the radial trap frequencies have a more complex mass dependence because of the different mass scaling of the RF-induced potential and the static potential.

If two ions are simultaneously trapped in the same linear Paul trap and strongly cooled close to 0K temperature, they will eventually crystallize at equilibrium positions along the trap axis, equally spaced at a distance

$$z_0 = \left( \frac{ed^2}{32U_0\pi\epsilon_0} \right)^{1/3} \quad (29)$$

from the trap center [179, 76]. The remaining motion of ions 1 and 2 can then be described as small, coupled oscillations  $q_1, q_2$  around these equilibrium positions. Along every principal axis the motion consists of a superposition of an out-of-phase mode (o) where the two ions always move in opposite directions and an in-phase mode (i) where the two ions move in the same direction. Following the approach of [83], the oscillations along a chosen direction are given by

$$q_1(t) = z_i b_1 \sin(\nu_i t + \phi_i) + z_o b_2 \cos(\nu_o t + \phi_o) \quad (30)$$

$$q_2(t) = \frac{z_i b_2}{\sqrt{\mu}} \sin(\nu_i t + \phi_i) - \frac{z_o b_1}{\sqrt{\mu}} \cos(\nu_o t + \phi_o) \quad (31)$$

where  $\nu_{i,o}, \phi_{i,o}$  are the angular eigenfrequencies and phases of the in-phase and out-of-phase modes, respectively, and  $b_{1,2}$  are the components of the normalized eigenvector of the in-phase mode, satisfying  $b_1^2 + b_2^2 = 1$ , in a coordinate system where the motion of the second ion is scaled by a factor of  $1/\sqrt{\mu}$  with  $\mu = m_2/m_1$ . The  $z_{i,o}$  are the modal amplitudes. The calculation of the modal frequencies

and the  $b_{1,2}$ -parameters can be performed following the methods of Reference [83]: For every ion the sum of the trap pseudopotential and the Coulomb potential due to repulsion from the other ion is developed around the equilibrium positions and the coupled equations of motions are solved in lowest order, neglecting higher order non-linear couplings [179, 119]. The results of this calculation for ions with different mass ratios  $\mu$  and different  $\epsilon$ -parameters are given by:

$$v_{i,z} = \sqrt{\frac{1 + \mu - \sqrt{1 - \mu + \mu^2}}{\mu}} v_z \quad (32)$$

$$v_{o,z} = \sqrt{\frac{1 + \mu + \sqrt{1 - \mu + \mu^2}}{\mu}} v_z \quad (33)$$

$$b_{1,z}^2 = \frac{1 - \mu + \sqrt{1 - \mu + \mu^2}}{2\sqrt{1 - \mu + \mu^2}} \quad (34)$$

$$v_{i,x,y} = \sqrt{-\frac{\mu + \mu^2 - \epsilon^2(1 + \mu^2) - \alpha}{2\mu^2}} v_z \quad (35)$$

$$v_{o,x,y} = \sqrt{-\frac{\mu + \mu^2 - \epsilon^2(1 + \mu^2) + \alpha}{2\mu^2}} v_z \quad (36)$$

$$b_{1,x,y}^2 = \frac{\mu - \mu^2 + \epsilon^2(-1 + \mu^2) + \alpha}{2\alpha} \quad (37)$$

where the parameter

$$\alpha = \sqrt{\epsilon^4(\mu^2 - 1)^2 - 2\epsilon^2(\mu - 1)^2\mu(1 + \mu) + \mu^2(1 + (\mu - 1)\mu)} \quad (38)$$

was introduced. The  $b_2$  parameters are given by  $b_2 = \sqrt{1 - b_1^2}$ . Figure 8 shows the calculated eigenmode amplitudes and frequencies in axial and radial directions. The heavier of the two ions has the largest amplitude for the mode with the lowest frequency, which is the axial in-phase mode and radial out-of-phase mode. It is worthwhile noting that the radial mode amplitudes are much more sensitive to a change in the mass ratio. As a consequence, the radial motion of the ions is nearly decoupled for ion species with mass ratios  $\mu < 0.25$  or  $\mu > 4$  in typical traps. This means for one mode ion 1 has a large normal mode amplitude and ion 2 has a small one, whereas for the other mode the situation is reversed. These asymmetries significantly alter the cooling behavior as explained in Chapter 6 and can also change the micromotion amplitudes (see Appendix A.2).

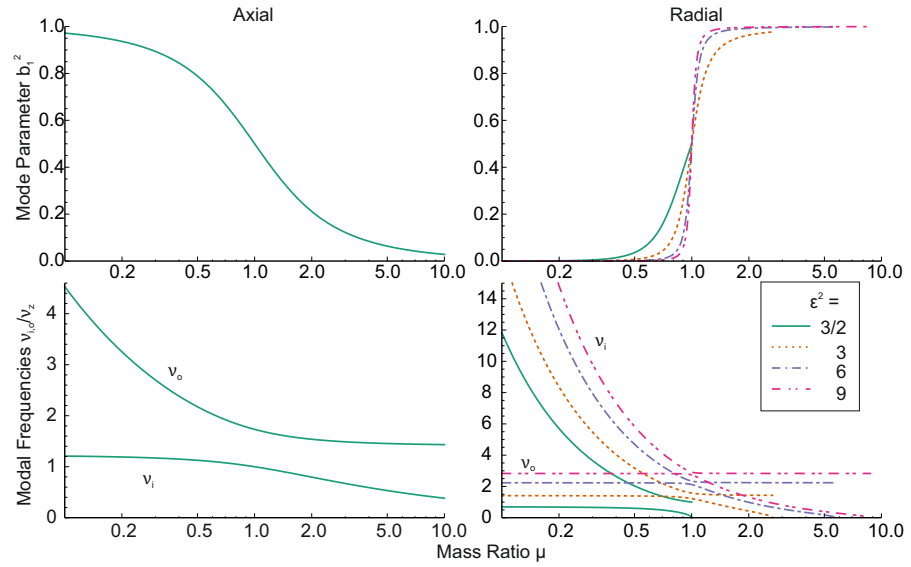


Figure 8: Normal mode frequencies and normalized amplitudes for a two-ion two-species crystal. The square of the normalized amplitude ( $b_1^2$ ) and the in-phase ( $\nu_i$ ) and out-of-phase ( $\nu_o$ ) trap frequencies normalized to the axial trap frequency of a single ion of mass  $m_1$  are shown for the axial and radial direction for different mass ratios  $\mu = m_2/m_1$  and  $\epsilon$ -parameters. The radial curves end at mass ratios where the radial out of phase mode frequencies reaches zero because for higher mass ratios the ion crystal turns from a linear axial configuration to a linear radial configuration [135, 155].



## QUANTUM MECHANICAL DESCRIPTION OF MOTION AND ATOM LIGHT INTERACTION

---

The derivation of the motion of a trapped ion in the previous chapter was purely classical. It cannot explain quantum mechanical effects like the quantization of the motional states apparent at low temperatures. Additionally, it is not guaranteed that the bounded solutions for the motion in the classical derivation correspond to bounded solutions when treating the problem quantum mechanically. In this chapter, it is shown that the stability criteria indeed match in the classical and quantum mechanical (QM) formulations. Furthermore, the quantum mechanical interaction of light fields with a trapped ion is derived semiclassically where the ion and the trapping potential are treated quantum mechanically and the light field classically. Special quantum mechanical states, the so called thermal states, are described and a method for measuring the temperature of such a state is introduced. This is needed later to quantify the performance of the laser cooling experiments performed within this thesis.

### 4.1 STABILITY OF THE QM EQUATIONS OF MOTION

In quantum mechanics, the motional state of a particle is described by its wave function  $\Psi(x, y, z, t)$ , where  $|\Psi(x, y, z, t)|^2$  gives the probability density of finding the particle at position  $(x, y, z)$  at time  $t$ . The dynamics of the wave function of a particle with charge  $e$  that is placed into a trapping potential  $\Phi(x, y, z, t)$  is described by the Schrödinger equation

$$i\hbar \frac{d}{dt} \Psi(x, y, z, t) = -\frac{\hbar^2}{2m} \nabla^2 \Psi(x, y, z, t) + e\Phi(x, y, z, t) \Psi(x, y, z, t). \quad (39)$$

If  $\Phi(x, y, z, t)$  is chosen to be the electrodynamic potential introduced in Equation 5, this equation can be shown to have bounded solutions (i.e.  $|\Psi(x, y, z, t)|^2 < \epsilon$  for  $\sqrt{x^2 + y^2 + z^2} > D(\epsilon)$  for any  $\epsilon > 0$  and a function  $D(\epsilon)$  for all  $t$ ).

It was first shown by Cook et al. [33] that the bounded solutions occur for exactly the same  $a$  and  $q$  parameters as in the classical derivation (see Section 3.1). They reduced the Wigner function  $f(x, p)$  equation of motion to a Mathieu equation equal to the classical equation given in Equation 6. Classically bounded solutions therefore lead to quantum mechanically bounded solutions and vice versa. In the following, the exact state  $\Psi(x, y, z, t)$  of the ion in these potentials is investigated.

#### 4.2 QUANTUM MECHANICAL BASIS STATES

To investigate interactions of trapped ions in Paul traps, an adequate set of basis states of the wave functions  $\Psi(x, y, z, t)$  is helpful. For a detailed derivation of the quantum mechanical solution of the equation of motion of single charged particles in these traps, the reader is referred to [92].

The state of an ion in the trap can be expressed as a superposition of basis states  $|n, t\rangle$  that have very similar properties as the Fock states  $|n\rangle$  of a static quantum mechanical oscillator. As for those, an annihilation operator  $\hat{a}(t)$ , a creation operator  $\hat{a}^\dagger(t)$  and a number operator  $\hat{n}(t) = \hat{a}^\dagger(t)\hat{a}(t)$  can be defined, that fulfill the relations

$$\hat{a}(t) |n, t\rangle = \sqrt{n} |n-1, t\rangle \quad (40)$$

$$\hat{a}^\dagger(t) |n, t\rangle = \sqrt{n+1} |n+1, t\rangle \quad (41)$$

$$\hat{n}(t) |n, t\rangle = n |n, t\rangle. \quad (42)$$

It has to be noted, however, that the states  $|n, t\rangle$  are time dependent and therefore not energy eigenstates. They exchange energy periodically with the RF field. Apart from this, they behave very similarly to static Fock states and special superpositions such as coherent, thermal or also nonclassical states can be constructed analogously. In many cases the time dependence can be ignored and in the following the notation  $|n\rangle$  will be used instead of  $|n, t\rangle$ . This corresponds to a quantum mechanical pseudo-potential approach and in this approximation the states  $|n\rangle$  are pseudo-energy eigenstates with energy  $E(|n\rangle) = \hbar\nu(n + \frac{1}{2})$ . This approximation is only valid if  $a$  and  $q$  are small ( $a, q^2 \ll 1$ ) and it cannot explain any effects of micromotion such as the resonant coupling of lasers to micromotion sidebands or the general reduction of all atom-light-interaction strengths by a factor of  $\approx \frac{1}{1+q/2}$  "due to wave packets breathing at the RF-drive frequency" [92]. As mentioned, neglecting these influences is approximately valid for many experiments but there are cases where the micromotion effects are important. One example is the compensation of micromotion, where the strength of resonant interaction of the applied laser field with a micromotion sideband is used to infer the amount of micromotion undergone by the ion in the trap (see Section 9.3).

#### 4.3 THERMAL STATES

In general, the motional state of a single ion along every trap axis can be described by a mixture of superpositions of motional states expressed by a density matrix  $\xi$ . Within this thesis, the particle is assumed to be almost exclusively in a so called thermal state, which

is a mixture of different basis states  $|n\rangle$  without any coherences. In other words:  $\xi$  is diagonal in the  $|n\rangle$  basis.

$$\xi_{\text{thermal}}(T) = \sum_{n=0}^{\infty} P_n(T) |n\rangle \langle n| \quad (43)$$

Here,  $P_n(T)$  is the probability of state  $n$  being occupied for a given ion temperature  $T$  and it is given by the Maxwell-Boltzmann distribution [129]

$$P_n(T) = \frac{e^{-(n+1/2)\hbar\nu/k_B T}}{\sum_{n=0}^{\infty} e^{-(n+1/2)\hbar\nu/k_B T}} \quad (44)$$

$$= e^{-(n+1/2)\hbar\nu/k_B T} \left( e^{\hbar\nu/2k_B T} - e^{-\hbar\nu/2k_B T} \right), \quad (45)$$

where  $k_B$  is Boltzmann's constant. A different characterization for a certain thermal state  $\xi$  is the average occupied oscillator level  $\bar{n}$ . It is given by

$$\bar{n} = \sum_{n=0}^{\infty} n \cdot P_n = \frac{1}{e^{\hbar\nu/k_B T} - 1}. \quad (46)$$

In practice, the  $\bar{n}$  parameter is used more frequently than  $T$  to describe a specific thermal state and it is useful to know  $P_n(\bar{n})$  as a function of  $\bar{n}$  instead of  $T$

$$P_n(\bar{n}) = \frac{\bar{n}^n}{(\bar{n} + 1)^{n+1}}. \quad (47)$$

The thermal distribution  $P_n$  for a state with  $\bar{n} = 10$  can be seen in Figure 9. For  $T \rightarrow 0$ , the thermal distribution will approach  $P_0 \approx 1$ ,  $P_{n>0} \approx 0$ , representing the almost pure motional ground state that is required for many quantum logic gates. The residual  $\bar{n} \approx P_1$  is a measure of the quality of this ground state preparation. In practice, these low temperature states are achieved by cooling the ion with lasers. Different techniques to do this will be explained in detail in Chapter 5. Beforehand, the general mechanism of the interaction of trapped ions with laser light has to be introduced.

#### 4.4 ATOM LIGHT INTERACTIONS

Coherent electromagnetic waves, such as laser light, couple the internal electronic levels of atoms. Additionally, also the motional degrees of freedom are affected by this coupling due to the spatial variations of the waves and the finite size of the ion's wave packet. In the simplest case, the ion has a two level transition  $|\downarrow\rangle \rightarrow |\uparrow\rangle$  with ground state  $|\downarrow\rangle$  and excited state  $|\uparrow\rangle$ . The transition frequency is  $\omega_0$  and driven near resonantly by a monochromatic laser with frequency  $\omega_l$ , detuned by  $\Delta = \omega_l - \omega_0$ . The coupling strength is commonly described by a parameter called Rabi frequency  $\Omega$ , which is for dipole

transitions proportional to the transition's dipole moment  $\mathbf{d}$  and the electric field amplitude  $\mathbf{E}$  of the laser radiation  $\Omega \propto \mathbf{E} \cdot \mathbf{d}$  (see textbooks as e.g. [55]). Here, the laser field is treated classically, the ions internal state and motion are treated quantum-mechanically. This is justified, since the laser intensities are high, resulting in large average photon numbers such that quantization does not play a significant role. The total Hamiltonian of the system, including the atom electronic state ( $H_a$ ), motional state ( $H_m$ ) and laser interaction ( $H_i$ ) is for a single direction of the trap (here for example the  $x$ -axis) given by

$$H = H_a + H_m + H_i, \quad \text{with} \quad (48)$$

$$H_a = -\hbar\omega_0 |\downarrow\rangle \langle\downarrow| \quad (49)$$

$$H_m = \hbar\nu \hat{a}^\dagger \hat{a} \quad (50)$$

$$H_i = \frac{\hbar\Omega}{2} \cos(k_x \hat{x} - \omega_l t) (|\uparrow\rangle \langle\downarrow| + |\downarrow\rangle \langle\uparrow|). \quad (51)$$

Here, the energy of the  $|\uparrow\rangle$  internal state has been defined as zero and the  $+\frac{1}{2}\hbar\nu$  motional ground state energy has been dropped. The time dependence of the motional Hamiltonian is ignored (cf. Section 4.2) which is reasonable as long as the dynamics of the system are much slower than the inverse drive frequency. It is helpful to transfer this Hamiltonian into a picture where it is time independent. This is achieved by going into the interaction picture where the  $|\downarrow\rangle$ -state rotates with the laser frequency  $\omega_l$  and applying the rotating wave approximation (see textbooks as e.g. [32]). The Hamiltonian  $H_{\text{int}}$  in this interaction picture is then given by

$$H_{\text{int}} = \hbar\Delta |\downarrow\rangle \langle\downarrow| + \hbar\nu \hat{a}^\dagger \hat{a} + \frac{\hbar\Omega}{2} (|\uparrow\rangle \langle\downarrow| e^{ik_x \hat{x}} + |\downarrow\rangle \langle\uparrow| e^{-ik_x \hat{x}}). \quad (52)$$

The  $e^{ik_x \hat{x}}$  operators are momentum displacement operators, representing a momentum transfer of  $\hbar k$  on every photon absorption or emission. They are responsible for the coupling of the laser to the motional levels of the harmonic oscillator. Expressed in terms of the ladder operators, Equation 52 can be written as

$$H_{\text{int}} = \hbar\Delta |\downarrow\rangle \langle\downarrow| + \hbar\nu \hat{a}^\dagger \hat{a} + \hbar\Omega/2 \left( |\uparrow\rangle \langle\downarrow| e^{i\eta(\hat{a} + \hat{a}^\dagger)} + |\downarrow\rangle \langle\uparrow| e^{-i\eta(\hat{a} + \hat{a}^\dagger)} \right) \quad (53)$$

where the Lamb Dicke factor  $\eta = \sqrt{E_{\text{rec}}/\hbar\nu}$  has been introduced. It is equal to the square root of the ratio of the recoil energy  $E_{\text{rec}} = \frac{\hbar k_x^2}{2m}$  transferred on photon absorption/emission and the energy spacing of the harmonic oscillator. It also equals the ratio of ground state wavefunction spread  $x_0$  to the laser wavelength. If  $\eta \ll 1$  the dis-

placement operator can be expanded in powers of  $\eta$ , resulting in a Hamiltonian of

$$\begin{aligned}
H_{\text{int}} &= \hbar\Delta |\downarrow\rangle \langle\downarrow| + \hbar\nu \hat{a}^\dagger \hat{a} \\
&+ \hbar\Omega/2 |\uparrow\rangle \langle\downarrow| + \text{h.c.} && \text{(CAR)} \\
&+ i\eta\hbar\Omega/2 |\uparrow\rangle \langle\downarrow| \hat{a} + \text{h.c.} && \text{(RSB)} \\
&+ i\eta\hbar\Omega/2 |\uparrow\rangle \langle\downarrow| \hat{a}^\dagger + \text{h.c.} + (O)(\eta^2). && \text{(BSB)} \quad (54)
\end{aligned}$$

Here, the second row represents the internal transition without motional change (the carrier transition CAR), whereas the third and fourth row represent the transition including phonon absorption and creation, respectively. These are the so called red (RSB) and blue (BSB) sidebands. The detunings  $\Delta$  at which these transitions are strong, appear at  $\Delta = \pm\nu$ . This can be seen in a further interaction picture with respect to the laser detuning and the trap levels. The Hamiltonian  $\tilde{H}_{\text{int}}$  in this picture is

$$\begin{aligned}
H_{\text{int}} &= \hbar\Omega/2 |\uparrow\rangle \langle\downarrow| e^{-i\Delta t} + \text{h.c.} && \text{(CAR)} \\
&+ i\eta\hbar\Omega/2 |\uparrow\rangle \langle\downarrow| e^{-i(\Delta+\nu)t} \hat{a} + \text{h.c.} && \text{(RSB)} \\
&+ i\eta\hbar\Omega/2 |\uparrow\rangle \langle\downarrow| e^{-i(\Delta-\nu)t} \hat{a}^\dagger + \text{h.c.} && \text{(BSB)} \quad (55)
\end{aligned}$$

A laser detuned by plus or minus the trap frequency results in a vanishing time dependence of the respective sideband, which makes it the dominant process compared to the rapidly oscillating carrier and other sideband.

This can also be reasoned from energy conservation by arguing that the incident photon must carry both the internal transition energy and the phonon energy for a BSB ( $\Delta = \nu$ ) or that the absorption of the phonon and the photon together must equal the internal transition energy for a RSB ( $\Delta = -\nu$ ). The transition matrix elements for the transitions  $|n, \downarrow\rangle \rightarrow |n \pm 1, \uparrow\rangle$  or vice versa are suppressed by a factor of  $\eta\sqrt{n}$  and  $\eta\sqrt{n+1}$  for the red and blue sideband, respectively. Including all orders in  $\eta$ , the coupling strengths are given by [179]

$$\Omega_{n,n+m} = \Omega |\langle n+m | e^{i\eta(\hat{a}+\hat{a}^\dagger)} |n\rangle| \quad (56)$$

$$= \Omega e^{-\eta^2/2} \eta^{|m|} \sqrt{\frac{n_{<}!}{n_{>}!}} L_{n_{<}}^{|m|}(\eta^2) \quad (57)$$

where  $n_{<} = \min(n, n+m)$ ,  $n_{>} = \max(n, n+m)$  and  $L_n^\alpha$  denotes the generalized Laguerre polynomial [21]. Figure 9 shows the coupling strengths  $\Omega_{n,n}, \Omega_{n,n\pm 1}, \Omega_{n,n\pm 2}, \Omega_{n,n\pm 3}$  as a function of  $n$  for a Lamb Dicke factor  $\eta = 0.15$  which is typical for the experiments performed in this thesis. As a comparison, the relative population of the different  $n$ -levels for a Doppler cooled (0.5 mK) 1 MHz oscillator mode is shown. The plot shows that for Doppler cooling temperatures ( $\bar{n} \approx 10$ ) 2<sup>nd</sup> and possibly 3<sup>rd</sup> order sidebands play a significant

role in the dynamics. For sideband cooling calculations ( $\bar{n} \ll 1$ ), only 1<sup>st</sup> order sidebands need to be considered. This regime is called the Lamb-Dicke regime and it formally holds when  $\eta^2(2\bar{n} + 1) \ll 1$  for thermal states.

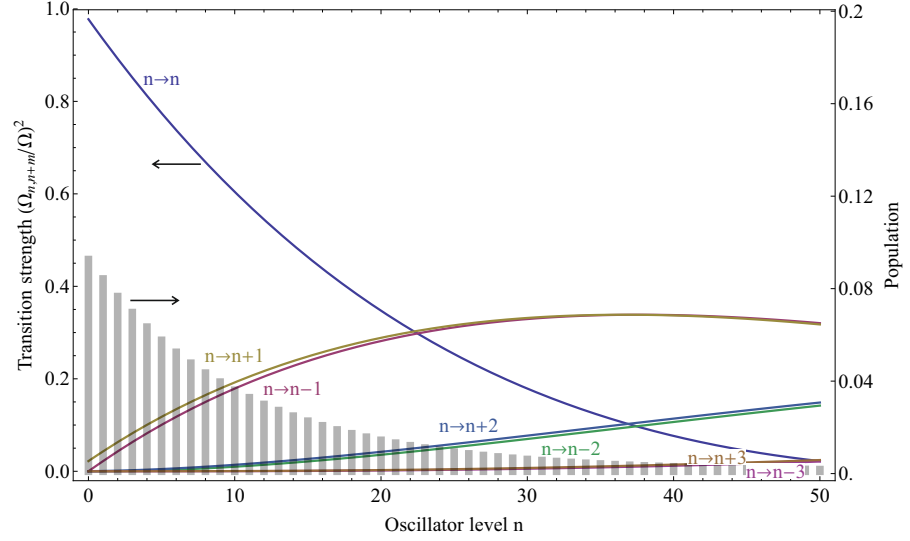


Figure 9: Relative transition strengths of carrier and sideband transitions. The left ordinate gives the normalized Rabi frequency  $\Omega_{n,n+m}/\Omega$  for the different transitions with  $\eta = 0.15$ . The right ordinate shows the excitation probability of an  $\bar{n} = 10$  thermal state for a trap frequency of  $\nu = 1$  MHz and a temperature of 0.5 mK.

#### 4.5 TEMPERATURE MEASUREMENTS

To measure the temperature or  $\bar{n}$  of a certain prepared thermal state  $\xi$ , in this thesis a technique described in [170] is used. There, a laser resonant with the  $k$ -th red sideband is applied to the ion and the excitation probability is compared to that of an interaction of a laser resonant with the  $k$ -th blue sideband with identical interrogation times  $t$  and Rabi frequencies  $\Omega$ . The excitation strength  $I_k^{\text{RSB}}, I_k^{\text{BSB}}$  is then the probability of being in the excited state after the interaction and is then for any thermal state given by

$$I_k^{\text{RSB}} = \sum_{m=k}^{\infty} P_m \sin^2 \frac{1}{2} \Omega_{m,m-k} t \quad (58)$$

$$= \left( \frac{\bar{n}}{1 + \bar{n}} \right)^k \sum_{m=0}^{\infty} P_m \sin^2 \frac{1}{2} \Omega_{m+k,m} t \quad (59)$$

$$= \left( \frac{\bar{n}}{1 + \bar{n}} \right)^k I_k^{\text{BSB}}. \quad (60)$$

This shows that for a thermal state, the  $k$ -th red sideband excitation will always be proportional to the  $k$ -th blue sideband excitation and the  $\bar{n}$  can be extracted from the ratio of the two measured signals

$$\bar{n} = \frac{(I_k^{\text{RSB}}/I_k^{\text{BSB}})^{1/k}}{1 - (I_k^{\text{RSB}}/I_k^{\text{BSB}})^{1/k}}. \quad (61)$$

One can show that optimal sensitivity of this technique is achieved when the sideband order  $k$  is close to the expected  $\bar{n}$  [170].

#### 4.6 CALCIUM LEVEL SCHEME

As mentioned in the introduction, the quantum logic clock that is prepared in this experiment will use a  $^{40}\text{Ca}^+$  ion as the logic and cooling ion. This choice has multiple reasons. First, calcium ions have a mass ratio to aluminum of  $27/40 \approx 0.7$  and therefore represent a good cooling ion species as presented in Chapter 6. Second,  $^{40}\text{Ca}^+$  features an atomic level scheme which is favorable in the sense that all the transitions can be driven with available diode lasers or frequency doubled diode lasers. Figure 10 shows these relevant levels. The broad ( $\Gamma \approx 2\pi \times 21$  MHz) transition at 397 nm is ideal for Doppler cooling and state detection and the narrow transition at 729 nm can be used for sideband cooling and the quantum logic operations. The 866 nm and 854 nm transitions are used primarily as repumpers. The 854 nm transition additionally assist the sideband cooling by quenching of the  $D_{5/2}$  state as explained in Sections 5.3 and 9.4.2 and the 866 nm transition is in this thesis used to enable a new laser cooling technique called double-EIT cooling (see Sections 5.4 and 9.5). The lasers themselves will be described in Section 7.5.

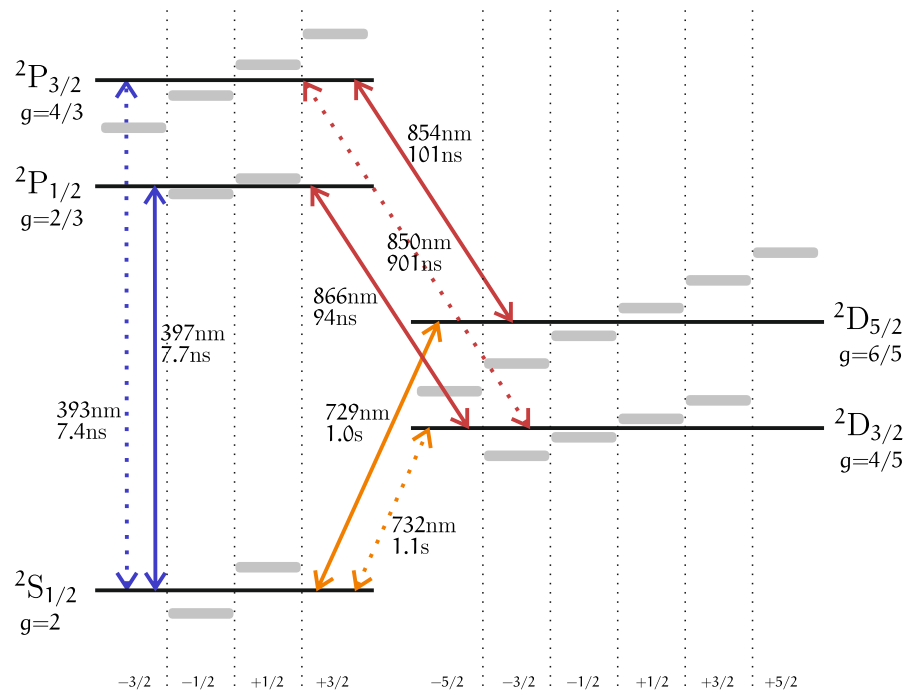


Figure 10:  $^{40}\text{Ca}^+$  level scheme. The gray bars represent the Zeeman sub-levels in a nonzero B-field. The transition wavelengths are stated together with their inverse decay rate. Dashed transitions are not driven with lasers in the experiments of this thesis. The transition data is taken from [76]. Distances are not to scale.



Lasers have been used for cooling trapped ions for now more than three decades [114, 177]. Since then, laser cooling has become an indispensable tool in precision spectroscopy of charged and neutral particles. In this chapter, the laser cooling techniques that have been investigated within this thesis are briefly reviewed. For a more detailed theoretical account of the cooling principles, the reader is referred to [103, 164].

Laser cooling relies on the radiation pressure force. The cooling works by shaping the velocity dependence of this force such that it is always opposing the ion's movement. Even though a classical radiation pressure force can be derived [164], it is often more useful to interpret the force quantum mechanically as resulting from the transfer of momentum from absorbed photons. To achieve cooling, the atoms have to absorb more photons when moving towards the laser than when resting or moving away from the laser.

Different regimes exist in laser cooling of trapped ions, depending on the relevant timescales given by the secular trap frequency  $\omega$  and the scattering rate, typically characterized by the linewidth  $\Gamma$  of the relevant atomic cooling transition. If  $\Gamma \gg \omega$ , scattering occurs instantly ( $\propto 1/\Gamma$ ) compared to the ion's oscillation period  $2\pi/\omega$ . This is called the weak binding regime [178] and in this limit, cooling can be explained by the full momentum transfer of every scattered photon onto the ion. Doppler cooling, as considered in Section 5.2, lies in this regime. If  $\omega \ll \Gamma$ , however, the scattering event stretches over many oscillation cycles and the ion will in general *not* receive the full photon momentum. This is the so called strong binding regime and is explained in Section 5.3.

Additionally to these well studied and frequently implemented cooling schemes, there exist more exotic approaches to shape the radiation pressure force even more advantageously. One of these approaches is cooling with electromagnetically induced transparency (EIT-cooling) which will be explained in Section 5.4.

### 5.1 GENERAL APPROACH TO COOLING IN AN ION TRAP

The dynamics of laser cooling are generally described by the full quantum mechanical master equation:

$$\frac{d}{dt}\tilde{\rho} = \mathcal{L}\tilde{\rho}. \quad (62)$$

Here,  $\tilde{\rho}$  is the density matrix of the combined atom/motional system and for product states it can be written as  $\tilde{\rho} = \rho \otimes \xi$  with  $\rho$  being the ions internal state and  $\xi$  the motional state.  $\mathcal{L}$  is the Liouvillian superoperator having contributions from the atom, the interaction with the light field and the trapping potential.

While for accurate results this large system of coupled differential equations has to be solved (see for example Section 5.4.6), the system can be simplified under a few assumptions. A laser is assumed to scatter between a ground state  $|\downarrow\rangle$  and an excited state  $|\uparrow\rangle$  that decays with a rate  $\Gamma$ . Furthermore, this transition is not saturated  $\Omega \ll \Gamma$  and consequently the electronic system can be assumed to be in zeroth order always in the ground state  $\rho \approx |\downarrow\rangle\langle\downarrow|$ . It can be shown [78] that the different diagonals of the density matrix  $\xi$ , i.e. the matrix elements  $\xi_{n,n+k}$  for varying  $k$ , span separate subspaces that are not coupled by the atom light interaction. Furthermore it has been shown there that all subspaces apart the main diagonal with  $k = 0$  decay to zero. This means that, after some initial relaxation time, the density matrix can be treated diagonally:  $\xi \approx \sum_{n=0}^{\infty} \xi_n |n\rangle\langle n|$ . The dynamics of the system can then be expressed as

$$\frac{d}{dt}\xi_k = \sum_{l=0}^{\infty} (A_{kl}\xi_l - A_{lk}\xi_k) \quad (63)$$

where the matrix elements  $A_{kl}$  give the transition rates of state  $|k\rangle$  to  $|l\rangle$ . Since every scattering event consists of photon absorption followed by photon emission, the matrix  $A$  is the product of an absorption matrix  $B$  and an emission matrix  $G$ . The latter is given by the relative sideband strengths  $(\Omega_{k,l-k}/\Omega)^2$  and the former is given by the free atom transition rates  $R(\Delta)$  reduced by the respective sideband strengths and shifted in frequency

$$A_{kl} = \sum_{m=0}^{\infty} G_{km}B_{ml} \quad (64)$$

$$B_{ml} = R(\Delta - (m-l)\nu)(\Omega_{m,l-m}/\Omega)^2 \quad (65)$$

$$G_{km} = (\Omega_{k,m-k}/\Omega)^2. \quad (66)$$

In the Lamb-Dicke regime, the  $n$ -th sideband transition rate scales with  $\eta^{-2n}$  (see Equation 57) and for  $\eta \ll 1$ , it often suffices to only consider first order sidebands in this calculation. The corresponding matrix elements  $A_{k,k\pm 1}$  are then given by

$$A_{k,k+1} = \eta^2(k+1)R(\Delta - \nu) + \tilde{\eta}^2(k+1)R(\Delta) \quad (67)$$

$$A_{k,k-1} = \eta^2kR(\Delta + \nu) + \tilde{\eta}^2kR(\Delta) \quad (68)$$

Two different Lamb-Dicke parameters  $\eta$  and  $\tilde{\eta}$  occur in the equations, because the spontaneous emission photon can have a different average recoil along the cooled axis than the cooling laser photon. In the

following it is assumed that these are equal  $\eta = e\tilde{\alpha}$ , which corresponds to isotropic spontaneous emission and equal projections of the cooling laser  $\mathbf{k}$ -vector along the three trap axes ( $k_x = \frac{1}{\sqrt{3}}k$ ). The summands occurring on the right hand side of these equations can be attributed to four different heating/cooling processes. Equation 67 describes the heating processes and the first term corresponds to heating due to blue sideband absorption and emission on the carrier. The second term gives the heating contribution of carrier absorption and blue sideband emission. The terms in Equation 68 are the equivalent processes on the red sideband, leading to cooling. These elementary cooling/heating events are depicted in Figure 11. Stenholm [164] in-

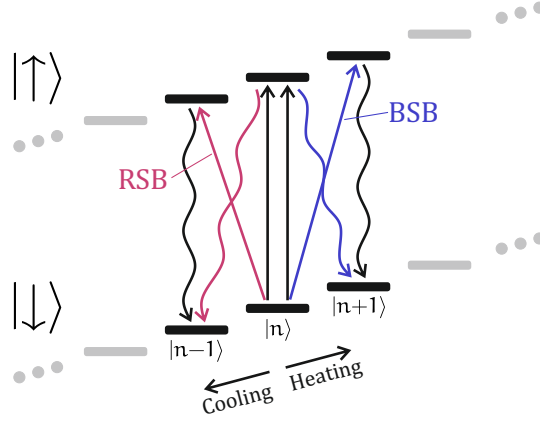


Figure 11: Elementary cooling and heating processes. In the Lamb Dicke regime, cooling and heating occurs due to the four depicted processes. Heating events are either due to carrier absorption and BSB emission or vice versa. Accordingly, cooling events always consist out of one carrier and one RSB transition. Absorption and emission on the carrier does not change the motional state and can therefore be neglected. Absorption and emission on one of the sidebands scales with  $\eta^4$  in the rate equations and can therefore also be neglected.

roduced the  $A_{+,-}$  parameters, combining both heating/cooling contributions into one term

$$A_{k,k+1} = \eta^2(k+1)R(\Delta - \nu) + \eta^2(k+1)R(\Delta) = \eta^2(k+1)A_+ \quad (69)$$

$$A_{k,k-1} = \eta^2kR(\Delta + \nu) + \eta^2kR(\Delta) = \eta^2kA_- \quad (70)$$

If the cooling term  $A_-$  is larger than the heating term  $A_+$ , cooling takes place and the steady state distribution of the cooling will always be a thermal distribution as given in Section 4.3. The  $\bar{n}$  of this thermal state is given by [114]

$$\bar{n} \approx \frac{A_+}{A_- - A_+} = \frac{R(\Delta - \nu) + R(\Delta)}{R(\Delta + \nu) - R(\Delta - \nu)} \quad (71)$$

In the two level system, the unsaturated scattering rate  $R$  is given by

$$R(\Delta) = \Gamma \frac{\Omega^2}{\Gamma^2 + 4\Delta^2}. \quad (72)$$

Using this, the cooling limit of Equation 71 can be calculated for two limiting cases where either the linewidth of the transition is very large ( $\Gamma \gg \nu$ ) or very small ( $\Gamma \ll \nu$ ) compared to the secular trap frequency. Explicit formulas for these cases are given in the next Sections.

## 5.2 DOPPLER COOLING

In Doppler cooling, the transition linewidth  $\Gamma$  is large ( $\Gamma \gg \nu$ ) and scattering will occur across a wide range of sidebands. If the laser is tuned to the red side of the carrier resonance ( $\Delta < 0$ ), the red sidebands will scatter more often, leading to cooling. Equation 71 can be expanded in  $\nu/\Gamma \ll 1$  and results in

$$\bar{n} = -\frac{\Gamma^2 + 4\Delta^2}{8\Delta\nu} - \frac{1}{2} + \mathcal{O}\left(\frac{\nu}{\Gamma}\right). \quad (73)$$

This is minimized for a detuning equal to half the transition linewidth  $\Delta = -\Gamma/2$ , resulting in

$$\bar{n} \approx \frac{\Gamma}{2\nu} - \frac{1}{2} \Leftrightarrow E \approx \frac{\hbar\Gamma}{2}, \quad (74)$$

which is the Doppler cooling limit. It is reached for any  $\nu$ , as long as  $\nu \ll \Gamma$ .

### 5.2.1 Realization in calcium

In  $^{40}\text{Ca}^+$ , the broad  $^2\text{S}_{1/2} \rightarrow ^2\text{P}_{1/2}$  transition at 397 nm is used for Doppler cooling. The linewidth of approximately 21 MHz satisfies  $\Gamma \gg \nu$  for the typical trap frequencies of 1 MHz and 3 MHz. Here, pure  $\pi$ -polarized light is used so that only the  $-1/2 \rightarrow -1/2$  and  $+1/2 \rightarrow +1/2$  Zeeman levels are coupled (cf. Figure 12). Due to the unequal Zeeman splitting of the S and P state, two effective detunings  $\Delta_1$  and  $\Delta_2$  arise and the optimal detuning of  $\Delta = -\Gamma/2$  cannot be fulfilled for both. An intermediate value must be chosen to achieve the lowest cooling limits. Since the  $\text{P}_{1/2}$  state also decays into the  $\text{D}_{3/2}$  state with a branching ratio of 1:14.5 [137], this state must be repumped. This is done by applying an 866 nm laser to the ion which should be tuned to a frequency where dark resonances with the 397 nm laser are avoided, e.g. on resonance or blue detuned.

## 5.3 SIDEBAND COOLING

Doppler cooling suffices to cool single  $^{40}\text{Ca}^+$  ions in traps with trap frequencies of  $\nu = 1$  MHz to a motional mean excitation of  $\bar{n} \approx 10$ .

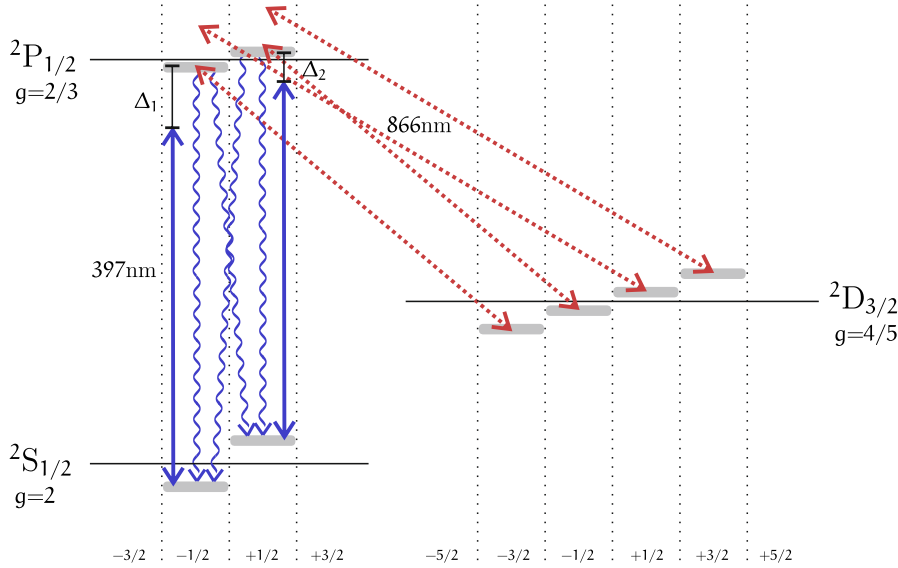


Figure 12: Doppler cooling in  $^{40}\text{Ca}^+$ . The Doppler cooling transition is the  $^2S_{1/2} \rightarrow ^2P_{1/2}$  transition, excited by a red detuned 397 nm laser. The Zeeman splitting of the two states prevents the use of an optimal detuning and the cooling limit will therefore be compromised. Additionally, the  $D_{3/2}$  state must be pumped out, which is here done with an 866 nm laser.

To achieve lower temperatures, according to Equation 74, a transition with a smaller linewidth  $\Gamma$  must be used. However, eventually the assumption  $\Gamma \gg \nu$  fails. In the other limit,  $\nu \gg \Gamma$ , one scattering event is stretched over many oscillation cycles of the ion. In the frame of the ion, the motion of the ion through the laser field is equivalent to interrogation with a phase modulated laser field where the phase modulation frequency is given by  $\nu$ . If the laser is red detuned by the trap frequency, the red sidebands will be resonant with the atomic transition and excitation can take place, where the energy difference between the photon and the transition is supplied by the ion's motion. Therefore, a repetitive excitation on the red sideband will lead to cooling of the ion. Laser cooling in this regime - the resolved sideband or strong binding regime - has been proposed very early [181] and is today a standard tool to cool single and multiple ions to the motional ground state [42, 142].

In this limit ( $\nu \gg \Gamma$ ), Equation 71 can be expanded in  $\Gamma/\nu \ll 1$  and results for  $\Delta = -\nu$  in

$$\bar{n} = \frac{5}{16} \frac{\Gamma^2}{\nu^2}. \quad (75)$$

### 5.3.1 Realization in calcium

The narrow transition  $^2S_{1/2} \rightarrow ^2D_{5/2}$  at 729 nm can be used to sideband cool  $^{40}\text{Ca}^+$  ions. The natural linewidth of this transition is

$\Gamma_{729} \approx 2\pi \times 0.15 \text{ Hz} \ll \nu$ . According to Equation 75, this would lead to extremely low cooling limits. But since every scattering event would take seconds, this linewidth is too small for practical use due to external heating. It is therefore broadened by the use of an auxiliary transition at 854 nm between the  $^2D_{5/2}$  and  $^2P_{3/2}$  states, where the latter has a linewidth of 21.5 MHz, dominated by the rapid decay to the ground state. This introduces a new loss channel for the  $^2D_{5/2}$ -state, effectively broadening the 729 nm transition to a value of [99]

$$\Gamma_{\text{eff}} = \frac{\Omega_{854}^2 \Gamma_{854}}{(\Gamma_{854} + \Gamma_{729})^2 + 4\Delta_{854}^2} + \Gamma_{729} \approx \frac{\Omega_{854}^2}{\Gamma_{854}} \quad (76)$$

where  $\Omega_{854}, \Delta_{854}$  are the  $^2D_{3/2} \rightarrow ^2P_{3/2}$  transition's Rabi frequency and detuning, respectively. This makes it possible to design the effective linewidth  $\Gamma_{\text{eff}}$  to achieve the optimal desired compromise between cooling speed and final temperature. This type of cooling is sometimes referred to as quench cooling and was first implemented by Diedrich et al. [42] on single mercury ions. On a single calcium ion, it was first implemented by Roos et al. who reached up to 99.9% motional ground state population [145].

Out of the many Zeeman sublevels, typically the  $m_J = -1/2$  for the S state, the  $m_D = -5/2$  for the D state and the  $m_J = -3/2$  for the P state are chosen to constitute the three necessary level in sideband cooling. The advantage is that the decay from the P state can then only occur back to the  $m_J = -1/2$  substate of the S state, automatically preparing the ion for the next cooling cycle. There are, however, some escape paths from this cooling cycle via the other  $D_{5/2}$  and some  $D_{3/2}$  states, that must be repumped. They are shown in Figure 13.

#### 5.4 EIT-COOLING

Figure 14 shows a comparison between Doppler and sideband cooling. The scattering rate  $R(\Delta - \Delta_0)$  is plotted as a function of detuning from the carrier transition where  $\Delta_0$  is the actual cooling laser detuning. It is plotted for both the narrow sideband cooling line and for the broad Doppler line. Additionally, the relative heating rates occurring as a consequence of scattering on the respective sideband transitions are depicted. Essentially, red sidebands extract phonons from the motion, cooling the system, while blue sidebands excite phonons, heating the system. Carrier absorption generally leads to a heating effect as well, since for small  $n$ , the decay will occur more frequently on the blue than on the red sideband. The cooling rate is given as the integral over the product of the scattering rate times the relative heating contributions. For a  $|n = 10\rangle$  Fock state, as in the Figure, it is evident that for Doppler cooling the scattering rate changes only slightly over the relevant spectral region ( $\omega_0 \pm 2\nu$ ) and the heating and cooling processes balance roughly so that no further cooling

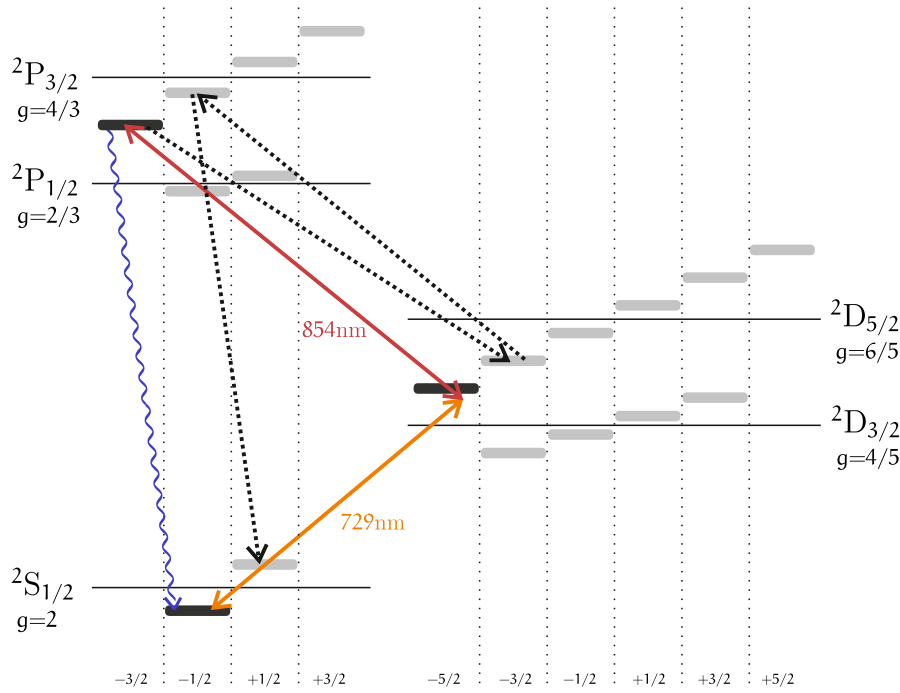


Figure 13: Sideband cooling in  $^{40}\text{Ca}^+$ . The narrow 729nm transition between the  $S_{1/2}$  and  $D_{5/2}$  is used for sideband cooling. It is broadened by coupling the D state to the  $P_{3/2}$ -state, to achieve acceptable cooling rates. The indicated cooling cycle is not completely closed, since escape paths to the  $D_{5/2}$  and  $D_{3/2}$  states exist (only one is shown) that must therefore be repumped.

takes place. In contrast, sideband cooling scatters almost exclusively on the 1st red sideband, leading to rapid cooling of this state. On the other hand, the second mode drawn into the picture with orange bars shows that Doppler cooling still works on other motional modes, whereas sideband cooling does not. This means that sideband cooling will generally only cool modes of an ion crystal that are very close to the chosen detuning. The plot also suggests a theoretically "perfect" scattering rate that scatters infinitely on all the red sidebands of all possible mode frequencies and not at all on the blue sidebands or the carrier. This would result in simultaneous cooling of all modes without any heating.

Different proposals exist to shape the scattering profile of a cooling laser in a manner closer to this ideal case by using interference of multiple beams [27, 139, 110, 111, 52]. One way is to use electromagnetically induced transparency (EIT) [110, 111, 52, 144, 159, 94]. In the simplest model, EIT cooling works by coupling two ground states to the same excited state with monochromatic lasers that have identical blue detuning  $\Delta > 0$  from the respective unperturbed transition. If one operates at a high power (the pump beam) it will "dress" the excited states, creating two resonances in the absorption spectra of the low power (the probe beam) laser [31]. In between the two resonances,

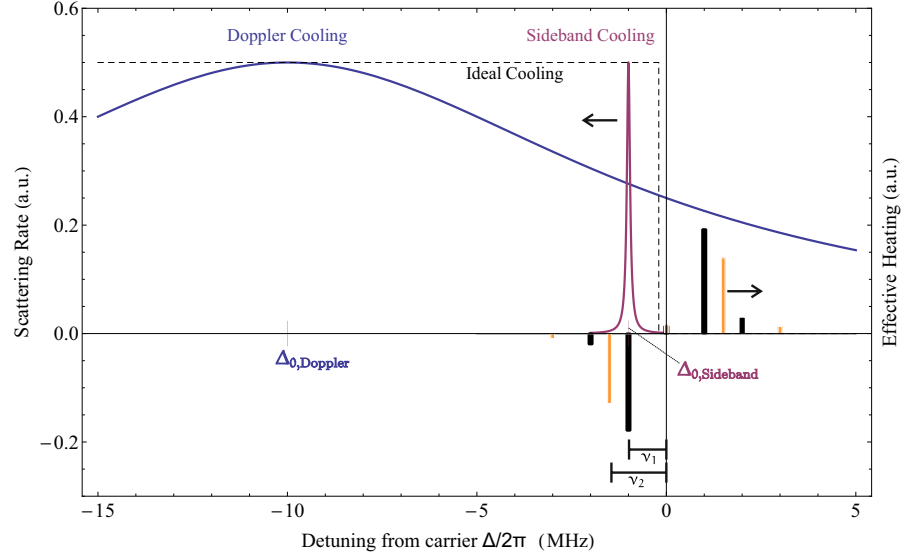


Figure 14: Comparison between Doppler and sideband Cooling. The scattering rates (curves, left ordinate) are plotted together with the relative heating rates of the different sideband/carrier transitions (bars, right ordinate) for two different motional modes  $\nu_1, \nu_2$ . The plot shows the rates for an ion in the Fock state with  $n = 10$  and a coupling with  $\eta = 0.145$  (typical for the experiments described here). Whereas the cooling and heating essentially cancel for the Doppler cooling case, the sideband cooling shows dominant scattering on the first red sideband, leading to strong cooling of this state. Second order sidebands are already quite suppressed at  $n=10$  and higher order sidebands are completely negligible.

there will always be a probe frequency where no scattering takes place. This "EIT"-condition is fulfilled exactly when  $\Delta_1 = \Delta_2 = \Delta$ . With correct laser parameters (detuning, powers), the spectrum can show this EIT-dip at exactly the carrier transition and the resonance at exactly the red sideband, leading to an absorption spectrum shown in Figure 16, which is a lot closer to the ideal case. It essentially represents sideband cooling without any carrier heating.

#### 5.4.1 Dressed atom - the Fano profile

In a three-level atom in  $\Lambda$ -configuration, as schematically drawn in Figure 15 a), coupling of the excited state  $|e\rangle$  to the ground state  $|2\rangle$  with parameters  $\Omega_2, \Delta_2$  will change the scattering rate  $R(\Delta_1)$  of a laser applied on the  $|1\rangle \rightarrow |2\rangle$  transition with parameters  $\Delta_1, \Omega_1$ . The decay rates to the states  $|1\rangle$  and  $|2\rangle$  shall be given by  $\Gamma_1$  and  $\Gamma_2$ , respectively. Since  $R(\Delta) = \Gamma_1 \langle e | \rho | e \rangle = \Gamma_1 \rho_{ee}$ , a solution of the quantum mechanical master equation for  $\rho_{ee}$  in steady state gives the scattering rate  $R(\Delta)$ . The analytical solution is [77]

$$R(\Delta_1) = \Gamma_1 \frac{4(\Delta_1 - \Delta_2)^2 \Omega_1^2 \Omega_2^2 (\Gamma_1 + \Gamma_2)}{Z} \quad (77)$$



with

$$\begin{aligned}
Z &= 8(\Delta_1 - \Delta_2)^2 \Omega_1^2 \Omega_2^2 (\Gamma_1 + \Gamma_2) \\
&+ 4(\Delta_1 - \Delta_2)^2 (\Omega_1^2 \Gamma_2 + \Omega_2^2 \Gamma_1) (\Gamma_1 + \Gamma_2)^2 \\
&+ 16(\Delta_1 - \Delta_2)^2 (\Delta_1^2 \Omega_2^2 \Gamma_1 + \Delta_2^2 \Omega_1^2 \Gamma_2) - 8\Delta_1 (\Delta_1 - \Delta_2) \Omega_2^4 \Gamma_1 \\
&+ 8\Delta_2 (\Delta_1 - \Delta_2) \Omega_1^4 \Gamma_2 + (\Omega_1^2 + \Omega_2^2)^2 (\Omega_1^2 \Gamma_2 + \Omega_2^2 \Gamma_1). \quad (78)
\end{aligned}$$

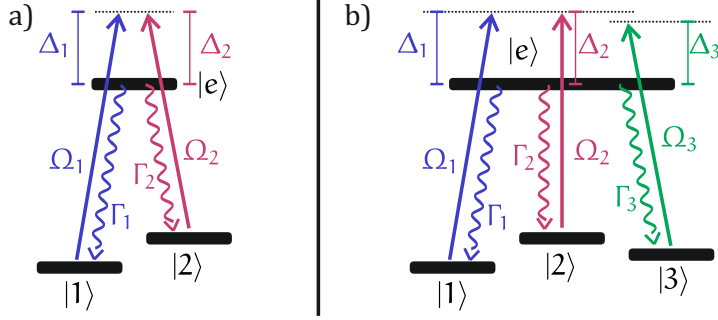


Figure 15: EIT cooling schemes. The  $\Lambda$  level schemes needed for EIT cooling are shown for the two-ground-state-case a), called single-EIT cooling and the three-ground-state-case b), called double-EIT cooling.

Figure 16 shows  $R(\Delta_1)$  for realistic settings. Two resonances become visible that appear in a fashion very similar to that of a Fano profile [53] appearing in autoionization processes. As shown by Lounis and Cohen-Tannoudji [95], the two resonances can be attributed to two different physical paths from state  $|1\rangle$  back to state  $|1\rangle$ . The broad resonance resembles the simple scattering due to absorption on  $|1\rangle \rightarrow |e\rangle$  followed by spontaneous emission on  $|e\rangle \rightarrow |1\rangle$ . The narrow resonance is the two photon Raman transition  $|1\rangle \rightarrow |2\rangle$ , followed by absorption on  $|2\rangle \rightarrow |e\rangle$  and then spontaneous emission on  $|e\rangle \rightarrow |1\rangle$ . The vanishing of  $R(\Delta_1)$  can be equivalently explained by quantum interference between these two pathways or by the so called coherent population trapping effect, where the ion evolves into a superposition of the two ground states that is "dark", i.e. it has no coupling to the excited state [58]. This dark ground state ( $\Psi_D$ ) and the two dressed states ( $\Psi_+$ ,  $\Psi_-$ ) of the combined atom/laser system are for the case of  $\Delta_1 = \Delta_2 = \Delta$  given by Morigi in [111]:

$$|\Psi_D\rangle = \frac{1}{\sqrt{\Omega_1^2 + \Omega_2^2}} (\Omega_2 |1\rangle - \Omega_1 |2\rangle) \quad (79)$$

$$|\Psi_+\rangle = \cos \theta |e\rangle + \sin \theta |\Psi_C\rangle \quad (80)$$

$$|\Psi_-\rangle = \sin \theta |e\rangle - \cos \theta |\Psi_C\rangle \quad (81)$$

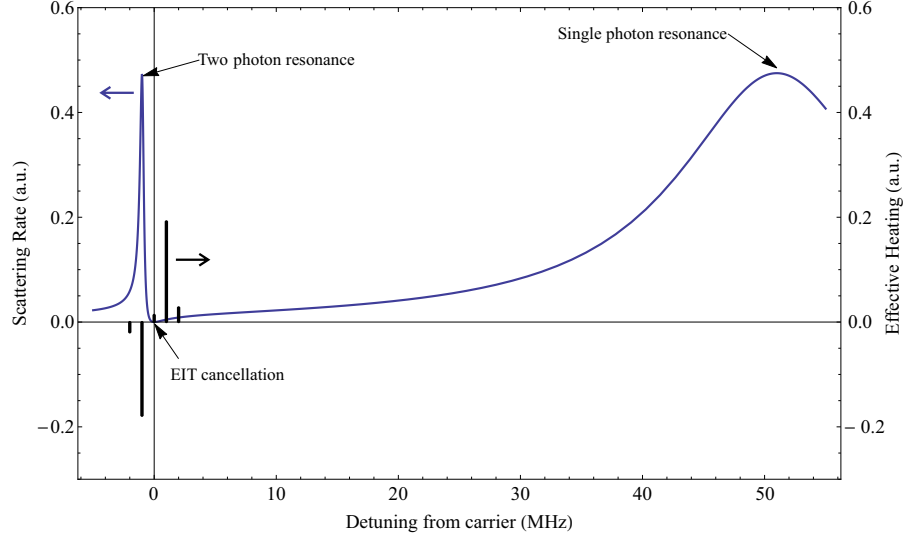


Figure 16: EIT cooling resonance. The figure shows the scattering rate  $R(\Delta_2 - \Delta_1)$  for EIT cooling (curve, left ordinate) and the effective heating of the different sidebands (bars, right ordinate). The assumed laser parameters were (all in MHz)  $\Gamma_1 = 20$ ,  $\Gamma_2 = 0$ ,  $\nu = 1$ ,  $\Delta_2 = 50$ ,  $\Omega_2 \approx 14.3$ . The two photon resonance that is Stark shifted onto the red sideband and the far detuned single photon transition are shown. The latter is not affecting the cooling severely, so that just as in sideband cooling scattering occurs primarily on the red sideband.

where

$$\tan \theta = \frac{\sqrt{\Delta^2 + \Omega_1^2 + \Omega_2^2} - \Delta}{\sqrt{\Omega_1^2 + \Omega_2^2}} \quad \text{and} \quad (82)$$

$$|\Psi_C\rangle = \frac{1}{\sqrt{\Omega_1^2 + \Omega_2^2}} (\Omega_1 |1\rangle + \Omega_2 |2\rangle). \quad (83)$$

Here  $\theta$  is a scaling parameter and  $|\Psi_C\rangle$  is the combination of the two ground states orthogonal to  $|\Psi_D\rangle$ . For  $\Omega_2 \gg \Omega_1$  the dark state is almost exactly equal to the state  $|1\rangle$  and since  $\theta$  is small for large  $\Delta$ , the state  $|\Psi_+\rangle$  has a large contribution of the excited state  $|e\rangle$  and the state  $|\Psi_-\rangle$  has a large contribution of  $|\Psi_C\rangle$ . The  $|\Psi_D\rangle \rightarrow |\Psi_+\rangle$  transition is therefore very close to the ideal single photon transition and the  $|\Psi_D\rangle \rightarrow |\Psi_-\rangle$  approximates the two photon transition.

#### 5.4.2 Single EIT cooling

As originally proposed by Morigi et al. [110], this effect can be used to shape the scattering rate  $R(\Delta)$  in laser cooling setups more favorably than possible with a simple two level scheme. The reason for this is, that for  $\Delta_1 = \Delta_2$  no scattering on the carrier excitation can take place, which means that in second order in  $\eta$  only blue sideband

heating remains. If the scattering transition is not saturated ( $\Omega_1 \ll \Gamma_1 + \Gamma_2$ ) and the dressing laser is much stronger than the scattering laser ( $\Omega_1 \ll \Omega_2$ ), the  $A_+$  and  $A_-$  parameters for EIT cooling can be obtained using Equations 77, 69 & 70.

$$A_{\pm} = \frac{\Omega_1^2 \Gamma^2 \nu^2}{\Gamma (\Gamma^2 \nu^2 + 4(\Omega_2^2/4 - \nu(\nu \mp \Delta)))^2} \quad (84)$$

where  $\Delta_1 = \Delta_2 = \Delta$  and  $\Gamma = \Gamma_1 + \Gamma_2$  was used. The optimal cooling conditions are achieved when  $A_-$  is maximal and  $A_+$  minimal. This will lead to both the lowest cooling limits as well as the largest cooling rates. They are achieved when the second term in the denominator vanishes for  $A_-$ , which corresponds to

$$\nu = (\sqrt{\Delta^2 + \Omega_2^2} - \Delta)/2. \quad (85)$$

This is equal to the Stark shift of the two photon resonance. This means that EIT cooling works best, when the red sideband scatters on the Stark shifted two photon resonance and the carrier is suppressed by the EIT condition. The final  $\bar{n}$  is given by

$$\bar{n} = \frac{\Gamma^2}{16\Delta^2}. \quad (86)$$

Large detunings are beneficial because they reduce the blue sideband scattering but also require higher laser powers, to produce the necessary Stark shifts.

### 5.4.3 Double-EIT cooling

EIT cooling as described in the previous Section effectively improves sideband cooling by removing carrier heating. Blue sideband heating is, however, on the same order of magnitude as carrier heating and in sideband cooling only suppressed by a factor of 4. This is because the first blue sideband is detuned twice as far from the cooling laser as the carrier. Therefore, in single EIT cooling, for equal  $A_-$  parameters, the  $A_+$  parameter is reduced by a factor of roughly 5 compared to sideband cooling, depending on the exact assumptions on the different laser and line parameters cf. [110]. To further increase the cooling performance of EIT cooling, Evers and Keitel [52] suggested to use an additional ground state to suppress also the blue sideband so that no second order heating process remains. By this technique the cooling limit can be reduced theoretically by another factor of  $\eta^2$  which lies typically between  $10^{-1}$  and  $10^{-2}$ .

In a scheme as depicted in Figure 15 b), the states  $|1\rangle$  and  $|2\rangle$  are both coupled to the excited state  $|e\rangle$  with the same detuning  $\Delta = \Delta_1 = \Delta_2$  just as in the previous Section. Now, additionally state  $|3\rangle$  is coupled to the excited state with detuning  $\Delta - \nu$ , preventing

scattering on the blue sideband. Assuming the excited state to only decay to ground state  $|1\rangle$  allows for an analytic expression for the  $A_+, A_-$  parameters, as given by [52]

$$A_{+,-} = \frac{\Omega_1^2 \Omega_2^2 \Gamma \nu^2}{(\Omega_1^2 + \Omega_2^2) (\Gamma^2 \nu^2 + 4((\Omega_1^2 + \Omega_2^2)/4 - \nu(\nu \mp \Delta) + \mathcal{E}_{\pm}))^2} \quad (87)$$

with

$$\mathcal{E}_{\pm} = \mp \frac{\nu \Omega_3^2}{4(\Delta - \Delta_3 \mp \nu)} \quad (88)$$

describing the influence of the third ground state. Choosing  $\Delta = \Delta_1 = \Delta_2$ ,  $\Delta_3 = \Delta - \nu$ , and  $\nu = \frac{1}{2} \left( \sqrt{\Delta^2 + \Omega_1^2 + \Omega_2^2 + \Omega_3^2/2} - \Delta \right)$ , scattering on the carrier and blue sideband ceases and the Stark shifted resonance coincides with the red sideband. It holds, that  $A_+ = 0$  and therefore

$$\bar{n} = 0 + \mathcal{O}(\eta^4). \quad (89)$$

In practice, the assumption  $\Gamma = \Gamma_1$  does often not hold and the  $A_-$  parameter can have lower values than indicated by the formula while the  $A_+$  parameter will always be larger than 0. Numerical simulations are necessary to compute the cooling performance in that case. A typical scattering rate  $R(\Delta_1)$  is shown in Figure 17. The red sideband is still on resonance, while both carrier and blue sideband are completely suppressed. The additional resonance appearing between blue sideband and carrier is the dressed state due to the third laser. It will not influence the cooling as long as there are no other motional frequencies on resonance.

#### 5.4.4 Noise sensitivity of EIT cooling

The preceding derivations always considered noise free monochromatic laser sources. Since EIT is a cooling process that relies on interference of the applied lasers, it is necessary to investigate the influence of frequency noise on the cooling performance. This will be done separately for the two and three ground state processes:

##### 5.4.4.1 Single EIT cooling noise sensitivity

For the single-EIT cooling scheme, the dominant heating effect of frequency noise is carrier scattering that is completely canceled in the ideal case only. The relevant heating scattering rates for the carrier transition can be calculated by integrating the power spectrum of the noisy laser times the scattering rate. Since this scattering only disappears for the power at exactly the carrier frequency, all the noise

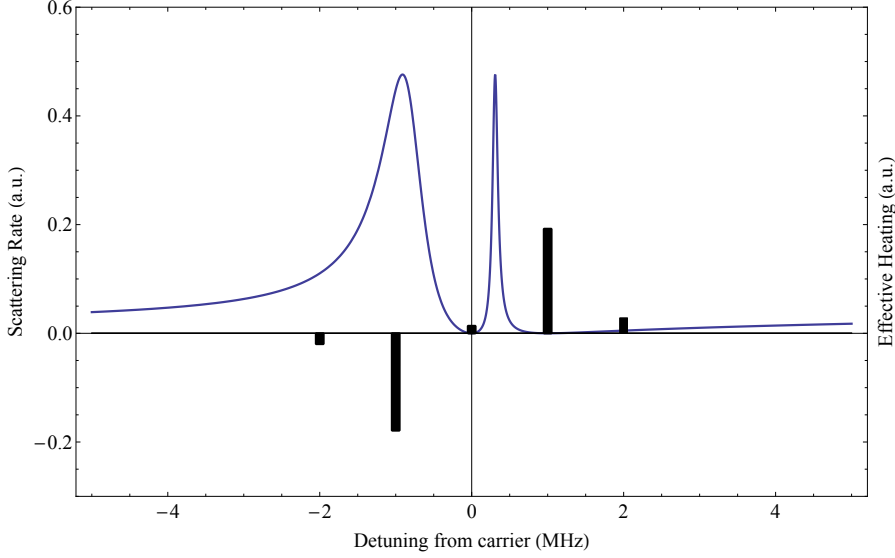


Figure 17: Double-EIT cooling resonance. The figure shows the scattering rate (blue line, left ordinate) for double-EIT cooling and the relative heating contribution of the different sidebands (bars, right ordinate). The parameters were  $\Gamma_1 = 21$ ,  $\Gamma_2 = 0$ ,  $\Gamma_3 = 0$ ,  $\nu = 1$ ,  $\Delta_2 = 42$ ,  $\Omega_2 = 7$ ,  $\Omega_3 = 15$  (all MHz). Both the carrier and the first blue sideband are completely suppressed. The lowest order heating process is now the second blue sideband which strength scales with  $\eta^4$ .

contributes to the carrier scattering. In the limit of  $\Omega_1 \ll \Omega_2$ , the carrier heating scattering rate is given by

$$R_{\text{car}} = \tilde{\eta}^2 \int_{-\infty}^{\infty} \frac{S_E(\omega)}{S_{\text{Et}}} \frac{\Gamma}{\Gamma_1} R(\Delta_1 = \omega - \omega_0 + \nu) d\omega. \quad (90)$$

Here, the  $\tilde{\eta}$  is the Lamb Dicke parameter for spontaneous emission which differs from  $\eta$  depending on the exact geometry of the experiment.  $S_E(\omega)$  is the power spectral density of the laser and  $S_{\text{Et}}$  its total power  $S_{\text{Et}} = \int_{-\infty}^{\infty} S_E(\omega) d\omega$ .  $R(\Delta_1)$  is the rate given in Equation 77. Here, all noise is attributed to the probe laser but since the relevant process is a two-photon transition, this is equivalent to effective noise in the frequency difference of the two lasers. For a Lorentzian lineshape with linewidth  $\gamma$ , Equation 90 simplifies to

$$R_{\text{car}} = \tilde{\eta}^2 \frac{\Gamma}{\Gamma_1} \gamma \frac{\Omega_1^2}{\Omega_2^2}. \quad (91)$$

This rate must be much smaller than  $\eta^2 A_+$  in order to not affect the cooling performance significantly. In a system with typical parameters ( $\Delta = 50$ ,  $\Gamma = 20$ ,  $\Omega_1 = 1$ ,  $\Omega_2 = 14.2$ ,  $\nu = 1$ , all MHz), this requires  $\gamma$  to be much smaller than  $2\pi \times 5$  kHz. This can be easily achieved if the two beams come from the same laser source but is a challenge if completely independent sources are used.

#### 5.4.4.2 Double-EIT cooling noise sensitivity

In the case of double-EIT cooling, the residual heating rate is suppressed on the order of  $\eta^2$  which means that the laser noise threshold is suppressed similarly. Calculations (see Appendix A.3) show that in the typical experimental case ( $\Delta = 42$ ,  $\Gamma = 21$ ,  $\Omega_1 = 3$ ,  $\Omega_2 = 7$ ,  $\Omega_3 = 15$ ,  $\nu = 0.94$ , all MHz) this requires the relative linewidth between laser 1 and laser 2 to be  $\gamma_{12} \ll 2\pi \times 0.3$  kHz and between laser 1 and 3 to be  $\gamma_{13} \ll 2\pi \times 2$  kHz. These calculations assume white frequency noise that is for diode lasers typically only a good approximation at high Fourier frequencies ( $> 100$  kHz). However, most of the noise induced scattering happens due to noise around the resonances seen in Figure 17. These are roughly at multiples of  $\nu/2$  and therefore in the MHz regime, making the white noise assumption reasonable. Additionally, it has to be noted that this relative linewidth includes not only laser frequency noise but can also have contributions from other sources, e.g. magnetic field noise that shifts the participating electronic states.

The scattering rate for the lowest order heating process on the second blue sideband was in this example around 16 Hz which is below the heating rate due to electronic noise observed in many ion traps (cf. Section 9.4.2.1). This means that not the laser induced heating but rather this background heating will limit the performance.

#### 5.4.5 Realization in calcium

The transition used for EIT cooling in  $^{40}\text{Ca}^+$  both for the first experimental demonstration by Roos et al. [144] and also for the experiments conducted within this thesis was the  $^2\text{S}_{1/2} \rightarrow ^2\text{P}_{1/2}$  transition. Here, the two Zeeman substates ( $m_J = \pm 1/2$ ) of the S-state are the two ground states and one of the Zeeman substates ( $m_J = -1/2$ ) of the P-state is the excited state. Selective coupling between the states is achieved by adjusting the laser polarization so that the strong dressing laser is purely  $\sigma_-$ -polarized, whereas the probe laser is purely  $\pi$ -polarized. In the two-level experiments, the  $\text{D}_{3/2}$  state is sometimes populated and simply repumped with an 866 nm laser. For the realization of the double-EIT experiments, the  $^2\text{D}_{3/2}(m_J = -3/2)$  state is used as the third ground state. All the  $\text{D}_{3/2}$ -states are coupled to the  $\text{P}_{1/2}$  states via light with equal  $\sigma_+$  and  $\sigma_-$  polarization contributions and no  $\pi$  component. This setup is shown in Figure 18.

The setup differs from the ideal three-level scheme described in Section 5.4.3 as follows

- The  $\pi$  polarized beam couples the  $\text{S}_{1/2}, m_J = +1/2$  state to the  $\text{P}_{1/2}, m_J = +1/2$  state. Here, no two-photon resonances play a role due to the large Zeeman shift, such that predominantly off-resonant carrier scattering takes place. This leads to heating and

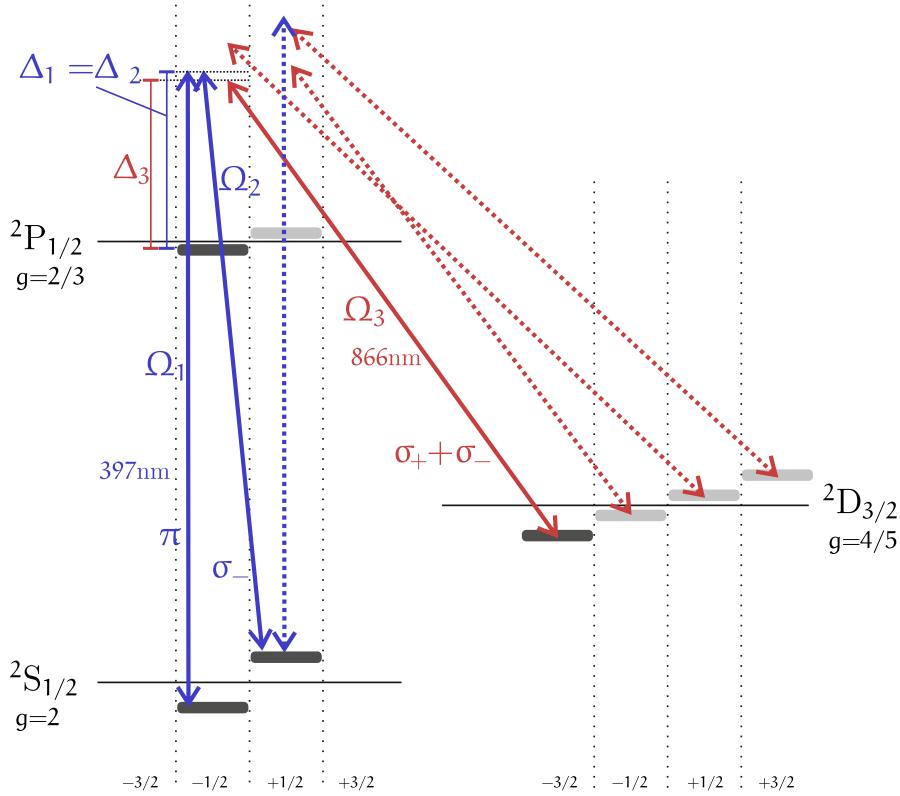


Figure 18: Double-EIT cooling in  $^{40}\text{Ca}^+$ . The double-EIT cooling scheme is realized by coupling the two Zeeman substates of the  $S_{1/2}$  ground state and the  $m_J = -3/2$  substate of the metastable  $D_{3/2}$  state to the  $m_J = -1/2$  substate of the excited  $P_{1/2}$  state. The  $\pi$ -polarized 397 nm beam also couples the  $+1/2$  substates of S and P, resulting in unwanted scattering on that transition. The  $D_{3/2}$  that were not used in the scheme are repumped off-resonantly by the 866 laser.

can only be avoided by choosing  $\Omega_2 \gg \Omega_1$  for the dark state to consist primarily of the  $S_{1/2}, m_J = -1/2$  state. This compromises the cooling speed, which is in the ideal setup optimal for  $\Omega_1 = \Omega_2$  [111].

- The other  $D_{3/2}$  states are excited both by spontaneous decay out of the  $P_{1/2}$ -states but also due to stimulated emission from the 866-laser. Repumping them into the cooling cycle requires scattering on the carrier which heats the ion. Choosing the polarization of the 866 nm laser to be purely  $\sigma_{\pm}$  helps because then coupling between the  $D_{3/2}, m_J = -1/2$  and the  $P_{1/2}, m_J = -1/2$  state is suppressed. This has the consequence that only one extra state, the  $D_{3/2}, m_J = +1/2$  state couples to the  $P_{1/2}, m_J = -1/2$  state and is populated via stimulated emission.

## 5.4.6 Simulations of EIT cooling

To investigate the complete dynamics of the system, including higher order sidebands and the effect of the other accessed metastable and excited states, the full quantum mechanical master equation (Equation 62) needs to be solved. In the case of the calcium ions, this includes 8 internal levels (2 S, 2 P, 4 D states) and infinite motional levels. It can be solved numerically by restricting the motional levels to an  $n_{\text{max}}$ . For the setup shown in Figure 18 the equation reads

$$\frac{d}{dt} \tilde{\rho} = \mathcal{L} \tilde{\rho} \quad (92)$$

$$= \frac{1}{i\hbar} [\hat{H}, \tilde{\rho}] + \mathcal{K} \tilde{\rho}. \quad (93)$$

Here  $\hat{H}$  is the total Hamiltonian including the trap, the atom and the interaction and is written out in Appendix A.4.

These simulations have been performed to find the optimal settings for the cooling. For a detuning of  $\Delta = 42$  MHz, the optimal cooling performance was found for  $\Omega_1 = 3$  MHz,  $\Omega_2 = 7$  MHz and  $\Omega_3 = 15$  MHz. The cooling process starting from a Doppler cooled state with  $\bar{n} = 10.8$  and taking into account 30 motional levels is shown in Figure 19. One important result is that the dynamic and steady state distribution do not correspond to thermal states as given for the first order rate equation model of Section 5.1. This is because higher order processes start to play a significant role especially for the heating terms.

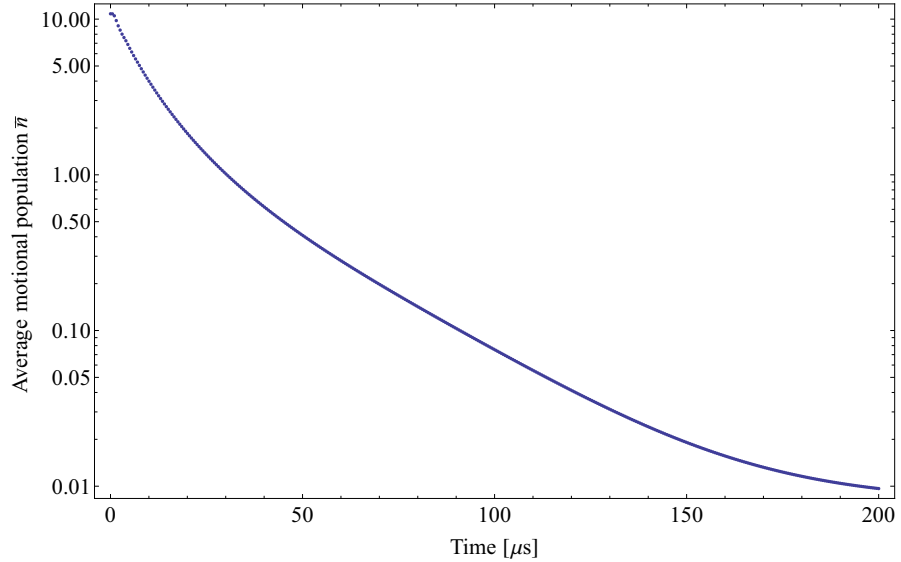


Figure 19: Simulation of double-EIT. The full master equation was solved numerically taking into account 30 motional levels. The initial state was a thermal state with  $\bar{n} = 10.8$ . The laser parameters were  $\Omega_1 = 3$  MHz,  $\Omega_2 = 7$  MHz and  $\Omega_3 = 15$  MHz,  $\Delta = 42$  MHz,  $\nu = 0.92$  MHz.



### 5.4.7 Discussion of the simulations

The optimal EIT-cooling parameters stated above do not correspond to the optimal parameters that can be deduced from Equation 87 or Reference [52]. There, for given detuning  $\Delta$  and trap frequency  $\nu$ , fastest and coldest cooling would always be achieved for  $\Omega_1^2 = \Omega_2^2 = 2\nu(\Delta + \nu)$  and  $\Omega_3 \rightarrow 0$ . For this choice, the red sideband scattering is maximized, while the carrier and blue sideband scattering are still completely suppressed. The theory formulas, however, neglect the spontaneous decay into the  $|3\rangle$ -state and the other three  $D_{3/2}$ -states. This decay makes it necessary to increase  $\Omega_3$  in order to achieve good cooling speeds because otherwise the ion is trapped in the nearly-dark  $D_{3/2}$ -state, slowing down the scattering. In practice, as shown in the previous section,  $\Omega_3$  needs to be larger than  $\Omega_1$  and  $\Omega_2$  for optimal performance. The asymmetry between  $\Omega_1$  and  $\Omega_2$  is necessary to produce a dark state with predominant  $S_{1/2}, m_J = -1/2$  population that does not scatter off-resonantly from the unused  $P_{1/2}, m_J = +1/2$  level. It turns out that to some extent cooling speed and cooling limit can be traded off each other by making  $\Omega_1$  and  $\Omega_2$  more asymmetric (slower, colder) or more symmetric (faster, hotter).

In both theory and simulations a larger detuning results in better cooling. Simulation results are shown in Figure 20. There, the achieved average motional populations  $\bar{n}$  are plotted for different detunings after 200  $\mu\text{s}$  of cooling, starting from a Fock state with  $n = 3$ . The Rabi frequencies of the three EIT beams have been adjusted for each detuning to achieve the coldest results. The general hierarchy  $\Omega_1 \ll \Omega_2 \ll \Omega_3$  for optimal cooling holds, independent of the chosen detuning. The final  $\bar{n}$  gets smaller for larger detuning, leveling off around  $5 \times 10^{-4}$  for detunings larger than 120 MHz. The simulation data are, however, consistent within errors with the further decrease in  $\bar{n}$  predicted by theory. The large error bars result mainly from the finite number of 100 simulations performed in the search for the optimum for each detuning and the associated risk of "missing" the optimum.

The theoretical reason for the decrease of the  $\bar{n}$  with large detunings is the asymmetry of the EIT-resonances. For larger detuning, the red sideband resonance gets larger but also narrower. However, even though this reduces  $\bar{n}$  in the simulations it may not be desirable in practice. Apart from the technical difficulties of achieving very large detunings and the corresponding high laser powers, this is also not desired in multi-mode cooling. There, a broad resonance is useful to achieve large red sideband scattering rates for multiple modes at different frequencies. The simulations indicate that it is possible to achieve average motional excitations of around  $\bar{n} \approx 1$  for all six modes of a two ion  $\text{Al}^+/\text{Ca}^+$  crystal in a single-EIT scheme with a detuning of  $\Delta = 2\pi \times 20 \text{ MHz}$ .

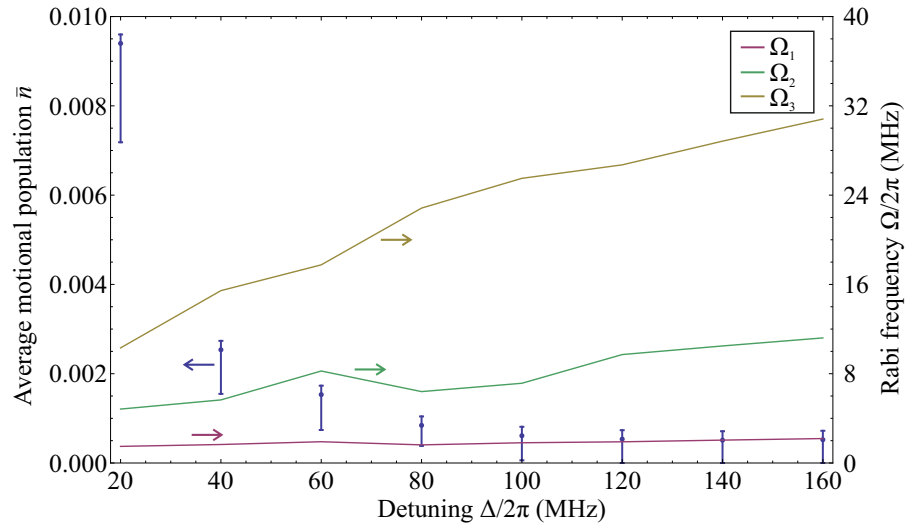


Figure 20: Detuning dependence of optimal Rabi frequencies and EIT cooling limit. The blue markers show the lowest  $\bar{n}$  achieved in the simulations for different detunings  $\Delta$  (left ordinate). The Rabi frequencies  $\Omega_{1-3}$  were optimized for every detuning and are also plotted (right ordinate). 100 simulations were performed for every detuning and the other parameters in the simulation were:  $B = 4.3$  G,  $\eta_{397} = 0.13$ ,  $\eta_{866} = 0.08$ ,  $\nu = 0.94$  MHz.

Experimental results for the double-EIT scheme are presented in Section 9.5 including a comparison to the simulations. The implications of EIT-cooling in quantum logic clocks are discussed in the outlook (Section 10.1).

## DOPPLER COOLING OF TWO ION CRYSTALS

---

In the Aluminum quantum logic clocks operated to date, the ion crystal was continuously Doppler cooled via the cooling ion during the clock interrogation pulse. This means that the second order Doppler shift of the clock is given by the steady-state energies during Doppler cooling, summed over all six normal modes. Since the relative amplitudes of the clock and the cooling ion in the different modes depend on their mass ratio (cf. Section 3.4), the cooling rates and limits will in general depend on this mass ratio as well. In this section, these cooling rates and limits for different two-species-two-ion crystals are derived analytically and compared to simulation results. The influence of external heating of the crystal by electric field fluctuations is explicitly taken into account. Additionally, the cooling dynamics of an  $\text{Al}^+/\text{Ca}^+$  crystal are investigated in order to derive an optimal cooling scheme for fastest recooling after a background collision.

*Parts of the following were published before by the author and his co-authors in [185].*

### 6.1 COOLING AND HEATING RATES

It can be shown (cf. Appendix A.1) that for cold ion crystals the six normal modes can be treated independently (i.e. the coupling between the modes is very weak). Because of this, rate equations like those given in Section 5.2 can be solved for each of the modes to get the cooling rates and limits. Since the Doppler cooling limit only depends on the cooling laser linewidth  $\Gamma$ , it will in general be the same for the different modes. However, since the cooling and heating rates scale with the Lamb Dicke parameter squared ( $\eta_{i,o}^2$ ), they can differ substantially. In terms of the mode parameters ( $b_{1,2}$ ) of Section 3.4, the in-phase ( $\eta_i$ ) and out-of-phase ( $\eta_o$ ) Lamb Dicke parameters along any of the trap axes are given in terms of the single ion parameter ( $\eta$ ) by

$$\eta_i = b_1 \eta \quad (94)$$

$$\eta_o = b_2 \eta. \quad (95)$$

This shows that for very asymmetric modes ( $b_1 \approx 0$  or  $b_2 \approx 0$ ), one of the modes will have a very small Lamb Dicke parameter, significantly reducing the heating and cooling rates. This renders the crystal very sensitive to external heating because the cooling might be too slow to compensate it quickly enough.

For an analytical treatment of these arguments, the heating and cooling rates are derived classically by averaging the radiation pressure force over the ion's oscillations in the trap. For the in-phase and out-of-phase modes with mode energy  $E_i$  or  $E_o$ , respectively, the cooling rates compute as (see Appendix A.1)

$$\frac{dE_i}{dt_{\text{cool}}} \approx \frac{2\hbar l_x^2 k^2}{m_1} \frac{I}{I_0} \frac{2\Delta/\Gamma}{(1 + I/I_0 + (2\Delta/\Gamma)^2)^2} b_1^2 E_i \quad (96)$$

$$\frac{dE_o}{dt_{\text{cool}}} \approx \frac{2\hbar l_x^2 k^2}{m_1} \frac{I}{I_0} \frac{2\Delta/\Gamma}{(1 + I/I_0 + (2\Delta/\Gamma)^2)^2} b_2^2 E_o. \quad (97)$$

Here  $I/I_0$  is the ratio of the applied laser intensity  $I$  to the transition's saturation intensity  $I_0$  and can also be expressed in terms of the Rabi frequency by  $I/I_0 = 2\Omega^2/\Gamma^2$ .  $l_x$  is the laser's  $k$ -vector projection onto the relevant trap axis and is for equal excitation along the three trap axes given by  $l_x = 1/\sqrt{3}$ .

The competing heating rates can be shown to be

$$\frac{dE_i}{dt_{\text{heat}}} \approx \hbar^2 (3l_x^2 + 1) k^2 \frac{I}{I_0} \frac{\Gamma}{12m_1} \frac{b_1^2}{1 + I/I_0 + (2\Delta/\Gamma)^2} \quad (98)$$

$$\frac{dE_o}{dt_{\text{heat}}} \approx \hbar^2 (3l_x^2 + 1) k^2 \frac{I}{I_0} \frac{\Gamma}{12m_1} \frac{b_2^2}{1 + I/I_0 + (2\Delta/\Gamma)^2}. \quad (99)$$

The heating rates due to stochastic electric field fluctuations can be written as [83]

$$\frac{dE_i}{dt_{\text{fluct}}} = \frac{q^2 S_E}{4m_1} \left( b_1 + \frac{1}{\sqrt{\mu}} b_2 \right)^2 \quad (100)$$

$$\frac{dE_o}{dt_{\text{fluct}}} = \frac{q^2 S_E}{4m_1} \left( b_2 - \frac{1}{\sqrt{\mu}} b_1 \right)^2. \quad (101)$$

Here  $S_E = S_E(\nu)$  denotes the electric field spectral density, which is assumed to be spectrally flat in the region of the relevant  $\nu_{i,o}$ . Additionally,  $S_E$  is in the following assumed to be isotropic. The homogeneous field fluctuations will only couple to center of mass motion and therefore much more strongly to the in-phase mode than the out-of-phase mode. In fact for  $\mu = 1$  it follows that  $b_1 = b_2$  and the out-of-phase mode is not heated at all. The total energy injected in one direction of motion is obtained by adding the in-phase and out-of-phase heating rates, which turns out to be proportional to  $m_1^{-1} + m_2^{-1}$ , showing the advantage of heavy cooling and clock ions.

The steady state cooling limit in the presence of external heating is obtained by solving

$$\frac{dE_i}{dt_{\text{cool}}} + \frac{dE_i}{dt_{\text{heat}}} + \frac{dE_i}{dt_{\text{fluct}}} = 0. \quad (102)$$

The steady state energy limit for the in-phase mode is then given by:

$$E_{\text{limit},i} = \frac{\Gamma (1 + (2\Delta/\Gamma)^2 + I/I_0)^2}{48|\Delta|\hbar I/I_0 l_x^2 k^2} \times \left[ \frac{\Gamma \hbar^2 I/I_0 (3l_x^2 + 1)k^2}{1 + (2\Delta/\Gamma)^2 + I/I_0} + \frac{3}{b_1^2} (b_1 + \frac{1}{\sqrt{\mu}} b_2)^2 q^2 S_E \right]. \quad (103)$$

The limit for the out-of-phase mode is gained by substituting  $b_1$  by  $b_2$  and  $b_2$  by  $-b_1$ .

The additional heating modifies the steady state solution for Doppler cooling Equation 74 by breaking the symmetry between cooling and heating processes: The photon-induced heating and cooling rates have the same dependence on the mode amplitudes, resulting in a Doppler limit independent of this parameter. The external heating rate has a more complex dependence on the mode amplitudes, resulting in a cooling limit that is a sensitive function of the modal amplitudes and therefore the  $\epsilon$  and  $\mu$  parameters. As a result, modes where the cooling ion has a large relative amplitude are cooled more efficiently than modes where it has a small amplitude.

The minimal mode energies are always achieved for a detuning of  $\Delta = -\Gamma/2$ , but the laser intensity  $I/I_0$  has to be adjusted, depending on the magnitude of the external heating  $S_E$ . In low external heating situations, low laser powers will give the best results. For large external heating the power must be increased, accepting the larger laser heating rates in order to better compensate the external heating rates with faster cooling.

The clock ion second order Doppler shift due to the motion along one principal axis is directly proportional to the clock ion energy  $E_c$  and given by [141]

$$\frac{\Delta\omega}{\omega} = -\frac{\langle v_2^2 \rangle}{2c^2} = -\frac{E_c}{2m_2 c^2} = -\frac{b_2^2 E_i + b_1^2 E_o}{2m_2 c^2}. \quad (104)$$

Here,  $\langle v_2^2 \rangle$  is the average squared clock ion velocity as measured in the laboratory frame of reference and  $c$  the speed of light. The  $b_{1,2}$  parameters have a different mass dependence for axial and radial modes making it necessary to treat the two cases separately.

### 6.1.1 External heating influence on axial modes

The axial mode parameters  $b_{1,2}$  only depend on the mass ratio  $\mu$  (see Equation 34) and therefore the energy limit of Equation 103 can be minimized for any combination of mass ratio and noise power spectral density  $S_E$ . The minimal achievable energies are shown in Figure 21. The spectral densities are given as multiples of a reference spectral density  $S_{E0}$ . This is the spectral density for which the two heating rates (Equation 98 and 100) in a symmetric ( $\mu = 1$ ) ion crystal equal. A value of  $S_E/S_{E0} = 0.02$  corresponds to a heating rate of

approximately 1500 quanta per second for a single  $\text{Ca}^+$  ion in a trap with trap frequencies of 2.5 MHz. It can be regarded as a worst case limit for most ion traps used for spectroscopy. It turns out that for any heating rate the minimal clock ion energy is always achieved at a mass ratio of  $\mu = 8/11$ . This corresponds to the cooling ion being slightly heavier than the clock ion and can be explained by the fact that the strongly heated in-phase mode has in that case a large cooling ion amplitude and is therefore also strongly cooled. Background heating predominantly affects the in-phase mode, so it's advantageous to optimize the in-phase cooling. Since the heavier ion moves more for the in-phase mode (and the lighter ion moves more for the out-of-phase mode), it is advantageous if the cooling ion is the heavier one to give faster cooling when fighting the dominant fixed heating rate. The plot is independent of  $\Gamma$  and the actual values of  $m_1, m_2$ . However, the normalization factor and therefore the absolute value for the cooling limit depends on the linewidth of the cooling transition. The figure shows that the clock ion's axial kinetic energy is only a weak function of the mass ratio. This is a direct consequence of the weak dependence of the axial mode amplitudes on this parameter, as shown in Figure 8.

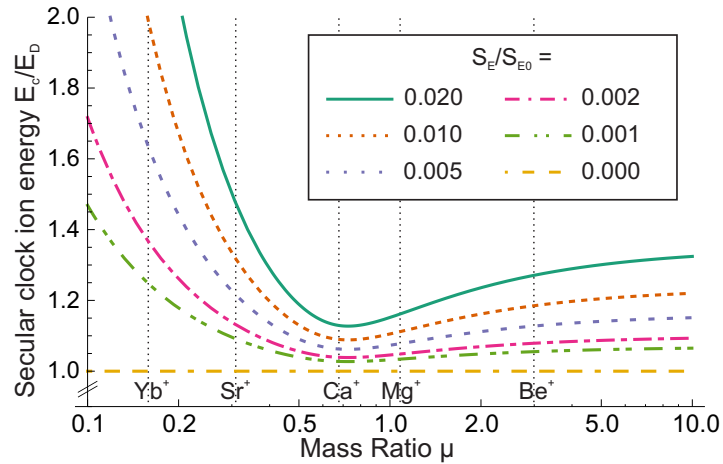


Figure 21: Normalized axial clock ion energy plotted against the mass ratio  $\mu$  of the ion crystal. The energy  $E_c$  of the clock ion is the sum of the clock ion energy in both modes. The calculations were performed for varying electric field spectral densities  $S_E$ . The cooling laser intensity  $I/I_0$  has been optimized for each value of  $S_E$ . The dashed lines show different logic ion species for an  $\text{Al}^+$  clock.

### 6.1.2 External heating influence on radial modes

The radial mode parameters  $b_{1,2}$  depend on the ratio of radial and axial confinement given by the  $\epsilon$ -parameter (cf. Equation 37) as well as on the mass ratio  $\mu$ . Therefore, Equation 103 must be optimized for each triple of  $\mu, \epsilon, S_E$  parameters. This is shown in Figure 22. Here, the

minimal clock ion energy is achieved for mass ratios slightly larger than 1 which is due to the cooling ion amplitude being large in the in-phase mode for light cooling ions. For a given mass ratio, the energy of the clock ion in the presence of external heating is lowest when operating the trap close to the point where the linear axial configuration flips to a linear radial configuration. The reason for this is that the larger the radial confinement, the more the modal amplitude in the radial modes tend towards  $b_1 \approx 1$ ,  $b_2 \approx 0$  or vice versa (see Equation 37 and Figure 8), i.e. the motion of the two ions decouples for strong RF drive. In that case, the mode with negligible motion of the cooling ion will cool very poorly, leading to an elevated steady state temperature in the presence of external fields. In this regime, the comparison of Figures 21 and 22 shows that the heating-induced radial clock ion energy is larger than the axial clock ion energy and will therefore dominate the clock frequency shifts.

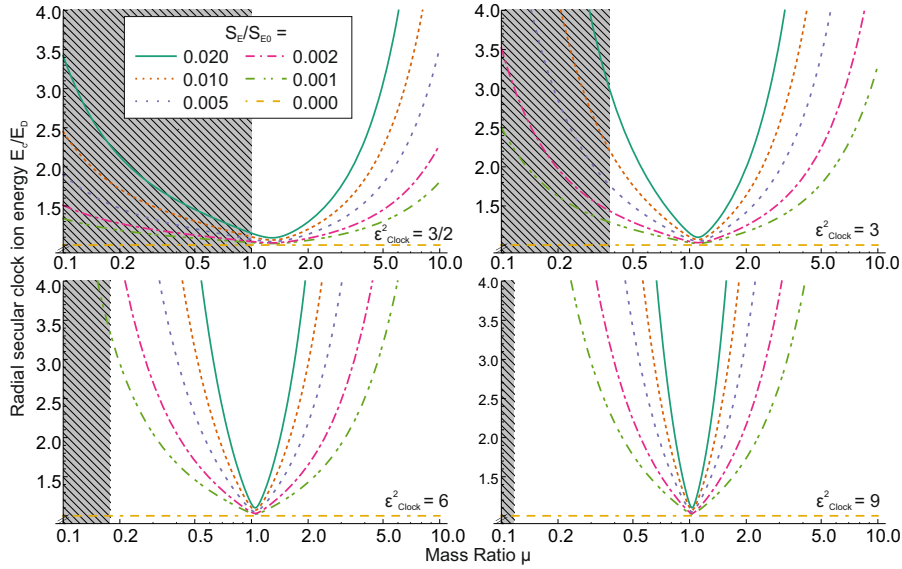


Figure 22: Normalized radial clock ion energy plotted against the mass ratio  $\mu$  of the ion crystal for radial modes. The energy  $E_c$  of the clock ion is the sum of the clock ion energy in both radial modes. The shaded region indicates parameters for which the ion crystal is no longer linear in axial direction. The cooling laser intensity  $I/I_0$  has been optimized for each value of  $S_E$ .

### 6.1.3 Micromotion considerations

Choosing an  $\epsilon$  parameter close to the instability regime improves the cooling limits, but at the same time increases the intrinsic micromotion amplitude of the radial modes (see Appendix A.2). Figure 23 shows the normalized total kinetic energy, equal to the sum of secular and micromotion kinetic energy, of the clock ion in an ion crystal

that has been cooled to the Doppler cooling limit (i.e. without external heating) plotted against the crystal mass ratio.

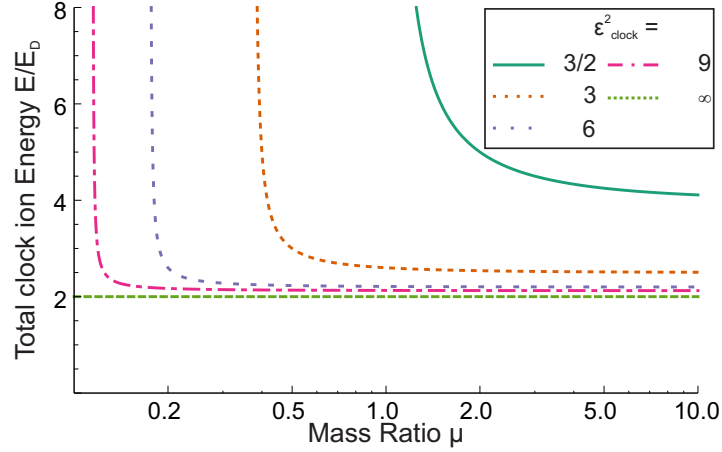


Figure 23: Total clock ion energy (secular energy + micromotion energy) of a clock ion in a Doppler cooled crystal along one radial direction. Here the mass ratio  $\mu$  and the  $\epsilon$ -parameters were varied and the energy was normalized to the Doppler cooling energy  $E_D$ . The absence of external heating was assumed. Due to large micromotion contributions the total energy diverges at the points where the crystal becomes unstable.

Since the micromotion kinetic energy contributes to the second-order Doppler shift in the same way the secular energy does, it is not advisable to perform spectroscopy in a trap operating close to the unstable regime. The operation in a trap with very strong radial confinement is equally bad because of the inefficient cooling of the weakly damped radial mode. For best cooling performance it is therefore advisable to optimize the  $\epsilon$ -parameter according to the observed heating rate in the trap.

#### 6.1.4 Total Doppler shift in aluminum ion quantum logic clocks for different cooling ion species

A comparison of the total second-order Doppler shift including the scaling factors due to micromotion for the radial modes in a linear ion trap for  $\text{Al}^+/\text{X}^+$  ion crystals with different possible cooling ions  $\text{X}^+$  is shown in Figure 24. The x-axis gives the normalized electric field spectral density  $S_E/S_{E0,\text{Ca}}$ <sup>1</sup>. The  $\epsilon^2$  value as well as the Doppler laser detuning  $\Delta$  and intensity  $I/I_0$  were optimized for each value of  $S_E$ .

The graph shows that an  $\text{Al}^+/\text{Mg}^+$  crystal suffers the least from external heating since its mass ratio is very close to 1. However, for traps with fairly low heating rates, the Doppler shift in  $\text{Al}^+/\text{Ca}^+$

<sup>1</sup>  $S_{E0,\text{Ca}} \approx 1.26 \times 10^{-9} \text{V}^2/\text{m}^2\text{Hz}$  for  $\text{Ca}^+$  ions.



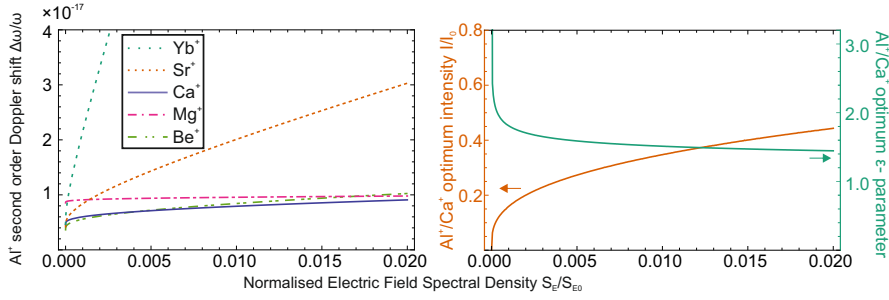


Figure 24: Comparison of secular motion-induced second-order Doppler shifts for  $\text{Al}^+/\text{X}^+$  crystals with different cooling ions  $\text{X}^+ = \{\text{Be}^+, \text{Mg}^+, \text{Ca}^+, \text{Sr}^+, \text{Yb}^+\}$  in the presence of external heating with an electric field spectral density of  $S_E$ . The right figure shows the parameters  $\epsilon$  and  $I/I_0$  for best cooling performance for an  $\text{Al}^+/\text{Ca}^+$  crystal. Those optimum parameters for a spectral energy density of  $S = 0.005S_{E0}$  are given by  $(2.63, 0.40)$ ,  $(3.17, 0.05)$ ,  $(1.12, 0.87)$  and  $(1.04, 1.61)$  for the Be, Mg, Sr and Yb crystals, respectively.

and  $\text{Al}^+/\text{Be}^+$  traps will be lower than that of  $\text{Mg}^+$ -systems because the linewidth of the cooling transition of  $\text{Mg}^+$  ions is approximately a factor of 2 larger than that of  $\text{Ca}^+$  and  $\text{Be}^+$  ions. The two other species  $\text{Yb}^+$  and  $\text{Sr}^+$  suffer from their small mass ratios and require traps with very small heating rates to reach comparable performance.

## 6.2 COOLING TIMES

An atomic clock will reach its maximum performance in terms of stability, if the clock transition is probed without any dead time between consecutive readings [40, 152, 125]. One contribution to the dead time is the time it takes to cool the ion crystal in case a collision with a hot background gas particle occurred. The large energy transfer to the ion crystal by a background gas collision leads to typical temperatures on the order of room temperature, resulting in the decrystallization of the ion crystal. As a consequence, it is necessary to take the nonlinear contributions of the Coulomb forces into account to evaluate the cooling dynamics at these high temperatures. The nonlinearities are usually neglected in the small oscillation approximation used to describe the low temperature dynamics of the system as in the previous sections. The dynamics of small ion crystals during laser cooling in various temperature regimes have first been studied in the context of phase-transitions and chaos theory [17, 18].

Here, the equations of motion resulting from the complete ponderomotive two ion potential have been solved numerically. The potential is given as

$$V(x_1, y_1, z_1, x_2, y_2, z_2) = \frac{1}{2}m_1 (\nu_{x_1}^2 x_1^2 + \nu_{y_1}^2 y_1^2 + \nu_{z_1}^2 z_1^2) + \frac{1}{2}m_2 (\nu_{x_2}^2 x_2^2 + \nu_{y_2}^2 y_2^2 + \nu_{z_2}^2 z_2^2) + \frac{e^2}{4\pi\epsilon_0} \frac{1}{\sqrt{(x_1 - x_2)^2 + (y_1 - y_2)^2 + (z_1 - z_2)^2}}, \quad (105)$$

where  $\nu_{kj}$  is the trap frequency of ion  $j$  in direction  $k \in x, y, z$ . For the simulations, the RF potential was neglected. However, only minor modifications to the results presented here are expected when micro-motion is included in the treatment [98]. An adaptive fourth order Runge-Kutta method was used, where the step size was reduced significantly every time the ions got close enough to explore the high non-linearities of the  $1/r$ -Coulomb potential. Cooling was simulated by applying random velocity kicks to the ion at rates computed from the relevant scattering rates. In detail, this was incorporated into the calculation by multiplying the instantaneous scattering rate  $R$  at every time step with the instantaneous step size  $dt$  at the same step and comparing the resulting value with a random number  $rn(0, 1)$  between 0 and 1 from a "Mersenne Twister"-type pseudo random number generator [100]. A scattering event that changed the velocity  $\mathbf{v}_1$  of the cooling ion according to the momentum change due to both absorption and spontaneous emission was therefore calculated whenever the condition

$$R dt = \frac{\Gamma}{2} \frac{I/I_0}{1 + I/I_0 + (2(\Delta - \mathbf{k} \cdot \mathbf{v}_1)/\Gamma)^2} dt < rn(0, 1). \quad (106)$$

was fulfilled.

With a small step size the simulation was robust and reproduced two-ion cooling limits as well as theoretical curves for the cooling duration of single ions (e.g. [176]).

A typical collision event with the background gas will be an elastic collision of a hydrogen molecule with either one of the two cold ions in the crystal. The maximum energy that can be transmitted in an elastic collision of two particles with masses  $m_1, m_2$  if one of them is initially at rest is given by  $\frac{4m_1 m_2}{(m_1 + m_2)^2}$  times the kinetic energy of the hot particle. In case of the collision of a cold aluminum ion and a hydrogen molecule at 300 K this results in a maximum energy of  $\approx 0.26 \times \frac{3}{2} k_B \times 300 \text{ K}$  that can be transferred to the aluminum ion. Here  $k_B$  denotes the Boltzmann constant. This corresponds to a temperature of the ion crystal of  $\approx 19.3 \text{ K}$ . Cooling an ion crystal from these high temperatures is aided by adding a far detuned laser beam additionally to the standard cooling beam at  $\Delta = -\Gamma/2$ . This enhances the scattering

rate of the rapidly moving cooling ion with large Doppler detuning. The optimum detuning of the second laser was found by simulating the cooling time for an aluminum/calcium ion pair starting at a temperature of 19.3 K as a function of the detuning. The results are shown in Figure 25.

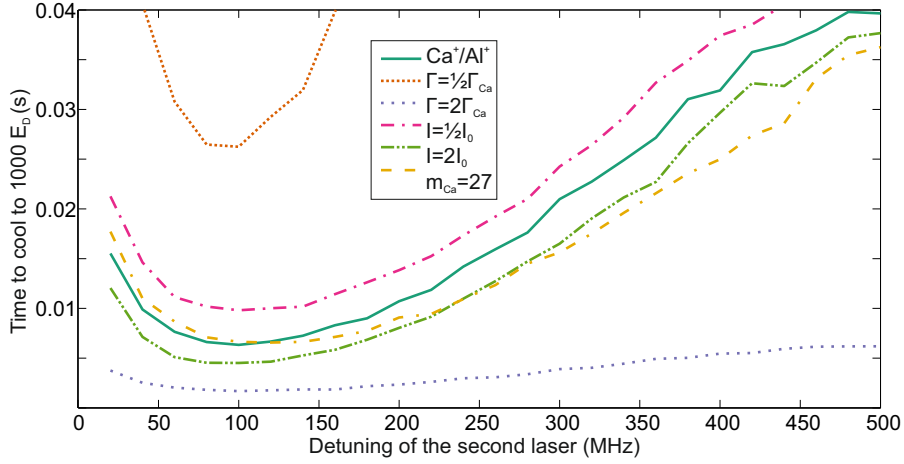


Figure 25: Time needed to cool an  $\text{Al}^+/\text{Ca}^+$  ion pair from 19.3 K to 1000 Doppler limits ( $\sim 800$  mK). The x-axis shows the detuning of a second laser at saturation intensity that is cooling the ion crystal in addition to the standard  $-\Gamma/2$ -detuned beam.

Both lasers were assumed to be directed onto the ion from the (1,1,1) direction and both had one saturation intensity at the position of the ion. To compare the performance of the different detunings, the time to reach a crystal energy of 1000 Doppler cooling limits was simulated. This energy roughly corresponds to the energy at which the ions crystallize. Fastest cooling was achieved at a detuning of  $\sim -100$  MHz. This optimum detuning of the second laser beam proved to be very robust against changes in the cooling parameters, such as a change in linewidth of the cooling transition, the intensity of the cooling laser, or the mass of the cooling ion. Since these changes mostly affect the scattering rate, the times needed to cool vary strongly. The general characteristics of the curve with the minimum close to  $-100$  MHz, however, stays the same. This can be explained by the fact that in a well-thermalized regime, the cooling ion will carry half the crystal energy and the optimal detuning should only depend on the average cooling ion velocity in the direction of the incoming laser. This is independent of the transition linewidth or the intensity of the cooling light. The change of mass of the cooling ion to smaller values shifts the optimal detuning to slightly higher values. This is because a lighter cooling ion has higher average velocities if it has the same energy as a heavier ion.

The difference in cooling dynamics between a two- and a single-ion system is shown in Figure 26. Besides the  $\text{Al}^+/\text{Ca}^+$  pair, the results for a single  $\text{Ca}^+$  ion in the trap with the second laser detuned

by 140 MHz is shown. This slightly higher optimum detuning arises, since a single ion will on average have higher velocities than the cooling ion in a two-ion system since the latter can exchange energy with the clock ion. For the simulation, the starting energy of the single  $\text{Ca}^+$  ion was set to the same value as that of the two-ion pair, although a collision with a hydrogen molecule would lead to a lower initial temperature.

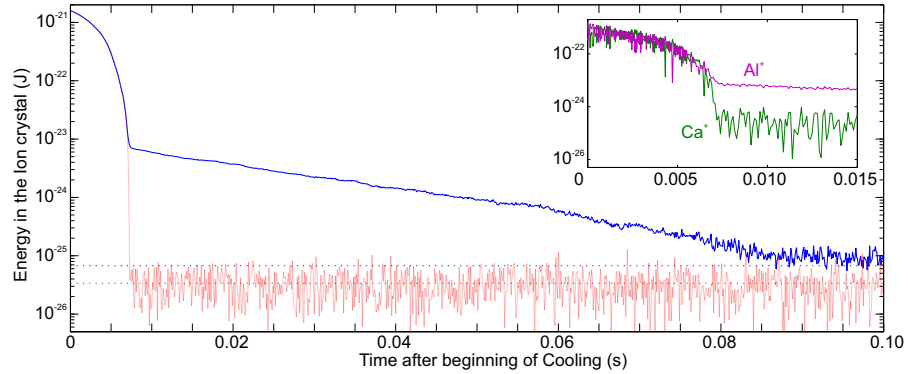


Figure 26: Cooling evolution of an  $\text{Al}^+/\text{Ca}^+$  ion pair after a collision event with an  $\text{H}_2$ -molecule (blue line). The red line shows the cooling evolution of a single  $\text{Ca}^+$  ion in the same trap with the same initial energy. The horizontal dotted lines denote the Doppler cooling limit and the inset shows the energies of the calcium and aluminum ion before and after crystallization occurred at around 7 ms.

At the beginning of the cooling process, the cooling rates for the  $\text{Al}^+/\text{Ca}^+$  crystal and for the single  $\text{Ca}^+$  ion match well. This is because both ions are still fairly hot and collide regularly, resulting in almost instant thermalization of all motional modes. At around 7 ms the ion pair crystallizes, meaning that the ions freeze out around their equilibrium positions and collisions cease to occur. This leads to heavily reduced cooling rates of the ion crystal owing to the weakly damped modes which are no longer thermalized with the well cooled modes. The transition between collisionally coupled and isolated motional modes manifests itself in the emerging difference between the energies of the aluminum and calcium ions (see inset of Fig. 26). For a theoretical description of the crystallization see for example [18], for a measurement of the damping of the weakly cooled modes see the supplementary material of [148].

Summarizing the simulation results of Figure 25 and 26, an optimum cooling strategy after a background gas collision can be derived: The fastest cooling is achieved by ramping the laser detuning according to the actual energy of the ion crystal, such that maximal scattering rates are maintained. Additionally, the intensity of the cooling laser should be large to increase the rates even further. Once crystallization occurs, the laser should be ramped to a detuning and an in-

tensity for which the lowest energies are achieved (typically  $\Delta \approx \Gamma/2$ ,  $I \sim I_0$ ).

In our simulations the time needed to cool an  $\text{Al}^+/\text{Ca}^+$ -crystal to 2 Doppler cooling limits is roughly 90 ms (which corresponds well to previous studies [156, 44]) while the time it takes to reach crystallization is only 7 ms. The total cooling time might be reduced to roughly the crystallization time by coupling the well-damped to the poorly-damped modes by a static radial electric field as has been demonstrated in [148]. Given typical cycle times of 230 ms in optical clocks [24], even Doppler cooling times as long as 100 ms will not compromise the stability of the clock significantly, provided a suitable vacuum environment under which the time between collisions typically is longer than 100 s [24]. It is, however, necessary that the collision events are detected and actions are taken to ensure fast recrystallization.



Part III

EXPERIMENT





## EXPERIMENTAL SETUP

In this chapter, the different components of the experiment are described. First, the parts related to the "physics package" are explained, consisting of the vacuum apparatus, the trap and trap drive as well as the atom ovens. In the second part, the laser system and the laser locks are described. The chapter concludes with a brief report on the implemented imaging optics and the experimental control system.

### 7.1 VACUUM SETUP

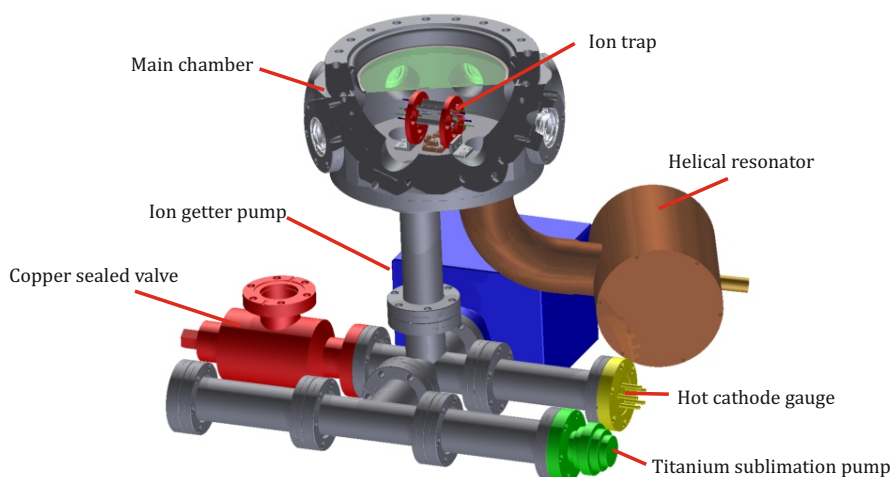


Figure 27: Vacuum setup. The picture shows a CAD sketch of the vacuum chamber including the atom ovens, the ion trap and the helical resonator. The main chamber is cut to see the inside. The vacuum is achieved by a 20l/s ion getter pump and occasional usage of a titanium sublimation pump (occupies the whole horizontal tube in the foreground). Additional vacuum equipment like a turbo pump can be connected to the copper sealed valve and the pressure is monitored with the hot cathode gauge.

The vacuum chamber consists of a Conflat (CF) 150 flange that acts as a base plate onto which an octagon<sup>1</sup> is set. The octagon has eight CF40 flange connections, to which the viewports for the laser beams (see Section 7.5) are connected. On top, a CF150 viewport enables the collection of photons scattered by the ions and gives additional optical access for lasers. The ion trap and the atom ovens are mounted onto the base plate where additionally three more CF40 flanges are

<sup>1</sup> Kimball Physics MCF800-SphOct-G2C8

connected. Two of them are used for electronic feedthroughs: a 19 pin feedthrough<sup>2</sup> for the compensation electrodes and atom ovens and a 4 pin feedthrough<sup>3</sup> for the trap RF voltage and the tip DC voltage. The remaining flange connects the main chamber to the vacuum pumps. These are a 20l/s ion getter pump<sup>4</sup> and a titanium sublimation pump<sup>5</sup>. Further vacuum equipment can be connected via a copper sealed full metal valve. The vacuum pressure is monitored via a hot cathode gauge<sup>6</sup>.

Evacuation of the chamber was done via a turbo pump with an upstream rotary vane pump. The chamber was baked out at a temperature of 190 °C for 11 days. Three of the viewports<sup>7</sup> were found to be damaged after bakeout and sealed with TorrSeal. After this, a final pressure of  $< 8 \times 10^{-11}$  mBar was achieved. Ion lifetimes were initially on the order of tens of minutes, but after 2 years of operation exceeded 6 hours. This suggests that a small virtual leak was present initially.

## 7.2 EVAPORATION OVENS

Ions are loaded into the ion trap by ionizing particles from a beam of neutral atoms as they pass the ion trap (see Section 9.1). The beam of neutral atoms is created by evaporation of solid aluminum and calcium samples in ovens.

The temperature needed for evaporation of aluminum and calcium at different ambient pressures is shown in Figure 28. Calcium atoms will evaporate directly from the solid phase, once they are heated up to 500-700 K. For aluminum atoms, it may barely be possible to operate the ovens in a temperature regime where the atoms make the solid-gaseous transition directly. However, as soon as the pressure at the position of the oven exceeds approximately  $2 \times 10^{-9}$  mBar, aluminum melts before it evaporates. This makes it necessary to construct the aluminum ovens such that liquid aluminum will not leak out. A further complication in the design of aluminum ovens is that aluminum forms low melting alloys with most other metals [65]. A nonmetallic oven design is therefore preferred.

### 7.2.1 Oven design

The oven design used for the experiments described here is schematically shown in Figure 29. It consists of an Al<sub>2</sub>O<sub>3</sub> ceramic tube<sup>8</sup> with

<sup>2</sup> Vacom CF35-MPC2-19-SE-CE-SSG

<sup>3</sup> Vacom CF35-MHV-4-GS-SE-CE-SS

<sup>4</sup> Varian Vaclon Plus 20 StarCell

<sup>5</sup> Varian titanium sublimation pump 9160050

<sup>6</sup> Varian UHV-24 Bayard-Alpert Gauge Tube

<sup>7</sup> TorrScientific VPZ38Q-NM

<sup>8</sup> Friatec F149R11004-07

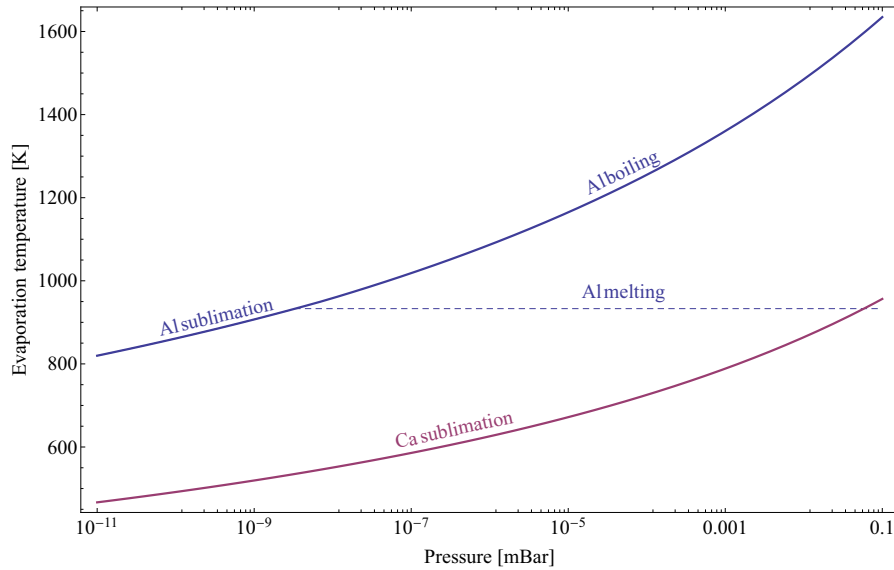


Figure 28: Evaporation temperatures of calcium and aluminum. Calcium atoms will directly evaporate from the solid phase at the pressures experienced in the experiment. Aluminum atoms, however will melt prior to evaporation once the ambient pressure around the ovens exceeds  $10^{-9}$  mBar.

six bores that are placed in a centered pentagonal fashion. The center bore is filled with either calcium or aluminum and through the outer six bores a 0.25 mm thick tantalum heating wire is wound. This wire also holds the oven and is itself connected conductively to the oven mount, from where the heating current is supplied. The current heats the tantalum wire and therefore also the tube and the calcium/aluminum inside. Tantalum was chosen because it has a very high melting point (2996 °C) compared to most other metals. Another option would have been tungsten with an even higher melting point but the smaller resistivity would have required a current too high for the vacuum feedthroughs. The ceramic tube is used to keep the aluminum from being in contact with other metals. Its central bore is tamped with ceramic glue<sup>9</sup> at its bottom end.

### 7.2.2 Oven temperature and time constant

The temperature dependence of the resistivity of the tantalum wire can be used to measure the temperature of the heating wire. The model used here assumes that the tantalum wire gets heated homogeneously while the rest of the electric circuit stays at room temperature. Figure 30 a) shows the temperature of the heating wire as a function of the applied current. More than 2000 K can be achieved, sufficient for aluminum evaporation. This was verified by fluorescence mea-

<sup>9</sup> Ceramabond 552

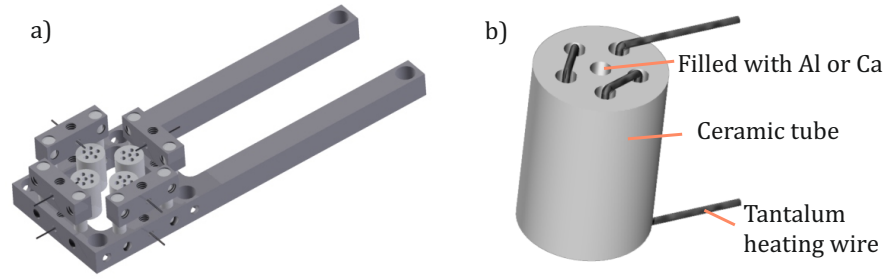


Figure 29: Evaporation oven design. Figure a) shows the four ovens (2 calcium, 2 aluminum) in the oven mount that is placed directly below the ion trap. Figure b) shows the ceramic tube together with the tantalum wire that is used to both heat the oven and to hold it. The center bore is filled with aluminum or calcium.

measurements as can be seen in the inset of Figure b), where fluorescence of aluminum atoms from a test oven is visible. Figure b) shows the step response of the temperature of the heating wire after applying a current step from 0 A to 4.5 A. It could be fitted by a second order exponential of the form

$$T(t) = T_{\text{end}} - (T_{\text{end}} - T_{\text{start}}) \times (\alpha e^{-t/\tau_1} + (1 - \alpha)e^{-t/\tau_2}). \quad (107)$$

The time constants are  $\tau_1 \approx 0.61$  s and  $\tau_2 \approx 21$  s. While the first

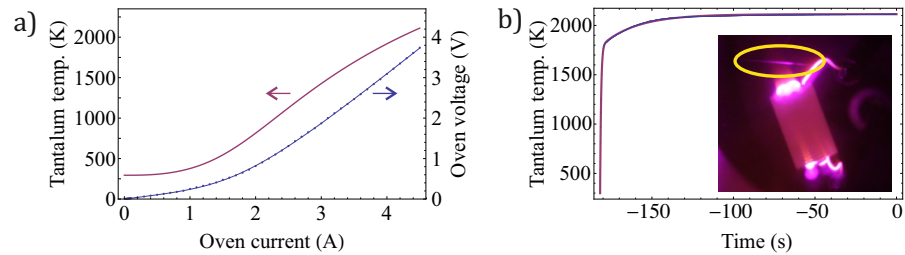


Figure 30: Oven temperature and time constant. Figure a) shows a steady state I-V curve of one of the ovens in the chamber (blue curve, right ordinate). From this the resistance of the tantalum wire and hence its temperature could be extracted (red curve, left ordinate). Figure b) shows the step response of the atom when a 4.5 A step is applied (blue dots). The data has been fitted with a second order exponential approach (red curve) with time constants of 0.61 s and 21 s. The inset shows fluorescence of a beam of aluminum atoms emerging from the hot ovens that have been exposed to a laser at 395 nm.

can be interpreted as the fast heating of the tantalum wire, the second reflects the slow heating of the ceramic tube until equilibrium is reached. To overcome this waiting time, the current in the experiment was typically set slightly too high initially and then reduced after some tens of seconds.

### 7.3 ION TRAP

Apart from the ovens, the next crucial ingredient of the experiment is the ion trap itself. The linear Paul trap (cf. Section 3.2) used for the experiments described here is introduced in the next subsection and thereafter finite element simulations of the trap are presented.

#### 7.3.1 Design

The trap design was adapted from the four-blade-two-tips design originally described in [60]. It has hence been used in many ion trap experiments, including those described in [60, 66, 25, 11, 140]. It is from now on referred to as the "Innsbruck-type" trap design. Photographs of the trap are shown in Figure 31. The design has

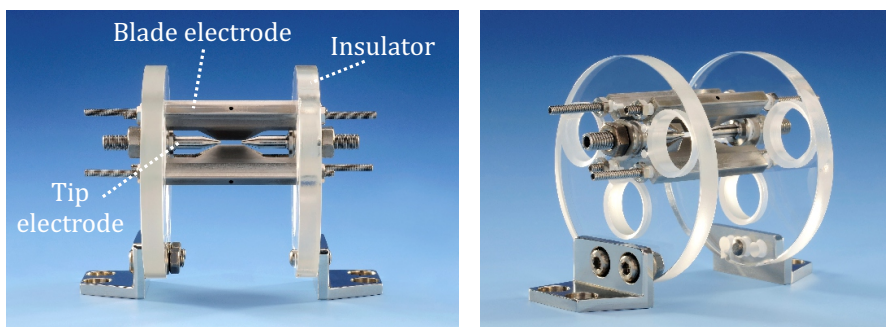


Figure 31: Photographs of the ion trap. The Figure shows the titanium blade and tip electrodes as well as the sapphire disk insulators.

been modified by the author and his colleagues with significant support and contributions from the PTB scientific instrumentation departments 5.51, 5.53 and 5.56.

The major changes compared to the original design were the materials used for the electrodes and the insulators. All metal parts were made of a titanium alloy (TiAl6V4) and the insulators of monocrystalline aluminum oxide  $\alpha\text{-Al}_2\text{O}_3$  (sapphire). Titanium was used because of its small magnetic susceptibility ( $1.8 \times 10^{-4}$  volumetric susceptibility [175]). The former traps of similar type were typically made of stainless steel which has a larger susceptibility which means that any susceptibility fluctuations (e.g. thermal) infer magnetic field changes at the ion's position, potentially worsening the clock performance. The electric and thermal conductivity of the used titanium alloy is comparable to stainless steel, so that no larger trap heating was expected (cf. Section 7.3.4). The blades were manufactured by wire erosion with a relative manufacturing precision of  $<1 \mu\text{m}$  and a surface roughness of  $<0.1 \mu\text{m}$ . The choice of sapphire as the insulating material is based on both its lower RF loss tangent ( $< 10^{-5}$  at 24 MHz [109]) and higher thermal conductivity ( $\approx 30\text{W}/(\text{m K})$  [43]) than those of macor (0.003 and  $1.5 \text{W}/(\text{m K})$ , respectively) which has been

used formerly. This means that the insulators will not absorb as much of the RF power applied to the blade electrodes and therefore heat up less. Due to the high thermal conductivity, the remaining heat will be conducted to the vacuum chamber base plate rapidly. This was assumed to be advantageous for clock operation because the ion will be surrounded by approximately room temperature surfaces, leading to homogeneous black body radiation. A temperature characterization of the trap is presented in Section 7.3.4. The geometry of the insulators was chosen to be a disk with bores to facilitate the machining of the brittle and hard sapphire material. The bores were required to enlarge the optical access to the trap.

### 7.3.2 *Alignment and x-ray tomography*

Symmetrical alignment of the trap blades is key for optimal operation in an ion clock since major misalignments will displace the RF quadrupole axis from the dc quadrupole axis, resulting in excess micromotion (cf. Section 3.3). The alignment was performed with the help of an alignment tool consisting of a cylindrical polymethyl methacrylate (PMMA) piece that was stuck into the tip electrodes and onto which the blades were pressed. Due to machining inaccuracies, the alignment tool turned out to be slightly too large and the blades could not be aligned pointing towards the trap center but instead acquired a slight angle. The symmetry of the resulting assembly was analyzed by x-ray computer tomography of the trap center. Figure 32 shows a 3-d picture of this scan as well as a cut perpendicular to the trap axis in the trap center. The angle by which the blades were tilted lies within  $2.1^\circ$ - $2.5^\circ$  for the single blades, resulting in an effective trap center-electrode distance of 0.87 mm. This is slightly larger than the designed distance of 0.8 mm and therefore higher RF voltages are required to achieve the same trap frequencies. To estimate the exact influence of the geometry on the trap performance, finite element method (FEM) simulations of the trap were necessary.

### 7.3.3 *FEM simulations*

In any ion trap, the quadrupole approximation  $\phi(x, y, z) \approx \alpha x^2 + \beta y^2 + \gamma z^2$  can only hold in the trap center and must fail near the electrodes, unless they have hyperbolic shapes. Hence, it is not possible to give an analytic expression for the exact potential  $\phi(x, y, z)$  in an ion trap such as the one presented here. The potential is therefore evaluated by numerical finite element simulations with proprietary software<sup>10</sup>. In the model, the tilt of the blades was taken into account and the results are given in the next sections. Simulations have been performed both for the traditional electrode wiring where one blade

<sup>10</sup> COMSOL multiphysics

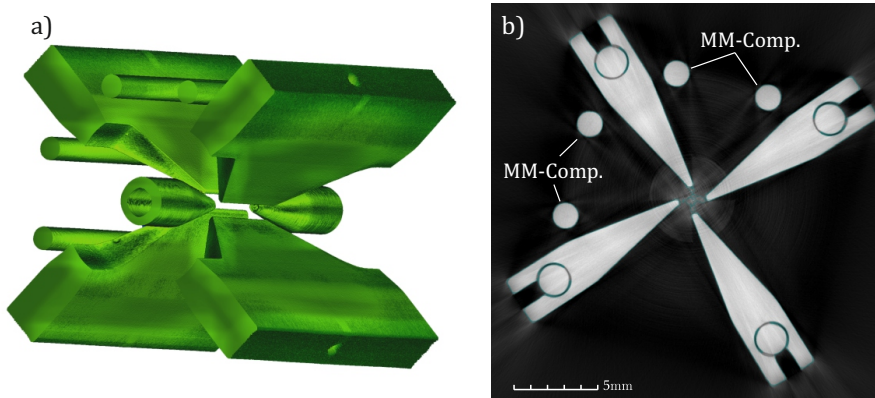


Figure 32: Computer tomography of the ion trap. Figure a) shows the 3D model that has been constructed from the computer-tomography data. Figure b) shows a cut perpendicular to the trap axis. The tilt of roughly  $2.3^\circ$  of the blades is visible. The four round electrodes are the micromotion compensation (MM-Comp.) electrodes.

pair is grounded as well as for the symmetric electrode wiring, where both electrode pairs are supplied with an RF-voltage.

The traditional wiring is used in all the previous ion traps of the "Innsbruck-type". It has the advantage of requiring only one feed-through for the RF voltage and it allows the use of a helical resonator with only one voltage output. However, due to the asymmetry between the blade pairs, field lines from the RF blades not only go to the ground blades, but also to the tip electrodes, creating an axial RF field. The symmetric wiring has the advantage of eliminating these RF electric field gradients along the axis. Figure 33 shows the circuit diagrams for the two cases. The tip electrodes are always connected

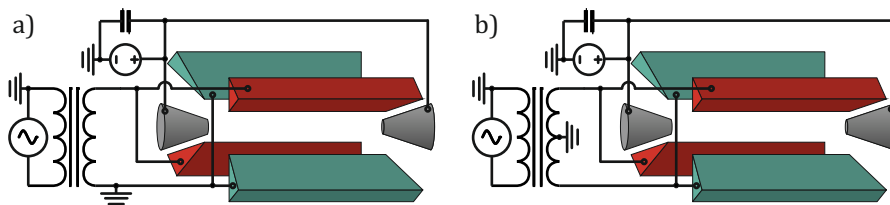


Figure 33: Comparison of trap wiring schemes. Figure a) shows the traditional way of wiring the ion trap where one of the blade pairs is wired directly to ground. Figure b) shows the symmetric wiring where the ground connection is made in the center of the helical resonator coil such that the two electrode pairs always have inverted voltages.

directly to a DC voltage supply through a low pass filter. This filter effectively grounds the tip voltages for the RF frequency. On the other hand, at DC the blade electrodes can be assumed to be grounded because of the vanishing impedance of the coil. The consequence for the FEM simulations is that the RF and DC potentials can be simulated in-

dependently. The nonrelevant electrodes are in both cases simulated to be on ground.

### 7.3.3.1 DC potential

The DC potential was simulated by assuming a voltage of 100 V to be applied to the tip electrodes and the four blade electrodes to be at 0 V. Figure 34 shows the result of this simulation. It can be seen that the blade electrodes shield the DC field, resulting in a strongly inharmonic axial potential. The potential curvature at the trap center is indicated by the dashed line in Figure 34 b) and significantly smaller than what might have been expected for a harmonic potential. In other words, due to the blade electrode shielding, the DC potential effective distance  $d$  from Equation 11 is 4 times larger than the ion electrode distance (10 mm vs. 2.5 mm). The field gradients along the trap axis and the radial direction towards the blade pairs are summarized in Table 2.

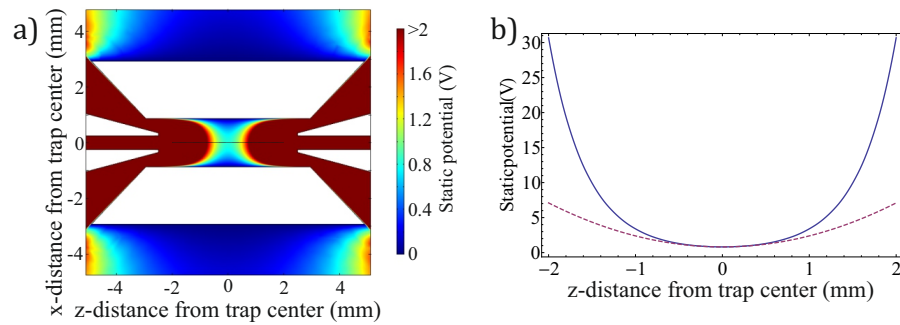


Figure 34: Simulation of the DC potential. The plot in a) shows the spatial dependence of the electric potential for a tip voltage of 100 V. The resulting potential is anharmonic and relatively flat at the trap center. This is highlighted in b), where the potential along the axis is plotted (blue line). The dashed, red line is a fit of a harmonic potential, only considering the central  $60\ \mu\text{m}$  along the axis. It represents the approximative static quadrupole potential seen by an ion in the trap center.

### 7.3.3.2 RF potential

The RF potential simulations have been performed for both the traditional as well as for the symmetric wiring. For the former, the tips and one of the blade pairs were grounded and a voltage of 100 V was applied to the other blade pair. For the latter, the tips were assumed to be on ground and the blade pairs on +50 V and -50 V, respectively. Figure 35 shows the results of these simulations. For the traditional drive, a nonzero potential gradient along the trap axis results in axial RF fields. These lead to excess micromotion for ions not located at exactly the trap center. The magnitude of this effect is investigated



in the next section. For symmetric wiring, the trap axis is a perfect symmetry axis with vanishing potential and field.

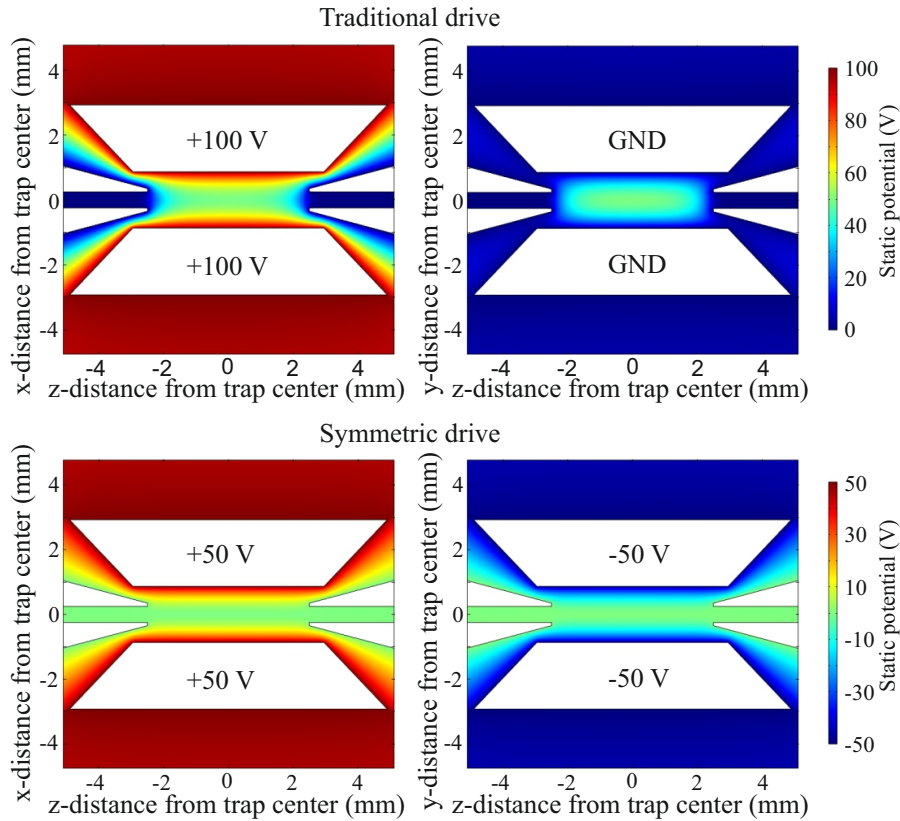


Figure 35: Simulation of the RF potential. The plot shows the spatial dependence of the electric potential for both the traditional (asymmetric) drive and for the symmetric drive. The left column represents the  $x - z$  plane (cutting through the blade pairs) and the right column the  $y - z$  plane. In the traditional drive, the RF potential along the trap axis is nonzero, meaning the trap is not perfectly linear.

### 7.3.3.3 Electric field gradients

To estimate the DC and RF voltages required to achieve the desired trap frequencies of 1 MHz and 3 MHz, the simulation data has been evaluated to obtain the gradients for the electric field along the  $x$ ,  $y$  and  $z$  directions. These can be seen in Table 2. With Equations 5, 8 and 9, the  $a$  and  $q$  parameters and with Equation 13 the trap frequencies can be evaluated. To achieve 1 MHz and 3 MHz trap frequencies for a single  $^{40}\text{Ca}^+$ -ion, an axial voltage of 521 V and a radial voltage of 1.50 kV are required. The experimentally determined tip voltage for 1 MHz axial trap frequency was 582 V, confirming the simulations with a discrepancy of roughly 10%.

in $10^5$ (V/m <sup>2</sup> )	Trad.	Sym.	Exp.	Tip
$dE_x/dx$	5.8	5.7	5.7	-0.079
$dE_y/dy$	-5.7	-5.7	-5.7	-0.079
$dE_z/dz$	-0.096	0	-0.0018	0.16

Table 2: Simulated electric field gradients. The first three columns give the electric field derivatives along the three principal axes of the trap for an applied voltage of 1 V between the two blade pairs. The ground potential tap was hereby assumed to be either directly at one blade pair (traditional, column 1), exactly symmetric between the blade pairs (symmetric, column 2) or slightly off the symmetry point (the experimental situation, column 3). The fourth column gives the data for applying a voltage of 1 V at the tip electrodes.

#### 7.3.3.4 Axial excess micromotion estimation

The excess micromotion due to the axial RF field in the traditional drive was estimated by assuming an  $Al^+/Ca^+$  crystal in a trap with single  $Ca^+$  trap frequencies of 1 MHz and 3 MHz. Furthermore, it was assumed that the  $Al^+$  ion is kept at the trap center where micromotion is compensated but it will occasionally swap its position with the  $Ca^+$  ion. Equation 29 was used to obtain the ion distance from the trap center and with Equation 25 the kinetic energy and therefore the second order Doppler shift could be evaluated. For the asymmetric drive, this amounts to a shift of  $8 \times 10^{-17}$ , too large for reliable clock operation in the  $10^{-18}$  regime. Therefore, we implemented the symmetric drive, where only a small asymmetry of 1.04 between the absolute blade voltages remains (cf. Section 7.4). For this case, the simulations indicate an expected axial excess micromotion induced second order Doppler shift of  $3 \times 10^{-20}$ . This means that the ion swapping could be tolerated and would not affect the clock performance in a measurable way. It must be noted here, that the trap simulations also showed significant axial RF-fields along the trap axis, if the alignment of the blade electrodes relative to each other was not perfect. For example, mrad tilts of the blade electrodes relative to the trap symmetry axis can already suffice to shift the axial micromotion compensation point almost all the way to a tip electrode. For the traditional drive, the strong axial potential curvature helped to mitigate this shift, but for the symmetric drive other means might have to be used as e.g. slightly worsening the symmetry or feeding small RF voltages to the tip electrodes as compensation fields. A thorough quantitative analysis of the micromotion must be performed, to evaluate the necessity of such measures for optimal optical clock performance.

### 7.3.4 Thermal characterization of the ion trap

Optical clocks suffer from frequency shifts of the clock transition due to AC Stark shifts induced by the thermal blackbody radiation at the position of the ion as mentioned in Section 2.2.1. The precise determination of this shift requires an accurate knowledge of the temperature environment of the ion. The major heat source in the ions vicinity is the ion trap itself, heating up due to absorption of the RF power running through the electrodes. To investigate this effect, the trap was imaged via a thermographic camera<sup>11</sup> for different applied RF powers. The temperature was measured across a roughly  $10 \times 4 \text{ mm}^2$  area on one of the sapphire disks. The measurement was calibrated by increasing the room temperature from  $24.7^\circ\text{C}$  to  $28.3^\circ\text{C}$  and observing the temperature change of the non-driven ion trap. The results of this measurement are presented in Figure 36 together with the thermal images for various trap drive powers. A close investigation of these images shows that the radiation received from the sapphire disks is masked by a reflection of the connectors between the copper RF leads and the blade electrodes. Neither the disks themselves nor the blades seem to emit a significant amount of radiation that would allow a determination of a substantial deviation from room temperature. This is promising on the one hand, since it means that they are probably even colder than what is shown in Figure 36, but on the other hand might require a better measurement of the actual temperature of the hot spots at the connectors. In any way, the measurements indicate a mean trap temperature of below  $30^\circ\text{C}$ , allowing to put a conservative range of the temperature seen by the ion as  $20^\circ\text{C} - 30^\circ\text{C}$ , already providing an uncertainty in the blackbody shift of the clock transition of  $1 \times 10^{-18}$  when evaluated with the measured sensitivity [146]. The uncertainty in this sensitivity itself is currently much larger so that no limitation due to the trap heating is to be expected in the near future.

## 7.4 TRAP VOLTAGE SUPPLY

a helical resonator is used [96, 161] to supply the trap with sufficiently high voltages. In a simplified picture, the helical resonator provides an inductance  $L$  and together with the capacitance of the trap  $C$  and the RF losses  $R$  they form a series RLC-circuit. The resonance frequency  $\omega_r$  and the quality factor (Q-factor) of such a circuit are given by [161]

$$\omega_r = \frac{1}{\sqrt{LC}}, \quad Q = \frac{1}{R} \sqrt{\frac{L}{C}}. \quad (108)$$

The design criteria for a high  $Q$  (i.e. high voltage on resonance) circuit are therefore a helical resonator with very small self capacitance

<sup>11</sup> DIAS S15008

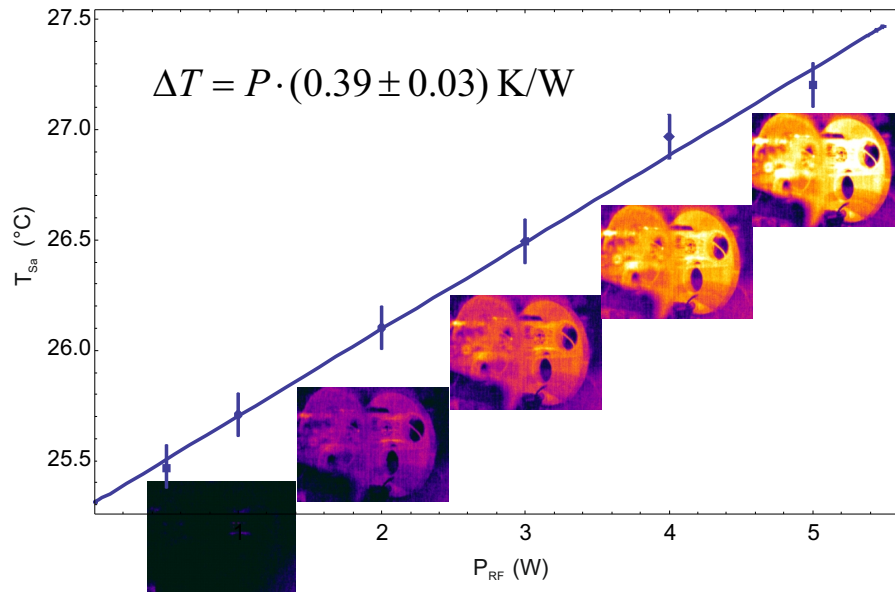


Figure 36: Temperature characterization of the ion trap. The abscissa shows the applied RF power and the ordinate the measured and calibrated temperature of the rear sapphire disk. The error bars are mostly due to uncertainties of the PT1000 resistors used to calibrate the absolute temperature and should hence be largely correlated between the data points.

and resistance and high inductance. Hence, the resonator was built as large as possible under the given space constraints. Typical helical resonators used in ion trap experiments provide one output voltage [161, 66, 133]. But to reduce micromotion, a resonator was needed that would provide two output voltages, both positive and negative to the different electrode pairs (see Section 7.3.3.4). This was achieved by applying the ground connection not to one end of the coil, but to the center instead. A CAD-drawing of the helical resonator used in this experiment is shown in Figure 37.

To evaluate the performance of the resonator, the quality factor was measured with a test trap. Figure 38 shows the result of this measurement and indicates a quality factor of approximately 230. This suffices to generate roughly 1 kV peak to peak voltages at the trap electrodes for 5 W of RF power coupled into the circuit (cf. Section 9.2.3).

For an estimation of the micromotion suppression due to the symmetric drive, the degree of symmetry between the two outputs was measured. Two capacitive voltage dividers were built to pick up the signal from the two outputs. To eliminate biases due to differences in the two dividers, a second measurement was performed where the dividers were swapped. The results are shown in Figure 39. The geometric mean of the amplitude measurements and the arithmetic mean of the phases give a resulting amplitude ratio between the two outputs of  $1.04 \pm 0.01$  and a phase difference of  $181^\circ \pm 0.1^\circ$ . This results in a suppression of axial micromotion in the trap by a factor of

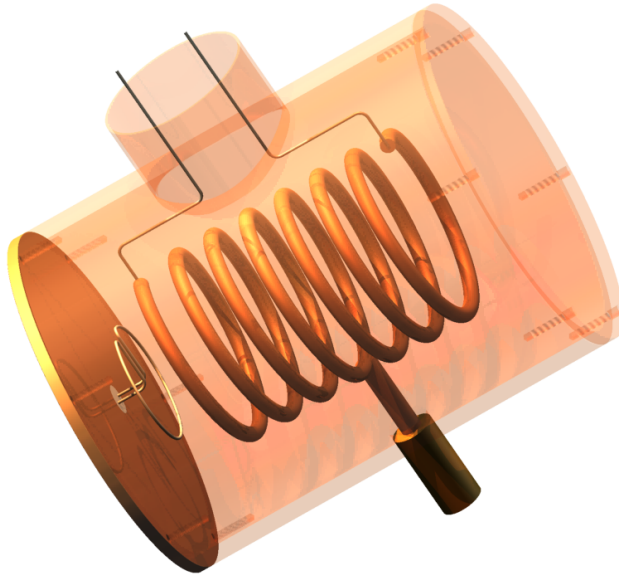


Figure 37: CAD drawing of the helical resonator. The copper shield and the front lid were made transparent. The tube has an outer diameter of 120 mm and a length of 154 mm. The coil has a diameter of 60 mm and a length of 91 mm. On the left the silver wire incoupling coil is visible.

more than 200 compared to the asymmetric drive (cf. Section 7.3.3). It must be stressed here that the occurring phase difference is between the two blade pairs and does not infer uncompensatable micromotion as a phase difference between the two electrodes of the same blade pair would [13].

## 7.5 THE LASER SYSTEM

Another major component of the experiment is the laser system. Lasers are needed for the photoionization of calcium and aluminum atoms and for the interaction with the trapped ions. In the following, the calcium lasers will be introduced. The aluminum lasers were still in preparation at the time of writing this thesis. The major design goal of the laser system was to make it robust and easily maintainable. This was achieved by using only commercial diode lasers as laser sources and by keeping the free space optical path lengths short, typically far less than 1 m. The major part of the optical path for all the lasers in the setup is through single mode optical fibers. They also divide the setup into small groups of optical elements, assembled on individual breadboards. A total of four breadboards (sized 60 cm × 90 cm) are used for the complete calcium laser system. Compared to a setup on bulk optical tables, this will greatly simplify the transport of a future transportable clock. In the next sections, the different lasers of the cal-

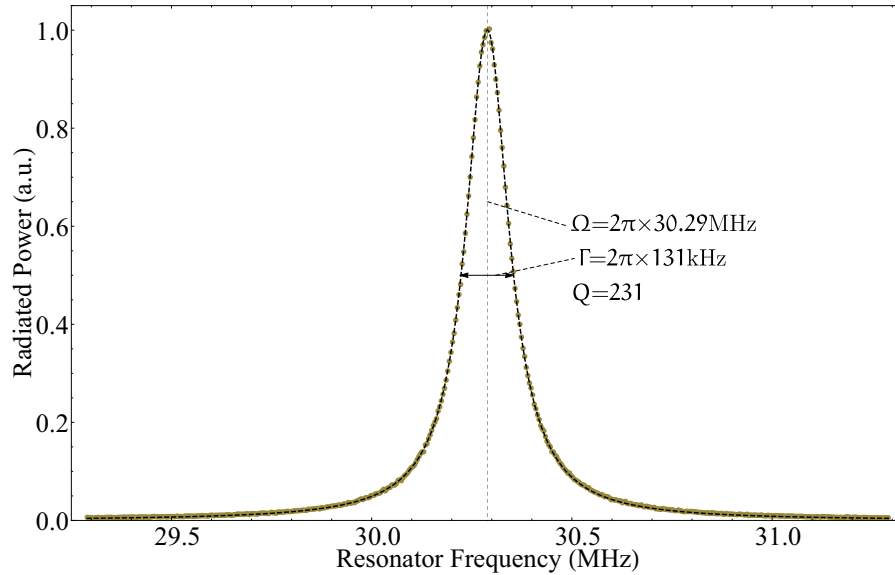


Figure 38: Quality factor of the loaded helical resonator. The measurement was performed with a trap that had the same dimensions as the one used in the experiment. An antenna was placed sufficiently far away to not couple too strongly to the circuit but still pick up the radiated power as a function of input frequency.

cium system will be introduced, concluding with a summary of the optical layout around the vacuum chamber and ion trap.

### 7.5.1 Calcium ionization lasers

Single calcium ions are loaded into the trap by photoionizing neutral calcium atoms from the evaporation ovens (Section 7.2). For this, a two-step ionization process is used. First, the  $^{40}\text{Ca}$ -atoms are excited from the  $^1\text{S}_0$  ground state into the excited  $^1\text{P}_1$  state via a laser at 422.8 nm. Then, a laser at 375 nm is used to excite the atoms just above the photoionization threshold. This is depicted in Figure 40 and has been described in detail before [184]. The 375 nm laser used here is a bare laser diode<sup>12</sup> that is placed into a commercial temperature controlled laser diode mount<sup>13</sup>. No active or passive frequency stabilization is performed since no narrow linewidth is required for the second ionization step.

The 423 nm laser system is shown in Figure 41. A commercial external cavity stabilized diode laser (ECDL) system at 845 nm is used<sup>14</sup>. Its wavelength is monitored by a wavemeter<sup>15</sup> and sent to the so called optics breadboard via a single mode polarization maintaining fiber (SM-PM). There, it is frequency-doubled in a resonant doubling cavity

<sup>12</sup> Nichia NDU1113E

<sup>13</sup> Thorlabs LDM21

<sup>14</sup> Toptica DL pro

<sup>15</sup> High Finesse WS/7

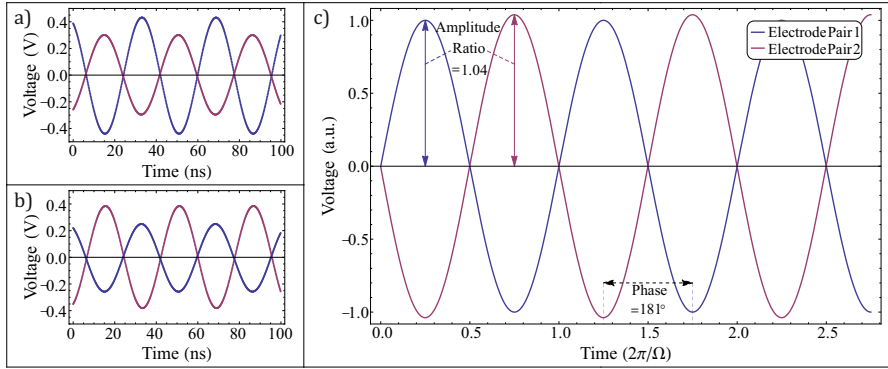


Figure 39: Symmetry of the helical resonator. The amplitude ratio and phase difference of the two helical resonator outputs was measured with capacitive voltage dividers. To eliminate the error due to differences of the two dividers, two measurements were taken with swapped dividers as shown in a) and b). c): The geometric mean of the amplitude measurements and the arithmetic mean of the phase differences results in an amplitude ratio of 1.04 and a phase difference of  $181^\circ$ .

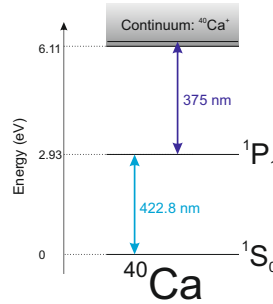


Figure 40: Reduced  $^{40}\text{Ca}$  level scheme. The levels used in the photoionization process are shown. Atoms are first excited into the  $1P_1$  state before a second photon brings them above photoionization threshold. Figure adopted from [184].

that is described in detail in [184] and produces up to 30 mW (typical 15 mW) of light at 423 nm. This is coupled into a photonic crystal fiber (PCF, cf. Section 7.5.5.1) together with light from other lasers and delivered to the vacuum chamber. Several mW of power can be sent onto the trap center. Both ionization lasers can be blocked via electronically driven mechanical shutters to stop the loading of ions.

### 7.5.2 Calcium repump lasers

Two repump lasers at 866 nm and 854 nm are required for the depopulation of the  $D_{3/2}$  and  $D_{5/2}$  states in  $^{40}\text{Ca}^+$  ions (cf. level scheme Figure 10). Additionally, the 854 nm laser acts as the quenching laser in sideband cooling (Sections 5.3.1 & 9.4.2) and the 866 nm laser is part of the double-EIT scheme (Sections 5.4.5 & 9.5). Both have a very

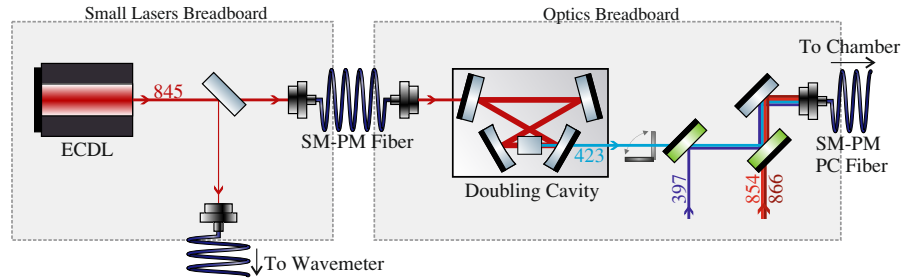


Figure 41: 423 nm laser system. An external cavity stabilized diode laser (ECDL) is frequency doubled in a resonant doubling cavity. Some components in the Figure are from [57].

similar setup that is shown in Figure 42. The lasers are housed on the same breadboard as the 845 nm ionization laser. A fraction of the light from both sources is sent to the wavemeter, and additionally the lasers are combined and sent to the frequency comb for active frequency locking (see Section 8.2). Both lasers are individually transferred to the optics breadboard where each wavelength passes through a double pass acousto optical modulator (AOM) setup<sup>16</sup>. These are used for switching the beams and for frequency tuning. The lasers are combined into the same PCF, together with the 423 nm laser and one part of the 397 nm laser. From both beams, up to several mW of power arrive at the trap.

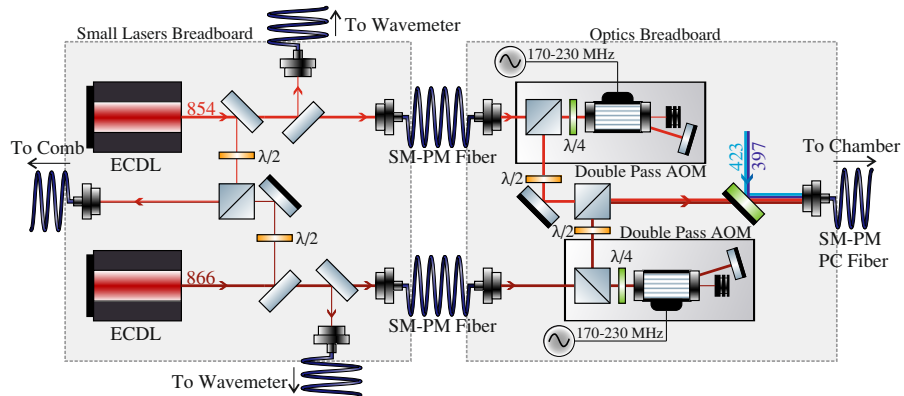


Figure 42: Repump laser system. Two ECDLs at 854 nm and 866 nm, respectively are used. Some components in the Figure are from [57].

### 7.5.3 Calcium doppler cooling and detection laser

A laser at 397 nm is required to drive the broad  $^2S_{1/2} \rightarrow ^2P_{1/2}$  transition for Doppler cooling and fluorescence detection. This light is produced in a commercial frequency doubled diode laser system<sup>17</sup>. It consists of an ECDL emitting light at 794 nm that is sent through a

<sup>16</sup> Brimrose TEF-200-50-854/866

<sup>17</sup> Toptica TA-SHG pro



tapered amplifier (TA) to produce up to 1.26 W of laser power. This is seeded into a resonant doubling cavity equipped with an LBO-crystal. Up to 167 mW of power at 397 nm are achieved at the output. Two beam pickups at 794 nm are placed before the cavity to send small amounts of light to the wavemeter and the frequency comb. The output at 397 nm is frequency shifted via a double pass AOM setup<sup>18</sup> and coupled into a SM-PM fiber for light transfer to the optics breadboard. There, the light is split into two paths that later deliver the  $\sigma$  and  $\pi$  polarized 397 nm beams to the ion (cf. Figure 45). They are individually sent through single pass AOMs<sup>19</sup> for separate switching. Both are then coupled into SM-PM fibers and sent to the chamber and typically have up to 1 mW of power that reaches the ion.

The zeroth order of the double pass AOM is not blocked but also coupled into a fiber and then overlapped on the optics breadboard with the repump beams and the 423 beam to be coupled into the PCF. It is used as a far detuned Doppler cooling beam to aid initial loading and recoiling. It can be blocked with an electronically driven mechanical shutter. The whole 397 nm laser system is sketched in Figure 43.

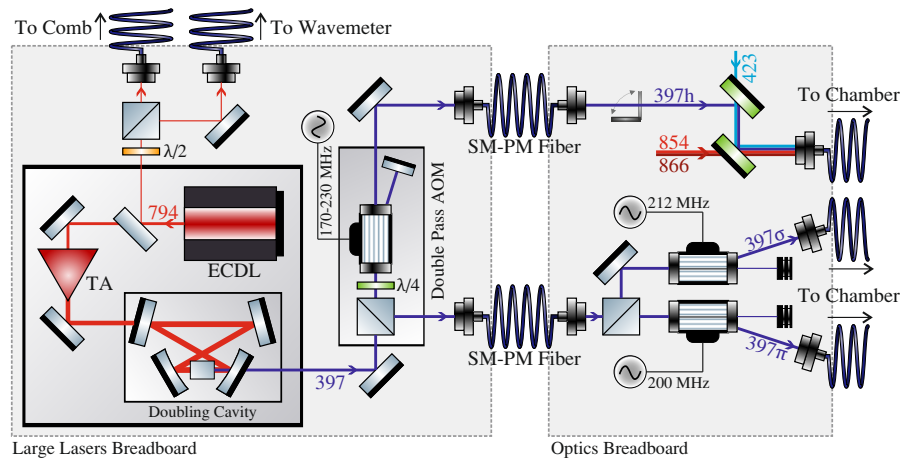


Figure 43: Cooling/Detection laser system at 397 nm. A commercial frequency doubled ECDL laser is split into two main legs called the  $\sigma$  and  $\pi$  beams. Both can be frequency tuned together with the double pass AOM and switched individually via single pass AOMs. A third leg is the zeroth order of the double pass AOM that makes a roughly 200 MHz red detuned beam, called the *helper* (397h) beam because it aids recoiling and loading. Some components in the Figure are from [57].

<sup>18</sup> Brimrose TEF-200-50-397

<sup>19</sup> IntraAction ASM-2002B8

7.5.4 *Calcium sideband cooling and logic laser*

The narrow  $^2S_{1/2} \rightarrow ^2D_{5/2}$  transition is driven with a laser at 729 nm. This is generated by a commercial amplified diode laser system that incorporates both an ECDL and a TA<sup>20</sup>. Beam pickoffs for the wavemeter and frequency comb are installed and the laser can be frequency shifted and switched via a double pass AOM<sup>21</sup>. The light is delivered to the chamber by an SM-PM fiber and typically 25 mW can be sent to the ion. The light can also be sent to a commercial Fabry Perot interferometer<sup>22</sup> to analyze the laser frequency noise (see Section 8.2). The setup is shown in Figure 44.

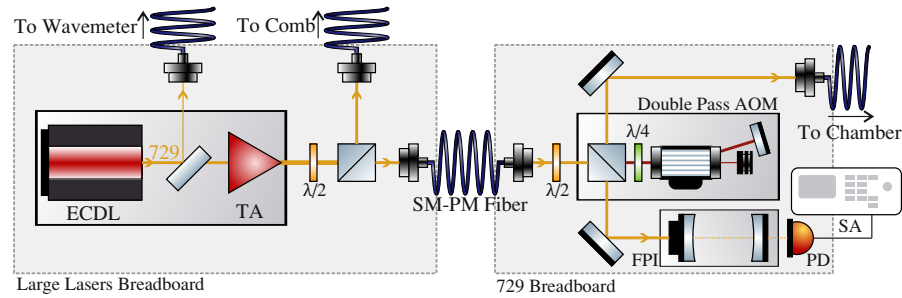


Figure 44: Calcium logic laser system at 729 nm. An amplified ECDL laser is frequency shifted via a double pass AOM and sent to the chamber. Alternatively, a Fabry Perot interferometer has been set up to measure the frequency noise of the laser. SA: spectrum analyzer, PD: photo detector. Some components in the Figure are from [57].

7.5.5 *Vacuum chamber breadboard*

A small amount of optical components is needed just in front of the ion to steer the pointing, focus the laser beams and control their polarization. These are placed on a breadboard directly beneath the vacuum chamber which is schematically shown in Figure 45. Every beam is delivered to this breadboard via a polarization maintaining fiber. After leaving the fiber, the beams are first collimated<sup>23</sup> and then polarization adjusted via retardation waveplates. Lenses with 150 mm focal length are used to focus the beams onto the ion. High polarization purity in the 397 beams is required for good optical pumping and efficient EIT-cooling and is assured by the use of  $\alpha$ -BBO Glan laser polarizers<sup>24</sup>. Calcite Glan laser polarizers were tried before but they had too high optical losses and cemented polarization beam splitters strongly degraded with time. The 729 nm beam can be sent onto the

<sup>20</sup> Toptica TA100 with extended cavity

<sup>21</sup> Brimrose TEF-280-100-729

<sup>22</sup> Toptica FPI100

<sup>23</sup> by Schäfter + Kirchhoff 60FC fiber collimators

<sup>24</sup> Thorlabs GLB10-405

ion from three different directions to enable micromotion compensation (cf. Section 9.3). Switching between the directions is performed by replugging fiber connectors. Not shown in the figure are the pick-ups and photodiodes for the intensity stabilization of the  $397\sigma$ ,  $397\pi$  and 866 beams. Four beams at wavelengths from 397 nm to 866 nm arrive at the chamber via the same PCF and are focused with the same lens. Out of those only the 866 nm beam is polarization controlled via a  $\lambda/2$  waveplate, accepting arbitrary polarization on the other beams. Achromatic influences of the fiber, the collimator and the lens onto those beams were investigated and are presented in the next section.

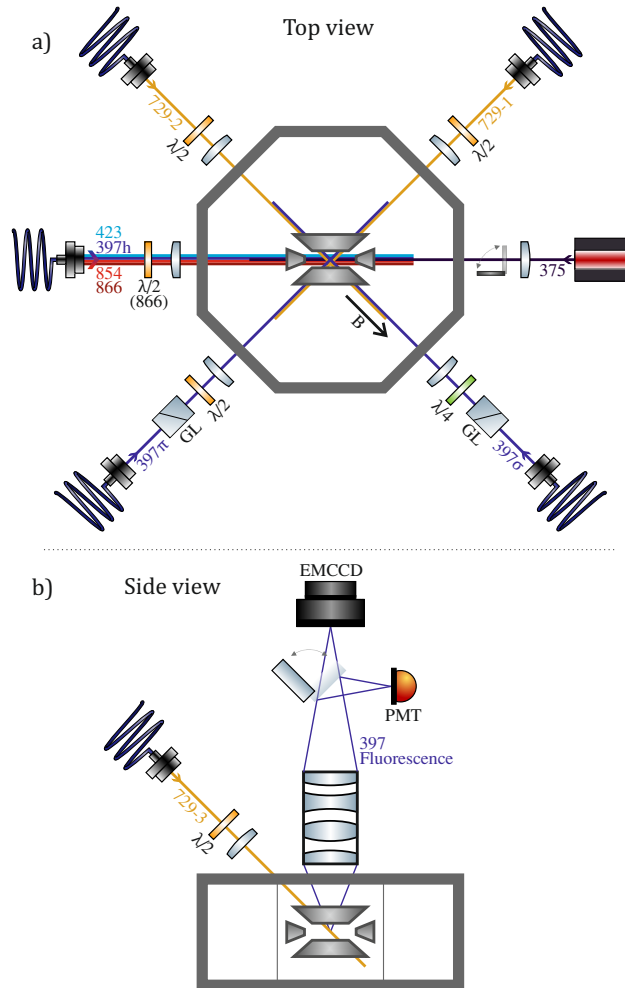


Figure 45: Optical access to ion trap. Figure a) shows a top view and Figure b) a side view onto the vacuum chamber. Only the calcium lasers are shown. The 729 nm beam can be inserted either via ports 729-1, 729-2 or 729-3 by replugging fiber connectors. Some components in the Figure are from [57].

### 7.5.5.1 *The multi wavelength fiber delivery setup*

Including the  $\text{Al}^+$  lasers, there are lasers at nine different wavelengths needed at the trap center to operate the quantum logic clock. This makes optical access to the ion a scarce resource and simultaneous use of the same optical path by multiple beams helps to make the most of it. Therefore, all necessary lasers for ionization, Doppler cooling and fluorescence detection are sent along the same path, through 0.5 mm holes in the tip electrodes. This not only saves optical access but also simplifies initial ion trapping, maintenance and troubleshooting because the beams are guaranteed to pass the trap center. This is achieved by sending in the 866 nm, 854 nm repumpers as well as the 397 nm cooling laser and the 423 nm photoionization laser via the same fiber. Overlapping of the beams with dichroic mirrors and polarization beam splitters (cf. previous Sections) is done on an optical breadboard where the required space is more easily available compared to a setup in front of the chamber.

The requirements for the PCF were to have high transmission efficiencies for the wavelengths between 397 nm and 866 nm and at the same time be single mode and polarization maintaining. These cannot be fulfilled with established solid-glass (step index) fibers because fibers with a single-mode-cut-off below 397 nm have very low transmission efficiencies at 866 nm due to high bend losses [86]. Photonic crystal fibers (also holey fibers), however have been produced that are *endlessly single mode*, i.e. do not possess a defined cut-off wavelength and show good transmission efficiencies across wide ranges of wavelengths (cf. first demonstration [15] and review [150]). With the fiber used in our experiments<sup>25</sup> we achieve transmission efficiencies along a 2 m fiber between 32% and 52% for the different wavelengths. While the incoupling beam shaping is implemented prior to overlapping for each beam individually, the outgoing beam shaping optics are shared for the different beams. Numerical OSLO simulations have been performed to test combinations of fiber output collimators and focusing lenses with the design goal to achieve 397 nm and 866 nm beam radii at the ions position that are smaller than 100  $\mu\text{m}$ . Simulation and measurement results of the chosen combination are shown in Figure 46. The small beam radii allow the use of small laser intensities, limiting stray light for detection and cutting requirements on the output power of the commercial laser modules.

## 7.6 IMAGING OPTICS

The fluorescence signal of the  $\text{Ca}^+$  ion at 397 nm is detected via imaging onto either a photo-multiplier-tube (PMT)<sup>26</sup> or an electron mul-

---

<sup>25</sup> NKT LMA-PM-05

<sup>26</sup> Hamamatsu H10682

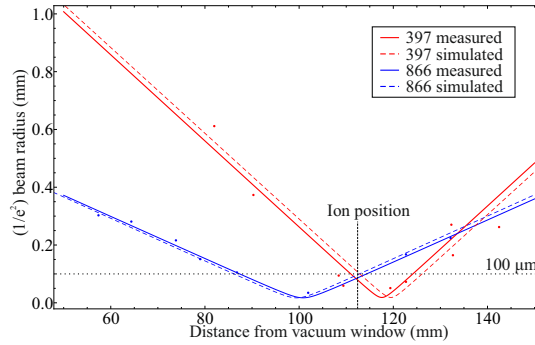


Figure 46: Simulations and measurements of the beam radius for 397 nm and 866 nm light emerging from the PCF. The dots show the measured beam radius data for the 397 nm (blue) and 866 nm (red) light. The solid lines are fits to this data, assuming Gaussian beam propagation. The dashed lines are simulated using the measured mode field diameters of the PCF and the specified lens properties.

tipling charged coupled device (EMCCD) camera<sup>27</sup>. The imaging is done via a multi lens objective that was designed by the Innsbruck ion trapping group in cooperation with an industry partner<sup>28</sup> and has been described before [11]. The imaging has a magnification of  $\sim 17$  and the required optical path of  $\sim 1.1$  m was folded repeatedly to fit it into a compact box just above the chamber. The measured overall detection efficiency of the imaging is 0.44 % as presented in Section 9.1.1.

## 7.7 EXPERIMENT CONTROL SYSTEM

For the experiments conducted within this thesis, a rapid and synchronized switching of the AOMs described in Section 7.5 is required. This is achieved by the implementation of a field programmable gate array (FPGA)-based pulse sequencer that facilitates a commercial FPGA<sup>29</sup> driven at 100 MHz clock frequency. It was originally designed by Paul Pham [127] and later extended with an interface for direct digital synthesis (DDS) chips by Philipp Schindler [157]. These DDS chips<sup>30</sup> are clocked with 800 MHz and provide frequency signals around 200 MHz for the AOMs. The experimental control is equipped with a total of 16 DDS of which 7 were needed for the experiments described within this thesis. Additionally, 32 TTL output ports are supplied by the pulse programmer to switch RF-switches, trigger the PMT gate or the intensity stabilizations. Typical DDS switching times are below 150 ns [66]. The communication between the FPGA and the main computer of the experiment is handled by an open source Python program [162].

<sup>27</sup> Andor iXon 885

<sup>28</sup> Silloptics, Germany

<sup>29</sup> altera Cyclone I

<sup>30</sup> Analog Devices AD9910

The user interface is a Labview program originally developed by the Innsbruck group, extended by the author with hardware support for the high voltage tip electrode supply<sup>31</sup> and the low noise magnetic field coils current supplies<sup>32</sup>.

---

<sup>31</sup> ISEG EHS 8240x

<sup>32</sup> TTi QL355TP

## FREQUENCY COMB AND LASER LOCKS

Every optical atomic clock nowadays is operated or validated by the use of a frequency comb. The frequency comb, together with counting electronics, establishes the clockwork necessary to measure time (cf. Chapter 2). For reviews of frequency combs in metrology, the reader is referred to [63, 64, 171]. In essence, frequency combs are mode locked lasers where the microwave repetition rate  $f_{\text{rep}}$  and microwave carrier envelope offset frequency  $f_{\text{CEO}}$  are phase locked or monitored such that the frequency of the  $n$ -th comb tooth of the laser can be expressed in terms of these frequencies as  $f_n = nf_{\text{rep}} + f_{\text{CEO}}$  (see Figure 47). A laser's frequency  $f_L$  that falls within the comb spectrum can then be measured by a heterodyne beat with the comb and expressed as

$$f_L = nf_{\text{rep}} + f_{\text{CEO}} \pm f_{\text{beat}}, \quad (109)$$

where the sign depends on whether the laser has a larger or smaller frequency than the nearest comb tooth. Since all the frequencies on the right hand side of this equation are in the microwave regime, they can be counted with established electronic counters.

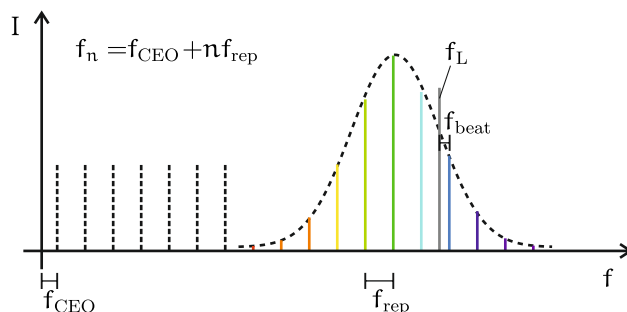


Figure 47: Output spectrum of a frequency comb. Every comb tooth can be expressed as a multiple of the repetition rate frequency added to the carrier envelope offset frequency. The beat of a cw laser with the nearest comb tooth will result in a frequency that is countable by established electronics.

The frequency comb can, however, not only be used to measure laser frequencies but also to stabilize them by applying the beat signal  $f_{\text{beat}}$  as the input to a control loop. This way, the frequency stability of either a microwave reference or an optical reference can be transferred to another laser. In the experiments described here, most of the diode lasers introduced in Chapter 7 were frequency stabilized by this technique. In the next section, the specific frequency comb

used within this thesis' work will be introduced and afterwards details of the frequency stabilization will be given. A universal lock scheme is presented with which three diode lasers are locked to the same reference frequency. This creates a set of mutual phase coherent lasers that can be used for quantum interferometric experiments. One example where this phase coherence was exploited is the double-EIT cooling with lasers at wavelengths spreading more than one octave (see Section 9.5).

## 8.1 THE FREQUENCY COMB

The frequency comb in the experiments described here is an Erbium doped fiber frequency comb [154, 167, 174, 87]. It facilitates a fiber gain medium combined with a free space resonator including dispersion compensation, cavity length adjustment and outcoupling (see Figure 48). A commercial product<sup>1</sup> was chosen which produces a  $\sim 35$  nm (77 nm) broad output spectrum at 3 dB (10 dB) suppression from maximal intensity, centered around 1.55  $\mu\text{m}$ . Erbium doped fiber amplifiers (EDFA) [102], highly nonlinear fibers (HNLF) [116, 117] and single pass free space frequency doublers are used to amplify, frequency shift and broaden this output. This way, an octave spanning spectrum for the  $f$ - $2f$  interferometer [80, 69] as well as output ports at 729 nm, 794 nm, 842-866 nm and 1070 nm are realized. The latter are used to generate microwave beat signals with all relevant  $\text{Ca}^+$  and  $\text{Al}^+$  lasers for monitoring or stabilization.

## 8.2 PHASE STABILITY TRANSFER VIA THE FREQUENCY COMB

Sideband cooling and quantum logic operations on  $\text{Ca}^+$  ions require a narrow laser at 729 nm. Both absolute frequency stability as well as low phase noise are required. Absolute frequency drifts must stay below approximately 10 kHz, being the minimal bandwidth of the Fourier broadened laser pulses. The phase noise should be below  $10^{-5}$   $\text{rad}^2/\text{Hz}$  at all Fourier frequencies to enable quantum gates with  $> 90\%$  fidelities. For this purpose, lasers are typically actively frequency stabilized to highly stable cavities based on ULE glass (see e.g. [25]). These setups generally require high levels of maintenance and in most cases lack portability. One supremely stable cavity for the  $\text{Al}^+$  clock laser is inevitably required in the final setup and has been designed and set up by Sana Amairi [5, 6]. Via the frequency comb, this stability will be transferred to all the other lasers that have to be stabilized, avoiding the need for any additional cavities.

In a first evaluation of this transfer stabilization, the 729 nm laser has been locked to an ultra stable laser at 1542 nm that was provided by a neighboring laboratory (reference laser 1 in [82]). It is based on a

<sup>1</sup> MenloSystems FC1500



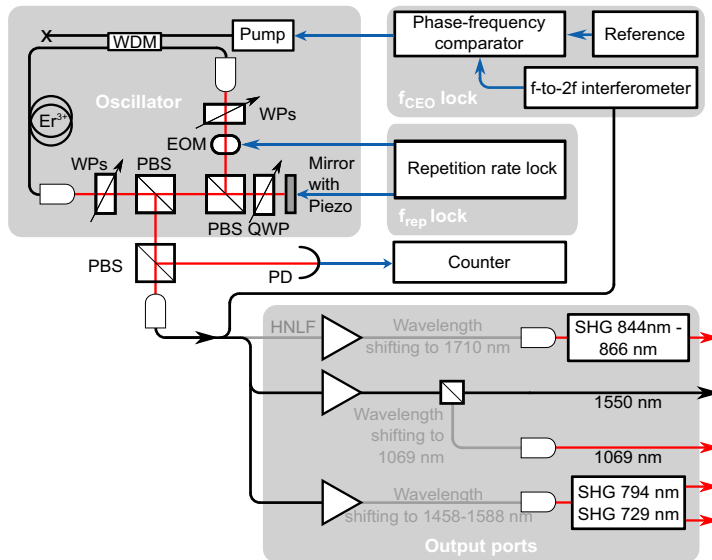


Figure 48: Schematics of the frequency comb. The femtosecond laser is made of an erbium doped fiber gain medium together with free space optics. The output of the laser is frequency shifted and spectrally broadened with highly nonlinear fibers (HNLF) to create the  $f$ - $2f$  interferometer and output ports at different spectral regions. WP: waveplate, EOM: electro optical modulator, PBS: polarization beam splitter, QWP: quarter wave plate, PD: photo detector, WDM: wavelength division multiplexing.

commercial continuous wave (CW) fiber laser<sup>2</sup> that is stabilized with a bandwidth of  $\sim 30$  kHz to an ULE cavity. It is almost permanently used for the characterization of cross-country fiber links [130, 45] and is therefore continuously available. It is amplified via an EDFA and sent to the comb via a 250 m long single mode fiber. The fiber length is stabilized with a scheme similar to the one described in [59] and the measured remaining fiber link noise is orders of magnitude smaller than the expected reference laser noise so that it does not limit the performance of the laser lock.

The frequency stability transfer works by controlling the phase of the beat between the 729 nm laser and a nearby combtooth. If this comb tooth has the noise properties of the reference laser, the phase transfer is complete. This can be achieved in two different ways. First, the offset and repetition rate frequencies of the comb can be actively phase locked to the reference, making the comb teeth stable in the *optical* regime. Second, via a feed forward scheme, the noise of  $f_{\text{rep}}$  and  $f_{\text{CEO}}$  can be measured and subtracted from the beat signal [163, 62, 118], creating a virtual stable beat *electronically*. In practice, often a combination is used, locking the repetition rate and subtracting the offset frequency [189, 105]. Both techniques reduce the comb noise only in a certain bandwidth which makes it necessary to study the

<sup>2</sup> Koheras Adjustik E15

remaining noise of the comb in detail to develop an optimal laser locking strategy. Especially for Fourier noise frequencies between 10 kHz and 1 MHz this turns out to be quite delicate because the locked fiber comb can have higher phase noise than the diode laser so that too tight locking in fact *decreases* the stability of the laser.

### 8.2.1 *The noise contributions in fiber frequency combs*

The noise in fiber frequency combs arises from different sources, including environmental acoustic and thermal noise, electronic noise and pump laser noise. These noise contributions can to some extent be suppressed by careful engineering. However, there are also fundamental noise processes such as photon shot noise on the beat photo detectors and quantum noise due to amplified spontaneous emission (ASE) inside the laser cavity [172, 115]. The latter limit is large in fiber frequency combs due to the high effective cavity loss and high intracavity gain leading to large amplification of the spontaneous emission. ASE is often the largest noise contribution in the  $10^4$ - $10^6$  Hz Fourier frequency regime. Up to some bandwidth, the noise can be suppressed by locking as described below.

### 8.2.2 *Locking of the repetition rate and offset frequency*

An independent locking of  $f_{\text{rep}}$  and  $f_{\text{CEO}}$  is best achieved if independent actuators for offset frequency and repetition rate are present. It can be shown that parameters changing only the cavity length but not the intracavity dispersion will mainly affect the repetition rate while parameters changing the dispersion only but not the carrier phase will mainly affect the offset frequency. This can also be explained in the fixed-point or elastic tape model [12] where every actuator is attributed a fixed point in frequency at which a (virtual) comb tooth does not move if the actuator is varied. For our comb, these fix points are at 0.78 THz (11  $\mu\text{m}$ ) for the modulation of the cavity length via the intracavity piezo, at 21 THz for the modulation of the intracavity EOM, and at 27 THz for the modulation of the pump laser diode current. This means that modifying the piezo voltage effectively changes almost exclusively the repetition rate, whereas the pump or EOM modulation affects both, the repetition rate and the offset frequency. Therefore, the offset stabilization is performed by actuation on the pump current with a low bandwidth and the repetition rate is locked with high bandwidth via the piezo. For locking at high Fourier frequencies (several tens of kHz), the repetition rate lock is supported by the intracavity EOM.

In our laser locking scheme (see Section 8.2.3), we electronically subtract the offset frequency from the beat frequency, so that only a low bandwidth lock of  $f_{\text{CEO}}$  is required to keep it from drifting.

This lock is established by a digital phase frequency comparator referenced to a 10 MHz microwave signal that is generated by a hydrogen maser which can be referenced to the primary Cs clocks at PTB.

The repetition rate lock is implemented by subtracting  $f_{\text{CEO}}$  from the beat with the 1542 nm reference and mixing it to DC with a 60 MHz signal from a maser-referenced DDS chip. This mixed signal is fed into a PID controller as the phase error signal and the output of the PID is applied to the intracavity piezo (slow part, bandwidth  $\leq 1$  kHz) and to the intracavity EOM (fast part, bandwidth  $\leq 600$  kHz). With this technique we achieved beats with more than 87% of the power in a 10 Hz band around the carrier after subtraction of  $f_{\text{CEO}}$  (see Figure 49). This is in good agreement with the performance of another group with a very similar setup [189]. The bandwidth of the lock is limited to  $\leq 600$  kHz due to resonances in the EOM and loop delays.

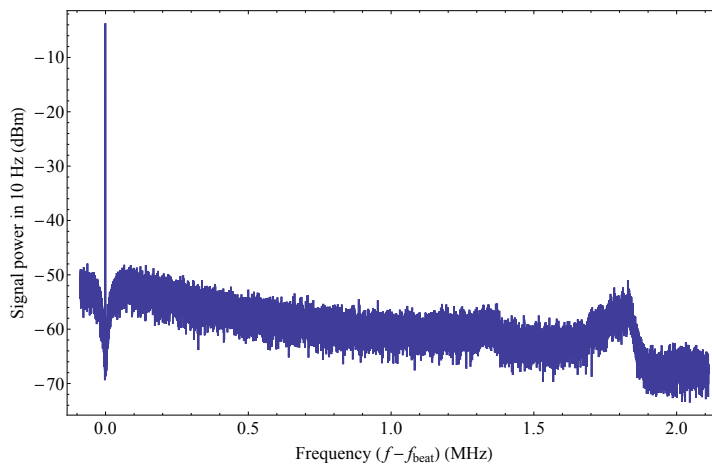


Figure 49: Lock of the repetition rate. The comb beat with the reference laser after subtracting  $f_{\text{CEO}}$  and locking the repetition rate is shown (the monitor path in Figure 51). More than 87% of the power is in a 10 Hz band around the carrier.

Figure 50 shows the locked phase noise of the comb-line at 729 nm after subtraction of  $f_{\text{CEO}}$ , as well as the free running phase noise of the 729 nm ECDL. The former has been measured via the  $f_{\text{CEO}}$  subtracted beat with the 1550 laser (the monitor in Figure 51) and scaled by a factor  $(1542/729)^2$  to account for the larger comb tooth number at 729 nm. The latter has been measured with a commercial Fabry-Perot cavity<sup>3</sup> that has been modified to have an Airy function full width at half maximum (FWHM) linewidth of 17.1 MHz by intentionally inserting a screw into the cavity to increase the round-trip-losses. The cavity has been locked to the laser with a low frequency lock ( $\sim 500$  Hz bandwidth). The cavity length was shifted by a piezo to which the incoupling mirror was attached and the laser was kept at one of the half power points. Intensity fluctuations on the transmit-

<sup>3</sup> Toptica FPI100

ted signal were monitored with a spectrum analyzer and could be translated into frequency fluctuations with the measured Airy function slope. One important result of Figure 50 is that the locked comb is only more quiet than the free running diode laser up to Fourier frequencies of  $\sim 200$  kHz and even at 20 kHz the comb noise is only one order of magnitude smaller than the laser noise. Therefore noise suppression by locking to this comb is only possible up to 200 kHz. It turns out that even this is problematic because any control loop with significant gain at 200 kHz will still have non negligible gain up to some MHz frequencies, potentially enough to drastically worsen the laser performance there.

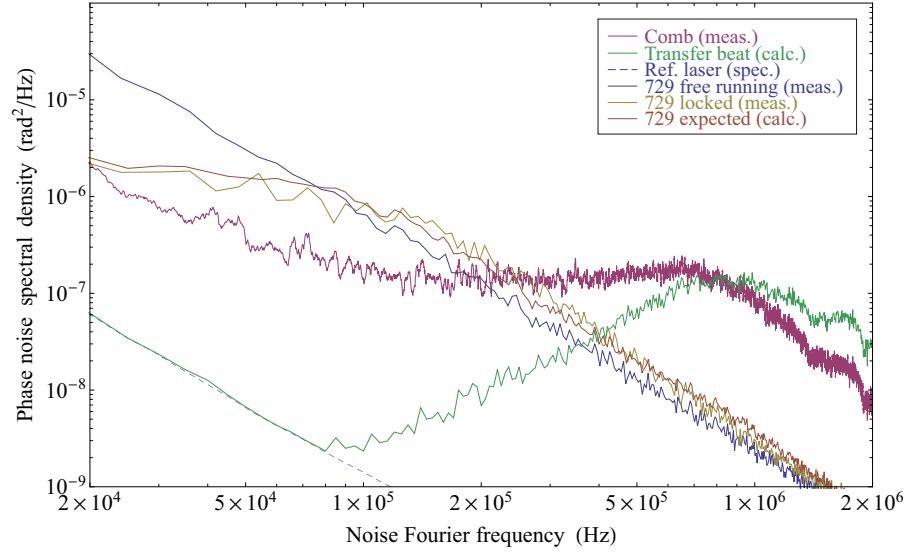


Figure 50: Phase noise of the frequency comb and 729 nm laser. The phase noise for the comb are plotted for the locked beat (red) and the transfer beat (green) that should at low Fourier frequencies be limited by the specified noise of the reference laser (blue, dashed). The 729 nm laser noise is given for the free running laser (blue) and locked laser (yellow). The orange curve is the calculated expected noise of the locked 729 nm laser, taking into account the lock transfer function as well as the free running and transfer beat noise.

### 8.2.3 Transfer lock scheme

To overcome these limitations, we implemented a high bandwidth version of the transfer scheme described in [163]. Here, not only the offset frequency is fed forward but also the repetition rate. The two beats at 729 nm and 1542 nm experience different amounts of repetition rate noise. According to the beat formulas

$$f_{\text{beat},729} = n_{729}f_{\text{rep}} + f_{\text{CEO}} - f_{729} \quad (110)$$

$$f_{\text{beat},1542} = n_{1542}f_{\text{rep}} + f_{\text{CEO}} - f_{1542}, \quad (111)$$

the repetition rate measurement at 1542 nm first has to be multiplied by  $n_{729}/n_{1542} = 1644158/777597 \approx 2.1144088776$  before it can be subtracted from the 729 nm beat. This was achieved by clocking a DDS chip with the repetition rate measurement  $f_{\text{clock}} = f_{\text{beat},1542} - f_{\text{CEO}}$  and programming it to create 0.11 times the clock input  $f_{\text{out}} = 0.11f_{\text{clock}}$ . A typically undesired but here exploited feature of DDS is that due to the digital nature they create *aliased* frequencies  $f_{\alpha}$  at

$$f_{\alpha} = (p \pm 0.11) \times f_{\text{clock}}, \quad p \in \mathbb{N}, \quad (112)$$

so that one of these aliased frequencies occurs at  $2.11f_{\text{clock}}$ . With this feed forward, the effective comb noise could be reduced significantly as given by the green curve in Figure 50. Below 80 kHz, the expected effective comb noise is even lower than the specified noise of the reference laser, therefore making the reference the limiting noise source at those Fourier frequencies. However, due to a signal delay of roughly 200 ns between the 729 nm beat signal and the multiplied 1542 nm beat, the transfer scheme only reduces the comb noise up to  $\sim 700$  kHz. Figure 51 shows the setup of this transfer lock, including most relevant electronic components. The mentioned delay is mostly due to RF filters that had to be placed at almost every mixer, analog doubler and DDS input and output port. Much care has been taken to minimize the delay as far as possible and further reduction would probably require custom designed RF filters. The use of tracking oscillators to make the electronic beat signals stable in output intensity and filter amplitude modulation was tried but in the end rejected because of the limited bandwidth of the phase locked loop (PLL) inside.

The 729 nm feedback loop is closed by mixing the transfer beat with a DDS reference to DC frequencies and applying this signal as the input into a commercial fast PID<sup>4</sup>. The fast branch of the PID modulates the laser diode current and the slow branch feeds back to the piezo that rotates the laser's external cavity grating. The performance of the locked laser has been measured and is given in Figure 50 by the yellow curve. It fits very well to a model that assumes the measured free running laser noise and transfer beat noise and a simple integrator transfer function for the loop. The unity gain of this transfer function was at 80 kHz, meaning laser noise is suppressed to roughly this frequency. Any higher bandwidth results in a large increase of laser noise around 1 MHz Fourier frequencies, leading to a decrease in the experimental Rabi flop fidelity as explained in the next section.

#### 8.2.4 Rabi flop error for observed phase noise

One aim of the phase locking described above was to reduce the noise of the 729 nm laser far enough to enable efficient qubit manipulations

---

<sup>4</sup> Toptica FALC

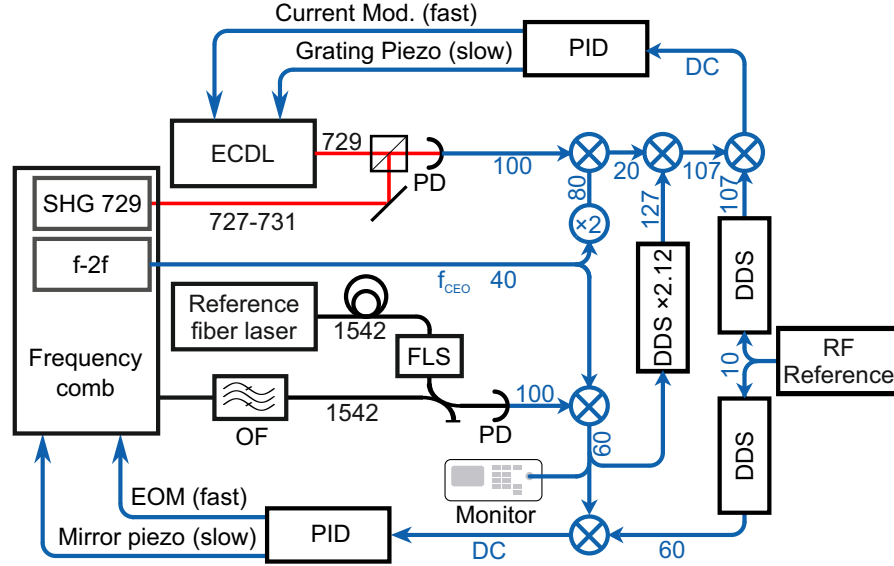


Figure 51: Transfer lock schematic. Blue signals are electronic, red are free space optic and black fiber optic signals. The blue numbers give the signal frequencies in MHz at the respective positions, the black numbers optical wavelengths in nm. PD: photo detector, OF: optical filter, FLS: fiber length stabilization.

on the  $\text{Ca}^+$  ion. As a figure of merit we analyze the spin flip probability for a single  $\pi$  pulse on the 729 nm carrier transition. Assuming laser phase noise  $S_\phi(f)$  to be the only noise process in the problem, the probability to *not* do this spin flip for a  $\pi$  pulse with a given Rabi frequency  $\Omega$  can be shown to be in lowest order of the phase noise [23]

$$\epsilon(\Omega) = \int_0^\infty S_\phi(f) \frac{1 + \cos \pi \frac{2\pi f}{\Omega}}{\left(\frac{\Omega}{2\pi f} - \frac{2\pi f}{\Omega}\right)^2} df. \quad (113)$$

This essentially resembles an integration over a bandpassed part of the phase noise with the bandpass centered roughly around the applied Rabi frequency. Higher Fourier frequency noise is fast enough to be averaged out effectively while lower frequency noise is too slow to significantly affect the process in the  $\pi$ -flop time  $\tau = \pi/\Omega$ . Applying this function onto the locked laser phase noise given in Figure 50, a Rabi flop error between 0.5% and 6.5% is expected for Rabi frequencies between 1 kHz and 500 kHz. This is shown in Figure 52. Errors in this range could be verified by the experiment, confirming the noise analysis of the preceding pages.

The achieved contrast suffices for the basic coherent manipulations needed for precise state detection, sideband cooling and state preparation. For optimal clock performance, the remaining error would reduce the stability of the clock and should be avoided if possible. Necessary improvements to the locking scheme described above could be made in multiple ways. The signal delay in the two branches of

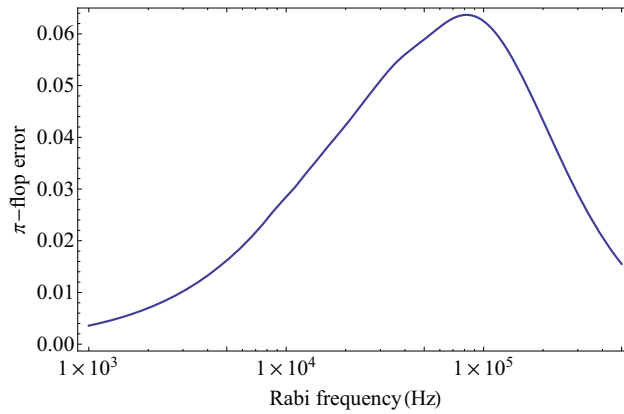


Figure 52: Expected phase noise induced Rabi flop error. Based on the measured locked laser phase noise, the expected Rabi flop error for a single  $\pi$  pulse at various Rabi frequencies is given.

the transfer beat could be tuned to be as equal as possible, to further reduce the effective repetition rate noise. The bandwidth of the repetition rate lock itself could be enhanced by the use of a different EOM that does not show resonances at around 1 MHz. Finally, as prepared while this thesis is written, a small reference cavity could be set up to stabilize the high Fourier frequency noise of the laser, leaving the comb lock active only at low frequencies.

Summarizing the results of the previous sections, we have for the first time stabilized an un-prestabilized ECDL with high bandwidth to an optical reference via a frequency comb for quantum logic operations. This was achieved by using a combined fast optical repetition rate lock and feed forward transfer scheme. Noise suppression of the laser took place up to roughly 80 kHz, orders of magnitude higher than previously realized transfer bandwidths [62, 118]. Additionally, this scheme was not only implemented to a single laser but copied and applied also to two more lasers at 866 nm and 794 nm, creating a set of mutual phase coherent lasers at wavelengths spanning more than an octave. This enables quantum interferometric experiments requiring phase coherence between different optical frequencies as for example two-color Raman transitions, high resolution dark state spectroscopy or (double) EIT cooling.





## EXPERIMENTS

---

In this chapter, the experiments performed with single  $\text{Ca}^+$  ions are presented. First, the loading of  $\text{Ca}^+$  ions and the spectroscopic signals from the atomic transitions at 397 nm, 729 nm and 866 nm are described. This leads to absolute frequency measurements and the characterization of trap frequencies, micromotion and magnetic fields. After these preparative measurements, results for Doppler cooling and sideband cooling are given, followed by the measurement of the external ion heating rates. Finally, the chapter and the main part of this thesis concludes with a report of the first experimental implementation of double-EIT cooling, surpassing the cooling speed of sideband cooling by more than one order of magnitude.

### 9.1 LOADING OF SINGLE IONS

For all the experiments described below, a single  $\text{Ca}^+$ -ion was loaded into the ion trap. Here, the typical loading procedure used on a daily basis is briefly explained. First, the necessary lasers were checked for power levels. Typically a few hundred  $\mu\text{W}$  of the 397 nm, 423 nm and 866 nm lasers and a few mW of 375 nm light arrived at the trap center, which was well sufficient for loading. Typical beam radii at the trap center were between  $40\ \mu\text{m}$  and  $150\ \mu\text{m}$ . The 866 nm laser was operated 10-100 MHz above resonance and the 397 nm laser detuned by 50-80 MHz below resonance. Additionally, the 397 nm far detuned beam was unblocked which had a typical power of  $\sim 1\ \text{mW}$ . When all the lasers were directed onto the trap center, a current of 1.8 A was applied to one of the  $\text{Ca}^+$  ovens. Corresponding to Figure 30 in Section 7.2, this lead to an oven temperature of 500-600 K, which suffices to initiate Ca sublimation at pressures of  $10^{-10}$  mBar. After a typical timescale of 1-2 minutes, an ion was detected on the EMCCD camera meaning that it was cooled to the bottom of the trap and sufficient fluorescence was collected. Frequently it happened that two or more ions appeared on this initial attempt. In this case, the best experimental strategy turned out to be reducing the oven current to 1.6 A to limit the loading rate and turn off the trap to release the ions and try loading again. It then took on average roughly 5 tries until a single ion was loaded. We attribute this to the extremely degenerate radial trap frequencies (see Section 9.2.3), that allow single ions to remain in hot oscillations in the radial direction perpendicular to the cooling beams. Once a second ion is loaded, the collisions between

the ions force them to move into other directions such that efficient cooling can take place.

### 9.1.1 Fluorescence detection

The Doppler cooled ion could be seen on the EMCCD camera by the fluorescence scattered from the cooling laser at 397 nm. Figure 53 shows a camera image of two  $\text{Ca}^+$  ions in our Paul trap. The ions are clearly separated from each other and the number of ions can immediately be seen. Such an ion pair would be dumped and a single ion would be loaded on a subsequent attempt. After assuring that only a single ion entered the trap, the imaging flip mirror was flipped and the fluorescence light directed onto the PMT. This allowed high fidelity determination of the internal state of the ion. Up to 146 counts per ms were detected by the PMT when both the 866 nm laser and the 397 nm laser were operated in saturation. The quantum efficiency of the detection can be evaluated by assuming a scattering rate of  $\Gamma/4$ , where  $\Gamma \approx 2\pi \times 21$  MHz is the 397 nm transition linewidth. The factor 4 arises because in saturation the population in the eight relevant states ( $2$   $^2\text{S}_{1/2}$  states,  $2$   $^2\text{P}_{1/2}$  states,  $4$   $^2\text{D}_{3/2}$  states) is split equally, resulting in a 25% chance of being in one of the  $^2\text{P}_{1/2}$  states. The maximal 397 nm photon scattering rate is hence 32 kcounts per ms so that the observed 146 counts correspond to a quantum detection efficiency of 0.44%. This is only slightly below the expected quantum efficiency of 0.48%, taking into account the fraction of photons collected by the objective (0.024), the shading due to the tilted blade electrode (0.8), the transmission of the objective (0.96), the reflectivity of 6 coated mirrors ( $0.99^6$ ), the transmission of the narrow optical filter (0.9) and the quantum efficiency of the PMT (0.31).

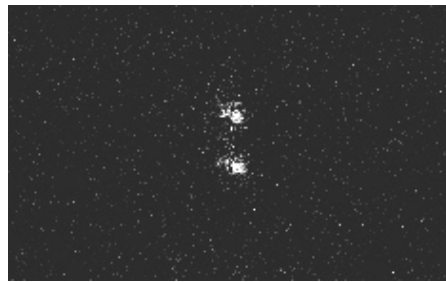


Figure 53: Camera imaging of two  $^{40}\text{Ca}^+$ -ions. Two  $\text{Ca}^+$  ions are trapped, Doppler cooled and their fluorescence observed on the EMCCD camera.

The dark counts, defined as counts if there is no ion or the ion is in a dark state, were minimized by adjusting a narrow slit in front of the PMT and by fine tuning of the 397 nm laser alignment to eliminate scattering from the trap blades. Here, it proved useful to operate in a mode where the 866 nm repump laser was switched on and off repeat-

edly. Switching it off resulted in immediate pumping into one of the dark  $^2D_{3/2}$ -states so that fluorescence ceased and the dark counts could be measured. The signal to noise ratio is measured by comparing these counts to the bright count rate. After optimization, the photon histograms for a  $250\ \mu\text{s}$  detection time are shown in Figure 54. They correspond to a signal to noise ratio of 303 for a dark count rate of 0.4 per ms and a fluorescence count rate of 124 per ms. By attributing every event with more than 5 photon counts to the bright state and every other event to the dark state, this corresponds to a state discrimination fidelity of  $1 - 10^{-8}$ , not limiting the experiments described below in any way. For 99% discrimination fidelity, a detection time of  $54\ \mu\text{s}$  is required. This makes the dead time contribution of the detection negligible in a quantum logic clock cycle of typically several 100 ms [148, 24].

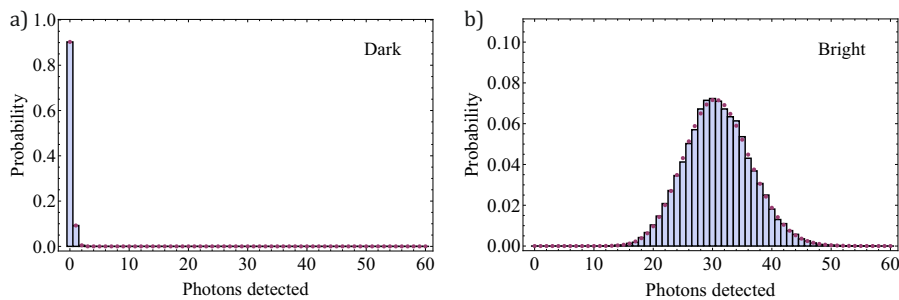


Figure 54: Dark and bright state histograms. The probability for the number of detected photons after a  $250\ \mu\text{s}$  detection pulse is shown for a) the ion being in the  $^2D_{3/2}$  dark state and b) the ion being in the  $^2S_{1/2}$  bright state. The purple dots give the corresponding probabilities for a fitted Poisson distribution with expectation values of 0.10 for the dark state and 31 for the bright state. The histograms are based on 11469 measurements for the dark state and 33831 measurements for the bright state.

## 9.2 THE CALCIUM TRANSITIONS

The ion trap and the laser system were tested by performing spectroscopy on some of the transitions in  $\text{Ca}^+$  ions. These experiments also resulted in the implementation of novel spectroscopy schemes, improving the uncertainty in the absolute frequency value of the 397 nm and 866 nm transitions.

### 9.2.1 The 397 nm transition

The 397 nm Doppler cooling and state detection transition is used by many groups around the world, its absolute frequency has however only been measured with an absolute uncertainty of 1.7 MHz [182] prior to the measurements of our group. The measurement described

in the following was a support measurement for a different experiment that demonstrated a novel form of quantum logic spectroscopy on this transition [173] using the lasers and frequency comb provided by the author and his colleagues. Nevertheless, also the direct fluorescence spectroscopy performed here resulted in an absolute frequency measurement presented in the next section.

#### 9.2.1.1 *The interleaved spectroscopy scheme and absolute frequency measurement*

One of the major limitations of the previous measurements of the 397 nm line was the influence of the repump beam at 866 nm. It needs to be applied in order to keep the ion from decaying into the dark  $D_{3/2}$  state. The 866 nm beam both Stark shifts the  $P_{1/2}$  level and disturbs the lineshape due to the appearance of dark resonances (cf. Section 9.2.2). The method applied here to circumvent this was to alternate the repump and spectroscopy pulses by quickly switching between them. A similar spectroscopy strategy has later been published by Pruttivarasin et. al [131] and the general concept of disabling the repumper during spectroscopy has been demonstrated in an indirect spectroscopy experiment before [183]. Figure 55 shows the spectroscopy sequence. First, the single  $\text{Ca}^+$  ion in the trap is Doppler cooled for 1 ms before the PMT is gated to measure the fluorescence from the Doppler cooling beam. Then, the 397 nm laser is switched by the double pass AOM to the desired spectroscopy frequency and intensity. Its intensity is stabilized to account for the frequency dependence of the AOM efficiency and slow drifts due to imperfect polarization maintenance of the single mode fibers that deliver the light to the chamber. For this purpose a sample and hold circuit is used that stabilizes the intensity when triggered and then holds the output until the next trigger. During this trigger time, the 866 nm laser is turned off, to shelve into the  $^2D_{3/2}$  state to neither heat nor cool the ion during the intensity stabilization. Then, 100 pulse pairs of alternating 397 nm and 866 nm pulses are performed. The 397 nm pulses are 500 ns and the 866 nm pulses are 800 ns long and they are separated in time by more than 150 ns which is sufficiently large compared to the excited state lifetime of 8 ns. During these pulses, the PMT events are counted, constituting the spectroscopy signal. After the spectroscopy, the ion is again Doppler cooled and the counts during Doppler cooling are again recorded. These recordings are used to discard events where the ion was not in its equilibrium temperature state prior or after the spectroscopy due to collisions with background particles (roughly 5% of the data is discarded). To minimize asymmetric Doppler cooling or heating during the spectroscopy, the intensity of the spectroscopy laser was kept very low ( $< 0.05$  saturation intensities) so that on resonance on average 160 photons were scattered during the 100 pulses. 160 transferred pho-

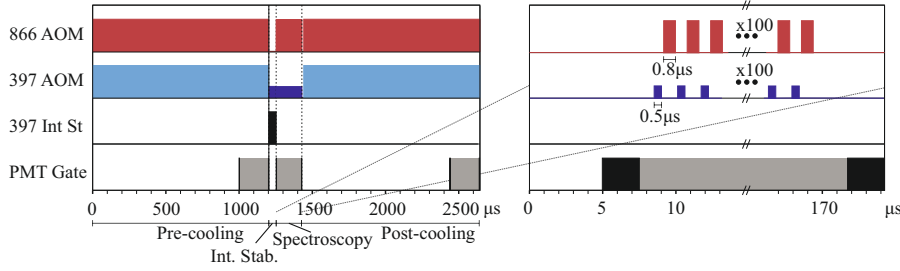


Figure 55: Interleaved spectroscopy scheme. The left plot shows the complete sequence of Doppler cooling, intensity stabilization, spectroscopy and again Doppler cooling. The times when the AOMs of the 397nm and 866nm lasers were switched on are shown, distinguishing between the 397 intensity and frequency settings for cooling (light blue) and spectroscopy (purple). The third row shows the time were the intensity stabilization is active and the fourth row shows the PMT gate times, where the gray areas show the counting periods. The right plot is a zoom into the  $\sim 175 \mu\text{s}$  of spectroscopy, showing the interleaved pulses.

ton momenta do not affect the temperature of the ion noticeably. The temperature has been determined by a fit of a lineshape model to the recorded line (see Figure 56 a). The model assumed the fluorescence signal to be the equal sum of two Voigt profiles centered around the Zeeman shifted  $^2S_{1/2}(m_J = -1/2) \rightarrow ^2P_{1/2}(m_J = -1/2)$  and  $^2S_{1/2}(m_J = +1/2) \rightarrow ^2P_{1/2}(m_J = +1/2)$  transitions at  $\pm 3.36 \text{ MHz}$  for a magnetic field of  $3.6(1) \text{ G}$ . The Lorentzian parts of the profiles were set to the natural linewidth of  $22.4 \text{ MHz}$  [79] and the Gaussian parts were fitted to the data, resulting in FWHM linewidths of  $14.1 \text{ MHz}$ , corresponding to a Doppler temperature of  $27 \text{ mK}$ . To get enough statistics for a frequency resolution  $< 100 \text{ kHz}$ , a two-point-sampling (tps) method [75] was used. The frequency was measured by alternating between the left and right half intensity points of the line. The signal difference was multiplied with the slope of the line to achieve a frequency reading. The measurement was performed for a total of 104 minutes with 20 minutes dead time due to reloading of the ion. This resulted in slightly more than 32 million non discarded spectroscopy pulses and allowed a shot noise limited statistical estimation of the line center with  $62 \text{ kHz}$  uncertainty. Figure 56 b) shows the Allan deviation for up to 500 s measurement intervals and indicates a good agreement with the assumption of purely white detection shot noise limiting the spectroscopy up to those times. The absolute frequency shift was estimated by using the experimentally determined Stark and Zeeman sensitivities of reference [173] and scaling them with the light intensities and magnetic fields present in our experiment. The major uncertainty arises from an uncalibrated AOM shift due to spectral changes in the 500 ns short pulses. The Fourier broadening of these short pulses is equivalent to a spectral width on the order of MHz. The frequency dependent response of the AOMs then

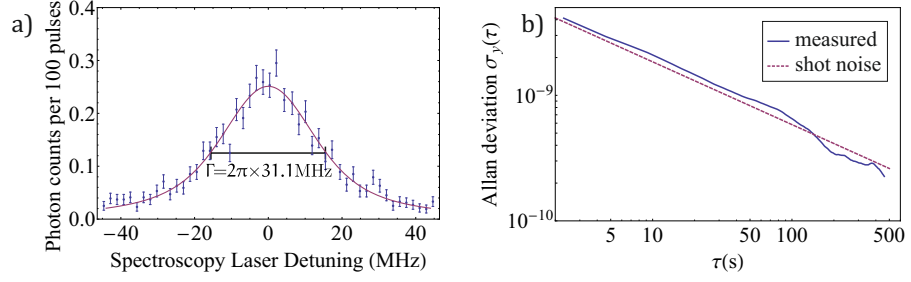


Figure 56: 397 nm frequency scan and spectroscopy stability. Figure a) shows the frequency scan across the resonance where the error bars are the shot noise of the individual measurements of 50,000 spectroscopy pulses each. For the fit, the sum of two Voigt profiles was assumed, with a Lorentzian FWHM natural linewidth of 22.4 MHz and a Gaussian linewidth of 14.1 MHz due to Doppler and Fourier broadening. Figure b) gives the Allan deviation of the fractional frequency measurements for up to 500 s measurement intervals. It agrees well with the expected deviation due to shot noise (dashed line).

leads to a non-negligible shift of the mean frequency of the pulses. The AOM had a Gaussian sensitivity curve with a FWHM linewidth of 31.8 MHz. Assuming, as a worst case scenario, that it was misaligned to be on resonance with one of the tps points, then the other pulse's mean frequency is shifted by 710 kHz, resulting in a systematic frequency measurement shift of half this value (355 kHz). This shift does not limit the usefulness of the technique because it can be measured and compensated to uncertainties of <16 kHz as demonstrated in [173] or strongly suppressed by going to longer pulse times. We were not aware of this shift during the measurement and have no ways of calculating it in post-processing. The resulting total error budget is given in Table 3 and the absolute frequency measurement for the 397 nm line is 755,222,765,479(362) kHz with 62 kHz statistical and 357 kHz systematic uncertainty. It is an absolute frequency measurement because the 397 nm laser was phase locked to the frequency comb described in Section 8, referenced to the hydrogen maser, directly linked to the primary Cs standards at PTB and therefore the SI second. This value is consistent with previous measurements by Wolf et al. [182] and the other measurement conducted in our group by Wan et al. [173] as shown in Figure 57.

### 9.2.2 The 866 nm transition

The 866 nm resonance was spectroscopically investigated by looking at the 397 nm fluorescence from the  $\text{Ca}^+$  ion, when both the 397 nm and the 866 nm laser were active and the 397 nm laser on resonance. Depending on the 866 nm laser frequency, EIT-quantum interference can be fulfilled for different pairs of  $S_{1/2}$  ground state and  $D_{3/2}$

Effect (origin)	Shift (kHz)
Zeeman (magnetic field)	$-5 \pm 37$
AC Stark (spectroscopy laser)	$9 \pm 7$
Spectroscopy pulse envelope shift (bandwidth)	$0 \pm 355$
Statistics	$0 \pm 62$
Total	$4 \pm 362$

Table 3: Error budget of 397 nm absolute frequency measurement. The uncertainties correspond to estimated  $1\sigma$  uncertainties for Zeeman and Stark shift, to a measured  $1\sigma$  uncertainty for statistics and to a worst case estimate for the pulse envelope shift.

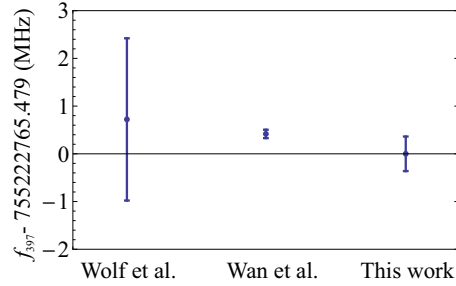


Figure 57: Comparison of the 397 nm transition absolute frequency measurement with previous experiments. The measured value agrees with the results from Wolf et. al [182] and Wan et. al [173].

metastable states. If one of these EIT conditions is fulfilled, the ion evolves into a dark state, where the fluorescence ceases. This dark state spectroscopy allows an absolute frequency measurement of the 866 nm transition if the 397 nm transition frequency is known. Figure 58 a) shows such a frequency scan together with a fit to a numeric calculation, solving the eight-levels-two-lasers quantum mechanical master equation. From these fits we can also extract other parameters such as the Rabi frequencies of the 397 nm and 866 nm beams and the magnetic field. In the measurement shown, the 397 nm beam was purely  $\pi$ -polarized and the 866 nm polarization had equal  $\sigma_+$ ,  $\sigma_-$ -polarization components, so that only four dark resonances appear (see Figure 58 b) ). After a single scan, the center frequency of the 866 nm transition can be determined to within 50 kHz, at which level the accuracy of an absolute frequency measurement is already limited by the accuracy of the best published 397 nm transition data [173]. This results in an absolute frequency measurement of the 866 nm transition in our experiment of  $346,000,235.14(10)$  MHz, where the uncertainty reflects the combined uncertainty of the inaccuracy in the knowledge of the 397 nm transition and the stochastic fit uncertainty. We have not evaluated systematic effects that might shift this frequency from the undisturbed transition. However, we assume them to be small, since the method is intrinsically insensitive to magnetic

fields and no change in frequency could be observed for variation of both lasers' intensities by factors of 2 or more.

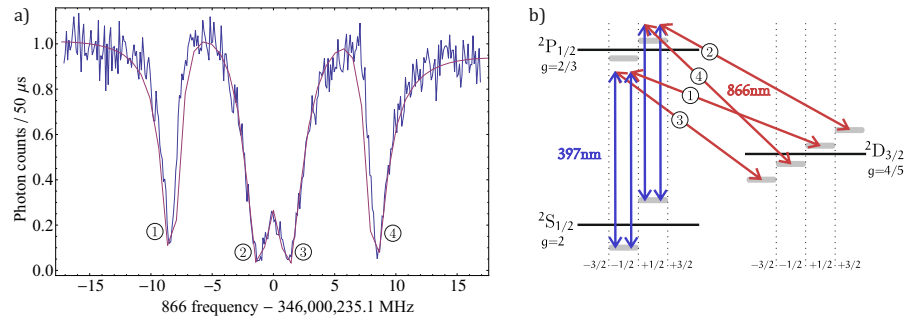


Figure 58: Dark state spectroscopy. Figure a) shows a frequency scan of the 866 nm laser around resonance. Four dark resonances appear that are attributed to EIT conditions between different Zeeman sub-levels of the ground and metastable states as shown in Figure b). The other possible dark resonances cannot occur because of selection rules due to polarization of the lasers. The red line shows a fit of numerical simulations of the full quantum master equation for a magnetic field of 4.25 G and Rabi frequencies of 6 MHz and 8 MHz for the 397  $\pi$  and 866  $\sigma$   $m_J = \pm 3/2 \rightarrow m_J = \pm 1/2$  transitions, respectively.

### 9.2.3 The 729 nm transition

The narrow 729 nm transition was used to spectroscopically resolve the motional sidebands in axial and radial directions. This enabled the precise determination of the secular motion trap frequencies. Additionally, the different Zeeman transitions could be separated, resulting in a measurement of the magnetic field complementary to the measurement of the previous section. Figure 59 shows as an example a broad scan around the  $^2S_{1/2}(m_J = -1/2) \rightarrow ^2D_{5/2}(m_J = -3/2)$  transition for three different applied trap drive RF powers.

The radial trap frequencies increase with enhanced RF power according to Equation 16. The axial sidebands remain constant, supporting the claim of negligible axial RF field for the symmetric drive. The measurement was used to calibrate the radial trap frequency vs. RF power dependence in our system as shown in Figure 60 a). The signal of this spectroscopy was an electron shelving signal as explained in Section 2.2, where after application of the 729 beam for a certain time, the population in the ground state was probed by observing (or not observing) fluorescence on the 397 nm transition. As mentioned in Section 9.1.1, this state discrimination could be performed with close to unity fidelity. After the state detection, the ion was reinitialized into the ground state by applying the 854 nm repumper for some  $\mu$ s. This type of spectroscopy could also be used to characterize the performance of the transfer phase lock of the 729 nm laser described



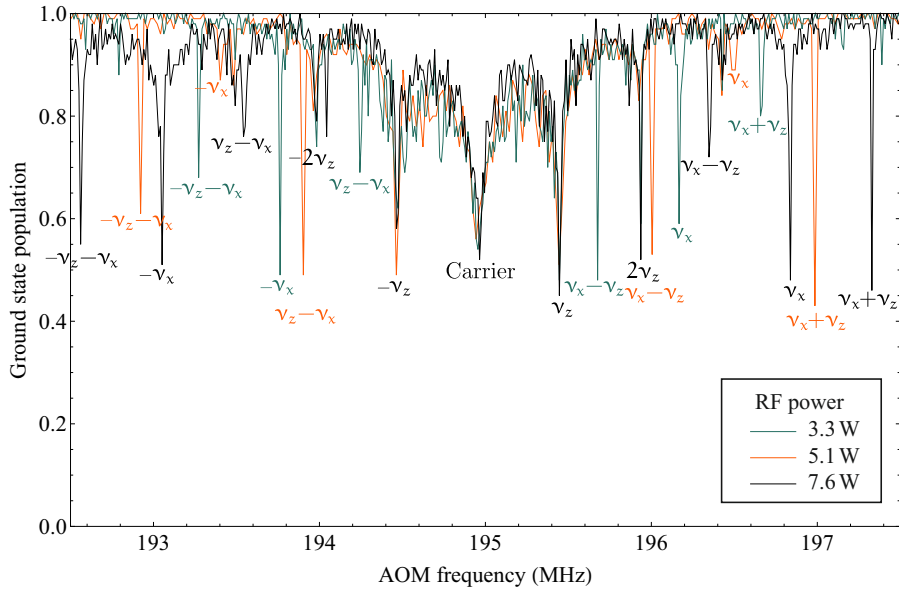


Figure 59: Spectroscopy of motional sidebands. The  ${}^2S_{1/2}(m_J = -1/2) \rightarrow {}^2D_{5/2}(m_J = -3/2)$  transition at 729 nm is shown. The strong carrier is surrounded by additional resonances corresponding to the motional radial and axial trap frequencies and sums and differences of these. The scan was performed for three different applied RF powers. The major resonances are labeled, where  $\nu_x$  represents the radial and  $\nu_z$  the axial sidebands. Axial sidebands coincide for the three cases and are color coded in black only. The scan had a resolution of 10 kHz.

in Section 8.2. Figure 60 b) shows a high resolution scan of the first blue sideband of the  ${}^2S_{1/2}(m_J = -1/2) \rightarrow {}^2D_{5/2}(m_J = -5/2)$  transition. A Gaussian fit to the line resulted in a residual linewidth of 2.3 kHz, posing an upper bound on the linewidth of the stabilized 729 nm laser for measuring times of roughly 20 minutes. The residual linewidth is believed to be magnetic field noise induced and hence the laser to be even narrower. This is motivated by the fact that the linewidth reduced from circa 10 kHz to the observed 2.3 kHz by probing with a fixed time delay to the 50 Hz power line phase. We plan on further investigating this by comparing spectroscopy results on transitions with different sensitivities to magnetic field fluctuations.

### 9.3 MICROMOTION COMPENSATION

One application of the narrow 729 nm laser is to spectroscopically resolve the micromotion sidebands of the 729 nm transition and use this signal to minimize excess micromotion. This and the other techniques for compensation that have been applied in the experiment will be explained here. Excess micromotion, as introduced in Section 3.3 leads not only to an increase in kinetic energy and therefore second order Doppler shifts, but also has other adverse influences on

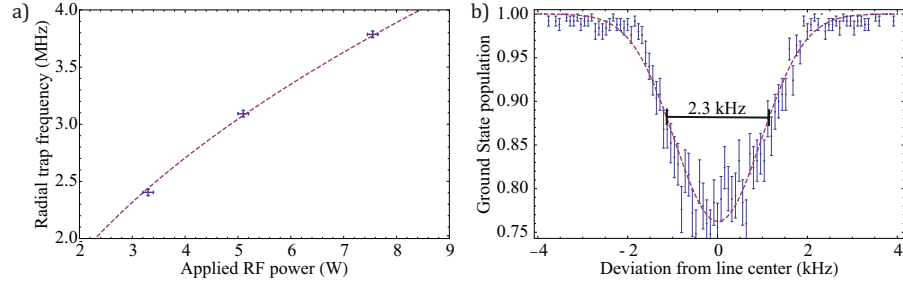


Figure 60: a): Radial trap frequency RF power dependence. The Figure shows the radial trap frequency measurement performed with the data of Figure 58. The power was measured with a standing wave ratio meter. The dashed line represents a fit to the model  $\nu_x = \sqrt{\alpha * P_{in} - 1/2} \nu_z$  with a fit constant  $\alpha = 2.01 \text{ W}^{-1}$ . b): high resolution spectroscopy on the first blue axial sideband of the  $^2S_{1/2}(m_J = -1/2) \rightarrow ^2D_{5/2}(m_J = -5/2)$  transition. The individual scan points are spaced by 80 Hz and every point represents an average of 250 experiments, triggered by the 50 Hz power line phase to reduce magnetic field noise.

single and multiple ion experiments. Examples include the worsening of Doppler cooling due to the cooling beam being blue detuned for certain micromotion sidebands, leading to heating [124, 28]. The major source for excess micromotion is the displacement of DC and RF quadrupole due to DC electric fields from either asymmetries in the trap or stray charges on the trap electrodes and insulators. Micromotion is compensated by applying DC voltages onto the four compensation electrodes at the side and below the ion trap and by adjusting the tip voltages independently from each other. This way, extra DC fields can be applied in all three dimensions, compensating arbitrary DC quadrupole displacements. An additional uncompensatable excess micromotion can result from a phase difference between the RF on opposing blade pairs [13] which was avoided by taking care to match the length of the RF feeds to the electrodes.

Three different methods have been used to find the optimal micromotion compensation voltages. A coarse tuning was performed using the CCD camera, the ion was parametrically heated by an applied trap RF modulation and finally sideband spectroscopy of the micromotion sidebands was performed.

### 9.3.1 Camera method

A displacement of DC and RF quadrupole leads to an ion position determined by a weighted sum of the two potentials (cf. Equation 23). A consequence is that this position moves, if one of the potential strengths is changed. The micromotion can hence be compensated, by finding the compensation voltages for which no movement of the ion is visible on the EMCCD camera if the RF power is varied. This

way, coarse compensation could be performed along the trap axis and in the horizontal direction. It could not be used to compensate the vertical direction because that direction is not imaged onto the camera.

### 9.3.2 *Parametric heating method*

A different compensation method is the recently published method [74, 166, 49] based on parametric heating of the ions. In this method, the radial RF trapping potential is modulated at one of the secular motion frequencies. This can lead to strong heating of the ions, if they are not placed at exactly the RF quadrupole center. We used one of the DDS boards of our experimental control box and mixed the secular frequency onto the RF frequency, creating modulation sidebands. The helical resonator strongly filtered these modulation sidebands but since tiny electric fields suffice for heating, this was not a limitation. The signal is observed by seeing a drastic decrease of Doppler cooling fluorescence counts on the PMT if heating is present. With this method the compensation voltages could be found with uncertainties of roughly 10%, corresponding to  $\sim 10$  V for typical compensation voltages of 100 V. The method was, however, found to be experimentally cumbersome, since small changes in the applied modulation power often sufficed to increase the heating from no observable effect to losing of the ion and having to reload. In practice, therefore the method presented in the next section was preferred.

### 9.3.3 *Micromotion sideband spectroscopy*

The micromotion of the ion through an applied laser field leads, in the reference frame of the ion, to an effective phase modulation of the laser frequency. This means that for a laser detuned by exactly the micromotion frequency, one of the phase modulation sidebands will be on resonance with the atomic transition, leading to resonant excitation. The strength of this excitation scales with the power in the sideband and is therefore a function of the micromotion amplitude (the square of the first Bessel function of the modulation index  $J_1^2(\beta)$  [39]) which can be used as a measure of the compensation quality. In practice, the 729 nm laser was tuned to a micromotion sideband and the excitation was minimized for a given pulse length and intensity. This, however, only lead to compensation of micromotion along the direction of the laser beam, since micromotion sidebands due to motion perpendicular to the beam were not driven. Therefore, the compensation voltages for minimal excitation were not uniquely defined for this measurement and a second measurement along a different spatial dimension had to be performed. Due to the symmetric drive, mainly micromotion along the radial trap directions occurred

(cf. Section 7.3.3.3). Nevertheless, a measurement along a third direction was used to compensate the remaining axial micromotion as well. Figure 61 shows the measurement results for compensation along all three axes. For every direction, a map of optimal radial compensation electrode voltages has been measured. The overall solution for best compensation was determined by the position where all three directions were compensated (i.e. where the dashed green lines cross, when the plots are overlaid). If no such position existed, this indicated axial micromotion and the tip voltages had to be adjusted until a unique crossing point was found. With this method, the micromotion compensation voltages could be determined up to  $\sim 1\%$ , surpassing the accuracy of the parametric heating method by a factor of 10.

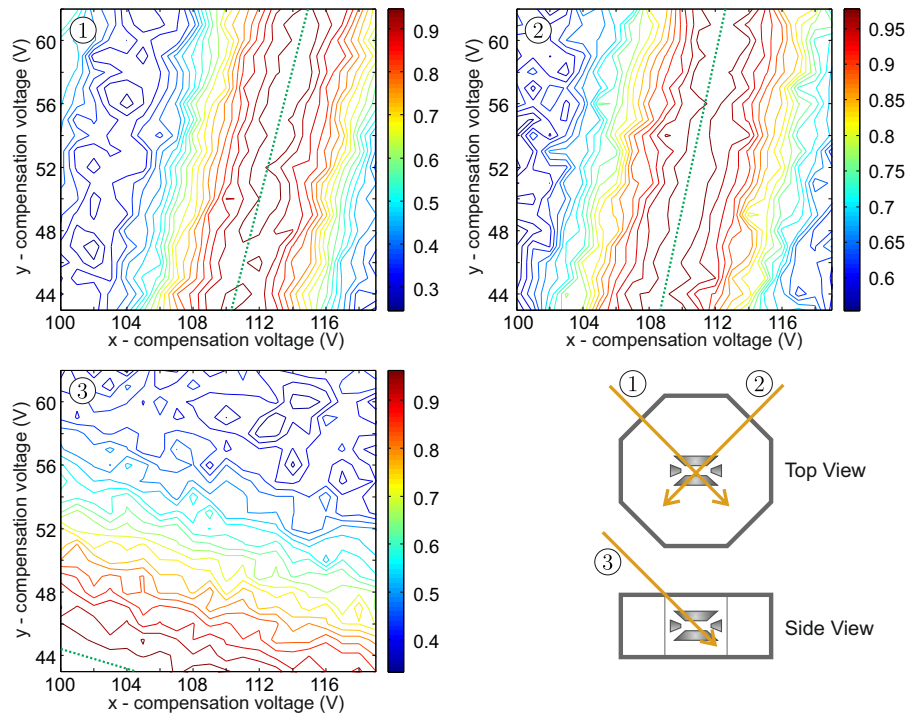


Figure 61: Micromotion compensation by sideband spectroscopy. The surface plots show the ground state probability (color code) after applying a pulse of 729 nm light on a micromotion sideband. The three plots correspond to measurements along three different directions as indicated by the sketch on the bottom right. The upper two plots probed along the horizontal plane and the bottom plot had an additional vertical component. The dashed green line is a guide to the eye of optimal micromotion compensation along the respective directions and the point where they cross is the overall point of compensation. In this measurement, this point (41 V, 109.5 V) falls outside the measurement region and had to be extrapolated.

## 9.4 COOLING EXPERIMENTS

The main focus of this thesis was to conduct laser cooling experiments on single  $\text{Ca}^+$  ions in preparation for a future  $\text{Al}^+/\text{Ca}^+$  quantum logic clock. The requirements for this cooling have been mentioned in Chapter 2. Summarized, a cooling of all six normal modes that is both *cold* and *fast* is required, to reduce residual Doppler shifts and dead times in the clock cycle. Additionally, it had to be investigated, whether cooling during the clock interrogation is necessary in the system. This was done by measuring the external heating rate and estimating its influence during realistic clock probe times. In this chapter, results for the three cooling mechanisms are given, starting with well established Doppler cooling followed by ground state sideband cooling and finally the first experimental demonstration of double-EIT cooling.

### 9.4.1 Doppler cooling

Doppler cooling, as introduced in Section 5.2 is a basic tool used in essentially all precision spectroscopy ion trap experiments. Doppler cooling is extremely robust and does not pose strict limits on laser frequency or intensity stability. Therefore, the first loading tries in the present experiment were successful by tuning the Doppler cooling beam roughly 100-300 MHz below resonance and waiting for the ion to appear on the camera. Since the Doppler cooling beam can drive transitions on a broad range of sidebands, it works, unlike sideband cooling, in a temperature regime starting from very high temperatures (room temperature and higher) down to the Doppler limit of  $\sim 0.5$  mK in the case of  $^{40}\text{Ca}^+$ . As explained in Section 6.2, the optimal laser parameters for detuning and power change severely for the different temperature regimes. Therefore two Doppler cooling beams were implemented. One close to resonance that was used for cooling near the Doppler cooling limit and one far detuned beam ( $\sim 200$  MHz red detuned) that was used to cool the ion after a collision with a background particle or for initial loading. Best Doppler cooling performance was achieved for a detuning of 24 MHz from the bare 397 nm resonance and powers below 0.1 saturation intensities. To measure the cooling performance, the red and blue axial sidebands of a 729 nm transition were compared and fitted with a model close to Equation 58, with additional 8 kHz decoherence due to magnetic field noise. The data and fits are shown in Figure 62 and resulted in a thermal state average motional excitation of  $\bar{n} = 11.8 \pm 4.3$ . The relatively large error bar results from the small difference of blue and red sideband Rabi frequencies at these motional excitations and more accurate results should be achievable by investigating higher order sidebands (cf. Section 4.5 and [170]). The measured  $\bar{n}$  agrees

with the expected Doppler limit of 11.1 for trap frequencies of 1 MHz. The shown measurement is for the axial directions, but similar results have been measured for one of the radial directions.

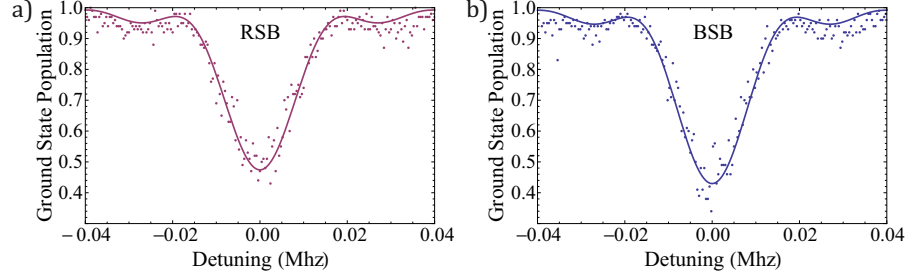


Figure 62: Doppler cooling performance. The difference between red a) and blue sideband b) scans across a 729 nm resonance with equal pulse length and power can be used to infer the temperature of the ion after Doppler cooling. Both scans have been fitted with a model close to Equation 58 assuming thermal states and the Lamb Dicke regime approximation. An additional 8 kHz decoherence width was assumed due to magnetic field noise during the measurement. The resulting fit corresponds to an average motional quantum number of  $\bar{n} = 11.8 \pm 4.3$ .

#### 9.4.2 Sideband cooling

Sideband cooling of single and multiple  $\text{Ca}^+$  ions is well understood and has been performed in many experiments before (e.g. [71, 143, 60]). It is the basis for many quantum information processing and quantum logic spectroscopy protocols relying on one or more motional modes being cooled to the ground state with high fidelity [158, 26, 173]. To selectively drive the red sidebands, the narrow 729 nm quadrupole transition is used. It is broadened (quenched) by the 854 nm repump laser as described in Section 5.3.1. The implemented experimental sequence is similar to what has been published [71, 60] and will be explained in the following. For a thorough theoretical investigation of the sideband cooling dynamics in  $\text{Ca}^+$  ions, the reader is referred to [143].

The sideband cooling scheme relies on a cycling transition between Zeeman sublevels of the  $^2\text{S}_{1/2}$ ,  $^2\text{D}_{5/2}$  and  $^2\text{P}_{3/2}$  states. The only combination of states (almost) without escape paths from the cycle are ( $^2\text{S}_{1/2}(m_J = -1/2) \rightarrow ^2\text{D}_{5/2}(m_J = -5/2) \rightarrow ^2\text{P}_{3/2}(m_J = -3/2)$ ) and the symmetric ( $^2\text{S}_{1/2}(m_J = +1/2) \rightarrow ^2\text{D}_{5/2}(m_J = +5/2) \rightarrow ^2\text{P}_{3/2}(m_J = +3/2)$ ). In principle both choices are possible and have been implemented but the former has the advantage of driving a transition at lower frequencies and therefore minimizing the risk of driving higher order blue sidebands of other 729 nm Zeeman substate transitions.

The generic sideband cooling cycle starts after typically 1 ms of Doppler cooling with an optical pumping pulse of  $\sigma^-$ -polarized light at 397 nm (see Sections 7.5.3 & 7.5.5). This efficiently prepares the ion in the  $^2S_{1/2}(m_J = -1/2)$  ground state. Subsequently, the sideband cooling 854 nm and 729 nm beams are switched on, cooling the axial (or radial) mode continuously. Eventually, one of the unlikely decay paths via the  $^2D_{3/2}$  or  $^2D_{5/2}(m_J = 3/2)$  states (cf. Section 5.3.1) results in the ion decaying into the wrong ( $^2S_{1/2}(m_J = +1/2)$ ) ground state. Therefore, additional short  $\sigma^-$  repump pulses are interleaved into the sideband cooling process, to reinitialize the cooling. After ten such cycles, the temperature is measured by applying red and blue sideband pulses and detection of their excitation strength. This sequence is schematically depicted in Figure 63.

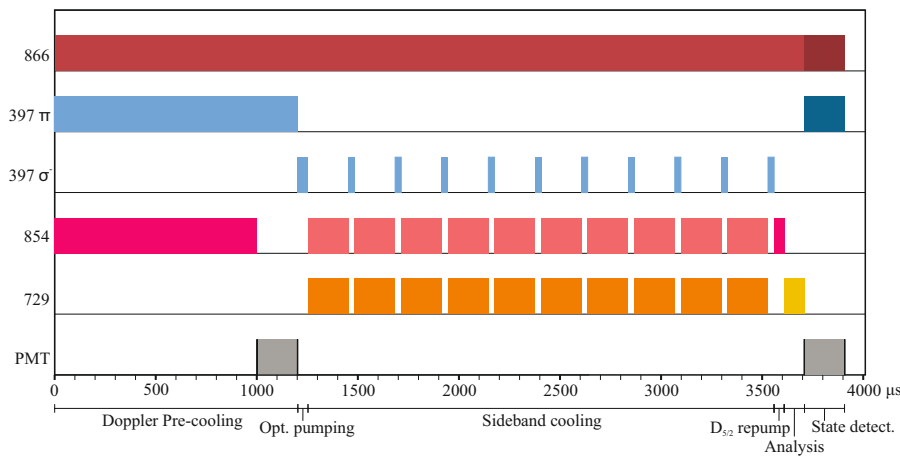


Figure 63: Generic sideband cooling sequence. Different colors in one row indicate possibly different laser settings for frequency and power. The analysis pulse length is shown as 200  $\mu\text{s}$  but varied strongly depending on the experiment performed (Rabi flopping, temperature measurements, line scans).

The cooling performance was optimized by applying an analysis pulse on the red sideband and trying to minimize excitation. Typically, multiple iterations of fine tuning of 729 nm and 854 nm laser frequency and intensity were necessary before optimal performance was reached. This method was also used to optimize the Doppler cooling beams' power and detuning, since lower temperatures at the beginning of the sideband cooling had a very positive effect on the ground state cooling success. The lowest measured average motional state excitation was  $0.032 \pm 0.006$ , corresponding to 97% ground state population. The blue and red sideband comparison that concluded in this number is shown in Figure 64. This is comparable with what has been achieved elsewhere [71, 60] but significantly worse than what is possible in single  $\text{Ca}^+$  systems [145] ( $\bar{n} < 10^{-3}$ , achieved for 4.5 MHz secular frequency). One plausible explanation for the remaining motional excitation could be the last 397 nm  $\sigma^-$  repump pulse after cool-

ing. It was not perfectly  $\sigma^-$  polarized and could therefore also scatter photons from the  $^2S_{1/2}(m_J = -1/2)$  state. Since a single photon scattered on this transition increases the  $\bar{n}$  by about  $\eta^2 \approx 0.02$ , this seems to be a conceivable limitation. It would also explain the strong fluctuations observed in the sideband cooling performance on a day-to-day basis, since the intensity of the  $\sigma^-$  beam was not controlled.

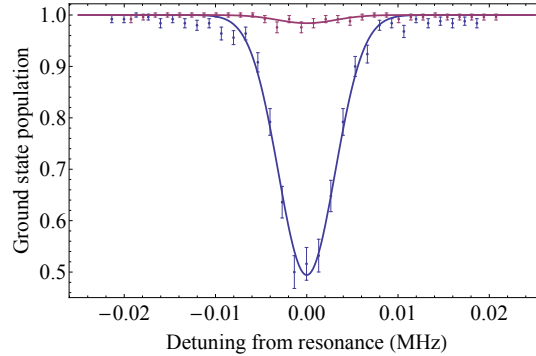


Figure 64: Sideband cooling results. Shown are line scans across the red (red curve) and blue (blue curve) sidebands after sideband cooling. The error bars are the quantum projection and quantization  $1\sigma$  errors and the fits are Gaussian resonance curves. From the average excitation a ground state probability of  $96.8 \pm 0.6\%$  can be deduced, where the error results from the standard error of the fit parameters.

Typically, after 2 ms of sideband cooling, the motional steady state was reached. Modeling  $\bar{n}(t)$  as an exponential decay,  $1/e$ -times of  $500 \mu\text{s}$  were evaluated, in rough accordance with other publications [71, 143, 60] (there typically  $200\text{-}1000 \mu\text{s}$ ). Considering six modes that have to be cooled individually in a future quantum logic clock ion crystal, this amounts to total cooling times of more than 10 ms. The consequence would be considerable dead time in the experiment, limiting the clock stability. Additionally, cooling during the clock interrogation would be difficult since one would have to iterate between the modes to keep all of them cold. An easier solution is offered by EIT cooling as described in Section 9.5.

#### 9.4.2.1 Heating rate measurements

In quantum logic clocks, the anomalous motional heating rate plays a crucial role in the final performance because of heating during the desired long clock interrogation times. Previous aluminum ion clocks operated with the Doppler cooling beam activated during the clock operation because of their large anomalous heating rates [148, 24]. This not only leads to a large second order Doppler shift since the ions are at Doppler cooling temperatures but also to an AC Stark shift of the clock transition due to the logic ion cooling laser. Ideally, ground state cooling of all modes is carried out prior to the interrogation



and then all cooling lasers are turned off during the interrogation. This would, however, require the heating rates to be low enough to not heat up the ions during the interrogation significantly. In existing clocks such interrogation times are 100-150 ms [148, 24], but future clocks might probe the transition for durations up to the  $\text{Al}^+$  upper clock state lifetime of 20.6 s.

There is an ongoing debate concerning the origins of anomalous heating with the general agreement that it cannot be explained by Johnson-Nyquist noise alone. Heating effects considered so far range from blackbody noise and electromagnetic interference from man-made and natural sources over technical noise and patch potentials to adatomic dipoles and the reader is referred to [170, 38, 37, 50, 88, 4, 47, 3] for some of the more general discussions. An experimentally verified observation is that generally in large, macroscopic traps lower heating rates are measured than in small, microscopic traps [38]. Consequently, the lowest published heating rate of  $< 1$  quantum/s was seen in a large 7 mm electrode distance trap [128]. A macroscopic trap geometry is hence desirable for quantum logic clocks, where smallness and scalability are not essential.

The measurement method for our 1.6 mm electrode spacing trap was to perform sideband cooling close to the ground state and then insert a variable waiting time before applying the temperature measurement 729 nm pulses (between the  $D_{5/2}$  repump and analysis intervals in Figure 63). The axial heating rate measurement results are presented in Figure 65 a) and resulted in  $13.6 \pm 0.6$  quanta/s for a single  $^{40}\text{Ca}^+$  ion at 940 kHz secular trap frequency. The radial heating rates for 3.1 MHz trap frequencies are  $5.2 \pm 1.1$  quanta/s and the results are shown in Figure 65 b). These results are comparable to what has been measured for similar trap frequencies in traps with similar electrode spacing (Roos et al.  $14 \text{ s}^{-1}$  at 2 MHz [145], Benhelm et al.  $3 \text{ s}^{-1}$  at 1.2 MHz [10], Rohde et al.  $10 \text{ s}^{-1}$  at 1.2 MHz [142], Home  $1\text{-}10 \text{ s}^{-1}$  at 800 kHz [70]) and significantly below what has been measured in our group with a very similar trap (Hemmerling  $100 \text{ s}^{-1}$  for  $\text{Mg}^+$  at 1.55 MHz, corresponding to  $63 \text{ s}^{-1}$  for  $\text{Ca}^+$  at 1.55 MHz [66]). To reach these heating rates, it was necessary to heavily filter the leads supplying the tip electrode voltage. A 10<sup>th</sup> order low pass filter with an RF power suppression of more than 75 dB at 500 kHz frequencies was implemented. A lump electronic filter and an SMA based filter have both been tested with no measurable difference in terms of heating rates. The difference between radial and axial heating rates can be explained by the different trap frequencies and is consistent with an isotropic and frequency independent electric field noise spectral density for 1 MHz and 3 MHz frequencies. It is not known at the moment, what the exact sources for the heating rates are. Additional information might be gained by a thorough analysis of the trap frequency dependence of the heating rate because different heating effects scale

differently with frequency. Then it might be possible to mitigate them further by appropriate means (e.g. further filtering of the electronic leads for the compensation electrodes, etc.).

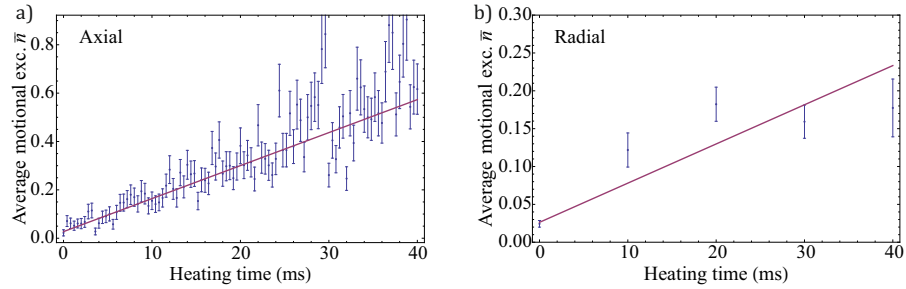


Figure 65: Heating rate measurement. The figures show the results of red and blue sideband comparisons on the axial a) and radial b) secular modes at 0.94 MHz and 3.1 MHz, respectively. The measurements of Figure a) have been obtained by scanning the heating time for analysis pulses at the center of the sidebands, the errors are based on the quantum projection noise of the single data points. The measurements of Figure b) represent fits to full motional sideband scans at five different waiting times with error bars equal to the standard fit errors. The slopes correspond to heating rates of  $13.6 \pm 0.6$  quanta per second for the axial and  $5.2 \pm 1.1$  quanta per second for the radial mode.

#### 9.4.2.2 Coherent manipulation of the ion state

The quantum logic spectroscopy protocol requires the ability to drive high fidelity sideband transitions (cf. Chapter 2 and [158]). For this, either narrow atomic transitions are driven with lasers stabilized to high-finesse-vibration-insensitive cavities or Raman schemes are used. In the first case, the remaining laser noise is well suppressed and in the second case only the relative laser noise between the Raman beams plays a role. Since the frequency difference in Raman schemes is typically in the MHz to GHz regime, relative frequency noise can be controlled well either by direct phase locks or by generating the beams from the same laser source via AOMs or EOMs. In the present experiment, the atomic transition is driven with a laser stabilized via a high bandwidth frequency comb transfer lock (see Section 8.2). And as explained earlier, especially the remaining high frequency noise is problematic for high fidelity fast Rabi flops. The implementation of ground state cooling allowed the investigation of the fidelity without significant decoherence due to motion (cf. [145] for a thorough analysis of motional decoherence).

98% fidelity for carrier  $\pi$ -flops and 91% fidelity on blue sideband flops was achieved after ground state cooling of the axial secular mode at a frequency of 0.94 MHz. These results are shown in Figure 66. The carrier fidelity corresponds well to the estimated fidelities

expected from the remaining 729 nm phase noise presented in Section 8.2.4. As indicated in that section, also a strong dependence of the  $\pi$ -flop error on the Rabi frequency was measured. At least for high Rabi frequencies, the decoherences could therefore be attributed to remaining laser noise. At low Rabi frequencies the limitations were initially the magnetic field noise, which broadened the carrier and sideband transitions to roughly 10 kHz. Only after implementing AC line triggering, this was improved to  $\sim 2$  kHz (see Figure 60). Even after implementing the line triggering, Hall probe measurements suggest that the magnetic field still fluctuates significantly which makes it the most probable cause for the low Fourier frequency Rabi flop errors seen in the experiments. Furthermore, it is not clear what limits the blue sideband fidelity to be below the carrier fidelity for similar flopping times. A possible cause might be laser phase noise due to lock servo bumps at the mode frequency, resulting in significant decoherence due to carrier excitation. Changing the lock parameters and deliberately increasing the servo bumps could help to verify or refute this hypothesis. Understanding and mitigating the remaining decoherence will be one of the next major steps towards the realization of a quantum logic clock in this laboratory.

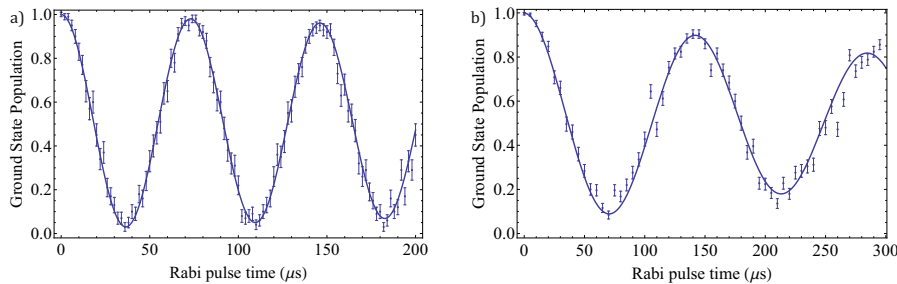


Figure 66: Rabi flopping results. The figures show the remaining ground state population after applying the 729 nm laser on the carrier transition a) and the axial blue sideband b), respectively. The solid lines are fits with a model allowing for exponential decay of the flopping contrast. The error bars represent quantum projection and quantization noise. The laser intensities were different in the two measurements.

## 9.5 EIT COOLING

Summarizing the previous cooling experiments, Doppler cooling is fast and robust but produces thermal states which are too hot for clocks that should operate at accuracies of  $10^{-18}$  or below. Sideband cooling is capable of achieving the cold temperatures required. But since every mode must be cooled individually, cooling all six modes of a quantum logic clock would take very long, possibly compromising clock stability. EIT cooling has successfully been implemented to

simultaneously cool multiple axial modes of multi ion crystals ( $\text{Be}^+$ - $\text{Mg}^+$ ) close to the ground state in less than  $100\ \mu\text{s}$  [94]. This capability to rapidly cool multiple modes makes it ideally suited for operation in quantum logic clocks. EIT cooling has also been implemented in  $^{40}\text{Ca}^+$  before and resulted in cooling of a single mode to roughly 80% ground state probability within 2 ms [144]. In both experiments, different Zeeman substates of the same ground state have been used to implement the EIT scheme. This made it possible to bridge the energy difference of the ground states of 335 MHz for the  $\text{Be}^+/\text{Mg}^+$  experiment and 12 MHz for the  $\text{Ca}^+$  experiment with acousto-optical modulators. The microwaves used to drive the AOMs can be generated in a sufficiently stable manner such that the residual phase noise between the EIT beams is far below the required level (cf. Section 5.4.4). One reason, why double-EIT has not been implemented prior to the experiments described here is that the typically experimentally employed ion species such as  $\text{Ca}^+$ ,  $\text{Mg}^+$ ,  $\text{Yb}^+$  only have two ground state levels, whereas double-EIT cooling as described in Section 5.4.3 requires three ground states. In the case of  $\text{Ca}^+$ , the four metastable substates of the  $^2\text{D}_{3/2}$  state can be used, but they have an energy difference corresponding to more than 400 THz to the  $^2\text{S}_{1/2}$  ground states. This excludes AOMs or EOMs to provide the required phase stability between the EIT beams.

The advantage of having a frequency comb transfer locking scheme as described in Chapter 8 that enables phase stability between multiple optical laser sources at different wavelengths, makes it possible to bridge this energy difference and use a  $^2\text{D}_{3/2}$  substate as the additional ground state in double-EIT. We realized double-EIT in this manner and the details of the experiment will be given in this section.

The general scheme of the double-EIT implementation has been described in Section 5.4.5. The two  $m_J = \pm 1/2$  substates of the  $^2\text{S}_{1/2}$  ground state are used as ground states  $|1\rangle$  and  $|2\rangle$ , being coupled to the  $^2\text{P}_{1/2}(m_J = -1/2)$  state via  $\sigma^-$ -polarized light and  $\pi$ -polarized light, respectively. Both lasers were switched with separate AOMs where the  $\pi$ -beam AOM was operated at 200 MHz and the  $\sigma$ -beam at 211.96 MHz and in both cases the -1st diffraction order was used. This implemented the necessary frequency difference due to the Zeeman splitting of the two ground states of 11.96 MHz, corresponding to a magnetic field of 4.27 G in the experiments. The blue detuning from resonance was chosen to be 72.3 MHz, limited by the double pass AOM (cf. Section 7.5.3) that was used for both Doppler cooling/state detection as well as for the creation of the EIT beams. Since for Doppler cooling it had to be red detuned and for EIT cooling it had to be blue detuned, it created the former for an RF frequency of 170 MHz and the latter for a frequency of 220.15 MHz, both being at the limits of its usable bandwidth. This detuning minus one axial

trap frequency of 0.94 MHz was matched by the 866 nm laser for the lowest ( $m_J = -3/2$ ) substate of the  $^2D_{3/2}$  state, being used as ground state  $|3\rangle$  (cf. Figure 18 in Section 5.4.5 for a level scheme). The single trapped  $\text{Ca}^+$  ion was Doppler cooled for 1 ms before the beams were tuned to their EIT frequencies and the EIT pulse began. After the EIT pulse, the ion was prepared into the  $^2S_{1/2}(m_J = -1/2)$  ground state by applying the 397 nm  $\sigma$ -beam for 200  $\mu\text{s}$ . Then, the 729 nm laser was used to analyze the motional state of the ion via blue or red sideband probe pulses on the  $^2S_{1/2}(m_J = -1/2) \rightarrow ^2D_{5/2}(m_J = -5/2)$  transition. The conducted full density matrix simulations have shown that a thermal state is not a good approximation for the motional state during and after double-EIT cooling. Therefore, the temperature evaluation method described in Section 4.5 and used for the evaluation of Doppler and sideband cooling is no longer valid. Instead, we limited the analysis to the determination of the motional ground state population. This was done by choosing a long pulse time for the 729 nm pulse, where the blue sideband excitation was incoherent and therefore roughly  $I_{\text{BSB}} \approx 0.5$ , independent of the cooling laser parameters and times. Accordingly, this was also the case for the red sideband for population not in the motional ground state. However, for the ground state population the red sideband cannot be driven so that from the deviation of  $I_{\text{RSB}}$  from 0.5, the ground state population  $P_0$  could be derived as

$$P_0 = 1 - I_{\text{RSB}}/0.5. \quad (114)$$

The cooling beam Rabi frequencies were optimized experimentally by observing the red sideband excitation after 200  $\mu\text{s}$  of cooling time and minimizing it. They were measured by two different methods. For the 866 nm and the 397 nm  $\pi$ -beam, a fitting of the dark resonances as in Section 9.2.2 was used to determine the Rabi frequencies to within roughly 10%. For the 397 nm  $\sigma$  beam, a method described in [144] was used where the Stark shift of the  $^2S_{1/2}(m_J = +1/2) \rightarrow ^2D_{5/2}(m_J = -3/2)$  729 nm transition was observed when the 397 nm  $\sigma$  beam was activated. To observe a signal of the 729 nm transition, the power of the  $\sigma$  beam had to be reduced by a factor of 10 compared to the EIT experiments, making the Rabi frequency prediction available only via extrapolation. The uncertainty of this method is estimated to be roughly 30%. The cooling parameters in the numerical simulations were also optimized and the optimal Rabi frequencies of  $(\Omega_\pi, \Omega_\sigma, \Omega_{866}) = (3.3 \text{ MHz}, 7.2 \text{ MHz}, 19.9 \text{ MHz})$  experimental and  $(4.6 \text{ MHz}, 7.0 \text{ MHz}, 21.0 \text{ MHz})$  from the simulations match within the experimental uncertainties, except for  $\Omega_\pi$ .

The cooling results of this measurement are presented in Figure 67. Ground state populations of more than 80% have been achieved within 200  $\mu\text{s}$  cooling time. After performing the experiments, it was realized that the remaining  $\sim 17\%$  population that are not in the ground state,

might result from the 200  $\mu\text{s}$  optical pumping pulse after the EIT interrogation. The pumping pulse was performed close to resonance and estimates of the power in the beam result in roughly 10 scattered photons due to a  $\sigma^+:\sigma^-$  polarization impurity of 1:1000. These 10 photons scattered on the carrier with a Lamb Dicke parameter of 0.145 would result in a blue sideband heating event probability of 20%, exactly explaining the discrepancy. The simulated data, scaled with this experimental "loss" factor of roughly 17% matches the experimental data well. If this turns out to be the limitation, ground state probabilities larger than 97% should be achievable within 200  $\mu\text{s}$ , starting from Doppler temperatures.

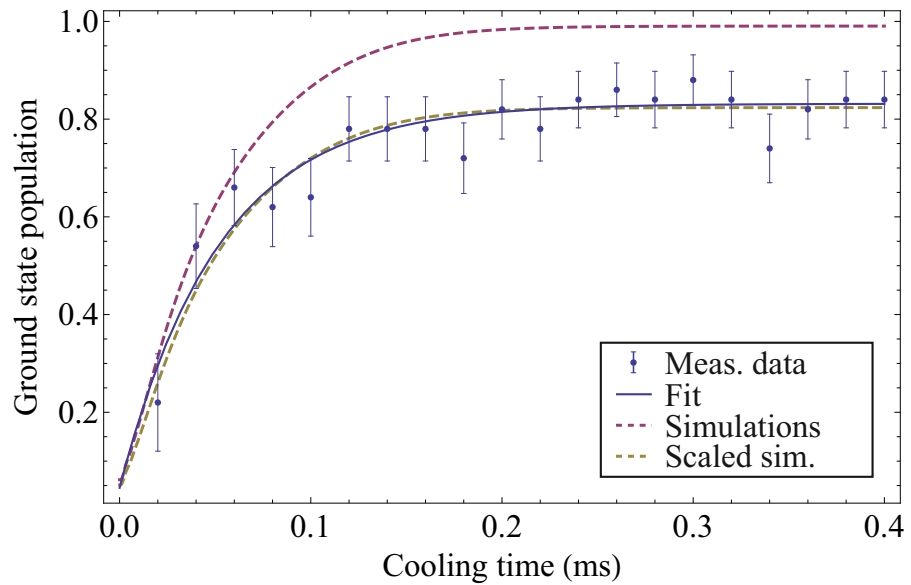


Figure 67: Double-EIT cooling results. The measured ground state population  $P_0$  is plotted with error bars corresponding to quantum projection and quantization noise. The blue line is a fit to an exponential approach as  $P_0 = a_1(1 - a_0 \exp(-t/\tau))$  where  $a_1 = 0.83$ ,  $a_0 = 0.95$ ,  $\tau = 52 \mu\text{s}$  are the least squared fitted parameters. The red, dashed line shows simulated data, where the full quantum master equation has been solved for 30 motional and 8 internal levels, starting with an approximately thermal state with  $\bar{n} = 11$ . The yellow curve shows the simulated data, when scaled with the experimental loss coefficient  $a_1$  which is presumably caused by additional heating due to optical pumping after the cooling.

The  $1/e$  cooling time constant is not defined for non-thermal states but can be estimated by assuming a thermal state with the same ground state probability as the state seen in the experiment. This estimation results in a cooling time constant of 5  $\mu\text{s}$ , almost two orders of magnitude faster than what has been measured with single EIT cooling in  $\text{Ca}^+$  and more than one order of magnitude faster than typically achieved sideband cooling results on  $\text{Ca}^+$  [71, 143, 60].

The rapid increase in the number of laboratories that possess frequency combs and can therefore implement the necessary phase locks between hundreds of THz detuned laser sources might lead to a widespread use of the technique. Applications are not only in quantum logic clocks but also in quantum computing and simulation experiments, where there is not only a need to cool fast to keep the cycle time short, but also to potentially cool many modes of large ion crystals simultaneously, optimally fulfilled by EIT cooling. In principle the technique is not limited to double-EIT, but can be extended to more than three ground states. For example in  $\text{Ca}^+$ , the remaining three substates of the  $D_{3/2}$  state can also be incorporated into the scheme with additional 866 beam paths without much experimental overhead. This could be used to either cancel further blue sidebands of other motional transitions or to go to a scheme where the ground states  $|1\rangle$  and  $|2\rangle$  are distributed among the  $S_{1/2}$  and  $D_{3/2}$  states and only coupled by one laser each, reducing the heating effect due to the off-resonant scattering of the  $\pi$ -laser.





Part IV

OUTLOOK AND SUMMARY



## OUTLOOK AND SUMMARY

---

This thesis presents theoretical and experimental preparations for a second generation, high accuracy, aluminum ion quantum logic clock. Some of the novel techniques developed within this context, namely the symmetric helical resonator, the high-bandwidth phase transfer lock, the interleaved and dark-state absolute frequency spectroscopy, and the double-EIT cooling might prove useful not only for metrology experiments but also for a broader scientific community. In this chapter, the future quantum logic clock performance will be estimated, based on the measurements presented in this thesis. The next steps necessary for successful and high-performance operation of this clock will be outlined wherever they can be anticipated. The chapter and the thesis will close with a summary of the scientific achievements accomplished as part of this work.

### 10.1 ALUMINUM ION QUANTUM LOGIC CLOCK ERROR BUDGET PREDICTION

The four largest frequency uncertainty contributions in  $\text{Al}^+$  quantum logic clocks are induced by the second order Doppler shift due to secular excess micromotion and secular motion, the AC-Stark shift due to the cooling laser and the AC-Stark shift resulting from the thermal blackbody background radiation (see Table 1). The first three of these shifts are directly linked to the ion's motion and a better control of the motional degrees of freedom is therefore crucial for a further improvement of this type of clock.

Excess micromotion is the motion at the RF-drive frequency undergone by an ion in a Paul trap due to imperfections in the trapping potential. It can result either from an imperfect overlap of RF and static quadrupoles or from a phase difference between opposing electrodes of the trap [13]. While the latter effect is typically avoided by symmetric wiring of the RF-leads, the former must be actively compensated to achieve low excess micromotion amplitudes. Even with compensation, a perfect nulling is possible only at a single point along the trap axis because of residual RF-fields present in all practical implementations of linear ion traps. In most of these implementations, two of the four electrodes creating the RF-quadrupole are held at ground potential and the other two carry the oscillating voltage. This asymmetry creates an uncompensatable micromotion equivalent to a second order Doppler shift of  $8 \times 10^{-17}$  for an  $\text{Al}^+$  ion displaced  $5 \mu\text{m}$  from the trap center for our trap geometry. This displacement along the trap

axis is typical for the distance between two ions in a linear ion trap operated at a few MHz secular motion trap frequencies. In this work, we presented a novel drive scheme that mitigates this effect. We modified the helical resonator that supplies the kV RF-trap voltages to provide two outputs with opposite voltage polarity. This way, the electrode pairs can be driven symmetrically, resulting in a cancellation of the RF-field along the trap axis. The ratio of the absolute voltages at the output of the helical resonator was measured to be 1.04, equivalent to an estimated remaining second order Doppler shift for the  $5\ \mu\text{m}$  displaced  $\text{Al}^+$  ion of  $3 \times 10^{-20}$ . It has to be noted, however, that the excess micromotion seen in the previous  $\text{Al}^+$  clocks is not only due to the remaining axial RF-field. There is also some radial micromotion that could not be compensated sufficiently. To infer whether this also occurs in the setup described here, a thorough quantitative analysis of the micromotion in the trap is necessary. All required tools and techniques for this study were prepared within this work. Remaining axial micromotion or micromotion due to a non-vanishing RF drive phase might be compensated by feeding small amounts of RF power to the tip electrodes or the micromotion compensation electrodes, respectively. If the low level of micromotion is verified experimentally, it will not only eliminate the excess micromotion contribution in the clock error budget, but also pave the way for extended clock protocols that incorporate multiple  $\text{Al}^+$  ions and possibly quantum entanglement in the same trap [7, 19, 72, 149, 67, 134, 133].

The secular-motion-induced Doppler shift and the Stark shift of the cooling laser have the same experimental source, namely the Doppler cooling laser applied on the logic ion. The continuous cooling employed during the clock interrogation pulse keeps the secular kinetic energies close to the Doppler cooling limit. The electric field of the cooling radiation is also present at the position of the clock ion and polarizes the two clock states inhomogeneously, resulting in a frequency shift. A first improvement of these effects is achieved by the choice of an adequate logic ion species.  $^{40}\text{Ca}^+$  is proposed here, having the advantage over  $^{25}\text{Mg}^+$  that it has a cooling transition with roughly half the linewidth, halving the Doppler cooling temperature and connected Doppler shifts. Theoretical models have been established to investigate the influence of the slightly worse mass ratio in the presence of external motional heating, leading to the conclusion that no significant increase in the Doppler cooling limit is to be expected for the experimental conditions present in our laboratory. Nonetheless, even perfect Doppler cooling to the  $\text{Ca}^+$  limit would still result in a Doppler shift of  $4.4 \times 10^{-18}$ . A better cooling strategy is therefore to not Doppler cool during the interrogation but use alternative cooling schemes such as the EIT cooling presented here. Simulations indicate that it is possible to cool all six motional modes of an  $\text{Al}^+/\text{Ca}^+$  ion crystal from 1.6 times the Doppler limit down

to motional quantum numbers of roughly 1 within 1.5 ms using a single-EIT scheme. This means that the second order Doppler shift can be reduced to  $6 \times 10^{-19}$  if cooling is performed during interrogation. The cooling laser Stark shift for this scenario is estimated to be  $9(3) \times 10^{-18}$ , too large for a  $1 \times 10^{-18}$  clock. The proposed solution would therefore be to EIT-cool only prior to interrogation, completely eliminating the cooling laser Stark shift. Taking into account the heating rates measured in this thesis, this would allow 250 ms interrogation times with an expected second order Doppler shift of  $\sim 2 \times 10^{-18}$ . Controlling this shift better than a factor 2 then results in the desired  $1 \times 10^{-18}$  performance. For highest clock stabilities, the interrogation time must be increased, making a reduction of the heating rates a requirement. The next experimental step must therefore be a more thorough analysis of the sources of the remaining heating rates and mitigation of these if possible. Alternatively, a pulsed EIT-cooling scheme could be implemented, keeping the ions cold and at the same time only exposing the  $\text{Al}^+$  ion to the AC-Stark shift of the cooling lasers for a fraction of the total interrogation time. Summarizing, a control of both shifts to within  $1 \times 10^{-18}$  seems challenging but feasible even for long interrogation times.

The blackbody radiation shift is the AC-Stark shift due to thermal blackbody radiation. It is one of the major limitations of modern optical clocks and it amounts to fractional frequency shifts of  $1.1 \times 10^{-16}$  in  $\text{Yb}^+$  [73], of  $5.6 \times 10^{-16}$  in  $\text{Sr}^+$  [46], of  $5.2 \times 10^{-15}$  in  $\text{Sr}$  [104, 16], of  $2.5 \times 10^{-15}$  in  $\text{Yb}$  [160] and of  $9 \times 10^{-18}$  in  $\text{Al}^+$  [24] at room temperature (300 K). It scales with the differential polarizability  $\Delta\alpha$  of the two clock states and the fourth power of the temperature  $\Delta\nu_{\text{BB}} \propto \Delta\alpha \times T^4$ . For most atomic clock species it therefore requires a precise determination of the temperature of the ambient radiation at the atoms' position. The stated numbers indicate that among the currently investigated species,  $\text{Al}^+$  requires the weakest relative bounds on such a temperature characterization due to the small magnitude of the shift. In fact, a temperature change from 300 K to 310 K only varies the fractional frequency by  $1 \times 10^{-18}$ . In this work, we preliminarily evaluated the temperature of the ion trap, which is the largest heat source in the vicinity of the ion, by thermal imaging. At typical operating powers of 5 W, we estimate a temperature increase versus room temperature of 2 K, well below the  $10^{-18}$  threshold. In the meantime a resistive temperature sensor has been attached to one of the insulating sapphire disks on which the trap is mounted to verify the measurements and additionally a cooperation within an EMRP project has been established with CMI and MIKES to support the thermal images with FEM simulation of the temperature distribution in the trap. From all we have measured so far, a future clock limitation due to an unknown temperature distribution at the ion seems unlikely. A more general problem arises from the fact, that the value of the differential polar-

izability  $\Delta\alpha$  is only measured with a 30% inaccuracy to date [146]. This makes it necessary to perform a more accurate measurement if a clock uncertainty of less than  $3 \times 10^{-18}$  is desired. We have attached a ZnSe viewport onto our chamber, which is transparent at  $10 \mu\text{m}$ , where the thermal blackbody radiation peaks at 300 K. This way, we have the opportunity to measure the polarizability directly at these wavelengths by using for example a  $\text{CO}_2$  laser source. Considering that for the other optical clock species, the polarizabilities have been determined to within one part in thousand inaccuracies [104], we do not believe this measurement to be a limitation for future  $10^{-18}$   $\text{Al}^+$  clock performance.

## 10.2 SUMMARY OF THE THESIS

Commencing with an empty laboratory, within this thesis the major parts of a single aluminum ion clock experiment have been set up. This included the laser system, the vacuum equipment, the experimental control and the ion trap apparatus. Most of the setup has been characterized with single  $\text{Ca}^+$  ions, giving rise to clock performance estimates in the  $10^{-18}$  regime. Novel experimental techniques have been implemented for the phase and frequency stabilization of external cavity diode lasers by high bandwidth transfer locking to an ultra-stable optical reference via a fiber frequency comb. The experiments performed here represent the first direct frequency stabilization of diode lasers to linewidths below 3 kHz without the use of optical cavities. A laser stabilized this way was used to perform high fidelity coherent manipulations and sideband cooling of a single  $\text{Ca}^+$  ion. Furthermore, the frequency stabilization technique was applied to multiple lasers, creating a set of four phase coherent optical sources from 397 nm to 1550 nm in our laboratory. Optical spectroscopy schemes have been developed to perform absolute frequency measurements of broad transitions in  $\text{Ca}^+$  with sub-MHz uncertainties, supporting new quantum logic spectroscopy experiments and demonstrating the absolute frequency link of our optical comb to the primary microwave frequency standards at PTB. The phase coherence between the 397 nm and 866 nm laser was utilized in the first demonstration of double-EIT cooling, incorporating quantum interference between three metastable states in  $\text{Ca}^+$ . Unprecedented  $^{40}\text{Ca}^+$  ground state  $1/e$  cooling times of  $5 \mu\text{s}$  have been reached and more than 80% ground state population was detected after less than  $200 \mu\text{s}$ , one order of magnitude faster than established sideband cooling techniques. Extensions to triple or higher order EIT cooling schemes are possible without much experimental overhead, giving the opportunity to apply this rapid cooling to simultaneous multi-mode ground state cooling in ion crystals. This might not only prove useful in quantum metrology experiments but also for the quantum computing and

information processing community where efficient scaling of ground state cooling to large crystals is desired. Additionally to multiple-EIT experiments, the phase coherence allowed by the transfer-locking scheme between different colors might also be exploited to drive Raman processes between optically separated metastable states. Typically applied on states separated by microwave frequencies, the established protocols for high fidelity quantum state manipulation might be translated to the optical regime. This makes for example the  $D_{3/2}$  states in  $\text{Ca}^+$  available for quantum information processing via the 397 nm and 866 nm transitions, without the need for a narrow laser directly at the  $S_{1/2} \rightarrow D_{3/2}$  transition, promising high gate speed thanks to the use of dipole allowed transitions, similar to what has been reported in [187].





Part V

APPENDIX



## APPENDIX

---

### A.1 DERIVATION OF THE TWO ION DOPPLER COOLING AND HEATING RATES

*Parts of the following were published before by the author and his co-authors in [185].*

The Doppler cooling rate of a two-ion crystal mode can be calculated by determining the energy change in this mode for every scattering event. The energy change in an in-phase mode (analogously for out-of-phase modes) with modal amplitudes  $z_i$  before and  $z'_i$  after the absorption of a cooling photon is given by

$$\Delta E_i = \frac{1}{2} m_1 \omega_i^2 (z_i'^2 - z_i^2). \quad (115)$$

$z'_i$  can be calculated by expressing the modal amplitude  $z_i$  as a function of the positions  $q_1, q_2$  and velocities  $v_1 = \dot{q}_1, v_2 = \dot{q}_2$  along the axis of the relevant modes of the two ions before the absorption

$$z_i = \sqrt{\frac{(\sqrt{\mu} b_2 v_2 + b_1 v_1)^2 + \omega_i^2 (\sqrt{\mu} b_2 z_2 + b_1 z_1)^2}{\omega_i^2}} \quad (116)$$

and then adding the velocity change  $dv = l_x \hbar k / m_1$  (exemplary for the  $x$ -direction) to the cooling ion velocity

$$z'_i = \sqrt{\frac{(\sqrt{\mu} b_2 v_2 + b_1 (v_1 + dv))^2 + \omega_i^2 (\sqrt{\mu} b_2 z_2 + b_1 z_1)^2}{\omega_i^2}}. \quad (117)$$

Substituting these equations into Eq. (115),  $\Delta E_i$  gives

$$\Delta E_i = \frac{1}{2} m_1 b_1^2 dv^2 + m_1 b_1 dv (b_1 v_1 + \sqrt{\mu} b_2 v_2) \quad (118)$$

$$= \frac{1}{2} m_1 b_1^2 dv^2 + m_1 b_1 dv \omega_i z_i \cos(\omega_i t + \phi_i). \quad (119)$$

The first term of this equation is a constant heating that is taken care of in the heating rate. The second term corresponds to mode cooling if  $\cos(\omega_i t + \phi_i)$  is negative and heating if it is positive. The rate  $R$  at which scattering events occur is given by Eq. (106). The cooling rate is computed by averaging the product  $R \times (\Delta E_i - \frac{1}{2} m_1 b_1^2 dv^2)$  over the oscillation periods of all six crystal modes

$$\frac{dE_i}{dt}_{\text{Cooling}} = \frac{1}{(2\pi)^6} \int_0^{2\pi} \int_0^{2\pi} \int_0^{2\pi} R (\Delta E_i - \frac{1}{2} m_1 b_1^2 dv^2) d^3 \phi_i d^3 \phi_o. \quad (120)$$

The integration over all six modes is necessary because the scattering rate depends on the product  $\mathbf{k} \cdot \mathbf{v}_1$  and therefore on the cooling ion velocity in all three spatial dimensions. This integral cannot be solved in general. But for cold crystals, where  $|\mathbf{k}v_1| \ll \Gamma$  in all three dimensions, the integrand can be expanded and higher order terms in  $kv_1/\Gamma$  can be neglected, leading to Eq. (96).

The heating rate computes similarly by averaging the product  $\mathbf{R} \times \frac{1}{2}m_1 b_1^2 d\mathbf{v}^2$  over the six modes which leads in first order to a velocity independent term

$$\hbar^2 3l_x^2 k^2 \frac{I}{I_0} \frac{\Gamma}{12m_1} \frac{b_1^2}{1 + I/I_0 + (2\Delta/\Gamma)^2}. \quad (121)$$

To this heating due to the absorption of the photons one has to add a contribution of the spontaneous emission. This is exactly as large as the absorption effect but does not depend on the direction of the cooling laser. Assuming an isotropic emission it is given by

$$\hbar^2 k^2 \frac{I}{I_0} \frac{\Gamma}{12m_1} \frac{b_1^2}{1 + I/I_0 + (2\Delta/\Gamma)^2} \quad (122)$$

so that the sum of Eq. (121) and (122) gives the total heating rate as in Eq. (98).

## A.2 DOPPLER SHIFT CONTRIBUTION OF INTRINSIC MICROMOTION

*Parts of the following were published before by the author and his co-authors in [185].*

To calculate the amplitude of the micromotion in the radial modes of the two-ion crystal, we generalize the derivation for single ions given in [13]. The force on a single ion in radial direction (we exemplary use the  $x$ -direction in the following) is given by

$$F_x = -\partial_x e\Phi(x, y, z, t) = 2x\alpha \frac{eU_0}{d^2} - x \frac{eV_0}{R^2} \cos \Omega_t t \quad (123)$$

where  $\Phi(x, y, z, t)$  from Equation 11 was used. In two-ion crystals an additional force arises due to the Coulomb potential  $U_C$  between the two ions

$$U_C(x_1, x_2, y_1, y_2, z_1, z_2) = \frac{e^2}{4\pi\epsilon_0} \frac{1}{\sqrt{(x_1 - x_2)^2 + (y_1 - y_2)^2 + (z_1 - z_2)^2}}. \quad (124)$$

The Coulomb-force in  $x$ -direction is given by

$$F_{C,x} = -\partial_x U_C(x_1, x_2, y_1, y_2, z_1, z_2) = \frac{e^2}{4\pi\epsilon_0} \frac{1}{\sqrt{(x_1 - x_2)^2 + (y_1 - y_2)^2 + (z_1 - z_2)^2}^3} (x_1 - x_2). \quad (125)$$

We now assume that the ion crystal is cold enough so that the ions oscillate with small amplitudes around their equilibrium positions

$$\mathbf{x}_1^{(0)} = (0, 0, z_0), \quad (126)$$

$$\mathbf{x}_2^{(0)} = (0, 0, -z_0) \quad (127)$$

where  $z_0 = \left(\frac{ed^2}{32U_0\pi\epsilon_0}\right)^{1/3}$  (see for example [76]). Linearising of Eq. (125) in  $(x_1 - x_2)$  around  $\mathbf{x}_1^{(0)}, \mathbf{x}_2^{(0)}$  gives

$$F_{C,x} \approx \frac{e^2}{4\pi\epsilon_0} \frac{1}{\sqrt{(2z_0)^2}^3} (x_1 - x_2) = \frac{eU_0}{d^2} (x_1 - x_2). \quad (128)$$

If we now consider only a single mode (i.e. the in-phase or the out-of-phase mode), we can write the  $x$ -motion of the second ion as a constant factor  $\beta$  times the motion of the first ion

$$x_2 = \beta x_1 \quad (129)$$

where  $\beta = b_2/(\sqrt{\mu}b_1)$  for in-phase and  $\beta = -b_1/(\sqrt{\mu}b_2)$  for out-of-phase modes as follows from Eq. (30) and (31).

Replacing  $x_2$  in Eq. (128) and adding the Coulomb-force to the force due to trap potentials, the total force  $G_x$  on the ion is given by

$$G_x = F_x + F_{C,x} = x_1 \frac{eU_0}{d^2} (2\alpha + 1 - \beta) - x_1 \frac{eV_0}{R^2} \cos \Omega_T t. \quad (130)$$

Introducing the  $\alpha_x = -\frac{8\alpha eU_0}{m_1 d^2 \Omega_T^2}$  and  $q_x = \frac{2eV_0}{m_1 R^2 \Omega_T^2}$  as in [13], the equation of motion for  $x_1$  can be given in typical Mathieu form

$$\ddot{x}_1 + \left( \alpha_x \left( 1 + \frac{1 - \beta}{2\alpha} \right) + 2q_x \cos(\Omega_T t) \right) \frac{\Omega_T^2}{4} x_1 = 0. \quad (131)$$

Compared to the equation of motion for a single ion, the only difference is that the  $\alpha_x$  is varied by a factor  $(1 + (1 - \beta)/(2\alpha))$  in the case of a two-ion crystal mode. Accordingly, the first order solution [89] (valid for  $q_x \ll 1$ ,  $\alpha_x(1 + (1 - \beta)/(2\alpha)) \ll 1$ ) of the single ion equation is still valid, if that factor is included:

$$x_1(t) \approx x_i b_1 \sin \omega_{x,i} t + \phi_{x,i} \left( 1 + \frac{q_x}{2} \cos(\Omega_T t) \right) \quad (132)$$

In this equation the amplitude  $x_i b_1$  of the oscillation was already chosen to comply with Eq. (30).  $\omega_{x,i}$  denotes the in-phase mode frequency and is given by

$$\omega_{x,i} = \frac{1}{2} \Omega_T \sqrt{\alpha_x (1 + (1 - \beta)/(2\alpha)) + \frac{1}{2} q_x^2}. \quad (133)$$

The average squared velocity of this motion is given by

$$\begin{aligned}
 \langle \dot{x}_1^2 \rangle &= \frac{1}{2}(x_i b_1)^2 \left( \omega_{x,i}^2 + \frac{1}{8} q_x^2 \Omega^2 \right) \\
 &= \frac{1}{2}(x_i b_1)^2 \omega_{x,i}^2 \left( 1 + \frac{q_x^2}{q_x^2 + 2a_x(1 + \frac{1-\beta}{2\alpha})} \right) \\
 &= \frac{1}{2}(x_i b_1)^2 \omega_{x,i}^2 \left( 1 + \frac{2\epsilon^2}{2\epsilon^2 - 2\alpha - (1-\beta)} \right) \quad (134)
 \end{aligned}$$

where in the last step the  $q_x$  and  $a_x$  were substituted by the  $\epsilon^2 = \frac{-\alpha q_x^2}{2a_x}$  factor introduced in Section 3.2. Equation 134 shows that for the radial modes the average squared velocity is not just given by the secular motion but that a micromotion term of the same order of magnitude has to be considered as well. For strong radial confinement  $\epsilon^2 \gg 1$ , the micromotion contribution approximately equals the contribution from the secular motion. However, for weak confinement, it can become much larger.

Figure 68 shows a plot of the relative kinetic energy of the micromotion of the clock ion compared to its secular energy for one pair of radial modes and for different  $\epsilon$ -parameters (again the stated  $\epsilon$  is that of a single clock ion) in the absence of external heating. The graph shows that the out-of-phase fractional micromotion energy contribution can get very large, when the trap is operated close to the instability limit.

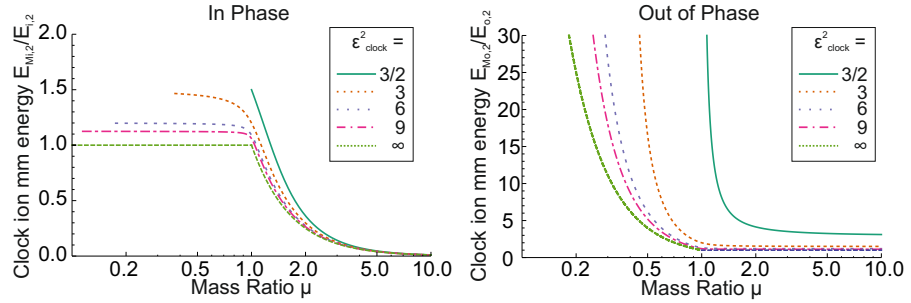


Figure 68: Relative micromotion energy of the clock ion in the in-phase and out-of-phase radial modes. The energy is normalized to the secular energy of the clock ion in the respective mode. In this graph the absence of external heating was assumed. The dashed lines denote the asymptotic behavior for very large radial confinement ( $\epsilon \rightarrow \infty$ ).

The micromotion contribution factor for the second ion (which is in this paper the clock ion and therefore the interesting one), can be calculated identically but the  $\epsilon_2 = \sqrt{m_1/m_2}\epsilon$  and  $\beta_2 = 1/\beta$  parameters for the second ion have to be used. Expressed in terms of the  $\epsilon$

and  $b_1, b_2$  parameters, the average squared velocity of the clock ion is therefore given by

$$\langle \dot{x}_{2,i}^2 \rangle = \frac{1}{2\mu} (x_i b_2)^2 \omega_{x,i}^2 \left( 1 + \frac{2\epsilon^2/\mu}{2\epsilon^2/\mu - 2\alpha - (1 - \sqrt{\mu} b_1/b_2)} \right) \quad (135)$$

$$\langle \dot{x}_{2,o}^2 \rangle = \frac{1}{2\mu} (x_o b_1)^2 \omega_{x,o}^2 \left( 1 + \frac{2\epsilon^2/\mu}{2\epsilon^2/\mu - 2\alpha - (1 + \sqrt{\mu} b_2/b_1)} \right) \quad (136)$$

for the in-phase and out-of-phase mode, respectively.

### A.3 ESTIMATION OF THE DOUBLE-EIT COOLING NOISE SENSITIVITY

The estimates for the noise sensitivity of double-EIT cooling stated in Section 5.4.4 were obtained by calculating the carrier heating rate (in motional quanta per second) for a noisy laser with resonant Rabi frequency  $\Omega_1$ . As long as  $\Omega_1^2 \ll \Omega_2^2$ , the carrier heating rate  $h_{\text{CAR}}(\delta)$  for a small frequency deviation  $\delta = \Delta_1 - \Delta_2$  between lasers  $\Omega_1$  and  $\Omega_2$  is approximately given by

$$h_{\text{CAR}}(\delta) \approx \frac{\Omega_1^2 \Gamma \delta^2}{\left( \Gamma^2 \delta^2 + 4(\Omega_2^2/4 - \delta(\delta + \Delta) + \frac{\delta \Omega_3^2}{4(\Delta - \Delta_3 + \delta)}) \right)^2 \tilde{\eta}^2}. \quad (137)$$

This follows from Equation 87 by substituting  $\nu$  with  $\delta$  and using  $\Omega_1^2/\Omega_2^2 \ll 1$ . The total noise induced heating rate  $h_{\text{tot,CAR}}$  for a white frequency noise process is then given by the integral of this function multiplied with a Lorentzian  $l(\delta) = \frac{1}{\pi} \frac{\gamma/2}{(\gamma/2)^2 + \delta^2}$  with FWHM linewidth  $\gamma \ll \Delta$  as

$$h_{\text{tot,CAR}} \approx \int_{-\infty}^{\infty} l(\delta) \times h_{\text{CAR}}(\delta) d\delta. \quad (138)$$

The threshold linewidth  $\gamma$  at which carrier heating becomes significant is calculated by comparing this equation with the heating rate due to second order sideband heating  $h_{2\text{ndBSB}}$  given by

$$h_{2\text{ndBSB}} \approx 2 \frac{\Omega_1^2 \Gamma (2\nu)^2}{\left( \Gamma^2 (2\nu)^2 + 4(\Omega_2^2/4 - 2\nu(2\nu + \Delta) + \frac{2\nu \Omega_3^2}{4(\Delta - \Delta_3 + 2\nu)}) \right)^2 \eta^4}. \quad (139)$$

Noise at Fourier frequencies around the EIT resonances constitutes the largest contribution to this total noise-induced heating rate. This is shown in Figure 69, where the functions  $l(\delta)$ ,  $h_{\text{CAR}}(\delta)$ , and  $l(\delta) \times h_{\text{CAR}}(\delta)$  are plotted for typical experimental parameters. From the  $2\pi \times 7$  kHz broad line, the Fourier components in the wings of the Lorentzian at roughly 300 kHz contribute the most to the total noise. This justifies the white noise assumption, since most laser sources

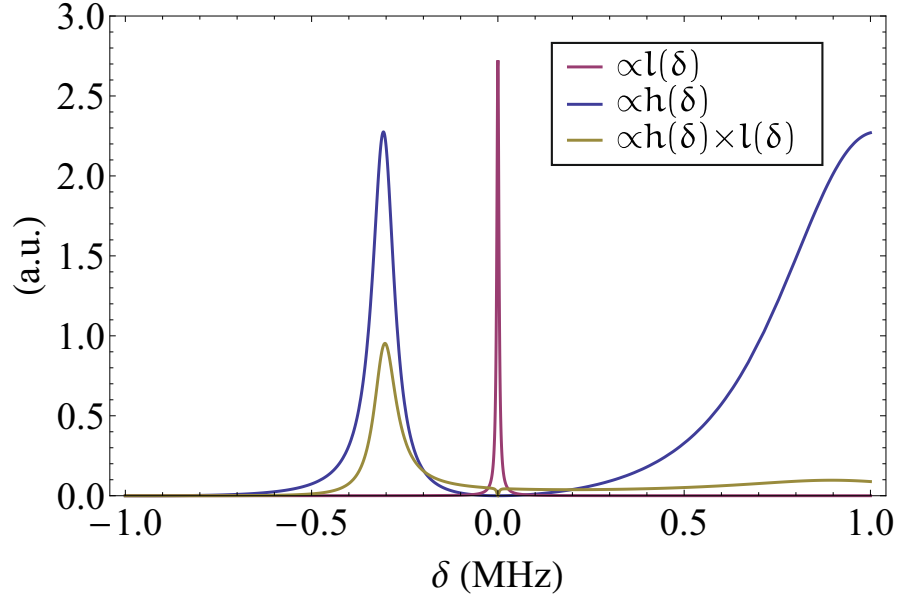


Figure 69: Double-EIT cooling noise estimation. The plot shows the detuning dependent noise induced carrier heating rate  $h(\delta)$ , the frequency distribution of a laser with Lorentzian noise with FWHM linewidth of 7 kHz  $l(\delta)$  as well as the product of the two, giving the frequency dependent contribution of the noise to the carrier heating rate. The cooling parameters were  $\Delta = 42$ ,  $\Gamma = 21$ ,  $\Omega_1 = 3$ ,  $\Omega_2 = 7$ ,  $\Omega_3 = 15$ ,  $\nu = 0.94$ , all MHz.

show white noise behavior at Fourier frequencies larger than 100 kHz. The threshold linewidth between lasers  $\Omega_1$  and  $\Omega_3$  follows equivalently by using the first order BSB heating, which is then not completely suppressed, given by

$$h_{\text{BSB}}(\delta) \approx \frac{\Omega_1^2 \Gamma \nu^2}{\left( \Gamma^2 \nu^2 + 4(\Omega_2^2/4 - \nu(\nu + \Delta) + \frac{\nu \Omega_3^2}{4(\Delta - \Delta_3 - \delta + \nu)}) \right)^2} \eta^2. \quad (140)$$



## A.4 DOUBLE-EIT COOLING HAMILTONIAN

The Hamiltonian used to simulate the full eight levels, three laser double-EIT dynamics (cf. Section 5.4.6) is given by:

$$\hat{H} = \hat{H}_a + \hat{H}_m + \hat{H}_i \quad (141)$$

$$\hat{H}_a = \hbar [\Delta_1 |S_{-1/2}\rangle \langle S_{-1/2}| + \Delta_2 |S_{+1/2}\rangle \langle S_{+1/2}| \quad (142)$$

$$+ (\Delta_2 - \Delta_1) |P_{+1/2}\rangle \langle P_{+1/2}| + \Delta_3 |D_{-3/2}\rangle \langle D_{-3/2}| \\ + (\Delta_2 - \Delta_1 + \Delta_3) |D_{-1/2}\rangle \langle D_{-1/2}| + \Delta_3 |D_{+1/2}\rangle \langle D_{+1/2}| \\ + (\Delta_2 - \Delta_1 + \Delta_3) |D_{+3/2}\rangle \langle D_{+3/2}|] \quad (143)$$

$$\hat{H}_m = \hbar \nu a^\dagger a \quad (144)$$

$$\hat{H}_i = \hbar \left[ \Omega_1/2 (|S_{-1/2}\rangle \langle P_{-1/2}| + |S_{+1/2}\rangle \langle P_{+1/2}|) e^{i\eta_1(\hat{a} + \hat{a}^\dagger)} + \right. \\ + \Omega_2/2 (|S_{+1/2}\rangle \langle P_{-1/2}|) e^{i\eta_2(\hat{a} + \hat{a}^\dagger)} \\ + \Omega_3/2 \left( |D_{-3/2}\rangle \langle P_{-1/2}| + \frac{1}{\sqrt{3}} |D_{-1/2}\rangle \langle P_{+1/2}| \right. \\ \left. + \frac{1}{\sqrt{3}} |D_{+1/2}\rangle \langle P_{-1/2}| + |D_{+3/2}\rangle \langle P_{+1/2}| \right) e^{i\eta_3(\hat{a} + \hat{a}^\dagger)} \left. \right] + \text{H.c.} \quad (145)$$

$\mathcal{K}$  is the Liouvillian describing the spontaneous decay of the two excited states and is given by [111]

$$\mathcal{K} = \mathcal{K}_- + \mathcal{K}_+ \quad (146)$$

$$\mathcal{K}_- = -\frac{\Gamma}{2} (|P_{-1/2}\rangle \langle P_{-1/2}| \tilde{\rho} + \tilde{\rho} |P_{-1/2}\rangle \langle P_{-1/2}|) \\ + \sum_{j=1}^6 \Gamma_j \int_{-1}^1 d \cos \phi \mathcal{N}(\cos \phi) |g_j\rangle \langle P_{-1/2}| e^{i\eta_j(\phi)(\hat{a} + \hat{a}^\dagger)} \\ \times \tilde{\rho} e^{-i\eta_j(\phi)(\hat{a} + \hat{a}^\dagger)} |P_{-1/2}\rangle \langle g_j| \quad (147)$$

$$\mathcal{K}_+ = -\frac{\Gamma}{2} (|P_{+1/2}\rangle \langle P_{+1/2}| \tilde{\rho} + \tilde{\rho} |P_{+1/2}\rangle \langle P_{+1/2}|) \\ + \sum_{j=1}^6 \Gamma_j \int_{-1}^1 d \cos \phi \mathcal{N}(\cos \phi) |g_j\rangle \langle P_{+1/2}| e^{i\eta_j(\phi)(\hat{a} + \hat{a}^\dagger)} \\ \times \tilde{\rho} e^{-i\eta_j(\phi)(\hat{a} + \hat{a}^\dagger)} |P_{+1/2}\rangle \langle g_j|. \quad (148)$$

Here,  $\Gamma$  is the total linewidth of the excited states and  $\Gamma_j$  the decay rates to the respective ground state  $|g_j\rangle$ .  $\eta_j(\phi)$  is the angle dependent Lamb-Dicke parameter for the decay to ground state  $j$  and  $\mathcal{N}(\cos \phi)$  describes the angular distribution of spontaneously emitted photons. In the simulations performed here, this integral was not implemented but an effective  $\eta_j$  of  $1/3$  of the maximal  $\eta$  for the respective transition was used. This is correct for isotropic emission and if no coherences between the motional states play a role.



## BIBLIOGRAPHY

---

- [1] D. Allan. Statistics of atomic frequency standards. *Proceedings of the IEEE*, 54(2):221–230, February 1966. doi: 10.1109/PROC.1966.4634. (Cited on page 9.)
- [2] D. Allan. Time and Frequency (Time-Domain) Characterization, Estimation, and Prediction of Precision Clocks and Oscillators. *IEEE Transactions on Ultrasonics, Ferroelectrics and Frequency Control*, 34(6):647–654, November 1987. doi: 10.1109/T-UFFC.1987.26997. (Cited on page 9.)
- [3] D. T. C. Allcock, L. Guidoni, T. P. Harty, C. J. Ballance, M. G. Blain, A. M. Steane, and D. M. Lucas. Reduction of heating rate in a microfabricated ion trap by pulsed-laser cleaning. *New J. Phys.*, 13(12):123023, December 2011. doi: 10.1088/1367-2630/13/12/123023. (Cited on page 115.)
- [4] D. T. C. Allcock, T. P. Harty, H. A. Janacek, N. M. Linke, C. J. Ballance, A. M. Steane, D. M. Lucas, R. L. Jarecki Jr., S. D. Habermehl, M. G. Blain, D. Stick, and D. L. Moehring. Heating rate and electrode charging measurements in a scalable, microfabricated, surface-electrode ion trap. *1105.4864*, May 2011. (Cited on page 115.)
- [5] S. Amairi. *A long optical cavity for sub-Hertz laser spectroscopy*. PhD thesis, Leibniz Universität Hannover, Hannover, 2014. in preparation. (Cited on page 90.)
- [6] S. Amairi, T. Legero, T. Kessler, U. Sterr, J. B. Wübbena, O. Mandel, and P. O. Schmidt. Reducing the effect of thermal noise in optical cavities. *Appl. Phys. B*, 113(2):233–242, May 2013. doi: 10.1007/s00340-013-5464-8. (Cited on page 90.)
- [7] A. André, A. Sørensen, and M. Lukin. Stability of Atomic Clocks Based on Entangled Atoms. *Phys. Rev. Lett.*, 92(23), June 2004. doi: 10.1103/PhysRevLett.92.230801. (Cited on page 126.)
- [8] C. Audoin and B. Guinot. *The Measurement of Time: Time, Frequency and the Atomic Clock*. Cambridge University Press, September 2001. ISBN 9780521003971. (Cited on page 3.)
- [9] H. Bateman and A. Erdelyi. *Higher Transcendental Functions, Vol. 3: Elliptic and Automorphic Functions, Lamé and Mathieu Functions*. McGraw Hill, New York, 1955. (Cited on page 19.)

- [10] J. Benhelm, G. Kirchmair, C. Roos, and R. Blatt. Experimental quantum-information processing with  $^{43}\text{Ca}^+$  ions. *Phys. Rev. A*, 77(6), June 2008. doi: 10.1103/PhysRevA.77.062306. (Cited on page 115.)
- [11] J. Benhelm. *Precision Spectroscopy and Quantum Information Processing with Trapped Calcium Ions*. PhD thesis, University of Innsbruck, 2008. (Cited on pages 71 and 87.)
- [12] E. Benkler, H. Telle, A. Zach, and F. Tauser. Circumvention of noise contributions in fiber laser based frequency combs. *Opt. Express*, 13(15):5662–5668, July 2005. doi: 10.1364/OPEX.13.005662. (Cited on page 92.)
- [13] D. J. Berkeland, J. D. Miller, J. C. Bergquist, W. M. Itano, and D. J. Wineland. Minimization of ion micromotion in a Paul trap. *J. Appl. Phys.*, 83(10):5025–5033, 1998. (Cited on pages 21, 22, 23, 79, 108, 125, 134, and 135.)
- [14] BIPM. *The international system of units (SI)*. International Bureau of Weights and Measures, 2006. (Cited on page 3.)
- [15] T. A. Birks, J. C. Knight, and P. S. Russell. Endlessly single-mode photonic crystal fiber. *Optics Letters*, 22(13):961–963, 1997. (Cited on page 86.)
- [16] B. J. Bloom, T. L. Nicholson, J. R. Williams, S. L. Campbell, M. Bishof, X. Zhang, W. Zhang, S. L. Bromley, and J. Ye. An optical lattice clock with accuracy and stability at the  $10^{-18}$  level. *Nature*, 506(7486):71–75, February 2014. doi: 10.1038/nature12941. (Cited on pages 4 and 127.)
- [17] R. Blümel, J. M. Chen, E. Peik, W. Quint, W. Schleich, Y. R. Shen, and H. Walther. Phase transitions of stored laser-cooled ions. *Nature*, 334(6180):309–313, July 1988. doi: 10.1038/334309a0. (Cited on page 59.)
- [18] R. Blümel, C. Kappler, W. Quint, and H. Walther. Chaos and order of laser-cooled ions in a Paul trap. *Phys. Rev. A*, 40(2): 808–823, July 1989. doi: 10.1103/PhysRevA.40.808. (Cited on pages 59 and 62.)
- [19] S. Boixo, A. Datta, M. Davis, S. Flammia, A. Shaji, and C. Caves. Quantum Metrology: Dynamics versus Entanglement. *Phys. Rev. Lett.*, 101(4), July 2008. doi: 10.1103/PhysRevLett.101.040403. (Cited on page 126.)
- [20] T. Brage, P. G. Judge, A. Aboussaid, M. R. Godefroid, P. Jönsson, A. Ynnerman, C. F. Fischer, and D. S. Leckrone. Hyperfine Induced Transitions as Diagnostics of Isotopic Composi-

- tion and Densities of Low-Density Plasmas. *The Astrophysical Journal*, 500:507, 1998. (Cited on page 11.)
- [21] I. Bronstein and G. Musiol. *Taschenbuch der Mathematik*. Deutsch, 2008. ISBN 9783817120079. (Cited on page 31.)
- [22] L. S. Brown and G. Gabrielse. Geonium theory: Physics of a single electron or ion in a Penning trap. *Rev. Mod. Phys.*, 58(1): 233, January 1986. doi: 10.1103/RevModPhys.58.233. (Cited on page 17.)
- [23] Z. Chen, J. G. Bohnet, J. M. Weiner, and J. K. Thompson. General formalism for evaluating the impact of phase noise on Bloch vector rotations. *Phys. Rev. A*, 86(3):032313, September 2012. doi: 10.1103/PhysRevA.86.032313. (Cited on page 96.)
- [24] C. W. Chou, D. B. Hume, J. C. J. Koelemeij, D. J. Wineland, and T. Rosenband. Frequency Comparison of Two High-Accuracy  $\text{Al}^+$  Optical Clocks. *Phys. Rev. Lett.*, 104(7):070802, February 2010. doi: 10.1103/PhysRevLett.104.070802. (Cited on pages 4, 12, 23, 63, 101, 114, 115, and 127.)
- [25] M. Chwalla. *Precision spectroscopy with  $^{40}\text{Ca}^+$  ions in a Paul trap*. PhD thesis, University of Innsbruck, 2009. (Cited on pages 71 and 90.)
- [26] J. I. Cirac and P. Zoller. Quantum Computations with Cold Trapped Ions. *Phys. Rev. Lett.*, 74(20):4091–4094, May 1995. doi: 10.1103/PhysRevLett.74.4091. (Cited on pages 23 and 112.)
- [27] J. I. Cirac, R. Blatt, P. Zoller, and W. D. Phillips. Laser cooling of trapped ions in a standing wave. *Physical Review A*, 46(5): 2668–2681, 1992. (Cited on page 41.)
- [28] J. I. Cirac, L. J. Garay, R. Blatt, A. S. Parkins, and P. Zoller. Laser cooling of trapped ions: The influence of micromotion. *Physical Review A*, 49(1):421–432, 1994. (Cited on page 108.)
- [29] A. Clairon, C. Salomon, S. Guellati, and W. D. Phillips. Ramsey Resonance in a Zacharias Fountain. *EPL*, 16(2):165, September 1991. doi: 10.1209/0295-5075/16/2/008. (Cited on page 4.)
- [30] C. R. Clark, J. E. Goeders, Y. K. Dodia, C. R. Viteri, and K. R. Brown. Detection of single-ion spectra by Coulomb-crystal heating. *Phys. Rev. A*, 81(4):043428, April 2010. doi: 10.1103/PhysRevA.81.043428. (Cited on page 23.)
- [31] C. Cohen-Tannoudji, J. Dupont-Roc, and G. Grynberg. *Atom-Photon Interactions: Basic Processes and Applications*. A Wiley-Interscience publication. Wiley, 1998. ISBN 9780471293361. (Cited on page 41.)

- [32] C. Cohen-Tannoudji, B. Diu, and F. Laloe. *Quantenmechanik*. Quantenmechanik. De Gruyter, 2007. ISBN 9783110193244. (Cited on page 30.)
- [33] R. J. Cook, D. G. Shankland, and A. L. Wells. Quantum theory of particle motion in a rapidly oscillating field. *Phys. Rev. A*, 31(2):564, February 1985. doi: 10.1103/PhysRevA.31.564. (Cited on page 27.)
- [34] H. G. Dehmelt. Radiofrequency Spectroscopy of Stored Ions I: Storage\*. *Advances in Atomic and Molecular Physics*, 3:53–72, 1968. (Cited on page 22.)
- [35] H. Dehmelt. Proposed  $10^{14}$  laser fluorescence spectroscopy on  $\text{Ti}^+$  mono-ion oscillator II (spontaneous quantum jumps). *Bull. Am. Phys. Soc*, 20:60, 1975. (Cited on page 10.)
- [36] H. Dehmelt. Monoion oscillator as potential ultimate laser frequency standard. *IEEE Transactions on Instrumentation and Measurement*, IM-31(2):83–87, June 1982. doi: 10.1109/TIM.1982.6312526. (Cited on page 10.)
- [37] L. Deslauriers, P. Haljan, P. Lee, K.-A. Brickman, B. Blinov, M. Madsen, and C. Monroe. Zero-point cooling and low heating of trapped  $^{111}\text{Cd}^+$  ions. *Phys. Rev. A*, 70(4), October 2004. doi: 10.1103/PhysRevA.70.043408. (Cited on page 115.)
- [38] L. Deslauriers, S. Olmschenk, D. Stick, W. Hensinger, J. Sterk, and C. Monroe. Scaling and Suppression of Anomalous Heating in Ion Traps. *Phys. Rev. Lett.*, 97(10):103007, September 2006. doi: 10.1103/PhysRevLett.97.103007. (Cited on page 115.)
- [39] R. G. DeVoe, J. Hoffnagle, and R. G. Brewer. Role of laser damping in trapped ion crystals. *Phys. Rev. A*, 39(9):4362–4365, May 1989. doi: 10.1103/PhysRevA.39.4362. (Cited on page 109.)
- [40] G. J. Dick. Local Oscillator Induced Instabilities in Trapped Ion Frequency Standards. In *Proc. 19th Annual Precise Time and Time Interval (PTTI) Application and Planning Meeting*, page 133, 1988. (Cited on page 59.)
- [41] S. A. Diddams, D. J. Jones, J. Ye, S. T. Cundiff, J. L. Hall, J. K. Ranka, R. S. Windeler, R. Holzwarth, T. Udem, and T. W. Hänsch. Direct link between microwave and optical frequencies with a 300 THz femtosecond laser comb. *Physical Review Letters*, 84(22):5102–5105, 2000. (Cited on page 8.)
- [42] F. Diedrich, J. C. Bergquist, W. M. Itano, and D. J. Wineland. Laser cooling to the zero-point energy of motion. *Physical Review Letters*, 62(4):403–406, 1989. (Cited on pages 39 and 40.)

- [43] E. Dobrovinskaya, L. Lytvynov, and V. Pishchik. *Sapphire: Material, Manufacturing, Applications*. Micro- and Opto-Electronic Materials, Structures, and Systems. Springer, 2009. ISBN 9780387856957. (Cited on page 71.)
- [44] M. Drewsen, I. S. Jensen, N. Kjærgaard, J. Lindballe, A. Mortensen, K. Mølhave, and D. Voigt. Non-stationary Coulomb crystals in linear Paul traps. *J. Phys. B*, 36(3):525, 2003. (Cited on page 63.)
- [45] S. Droste, F. Ozimek, T. Udem, K. Predehl, T. W. Hänsch, H. Schnatz, G. Grosche, and R. Holzwarth. Optical-Frequency Transfer over a Single-Span 1840 km Fiber Link. *Phys. Rev. Lett.*, 111(11), September 2013. doi: 10.1103/PhysRevLett.111.110801. (Cited on page 91.)
- [46] P. Dube, A. A. Madej, Z. Zhou, and J. E. Bernard. Evaluation of systematic shifts of the  $^{88}\text{Sr}^+$  single-ion optical frequency standard at the  $10^{-17}$  level. *Phys. Rev. A*, 87(2):023806, February 2013. doi: 10.1103/PhysRevA.87.023806. (Cited on pages 4 and 127.)
- [47] R. Dubessy, T. Coudreau, and L. Guidoni. Electric field noise above surfaces: A model for heating-rate scaling law in ion traps. *Phys. Rev. A*, 80(3), September 2009. doi: 10.1103/PhysRevA.80.031402. (Cited on page 115.)
- [48] S. Earnshaw. On the nature of the molecular forces which regulate the constitution of the luminiferous ether. *Transactions of the Cambridge Philosophical Society*, 7(1), 1833. (Cited on page 17.)
- [49] A. M. Eltony. *Sensitive, 3D micromotion compensation in a surface-electrode ion trap*. Thesis, Massachusetts Institute of Technology, 2013. Thesis (S.M.)—Massachusetts Institute of Technology, Dept. of Electrical Engineering and Computer Science, 2013. (Cited on page 109.)
- [50] R. Epstein, S. Seidelin, D. Leibfried, J. Wesenberg, J. Bollinger, J. Amini, R. Blakestad, J. Britton, J. Home, W. Itano, J. Jost, E. Knill, C. Langer, R. Ozeri, N. Shiga, and D. Wineland. Simplified motional heating rate measurements of trapped ions. *Phys. Rev. A*, 76(3), September 2007. doi: 10.1103/PhysRevA.76.033411. (Cited on page 115.)
- [51] L. Essen and J. V. L. Parry. An Atomic Standard of Frequency and Time Interval: A Cæsium Resonator. *Nature*, 176(4476):280–282, August 1955. doi: 10.1038/176280a0. (Cited on pages 3 and 4.)
- [52] J. Evers and C. H. Keitel. Double-EIT ground-state laser cooling without blue-sideband heating. *EPL*, 68(3):370, November

2004. doi: 10.1209/epl/i2004-10207-5. (Cited on pages 41, 45, 46, and 51.)
- [53] U. Fano. Effects of Configuration Interaction on Intensities and Phase Shifts. *Phys. Rev.*, 124(6):1866–1878, December 1961. doi: 10.1103/PhysRev.124.1866. (Cited on page 43.)
- [54] C. F. Fischer and M. Godefroid. Lifetime trends for the  $n=3$  singlet states in the Mg sequence. *Nuclear Instruments and Methods in Physics Research*, 202(1–2):307–322, November 1982. doi: 10.1016/0167-5087(82)90411-2. (Cited on page 11.)
- [55] C. Foot. *Atomic Physics*. Oxford Master Series in Physics. OUP Oxford, 2005. ISBN 9780198506966. (Cited on page 30.)
- [56] P. Forman. Atomichron: The atomic clock from concept to commercial product. *Proceedings of the IEEE*, 73(7):1181–1204, July 1985. doi: 10.1109/PROC.1985.13266. (Cited on page 4.)
- [57] A. Franzen. ComponentLibrary, 2009. "http://www.gwoptics.org/ComponentLibrary/". Changes were made. Published according to "http://creativecommons.org/licenses/by-nc/3.0/". (Cited on pages 82, 83, 84, and 85.)
- [58] H. R. Gray, R. M. Whitley, and C. R. Stroud. Coherent trapping of atomic populations. *Opt. Lett.*, 3(6):218–220, December 1978. doi: 10.1364/OL.3.000218. (Cited on page 43.)
- [59] G. Grosche. Eavesdropping time and frequency: phase noise cancellation along a time-varying path, such as an optical fiber. *arXiv:1309.0728 [physics]*, September 2013. (Cited on page 91.)
- [60] S. Gulde. *Experimental realization of quantum gates and the Deutsch-Josza algorithm with trapped  $^{40}\text{Ca}^+$  ions*. PhD thesis, University of Innsbruck, 2003. (Cited on pages 71, 112, 113, 114, and 120.)
- [61] H. Häffner, C. F. Roos, and R. Blatt. Quantum computing with trapped ions. *Physics Reports*, 469(4):155–203, December 2008. doi: 10.1016/j.physrep.2008.09.003. (Cited on page 23.)
- [62] C. Hagemann, C. Grebing, T. Kessler, S. Falke, N. Lemke, C. Lisdat, H. Schnatz, F. Riehle, and U. Sterr. Providing Short-Term Stability of a 1.5  $\mu\text{m}$  Laser to Optical Clocks. *IEEE Trans. Instrum. Meas.*, 62(6):1556–1562, 2013. doi: 10.1109/TIM.2013.2242597. (Cited on pages 91 and 97.)
- [63] J. Hall. Nobel Lecture: Defining and measuring optical frequencies. *Rev. Mod. Phys.*, 78(4):1279–1295, November 2006. doi: 10.1103/RevModPhys.78.1279. (Cited on page 89.)



- [64] T. Hänsch. Nobel Lecture: Passion for precision. *Rev. Mod. Phys.*, 78(4):1297–1309, November 2006. doi: 10.1103/RevModPhys.78.1297. (Cited on page 89.)
- [65] J. E. Hatch. *Aluminum: Properties and Physical Metallurgy*. ASM International, January 1984. ISBN 9781615031696. (Cited on page 68.)
- [66] B. Hemmerling. *Towards Direct Frequency Comb Spectroscopy using Quantum Logic*. PhD thesis, Hannover, 2011. (Cited on pages 71, 78, 87, and 115.)
- [67] N. Herschbach, K. Pyka, J. Keller, and T. E. Mehlstäubler. Linear Paul trap design for an optical clock with Coulomb crystals. *Appl. Phys. B*, 107(4):891–906, June 2012. doi: 10.1007/s00340-011-4790-y. (Cited on page 126.)
- [68] K. Higgins, D. Miner, C. Smith, and D. Sullivan. A Walk Through Time (version 1.2.1), 2010. (Cited on page 3.)
- [69] R. Holzwarth, T. Udem, T. W. Hänsch, J. C. Knight, W. J. Wadsworth, and P. S. J. Russell. Optical Frequency Synthesizer for Precision Spectroscopy. *Phys. Rev. Lett.*, 85(11):2264–2267, September 2000. doi: 10.1103/PhysRevLett.85.2264. (Cited on page 90.)
- [70] J. Home. *Entanglement of two trapped-ion spin qubits*. PhD thesis, University of Oxford, 2006. (Cited on page 115.)
- [71] G. Huber. *Quantum Thermodynamics with Trapped Ions*. PhD thesis, Ulm, 2010. (Cited on pages 112, 113, 114, and 120.)
- [72] S. F. Huelga, C. Macchiavello, T. Pellizzari, A. K. Ekert, M. B. Plenio, and J. I. Cirac. Improvement of frequency standards with quantum entanglement. *Physical Review Letters*, 79(20):3865–3868, 1997. (Cited on page 126.)
- [73] N. Huntemann, M. Okhapkin, B. Lipphardt, S. Weyers, C. Tamm, and E. Peik. High-Accuracy Optical Clock Based on the Octupole Transition in  $^{171}\text{Yb}^+$ . *Phys. Rev. Lett.*, 108(9):090801, February 2012. doi: 10.1103/PhysRevLett.108.090801. (Cited on pages 4 and 127.)
- [74] Y. Ibaraki, U. Tanaka, and S. Urabe. Detection of parametric resonance of trapped ions for micromotion compensation. *Appl. Phys. B*, 105(2):219–223, November 2011. doi: 10.1007/s00340-011-4463-x. (Cited on page 109.)
- [75] W. M. Itano, J. C. Bergquist, J. J. Bollinger, J. M. Gilligan, D. J. Heinzen, F. L. Moore, M. G. Raizen, and D. J. Wineland. Quantum projection noise: Population fluctuations in two-level systems. *Phys. Rev. A*, 47(5):3554–3570, 1993. (Cited on page 103.)

- [76] D. F. V. James. Quantum dynamics of cold trapped ions with application to quantum computation. *Appl. Phys. B*, 66:181–190, 1998. (Cited on pages 23, 24, 34, and 135.)
- [77] G. Janik, W. Nagourney, and H. Dehmelt. Doppler-free optical spectroscopy on the  $\text{Ba}^+$  mono-ion oscillator. *J. Opt. Soc. Am. B*, 2(8):1251–1257, 1985. doi: 10.1364/JOSAB.2.001251. (Cited on page 42.)
- [78] J. Javanainen, M. Lindberg, and S. Stenholm. Laser cooling of trapped ions: dynamics of the final stages. *Journal of the Optical Society of America B*, 1(1):111–115, 1984. (Cited on page 36.)
- [79] J. Jin and D. A. Church. Precision lifetimes for the  $\text{Ca}^+$   $4p^2P$  levels: Experiment challenges theory at the 1% level. *Phys. Rev. Lett.*, 70(21):3213, May 1993. doi: 10.1103/PhysRevLett.70.3213. (Cited on page 103.)
- [80] D. J. Jones, S. A. Diddams, J. K. Ranka, A. Stentz, R. S. Windeler, J. L. Hall, and S. T. Cundiff. Carrier-envelope phase control of femtosecond mode-locked lasers and direct optical frequency synthesis. *Science*, 288(5466):635, 2000. (Cited on pages 8 and 90.)
- [81] W. T. B. Kelvin and P. G. Tait. *Elements of Natural Philosophy*. University Press, 1879. (Cited on page 4.)
- [82] T. Kessler, C. Hagemann, C. Grebing, T. Legero, U. Sterr, F. Riehle, M. J. Martin, L. Chen, and J. Ye. A sub-40-mHz-linewidth laser based on a silicon single-crystal optical cavity. *Nat Photon*, 6:687–692, 2012. doi: 10.1038/nphoton.2012.217. (Cited on page 90.)
- [83] D. Kielpinski, B. E. King, C. J. Myatt, C. A. Sackett, Q. A. Turchette, W. M. Itano, C. Monroe, D. J. Wineland, and W. H. Zurek. Sympathetic cooling of trapped ions for quantum logic. *Phys. Rev. A*, 61(3):32310, 2000. (Cited on pages 24, 25, and 54.)
- [84] D. Kielpinski, C. Monroe, and D. J. Wineland. Architecture for a large-scale ion-trap quantum computer. *Nature*, 417(6890):709–711, June 2002. doi: 10.1038/nature00784. (Cited on pages 22 and 23.)
- [85] S. A. King, R. M. Godun, S. A. Webster, H. S. Margolis, L. A. M. Johnson, K. Szymaniec, P. E. G. Baird, and P. Gill. Absolute frequency measurement of the  $^2S_{1/2}$ - $^2F_{7/2}$  electric octupole transition in a single ion of  $^{171}\text{Yb}^+$  with  $10^{-15}$  fractional uncertainty. *New Journal of Physics*, 14(1):013045, January 2012. doi: 10.1088/1367-2630/14/1/013045. (Cited on page 4.)

- [86] J. C. Knight, T. A. Birks, R. F. Cregan, P. S. J. Russell, and J. P. de Sandro. Photonic crystals as optical fibres – physics and applications. *Optical Materials*, 11(2–3):143–151, January 1999. doi: 10.1016/S0925-3467(98)00040-8. (Cited on page 86.)
- [87] P. Kubina, P. Adel, F. Adler, G. Grosche, T. Hänsch, R. Holzwarth, A. Leitenstorfer, B. Lipphardt, and H. Schnatz. Long term comparison of two fiber based frequency comb systems. *Optics express*, 13(3):904–909, 2005. (Cited on page 90.)
- [88] J. Labaziewicz, Y. Ge, D. Leibbrandt, S. Wang, R. Shewmon, and I. Chuang. Temperature Dependence of Electric Field Noise above Gold Surfaces. *Phys. Rev. Lett.*, 101(18), October 2008. doi: 10.1103/PhysRevLett.101.180602. (Cited on page 115.)
- [89] L. Landau and E. Lifshitz. *Atomic and Molecular Frequency References*, pages 93–95. Pergamon, New York, 1976. (Cited on page 135.)
- [90] L. Landau and E. Lifshitz. *Mechanics*. Butterworth Heinemann. Butterworth-Heinemann, 1976. ISBN 9780750628969. (Cited on page 18.)
- [91] D. J. Larson, J. C. Bergquist, J. J. Bollinger, W. M. Itano, and D. J. Wineland. Sympathetic cooling of trapped ions: A laser-cooled two-species nonneutral ion plasma. *Phys. Rev. Lett.*, 57(1):70, July 1986. doi: 10.1103/PhysRevLett.57.70. (Cited on page 11.)
- [92] D. Leibfried, R. Blatt, C. Monroe, and D. J. Wineland. Quantum dynamics of single trapped ions. *Rev. Mod. Phys.*, 75:281–324, 2003. (Cited on page 28.)
- [93] M. A. Levine, R. E. Marrs, J. R. Henderson, D. A. Knapp, and M. B. Schneider. The Electron Beam Ion Trap: A New Instrument for Atomic Physics Measurements. *Phys. Scr.*, 1988 (T22):157, January 1988. doi: 10.1088/0031-8949/1988/T22/024. (Cited on page 17.)
- [94] Y. Lin, J. P. Gaebler, T. R. Tan, R. Bowler, J. D. Jost, D. Leibfried, and D. J. Wineland. Sympathetic Electromagnetically-Induced-Transparency Laser Cooling of Motional Modes in an Ion Chain. *Phys. Rev. Lett.*, 110(15):153002, April 2013. doi: 10.1103/PhysRevLett.110.153002. (Cited on pages 5, 41, and 118.)
- [95] B. Lounis and C. Cohen-Tannoudji. Coherent population trapping and Fano profiles. *Journal de Physique II*, 2(4):579–592, April 1992. doi: 10.1051/jp2:1992153. (Cited on page 43.)
- [96] W. W. Macalpine and R. O. Schildknecht. Coaxial resonators with helical inner conductor. *Proceedings of the IRE*, 47(12): 2099–2105, 1959. (Cited on page 77.)

- [97] F. G. Major, V. N. Gheorghie, and G. Werth. *Charged particle traps: physics and techniques of charged particle field confinement*, volume 37. Springer, 2006. (Cited on pages 19 and 21.)
- [98] M. Marcianti, C. Champenois, A. Calisti, J. Pedregosa-Gutierrez, and M. Knoop. Ion dynamics in a linear radio-frequency trap with a single cooling laser. *Phys. Rev. A*, 82: 033406, Sep 2010. doi: 10.1103/PhysRevA.82.033406. (Cited on page 60.)
- [99] I. Marzoli, J. I. Cirac, R. Blatt, and P. Zoller. Laser cooling of trapped three-level ions: designing two-level systems for side-band cooling. *Physical Review A*, 49(4):2771–2779, 1994. (Cited on page 40.)
- [100] M. Matsumoto and T. Nishimura. Mersenne Twister: A 623-dimensionally equidistributed uniform pseudorandom number generator. *ACM Trans. Model. Comput. Simul.*, 8(1):3–30, 1998. (Cited on page 60.)
- [101] J. C. Maxwell. *A Treatise on Electricity and Magnetism*. Clarendon Press, 1873. (Cited on page 4.)
- [102] R. J. Mears, L. Reekie, I. M. Jauncey, and D. N. Payne. Low-noise erbium-doped fibre amplifier operating at 1.54 $\mu\text{m}$ . *Electronics Letters*, 23(19):1026–1028(2), September 1987. (Cited on page 90.)
- [103] H. Metcalf and P. van der Straten. *Laser Cooling and Trapping*. Graduate Texts in Contemporary Physics. Springer New York, 1999. ISBN 9780387987286. (Cited on page 35.)
- [104] T. Middelmann, S. Falke, C. Lisdat, and U. Sterr. High Accuracy Correction of Blackbody Radiation Shift in an Optical Lattice Clock. *Phys. Rev. Lett.*, 109(26):263004, December 2012. doi: 10.1103/PhysRevLett.109.263004. (Cited on pages 127 and 128.)
- [105] J. Millo, M. Abgrall, M. Lours, E. M. L. English, H. Jiang, J. Guena, A. Clairon, M. E. Tobar, S. Bize, Y. Le Coq, and G. Santarelli. Ultralow noise microwave generation with fiber-based optical frequency comb and application to atomic fountain clock. *Appl. Phys. Lett.*, 94(14):141105, 2009. doi: 10.1063/1.3112574. (Cited on page 91.)
- [106] I. M. Mills, P. J. Mohr, T. J. Quinn, B. N. Taylor, and E. R. Williams. Adapting the International System of Units to the twenty-first century. *Phil. Trans. R. Soc. A*, 369(1953):3907–3924, October 2011. doi: 10.1098/rsta.2011.0180. PMID: 21930556. (Cited on page 4.)

- [107] I. Mills, T. Quinn, and B. Taylor. Draft Chapter 2 for SI Brochure, following redefinitions of the base units. *CCU Report*, 27th September, 2010. (Cited on page 4.)
- [108] J. Mitroy, J. Zhang, M. Bromley, and K. Rollin. Blackbody radiation shift of the Al clock transition. *Eur. Phys. J. D*, 53(1):5, 2009. doi: 10.1140/epjd/e2009-00098-4. (Cited on page 4.)
- [109] J. Mollá, R. Heidinger, and A. Ibarra. Alumina ceramics for heating systems. *Journal of Nuclear Materials*, 212–215, Part B: 1029–1034, September 1994. doi: 10.1016/0022-3115(94)90989-X. (Cited on page 71.)
- [110] G. Morigi, J. Eschner, and C. H. Keitel. Ground state laser cooling using electromagnetically induced transparency. *Physical Review Letters*, 85(21):4458–4461, 2000. (Cited on pages 5, 41, 44, and 45.)
- [111] G. Morigi. Cooling atomic motion with quantum interference. *Phys. Rev. A*, 67(3):033402, March 2003. doi: 10.1103/PhysRevA.67.033402. (Cited on pages 41, 43, 49, and 139.)
- [112] F. R. Moulton. *An Introduction to Celestial Mechanics*. Courier Dover Publications, April 2012. ISBN 9780486140681. (Cited on page 3.)
- [113] W. Nagourney, J. Sandberg, and H. Dehmelt. Shelved optical electron amplifier: Observation of quantum jumps. *Phys. Rev. Lett.*, 56(26):2797–2799, June 1986. doi: 10.1103/PhysRevLett.56.2797. Copyright (1986) by the American Physical Society. <http://journals.aps.org/prl/abstract/10.1103/PhysRevLett.56.2797>. (Cited on page 10.)
- [114] W. Neuhauser, M. Hohenstatt, P. Toschek, and H. Dehmelt. Optical-sideband cooling of visible atom cloud confined in parabolic well. *Physical Review Letters*, 41(4):233–236, 1978. (Cited on pages 5, 35, and 37.)
- [115] N. R. Newbury and W. C. Swann. Low-noise fiber-laser frequency combs (Invited). *J. Opt. Soc. Am. B*, 24(8):1756–1770, August 2007. doi: 10.1364/JOSAB.24.001756. (Cited on page 92.)
- [116] J. W. Nicholson, M. F. Yan, P. Wisk, J. Fleming, F. DiMarcello, E. Monberg, A. Yablon, C. Jørgensen, and T. Veng. All-fiber, octave-spanning supercontinuum. *Opt. Lett.*, 28(8):643–645, April 2003. doi: 10.1364/OL.28.000643. (Cited on page 90.)
- [117] J. W. Nicholson, P. S. Westbrook, K. S. Feder, and A. D. Yablon. Supercontinuum generation in ultraviolet-irradiated fibers. *Opt. Lett.*, 29(20):2363–2365, October 2004. doi: 10.1364/OL.29.002363. (Cited on page 90.)

- [118] D. Nicolodi, B. Argence, W. Zhang, R. Le Targat, G. Santarelli, and Y. Le Coq. Spectral purity transfer between optical wavelengths at the  $10^{-18}$  level. *Nat Photon*, 8(3):219–223, March 2014. doi: 10.1038/nphoton.2013.361. (Cited on pages 91 and 97.)
- [119] X. R. Nie, C. F. Roos, and D. F. James. Theory of cross phase modulation for the vibrational modes of trapped ions. *Phys. Lett. A*, 373(4):422–425, January 2009. doi: 10.1016/j.physleta.2008.11.045. (Cited on pages 23 and 25.)
- [120] F. W. J. Olver, D. W. Lozier, R. F. Boisvert, and C. W. Clark, editors. *NIST Handbook of Mathematical Functions*. Cambridge University Press, New York, NY, 2010. (Cited on page 19.)
- [121] W. Oskay, S. Diddams, E. Donley, T. Fortier, T. Heavner, L. Hollberg, W. Itano, S. Jefferts, M. Delaney, K. Kim, F. Levi, T. Parker, and J. Bergquist. Single-Atom Optical Clock with High Accuracy. *Phys. Rev. Lett.*, 97(2):020801, July 2006. doi: 10.1103/PhysRevLett.97.020801. (Cited on page 4.)
- [122] W. Paul and M. Raether. Das elektrische Massenfilter. *Zeitschrift für Physik A Hadrons and Nuclei*, 140(3):262–273, May 1955. doi: 10.1007/BF01328923. (Cited on page 18.)
- [123] W. Paul, O. Osberghaus, and E. Fischer. Ein Ionenkäfig. *Forschungsberichte Wirtschafts-und Verkehrsministerium Nordrhein-Westfalen, Westdeutscher Verlag, Köln und Opladen*, 1958. (Cited on page 18.)
- [124] E. Peik, J. Abel, T. Becker, J. von Zanthier, and H. Walther. Sideband cooling of ions in radio-frequency traps. *Physical Review A*, 60(1):439–449, 1999. (Cited on page 108.)
- [125] E. Peik, T. Schneider, and C. Tamm. Laser frequency stabilization to a single ion. *J. Phys. B*, 39(1):145–158, January 2006. doi: 10.1088/0953-4075/39/1/012. (Cited on page 59.)
- [126] F. Penning. Die Glimmentladung bei niedrigem Druck zwischen koaxialen Zylindern in einem axialen Magnetfeld. *Physica*, 3(9):873–894, November 1936. doi: 10.1016/S0031-8914(36)80313-9. (Cited on page 17.)
- [127] P. T. T. Pham. *A general-purpose pulse sequencer for quantum computing*. Master thesis, MIT, Boston, USA, 2005. (Cited on page 87.)
- [128] G. Poulsen, Y. Miroshnychenko, and M. Drewsen. Efficient ground-state cooling of an ion in a large room-temperature linear Paul trap with a sub-Hertz heating rate. *Phys. Rev. A*, 86(5):051402, November 2012. doi: 10.1103/PhysRevA.86.051402. (Cited on page 115.)

- [129] G. Poulsen. *Sideband Cooling of Atomic and Molecular Ions*. PhD thesis, University of Aarhus, 2011. (Cited on page 29.)
- [130] K. Predehl, G. Grosche, S. M. F. Raupach, S. Droste, O. Terra, J. Alnis, T. Legero, T. W. Hänsch, T. Udem, R. Holzwarth, and H. Schnatz. A 920-Kilometer Optical Fiber Link for Frequency Metrology at the 19th Decimal Place. *Science*, 336(6080):441–444, April 2012. doi: 10.1126/science.1218442. (Cited on page 91.)
- [131] T. Pruttivarasin, M. Ramm, and H. Häffner. Direct spectroscopy of the  $^2S_{1/2} \rightarrow ^2P_{1/2}$  and  $^2D_{3/2} \rightarrow ^2P_{1/2}$  transitions and observation of micromotion modulated spectra in trapped  $\text{Ca}^+$ . *arXiv:1312.7617 [physics, physics:quant-ph]*, December 2013. (Cited on page 102.)
- [132] Ptolemy and G. J. Toomer. *Ptolemy's Almagest*. Princeton University Press, 1998. ISBN 9780691002606. (Cited on page 3.)
- [133] K. Pyka. *High-precision ion trap for spectroscopy of Coulomb crystals*. PhD thesis, Leibniz Universität Hannover, Hannover, 2013. (Cited on pages 78 and 126.)
- [134] K. Pyka, N. Herschbach, J. Keller, and T. E. Mehlstäubler. A high-precision segmented Paul trap with minimized micromotion for an optical multiple-ion clock. *Appl. Phys. B*, pages 1–11, 2013. doi: 10.1007/s00340-013-5580-5. (Cited on pages 4 and 126.)
- [135] R. Rafac, J. P. Schiffer, J. S. Hangst, D. H. Dubin, and D. J. Wales. Stable configurations of confined cold ionic systems. *Proceedings of the National Academy of Sciences*, 88(2):483–486, January 1991. (Cited on page 26.)
- [136] M. G. Raizen, J. M. Gilligan, J. C. Bergquist, W. M. Itano, and D. J. Wineland. Linear Trap for High-accuracy Spectroscopy of Stored Ions. *J. Mod. Opt.*, 39(2):233, 1992. doi: 10.1080/09500349214550241. (Cited on page 19.)
- [137] M. Ramm, T. Pruttivarasin, M. Kokish, I. Talukdar, and H. Häffner. Precision Measurement Method for Branching Fractions of Excited  $P_{1/2}$  States Applied to  $^{40}\text{Ca}^+$ . *Phys. Rev. Lett.*, 111(2):023004, July 2013. doi: 10.1103/PhysRevLett.111.023004. (Cited on page 38.)
- [138] J. Reichert, M. Niering, R. Holzwarth, M. Weitz, T. Udem, and T. W. Hänsch. Phase coherent vacuum-ultraviolet to radio frequency comparison with a mode-locked laser. *Physical Review Letters*, 84(15):3232–3235, 2000. (Cited on page 8.)

- [139] A. Retzker and M. B. Plenio. Fast cooling of trapped ions using the dynamical Stark shift. *New J. Phys.*, 9(8):279–279, August 2007. doi: 10.1088/1367-2630/9/8/279. (Cited on page 41.)
- [140] M. Riebe. *Preparation of entangled states and quantum teleportation with atomic qubits*. PhD, University of Innsbruck, 2005. (Cited on page 71.)
- [141] F. Riehle. *Frequency standards: basics and applications*. Wiley-VCH, Weinheim, 2004. ISBN 9783527402304. (Cited on pages 4, 7, 9, and 55.)
- [142] H. Rohde, S. T. Gulde, C. F. Roos, P. A. Barton, D. Leibfried, J. Eschner, F. Schmidt-Kaler, and R. Blatt. Sympathetic ground-state cooling and coherent manipulation with two-ion crystals. *J. Opt. B: Quantum Semiclass. Opt.*, 3:S34, 2001. (Cited on pages 39 and 115.)
- [143] C. Roos. *Controlling the quantum state of trapped ions*. PhD thesis, University of Innsbruck, 2000. (Cited on pages 112, 114, and 120.)
- [144] C. F. Roos, D. Leibfried, A. Mundt, F. Schmidt-Kaler, J. Eschner, and R. Blatt. Experimental demonstration of ground state laser cooling with electromagnetically induced transparency. *Physical Review Letters*, 85(26):5547–5550, 2000. (Cited on pages 5, 41, 48, 118, and 119.)
- [145] C. Roos, T. Zeiger, H. Rohde, H. C. Nägerl, J. Eschner, D. Leibfried, F. Schmidt-Kaler, and R. Blatt. Quantum State Engineering on an Optical Transition and Decoherence in a Paul Trap. *Phys. Rev. Lett.*, 83(23):4713–4716, December 1999. doi: 10.1103/PhysRevLett.83.4713. (Cited on pages 40, 113, 115, and 116.)
- [146] T. Rosenband, W. Itano, P. O. Schmidt, D. B. Hume, J. C. J. Koelemeij, J. Bergquist, and D. Wineland. Blackbody radiation shift of the  $^{27}\text{Al}^+ \ ^1\text{S}_0 \rightarrow \ ^3\text{P}_0$  transition. In *Frequency and Time Forum (EFTF), 2006 20th European*, pages 289–292, March 2006. (Cited on pages 4, 77, and 128.)
- [147] T. Rosenband, P. O. Schmidt, D. B. Hume, W. M. Itano, T. M. Fortier, J. E. Stalnaker, K. Kim, S. A. Diddams, J. C. J. Koelemeij, J. C. Bergquist, and D. J. Wineland. Observation of the  $^1\text{S}_0 \rightarrow \ ^3\text{P}_0$  Clock Transition in  $^{27}\text{Al}^+$ . *Phys. Rev. Lett.*, 98(22):220801, May 2007. doi: 10.1103/PhysRevLett.98.220801. (Cited on page 11.)
- [148] T. Rosenband, D. B. Hume, P. O. Schmidt, C. W. Chou, A. Brusch, L. Lorini, W. H. Oskay, R. E. Drullinger, T. M. Fortier, J. E.



- Stalnaker, S. A. Diddams, W. C. Swann, N. R. Newbury, W. M. Itano, D. J. Wineland, and J. C. Bergquist. Frequency Ratio of  $\text{Al}^+$  and  $\text{Hg}^+$  Single-Ion Optical Clocks; Metrology at the 17th Decimal Place. *Science*, 319(5871):1808–1812, March 2008. doi: 10.1126/science.1154622. PMID: 18323415. (Cited on pages 4, 12, 23, 62, 63, 101, 114, and 115.)
- [149] S. Roy and S. Braunstein. Exponentially Enhanced Quantum Metrology. *Phys. Rev. Lett.*, 100(22), June 2008. doi: 10.1103/PhysRevLett.100.220501. (Cited on page 126.)
- [150] P. Russell. Photonic Crystal Fibers. *Science*, 299(5605):358–362, January 2003. doi: 10.1126/science.1079280. (Cited on page 86.)
- [151] M. S. Safronova, M. G. Kozlov, and C. W. Clark. Precision Calculation of Blackbody Radiation Shifts for Optical Frequency Metrology. *Phys. Rev. Lett.*, 107(14):143006, 2011. doi: 10.1103/PhysRevLett.107.143006. (Cited on page 4.)
- [152] G. Santarelli, C. Audoin, A. Makdissi, P. Laurent, G. Dick, and A. Clairon. Frequency stability degradation of an oscillator slaved to a periodically interrogated atomic resonator. *IEEE Trans. Ultrason. Ferroelectr. Freq. Control*, 45(4):887–894, 1998. doi: 10.1109/58.710548. (Cited on page 59.)
- [153] A. Scheibe and U. Adelsberger. Variations in the Length of the Astronomical Day and Time Determinations by the PTR Quartz Clocks. *Physikalische Zeitschrift*, 37:185, 1936. (Cited on page 3.)
- [154] T. R. Schibli, K. Minoshima, F.-L. Hong, H. Inaba, A. Onae, H. Matsumoto, I. Hartl, and M. E. Fermann. Frequency metrology with a turnkey all-fiber system. *Opt. Lett.*, 29(21):2467–2469, November 2004. doi: 10.1364/OL.29.002467. (Cited on page 90.)
- [155] J. P. Schiffer. Phase transitions in anisotropically confined ionic crystals. *Phys. Rev. Lett.*, 70(6):818–821, February 1993. doi: 10.1103/PhysRevLett.70.818. (Cited on page 26.)
- [156] S. Schiller and C. Lämmerzahl. Molecular dynamics simulation of sympathetic crystallization of molecular ions. *Phys. Rev. A*, 68:053406, Nov 2003. doi: 10.1103/PhysRevA.68.053406. (Cited on page 63.)
- [157] P. Schindler. *Frequency synthesis and pulse shaping for quantum information processing with trapped ions*. Diploma thesis, Universität Innsbruck, Innsbruck, Austria, 2008. (Cited on page 87.)
- [158] P. O. Schmidt, T. Rosenband, C. Langer, W. M. Itano, J. C. Bergquist, and D. J. Wineland. Spectroscopy Using Quantum Logic. *Science*, 309(5735):749–752, July 2005. doi: 10.1126/science.1114375. (Cited on pages 12, 23, 112, and 116.)

- [159] F. Schmidt-Kaler, J. Eschner, G. Morigi, C. Roos, D. Leibfried, A. Mundt, and R. Blatt. Laser cooling with electromagnetically induced transparency: application to trapped samples of ions or neutral atoms. *Applied Physics B: Lasers and Optics*, 73(8):807–814, December 2001. doi: 10.1007/s003400100721. (Cited on page 41.)
- [160] J. A. Sherman, N. D. Lemke, N. Hinkley, M. Pizzocaro, R. W. Fox, A. D. Ludlow, and C. W. Oates. High-Accuracy Measurement of Atomic Polarizability in an Optical Lattice Clock. *Phys. Rev. Lett.*, 108(15):153002, April 2012. doi: 10.1103/PhysRevLett.108.153002. (Cited on page 127.)
- [161] J. D. Siverns, L. R. Simkins, S. Weidt, and W. K. Hensinger. On the application of radio frequency voltages to ion traps via helical resonators. *arXiv:1106.5013*, June 2011. (Cited on pages 77 and 78.)
- [162] Sourceforge. project: Pulse Programmer, 2014. <http://pulse-programmer.org>, accessed on 05.05.2014. (Cited on page 87.)
- [163] J. Stenger, H. Schnatz, C. Tamm, and H. Telle. Ultraprecise Measurement of Optical Frequency Ratios. *Phys. Rev. Lett.*, 88(7):073601, February 2002. doi: 10.1103/PhysRevLett.88.073601. (Cited on pages 91 and 94.)
- [164] S. Stenholm. The semiclassical theory of laser cooling. *Rev. Mod. Phys.*, 58(3):699–739, 1986. doi: 10.1103/RevModPhys.58.699. (Cited on pages 35 and 37.)
- [165] M. Takamoto, F.-L. Hong, R. Higashi, and H. Katori. An optical lattice clock. *Nature*, 435(7040):321–324, May 2005. doi: 10.1038/nature03541. (Cited on page 4.)
- [166] U. Tanaka, K. Masuda, Y. Akimoto, K. Koda, Y. Ibaraki, and S. Urabe. Micromotion compensation in a surface electrode trap by parametric excitation of trapped ions. *Appl. Phys. B*, 107(4):907–912, June 2012. doi: 10.1007/s00340-011-4762-2. (Cited on page 109.)
- [167] F. Tauser, A. Leitenstorfer, and W. Zinth. Amplified femtosecond pulses from an Er: fiber system: Nonlinear pulse shortening and selfreferencing detection of the carrier-envelope phase evolution. *Optics Express*, 11(6):594–600, 2003. (Cited on page 90.)
- [168] J. Terrien. News from the International Bureau of Weights and Measures. *Metrologia*, 4(1):41, January 1968. doi: 10.1088/0026-1394/4/1/006. (Cited on page 3.)

- [169] E. Träbert, A. Wolf, J. Linkemann, and X. Tordoir. Measurement of the  $B^+$  and  $Al^+$  intercombination and  $Sc^{12+}$  forbidden transition rates at a heavy-ion storage ring. *J. Phys. B: At. Mol. Opt. Phys.*, 32(2):537, 1999. (Cited on page 11.)
- [170] Q. A. Turchette, Kielpinski, B. E. King, D. Leibfried, D. M. Meekhof, C. J. Myatt, M. A. Rowe, C. A. Sackett, C. S. Wood, W. M. Itano, C. Monroe, and D. J. Wineland. Heating of trapped ions from the quantum ground state. *Phys. Rev. A*, 61(6):063418, May 2000. doi: 10.1103/PhysRevA.61.063418. (Cited on pages 32, 33, 111, and 115.)
- [171] T. Udem, R. Holzwarth, and T. W. Hänsch. Optical frequency metrology. *Nature*, 416(6877):233–237, 2002. (Cited on page 89.)
- [172] J. K. Wahlstrand, J. T. Willits, C. R. Menyuk, and S. T. Cundiff. The quantum-limited comb lineshape of a mode-locked laser: Fundamental limits on frequency uncertainty. *Optics Express*, 16(23):18624–18630, 2008. (Cited on page 92.)
- [173] Y. Wan, F. Gebert, J. B. Wübbena, N. Scharnhorst, S. Amairi, I. D. Leroux, B. Hemmerling, N. Lörch, K. Hammerer, and P. O. Schmidt. Precision spectroscopy by photon-recoil signal amplification. *Nat Commun*, 5, January 2014. doi: 10.1038/ncomms4096. (Cited on pages 23, 102, 103, 104, 105, and 112.)
- [174] B. R. Washburn, S. A. Diddams, N. R. Newbury, J. W. Nicholson, M. F. Yan, and C. G. Jrgensen. Phase-locked, erbium-fiber-laser-based frequency comb in the near infrared. *Optics letters*, 29(3):250–252, 2004. (Cited on page 90.)
- [175] G. Welsch, R. Boyer, and E. Collings. *Materials Properties Handbook: Titanium Alloys*. Materials properties handbook. ASM International, 1993. ISBN 9780871704818. (Cited on page 71.)
- [176] J. H. Wesenberg, R. J. Epstein, D. Leibfried, R. B. Blakestad, J. Britton, J. P. Home, W. M. Itano, J. D. Jost, E. Knill, C. Langer, R. Ozeri, S. Seidelin, and D. J. Wineland. Fluorescence during Doppler cooling of a single trapped atom. *Phys. Rev. A*, 76:053416, Nov 2007. doi: 10.1103/PhysRevA.76.053416. (Cited on page 60.)
- [177] D. Wineland. Radiation-Pressure Cooling of Bound Resonant Absorbers. *Phys. Rev. Lett.*, 40(25):1639–1642, 1978. doi: 10.1103/PhysRevLett.40.1639. (Cited on page 35.)
- [178] D. J. Wineland and W. M. Itano. Laser cooling of atoms. *Phys. Rev. A*, 20(4):1521, October 1979. doi: 10.1103/PhysRevA.20.1521. (Cited on page 35.)

- [179] D. J. Wineland, C. Monroe, W. M. Itano, D. Leibfried, B. E. King, and D. M. Meekhof. Experimental issues in coherent quantum-state manipulation of trapped atomic ions. *J. Res. Natl. Inst. Stand. Technol.*, 103(3):259–328, 1998. (Cited on pages 22, 23, 24, 25, and 31.)
- [180] D. J. Wineland, J. C. Bergquist, J. J. Bollinger, R. E. Drullinger, and W. M. Itano. Quantum Computers and Atomic Clocks. In *Proceedings of the 6th Symposium on Frequency Standards and Metrology*, pages 361–368, University of St Andrews, Fife, Scotland, 2002. doi: 10.1142/9789812777713\_0040. (Cited on page 12.)
- [181] D. Wineland and H. Dehmelt. Proposed  $10^{14}$  laser fluorescence spectroscopy on  $\text{Ti}^+$  mono-ion oscillator III. *Bull. Am. Phys. Soc.*, 20:637, 1975. (Cited on page 39.)
- [182] A. Wolf, S. van den Berg, C. Gohle, E. Salumbides, W. Ubachs, and K. Eikema. Frequency metrology on the  $4s^2S_{1/2}$ - $4p^2P_{1/2}$  transition in  $^{40}\text{Ca}^+$  for a comparison with quasar data. *Phys. Rev. A*, 78(3):032511, September 2008. doi: 10.1103/PhysRevA.78.032511. (Cited on pages 101, 104, and 105.)
- [183] A. Wolf, S. van den Berg, W. Ubachs, and K. Eikema. Direct Frequency Comb Spectroscopy of Trapped Ions. *Phys. Rev. Lett.*, 102(22):223901, June 2009. doi: 10.1103/PhysRevLett.102.223901. (Cited on page 102.)
- [184] J. B. Wübbena. *Photoionisation von Calcium*. Diploma thesis, Leibniz Universität Hannover, 2011. (Cited on pages 80 and 81.)
- [185] J. B. Wübbena, S. Amairi, O. Mandel, and P. O. Schmidt. Sympathetic cooling of mixed-species two-ion crystals for precision spectroscopy. *Phys. Rev. A*, 85(4):043412, April 2012. doi: 10.1103/PhysRevA.85.043412. (Cited on pages 24, 53, 133, and 134.)
- [186] T. W. Wübbena. *Spektroskopie des  $^1S_0 \rightarrow ^3P_0$  Uhrenübergangs von  $^{24}\text{Mg}$  in einem optischen Gitter bei der vorhergesagten magischen Wellenlänge*. PhD thesis, Leibniz Universität Hannover, 2013. (Cited on page 4.)
- [187] R. Yamazaki, T. Iwai, K. Toyoda, and S. Urabe. Phase-locked laser system for a metastable states qubit in  $^{40}\text{Ca}^+$ . *Opt. Lett.*, 32(15):2085–2087, August 2007. doi: 10.1364/OL.32.002085. (Cited on page 129.)
- [188] N. Yu, H. Dehmelt, and W. Nagourney. The  $^1S_0 - ^3P_0$  transition in the aluminum isotope ion  $^{26}\text{Al}^+$ : a potentially superior passive laser frequency standard and spectrum analyzer. *Proc. Natl. Acad. Sci. U.S.A.*, 89(16):7289, 1992. (Cited on page 10.)

- [189] W. Zhang, M. Lours, M. Fischer, R. Holzwarth, G. Santarelli, and Y. L. Coq. Characterizing a fiber-based frequency comb with electro-optic modulator. *arXiv:1109.3123*, September 2011. (Cited on pages 91 and 93.)



## ACKNOWLEDGMENTS

---

I thank Prof. Piet O. Schmidt for giving me the opportunity to write this thesis in his institute. I also thank Prof. Christian Ospelkaus and Prof. Klemens Hammerer for agreeing to be part of the PhD examination committee.

I acknowledge the financial support from the Hannover School for Laser, Optics and Space-Time Research (HALOSTAR) and the German National Academic Foundation, represented by Dr. Stefan Pfalz and Dr. Peter Antes, respectively.

I acknowledge the support of my present and former colleagues at the iQloc experiment Sana Amairi, Stephan Hannig, Ian D. Leroux, Olaf Mandel, Jonathan Martinez, Nils Scharnhorst, Piet O. Schmidt, Ivan Sherstov, and Vu Phan Tanh, who were involved in much of the experimental work.

I thank the present and former members of the DIFCOS experiment, namely Florian Gebert, Børge Hemmerling, Piet O. Schmidt, Ivan Sherstov, Yong Wan, and Fabian Wolf for providing helpful advice during the setup of the laboratory and being very generous with the lending of their equipment.

I thank Gesine Grosche, Sebastian Raupach and Thomas Legero for providing the stable 1542 nm reference laser and setting up the fiber stabilization to our laboratory.

I thank Christopher Bleuel, Peter-Christian Carstens, Julia-Aileen Fenske, and Olga Lick from the electronic workshop and Sven Klitzing, Rebecca Müller, and Alexander Pablocki from the mechanical workshop for their efforts in building so much of the equipment of the experiment.

I thank Sandra Ludwig and Birgit Ohlendorf for administrative support.

Finally I acknowledge the many hours that Stephan Hannig, Christiane Kellner, Ian D. Leroux, Olaf Mandel, Nils Scharnhorst, Piet O. Schmidt, and Temmo Wübbena spent in careful reading of this manuscript.





## CURRICULUM VITAE

---

### PERSONAL DETAILS

Name	Jannes Bernhard Wübbena
Date of birth	17.07.1986
Place of birth	Hannover
Marital status	unmarried

### POSTGRADUATE STUDIES

since 2011	Doctoral studies at the QUEST Institute for Experimental Quantum Metrology, PTB and Leibniz Universität Hannover, Braunschweig, Germany
2010	Master of Photonics from the Australian National University, Canberra, Australia
2009-2010	Student of photonics at the Australian National University, Canberra, Australia

### UNDERGRADUATE STUDIES

2011	Diplom in Physik, Studienrichtung technische Physik from the Leibniz Universität Hannover, Hannover, Germany
2010 - 2011	Diploma thesis, "Photoionisation von Calcium"
2007	Vordiplom in Physik from the Leibniz Universität Hannover, Hannover, Germany
2005-2011	Student of physics at the Leibniz Universität Hannover, Hannover, Germany

### HIGH SCHOOL

2005	Abitur from the Geschwister-Scholl-Gymnasium Berenbostel, Garbsen, Germany
1998 - 2005	Geschwister-Scholl-Gymnasium Berenbostel, Garbsen, Germany



#### COLOPHON

This document was typeset using the typographical look-and-feel `classicthesis` developed by André Miede. The style was inspired by Robert Bringhurst's seminal book on typography "*The Elements of Typographic Style*". `classicthesis` is available for both  $\text{\LaTeX}$  and  $\text{\LyX}$ :

<http://code.google.com/p/classicthesis/>

*Final Version* as of July 10, 2014 (`classicthesis` version 4.1).